Electromobility

Materials and Manufacturing Economics

Fyhr, Pontus

2018

Link to publication

Electromobility
Materials and Manufacturing Economics

Electromobility
Materials and Manufacturing Economics

Pontus Fyhr

DOCTORAL DISSERTATION
by due permission of the Faculty of Engineering, Lund University, Sweden
to be defended at lecture hall M:E, M-building, LTH, Ole Römers väg 1,
221 00, Lund
on June 7th 2018 at 10:15 a.m.

Faculty opponent

Prof. Lennart Josefson

Title

Electromobility - Materials and Manufacturing Economics

Abstract

Electromobility is the most promising solution to reduce emissions from road transport, which is necessary in order to stay below global temperature increase targets. Battery electric vehicles and plug-in hybrids show strong growth, but they represent only around 1% of total yearly light vehicle production. Cost, range and lacking infrastructure are cited as reasons.

A number of models to study the cost of materials and manufacturing in electric drivetrains are presented. A drivetrain is not a fixed point, but rather a continuum that can be created by the combination of interconnected subsystems. Thus leading to a necessity in first deriving requirements for the powertrain, and for the model to be able to scale with those requirements in terms of size, performance and production volumes. This is achieved by studying each subsystem in detail, down to the materials, parts and operations that are required to create each component. Due to uncertainties from for example fluctuating prices of materials the model also has the capability to account for uncertain data.

An important result shows how high speed electric machines paired with two-speed transmissions can reduce drivetrain cost. Drivetrains must be studied as a whole in order to understand trade-offs and reach cost efficient solutions, from the generation of specifications to the interconnected relationships between design and manufacturing. Result figures for powertrains and charging systems have also been used in a study of a binary shift to fully electric exemplified in the Swedish road transportation system. This study shows that electric roads should be made available to all road vehicles, not solely heavy vehicles, due to a dramatic lowering of total societal costs.

Keywords

electromobility, electric drivetrain, electric machine, power electronic converter, manufacturing economics

Classification system and/or index terms (if any)

Signature _____   Date ____2018-05-10____

Electromobility
Materials and Manufacturing Economics

Pontus Fyhr

LUND
UNIVERSITY

Improving the transportation system, one napkin at a time

Acknowledgements

The work presented in this doctoral thesis has been carried out with the help of many great, inquisitive and curious minds. It is very much a case of the old adage, *standing on the shoulders of giants* with balance provided by many CPU cores.

The giant Gabriel Domingues-Olavarría with whom I collaborated on a large part of this work; I have learned so much and hope to have taught you something too.

Many discussions have also been had with, Francisco Márquez-Fernández, Sebastian Hall, Stefan Skoog, Pär Ingelström, Zhe Huang, Rasmus Andersson, Mattias Svahn, Rikard Hjelm, Ville Akujärvi, Lanny Kirkhorn, Mats Alaküla, Avo Reinap, Sampsa Laakso, Carin Andersson, Christer Lundh, Anders Göransson, Fredrik Henriksson, Filip Lenrick, Pär Olsson, Martin Tunér, Krister Olsson, Theodore Zannakis, Martin West, Åke Nyström and many other at Iprod and IEA. A special thanks to my always insightful supervisors Mats Andersson, Kenneth Frogner, and Tord Cedell.

I also have my parents to thank for so much, my engineer-in-spirit father and brilliant undercover economist mother, both as supportive, encouraging and patient as my other family members. I remain equally grateful to friends who put up with endless rants, and still manage to offer fresh perspectives.

Most grateful of all I remain to my loving fiancée-sambo, and math wizard, Naji-san-jan.

Lund, May 2018

Pontus Fyhr

Abstract

Electromobility is the most promising solution to reduce emissions from road transport, which is necessary in order to stay below global temperature increase targets. Battery electric vehicles and plug-in hybrids show strong growth, but they represent only around 1% of total yearly light vehicle production. Cost, range and lacking infrastructure are cited as reasons.

A number of models to study the cost of materials and manufacturing in electric drivetrains are presented. A drivetrain is not a fixed point, but rather a continuum that can be created by the combination of interconnected subsystems. Thus leading to a necessity in first deriving requirements for the powertrain, and for the model to be able to scale with those requirements in terms of size, performance and production volumes. This is achieved by studying each subsystem in detail, down to the materials, parts and operations that are required to create each component. Due to uncertainties from for example fluctuating prices of materials the model also has the capability to account for uncertain data.

An important result shows how high speed electric machines paired with two-speed transmissions can reduce drivetrain cost. Drivetrains must be studied as a whole in order to understand trade-offs and reach cost efficient solutions, from the generation of specifications to the interconnected relationships between design and manufacturing. Result figures for powertrains and charging systems have also been used in a study of a binary shift to fully electric exemplified in the Swedish road transportation system. This study shows that electric roads should be made available to all road vehicles, not solely heavy vehicles, due to a dramatic lowering of total societal costs.

Popular Scientific Description

Emissions from road vehicles make up approximately 20% of total global CO_2, they also create local pollution of NO_x and particulates. In order to lower emissions, the way vehicles are propelled needs to change, electrified vehicles are as capable as those driven solely by internal combustion engines. Emissions performance centers on grams CO_2/km over a predefined driving cycle. The average value for vehicles sold in the EU in 2016 was 118 g CO_2/km, and the target for 2021 is 95 g CO_2/km, these regulations also define extremely low emissions as below 50 g CO_2/km. In order to reach extremely low tailpipe emissions, the tractive effort must come from a drivetrain which primarily does not use energy stored in covalent bonds between carbon atoms. The problem at hand, is that the addition of electrified traction components in both battery electric and plug-in hybrids, add complexity and cost to the vehicles. In order to offset these added costs, many countries offer tax credits and incentives for both low and zero emissions vehicles, in the hope that economies of scale will lead to price levels low enough to allow electrified vehicles to stand on their own four wheels. My work analyzes how the components in electrified vehicles are sized and built, by breaking down the vital components, like electric machines and power electronic converters, into the constituents that make up the components and the manufacturing processes required to reshape those constituents into useful parts. This allows for discussions on critical materials that often emerge, regarding elements such as neodymium and dysprosium. The analysis of how the performance of individual components relate to the cost of materials and processes that shape them, and in turn how each individual component affects the performance and cost of the final system.

The work has centered on deriving maps of the cost, performance, and scale relationship of electrified drivetrains and components such as chargers. These maps can be used to answer questions of if, how, and at what scale the cost of electrified vehicles will reach a point where they can lower ownership costs and emissions, without substantial incentives. From these analyses, a major conclusion is that an electric road network (large scale slotcar track) for both passenger cars and heavy traffic would lower total societal costs and emissions.

List of Papers

I **The scale of permanent magnet materials for automotive traction motors**

Pontus Fyhr, Mats Andersson, Jan-Eric Ståhl
2012 2nd International Electric Drives Production Conference (EDPC)
Year: 2012 Pages: 1 - 7

II **A modular framework for evaluation of electrical machine production costs**

Pontus Fyhr, Mats Andersson, Jan-Eric Ståhl
2013 3rd International Electric Drives Production Conference (EDPC)
Year: 2013 Pages: 1-5

III **Statistical interfaces for production of a permanent magnet based rotor**

Pontus Fyhr, Mats Andersson, Jan-Eric Ståhl
2014 4th International Electric Drives Production Conference (EDPC)
Year: 2014 Pages: 1-6

IV **Performance and Manufacturability Tradeoffs of Different Electrical Machine Designs**

Pontus Fyhr, Gabriel Domingues, Avo Reinap, Mats Andersson, Mats Alaküla
International Electric Machines and Drives Conference (IEMDC), Miami
Year: 2017 Pages: 1-7

V **From Chip to Converter: a Complete Cost Model for Power Electronics Converters**

Gabriel Domingues-Olavarría, Pontus Fyhr, Avo Reinap, Mats Andersson, Mats Alaküla
IEEE Transactions on Power Electronics Year: 2017 Pages: 8681 - 8692

VI **Optimization of Electric Powertrains Based on Scalable Cost and Performance Models**

Gabriel Domingues, Francisco J. Márquez-Fernández, Pontus Fyhr, Mats Andersson, Mats Alaküla

IEEE Transactions on Industry Applications (under review) Year: 2018

VII **Electric Roads: Reducing the Societal Cost of Automotive Electrification**

Pontus Fyhr, Gabriel Domingues, Mats Andersson, Francisco J. Márquez-Fernández, Hans Bängtsson, Mats Alaküla

International Transport Electrification Conference (ITEC), Chicago Year: 2017 Pages: 773 - 778

List of Symbols

a	Area, m^2
$\vec{B}$	Flux density, T
B_r	Remanent induction, T
B_m	Magnetic induction at load point, T
BH_{max}	Maximum energy product, J/m^3
C	Ultimate tensile strength, Pa
C_{ref}	Ultimate tensile strength reference, Pa
c_d	Drag coefficient, -
D	Diameter, m
d	Distance, m
e	Euler's number, -
$\vec{\mathcal{F}}$	Magnetomotive force, A turns
F	Force, N
f	Unknown distribution, contextual
$\widehat{f}$	Probability distribution, -
f_{lw}	Function of complexity and size of die, mm^{-1}
g	Gravity of Earth, m/s^2
g_i	Known function, contextual
H	External field, kA/m
H_{cJ}	Intrinsic coercivity, kA/m
H_{cB}	Coercive force at B=0, kA/m
H_m	Coercive force at load point, T
h_{cg}	Centroid distance to ground, m
$\vec{i}$	Current, A
K_A	Annuity cost of tool, €
K_B	Material cost, €
K_{CP}	Cost during production, €/s
K_{CS}	Cost during downtime, €/s
K_D	Wage cost, €/s
K_{die}	Die cost, €
K_{prod}	Production cost, €/h
k	Cost, €

k_p	Blanking pressure, Pa
l	Length, m
L	Inductance, H
M_{po}	Term proportional to area, s
m	Mass, kg
m_v	Vehicle mass, kg
n	Natural number, -
n_p	Number of poles, -
P	Power, W
p	Probability function, -
$\mathbf{p}_n$	Point, (m,m)
p_{BME}	Brake mean effective pressure, Pa
q_Q	Quality yield, -
q_s	Downtime fraction, -
$\mathcal{R}$	Reluctance, A turns/Wb
R	True distribution, -
$R*$	Approximate distribution, -
R_{hexUn}	Uneven hexagonal packing ratio, -
R_{hexEv}	Even hexagonal packing ratio, -
R_{square}	Square hexagonal packing ratio, -
r	Radius, m
r_0	Initial radius, m
r_1	Processed radius, m
r_s	Winding resistance, Ω
r_w	Wheel radius, m
s	Standard deviation, contextual
T	Temperature, K
t	Material thickness, m
t_0	Nominal cycle time, s
t_{0-100}	Acceleration time, s
u	Index of parallel manufacturing operations, -
V_d	Displacement volume, m^3
V_g	Air gap volume, m^3
V_m	Magnet volume, m^3
v	Number of manufacturing operations, -
w	Index of sequential manufacturing operations, -
w_r	Rear static load fraction, -
$\mathbf{X}$	Dataset, -
$\mathbf{X}^*$	Bootstrap samples, -
$\dot{x}$	Velocity in x, m/s
$\ddot{x}$	Acceleration in x, m/s^2
Y_s	Number of seconds in a year, s
z	function, contextual

α	Temperature coefficient of remanent induction, -
α_c	Temperature coefficient of resistivity, -
α_v	Temperature coefficient of thermal expansion, -
β	Temperature coefficient of coercivity, -
γ	Manufacturing operation, -
δ	Skin depth, m
ϵ_i^*	Residual, contextual
η	Energy conversion efficiency, -
θ	Rotor angular position, rad
κ	Confidence range, -
$\vec{\lambda}$	Flux linkage, Vs
μ	Relative permeability, -
μ_0	Vacuum permeability, H/m
μ_{rec}	Recoil permeability, -
μ_t	Friction coefficient, -
ξ	Unknown parameter, contextual
π	pi, -
ϱ	Resistivity, Ωm
ρ	Density, kg/m^3
σ	Stress, Pa
τ	Torque, Nm
ψ	Inclination, rad
ω_e	Electrical angular frequency, rad/s
ω_m	Mechanical angular frequency, rad/s

Contents

Part I

COMPREHENSIVE SUMMARY

Chapter 1

Road Vehicles
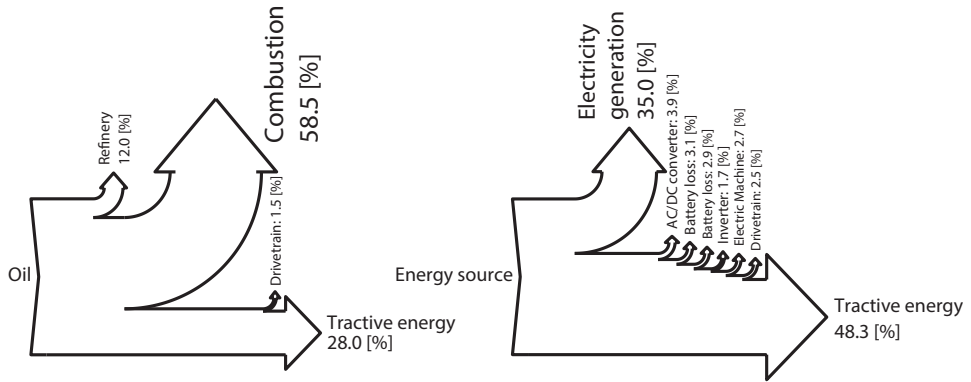
Figure 1.1: Two Sankey charts depicting a diesel vehicle on the left and a battery electric vehicle on the right, representing a simple well to wheel analysis of the two. One is powered by oil, which is refined and then burned, the other powered by electricity generated from some energy source. The electric energy is converted multiple times, from AC to DC and back to AC. The conversion efficiencies are averages of those listed in table 1.1.

1.1 Simplified Well to Wheel

The total efficiency of a serial system with a number n conversion steps is the partial product of each conversion efficiency in the sequence

$$\eta_{tot} = \prod_{i=1}^{n} \eta_i, \quad \eta_i < 1 \tag{1.1}$$

with this in mind, it is in general preferable to convert energy as few times as possible, with as high efficiency as possible in each conversion before making practical use of it, an example of two systems is shown in figure 1.1.

Well to wheel analysis is often used to estimate the total efficiency of a vehicle traction system, and it historically refers to how a chemical fuel from a well, typically crude oil, is converted or refined into useful fuel for a spark ignition (SI) or compression ignition (CI) such as gasoline or diesel, summarized as the internal combustion engine (ICE). After the refinement step, the fuel is transported to a gas station, where it is pumped into an on-board storage system, the fuel tank. Then it is pumped or sucked into injection systems or carburetors, ignited to generate a useful torque, and via a series of mechanical linkages transmitted to the wheels and tires, which generate a force on the road to propel the vehicle in the desired direction.

In battery electric vehicles (BEV), the well is typically a power plant, nuclear, hydro-electric, coal, wind, photo-voltaic, which typically generate very high voltage alternating current (AC). The plant is connected to the electrical power grid, which transmits the electric energy to a transformer station, transformed to transmission grid voltage, then transmitted again and transformed to a local low voltage distribution grid, transformed again to customer voltages, rectified to DC, converted to high frequency AC and passed through a high frequency transformer for galvanic isolation, rectified again to DC for charging and stored in the batteries. Then drawn from the batteries, converted to AC at a suitable variable frequency to drive the electric machine, transmitted via a series of mechanical linkages to the wheels and tires, which generate a force on the road to propel the battery electric vehicle in the desired direction.

Hydrogen (H_2) fuel-cell electric vehicles (FCEV) are similar to a BEVs, but a large part of the batteries are replaced with high pressure tanks and conversion systems to oxidize hydrogen in order to generate a DC voltage in the fuel cell. Hydrogen can be produced at centralized locations where electric power is cheap, by electrolysis of water, though currently more than 90% is produced from fossil sources [1]. The distribution is imagined to look similar to that of our current fossil-fuel world, one benefit being that whoever has water and electrical power may start their own well.

Other solutions, such as plug in hybrid electric vehicles (PHEV), exist in many configurations. The two most straightforward variants are series hybrids, which is a BEV with an on-board ICE connected to a generator, and parallel hybrids, which is the same as a normal ICE vehicle with an electric machine somewhere in the path of the mechanical torque transmission to the ground. A more complex variant is called the power-split hybrid, which has electric machines and gear-sets connected to the ICE, allowing variable combinations of power to the road or the battery.

Table 1.1: Energy conversion efficiencies to and from common energy carriers.

Energy type	Conversion efficiency η (-)	
	Efficiency to	Efficiency from
H_2	0.70[a]–0.90[b]	0.32[c]-0.4[d]
Diesel	0.87–0.90[e]	0.26–0.41[6, 7]
Gasoline	0.83–0.88[e]	0.26–0.28[8]
Ethanol (E100)	0.31–0.71[f]	0.27–0.31[8]
Methanol (M100)	0.69[10]–0.73[11]	0.34–0.43[6]
Li battery	0.93–0.98[g]	0.93–0.98[g]
AC/DC converter	-	0.93[14]–0.95[15]
Electric power generation	-	0.625[h]

[a]Polymer Electrolyte Membrane [2]
[b]Solid Oxide Electrolysis [1]
[c]Combustion in ICE [3]
[d]PEM Fuel cell [4]
[e]Refinery efficiency [5]
[f]Biomass to ethanol ratio [9]
[g]Simplified model from resistance and power [12, 13]
[h]Electric power generation efficiency incl. transmission [16]

Table 1.2: Gravimetric and volumetric energy density of different energy storage entities.

Storage type	Energy densities	
	Gravimetric (kWh / kg)	Volumetric (kWh / dm^3)
H_2 (700 bar)	$2-3$[a]	$1.5-2.5$[a]
Diesel	11.8[18]–13[19]	9.8[18]–9.9[20]
Gasoline	12.1[20]	8.9[20]
Ethanol (E100)	7.4[18]	5.84[18]
Methanol (M100)	6.2[19]	4.94[19]
Li battery	$0.15-0.25$[b]	$0.2-1.1$[b]

[a]System figures [17]
[b]Lithium cobalt oxide cathode, graphite cathode [21, 22, 23]

Table 1.1 lists conversion efficiency ranges to and from some common energy carriers for vehicles found in literature. These energy carriers require different conversion systems, both in stationary and on-board vehicles. Comparisons of vehicle economics and emissions for different powertrain layouts, including combinations such as hybrids/plug-in hybrids, range-extended BEV, fuel-cell range extended BEVs in powertrain simulations over a number of driving cycles by Campanari et al. [24]. Thomas [25] concludes that "Fuel cell electric vehicles are superior to advanced lithium-ion full function battery electric vehicles, since the fuel cell EV:" followed by a list of benefits: weight, space, cost, well to

wheel emissions from fossil or biomass sources, and time to refuel. Thomas [25] concedes that BEVs do have some advantages as well, including lower fuel cost per distance, lower well to wheel from wind or solar and better access to initial stored energy. Offer et al. [26] conclude that the results are very sensitive to the input data regarding capital costs. They also point to a need for more detailed analysis regarding power electronic converters. Felgenhauer et al. [27] investigate the synergies of BEV and FCEV transport systems in a community, taking into account conversion efficiencies and effects on the grid. Common to these all these works is that the vehicles require an electric propulsion system, and thorough understanding of the associated performance and cost of these components.

1.2 Longitudinal Vehicle Dynamics

A moving vehicle traveling at a constant speed must maintain a force equilibrium, the tractive force exerted by the driving wheels on the road equal the sum of the forces opposing it. The forces can be described by rolling resistance F_{roll}, aerodynamic drag F_{drag}, any potential energy gained or lost due to inclines F_{incl}. Equations describing the parameters can be found in for example Rajamani [28].

$$F_{trac} = F_{roll} + F_{drag} + F_{incl} + F_m \qquad (1.2)$$

F_{trac} is the sum of these dissipative forces, with the term F_m accounting for changes in momentum. The rolling resistance is a function of gravitational load $m_v g \cos \psi$ and a rolling resistance coefficient c_r. Aerodynamic drag is a function of the vehicle shape and frontal area, $c_d a_f$, the density of the media the vehicle is traveling through, here ρ_{air} and vehicle speed squared, $\dot{x}^2$. External wind velocity is disregarded here.

$$
\begin{aligned}
F_{roll} &= m_v g c_r \cos \psi \\
F_{drag} &= \frac{c_d a_f \rho_{air} \dot{x}^2}{2} \\
F_{incl} &= m_v g \sin \psi \\
F_m &= m_v \ddot{x}
\end{aligned}
\qquad (1.3)
$$

If this vehicle happens to find itself traveling on an inclination, any gain or loss in potential energy gives a nonzero ψ, in F_{incl}, and an accelerating vehicle will need to gain momentum according to F_m. Furthermore, the vehicles in this work follow the Roll Pitch Yaw convention, with x in the direction of travel, y to the left and z up, see figure 1.2.

If a small car, such as a BMW i3, appears behind the truck on the highway and wants to overtake as depicted in figure 1.3, it applies all its available torque. The resulting vehicle positions can be found by solving the time integral of equation 1.2. This event is depicted in figure 1.4.
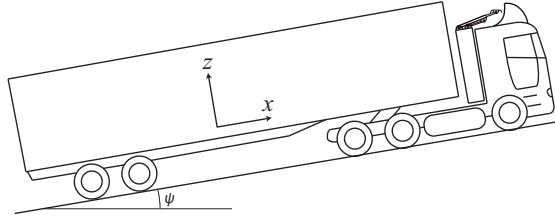

Figure 1.2: A truck traveling up a slope at constant velocity, in doing so it encounters aerodynamic drag, rolling resistance and it is gaining potential energy. Its $m_v = 40000$ kg, $c_d a_f = 5.34$ m^2 and $r_w = 0.5$ m.
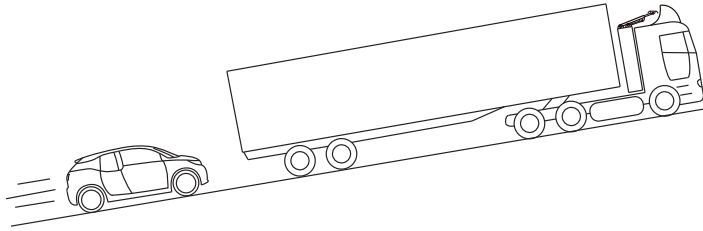
Figure 1.3: Suddenly, a wild i3 appears and overtakes the truck. Its $m_v = 1370$ kg, $c_d a_f = 0.69$ m^2 and $r_w = 0.35$ m

The momentum component of equation 1.3 increases the road load under acceleration to match the available torque, as depicted in figure 1.4. The entire maneuver takes 4.7 s up a 2.5 degree slope, with both vehicles traveling at 80 km/h initially, the i3's front is 8 m behind the 25.25 m long European long haul truck. The maneuver is complete when the rear of the i3 is 8 m ahead of the truck. The same principles are applied in drive-cycle simulations and tests, which can be used for studies of energy consumption, component sizing, thermal analysis and certification.

1.3 Traction Systems

As stated in section 1.1, the purpose of a traction system is to generate a force on the road to propel the vehicle in the desired direction. Equations 1.2-1.3 describe the torque requirement on the wheels as a function of desired speed, vehicle mass, rolling resistance, aerodynamic drag and gradient loads.
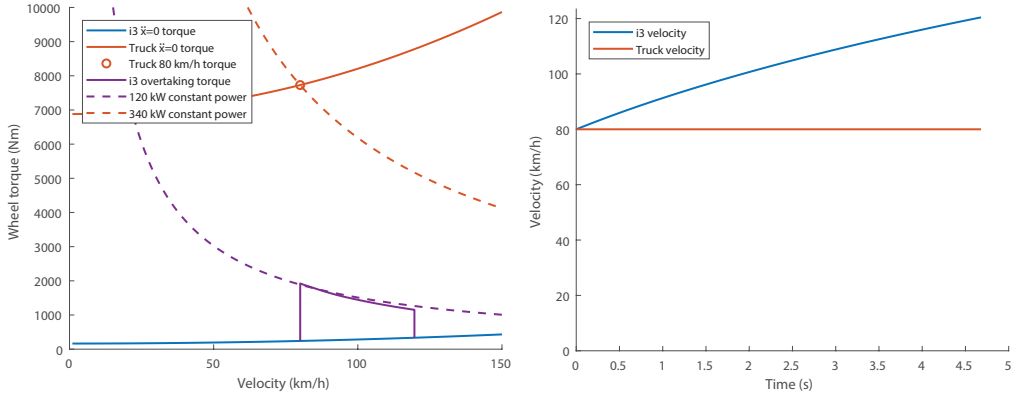
Figure 1.4: When the wheel torque of the i3 increases above the steady state load, it accelerates due to the momentum component of equation 1.2. The peak acceleration of the i3 is 1.26 m/s^2. The wheel torque of the truck is more than three times the peak torque of the i3, in order to maintain a constant speed on this grade. The i3 uses a peak power of 120 kW, while the truck is using a continuous 340 kW.

1.3.1 Electric Drivetrains
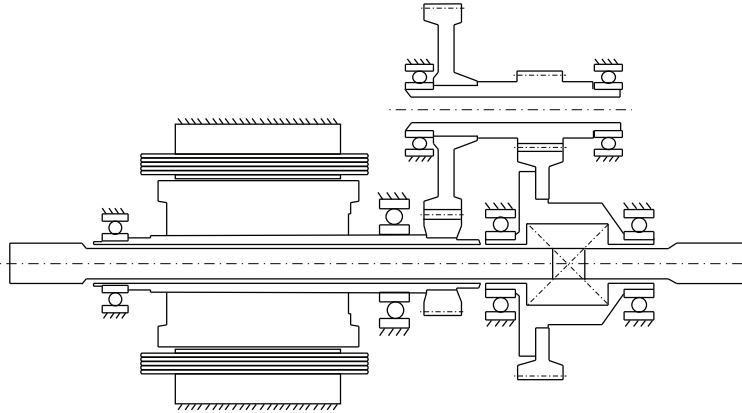
Figure 1.5: A schematic illustration of the Chevrolet Bolt powertrain layout, featuring a hairpin wound stator, interior permanent magnet rotor, 6 bearings, two hollow shafts, 4 helical gears, 4 differential gears and two driveshafts.

Grunditz and Thiringer [29] have performed a review of drivetrain specifications for BEVs. A very large range of powertrain configurations are possible in a BEV, FCEV or PHEV, the most straightforward one being the replacement of a combustion machine with an electric machine, and the gearbox with a fixed reduction gear. One elegant example is the Chevrolet Bolt powertrain, illustrated in figure 1.5.
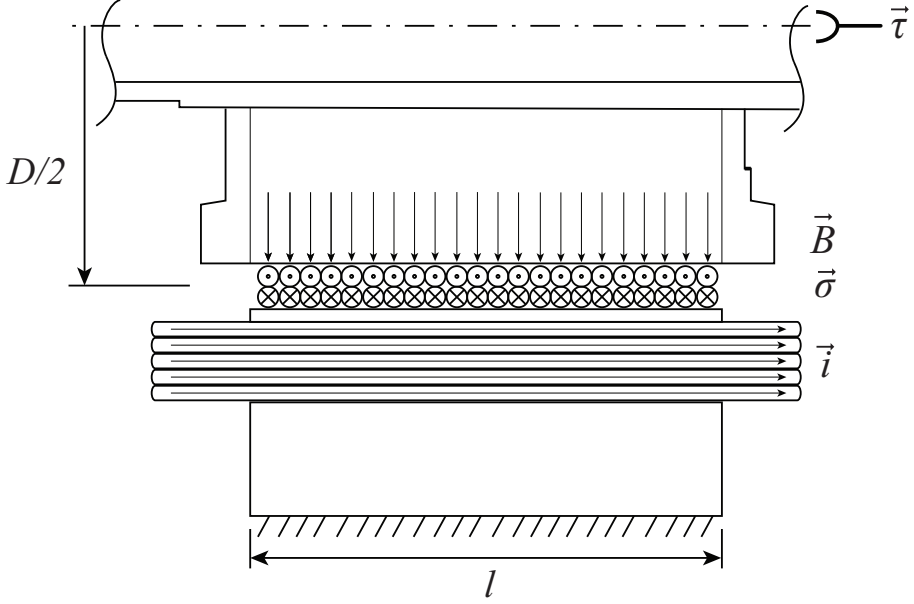
Figure 1.6: A cross section view of the torque ($\vec{\tau}$) generated in a rotating machine, by the airgap shear stress ($\vec{\sigma}$), as generated by the magnetic field ($\vec{B}$) and the linear current density ($\vec{ni}/\pi D$).

Soong [30] describes the torque produced by an electric machine as

$$\vec{\tau} = \frac{\pi}{2} D^2 l \vec{\sigma} \tag{1.4}$$

$$\vec{\sigma} = \vec{B} \times \frac{\vec{ni}}{\pi D} \tag{1.5}$$

where $\vec{ni}/\pi D$ is a linear current density around the air-gap in A/m. $\vec{\sigma}$ is a shear stress that exists between distributed conductors and a magnetic field, and thus the torque ($\vec{\tau}$) developed in the air gap of a rotating machine increases with the square of the air gap diameter, and linear active with length, flux density and linear current density.

This equation does not account for any non-linearities, such as magnetic saturation of materials, practical voltage limits or shape of the torque curve, but it is very useful for reasoning on sizing. If more torque is required, a larger machine, higher current density, or a higher magnetization are all ways to achieve this. The parameters from equations 1.4-1.5 are shown in figure 1.6, which is a cut-out view of the stator and rotor. A further discussion on torque in electric machines follows in chapter 4.

1.3.2 Internal Combustion Drivetrains

Figure 1.7: Schematic internal combustion engine, attached to a five speed gearbox, feeding torque to the differential through a final gear.

Internal combustion engines (ICE) generate a torque by combustion of an air-fuel mix inside an enclosed container with a pist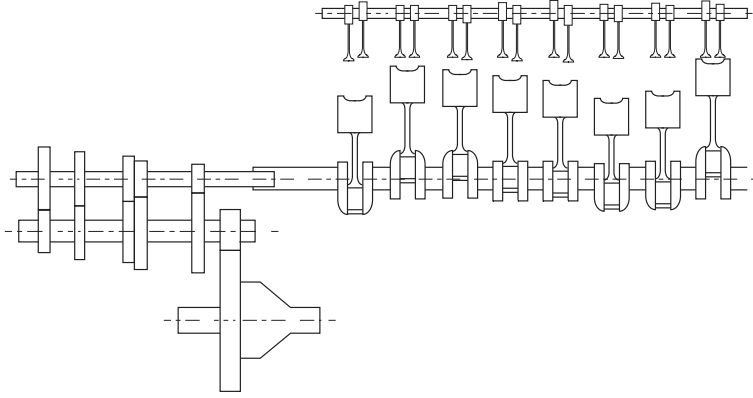on connected to an eccentric shaft. The torque τ produced on the output shaft, can be found from the Brake Mean Effective Pressure (p_{BME}), displacement V_d and revolutions per power stroke n_c according to Lancaster et al. [31]:

$$\tau = \frac{p_{BME}V_d}{n_c 2\pi} \tag{1.6}$$

The p_{BME} of an ICE varies with a large range of parameters, including engine speed, compression ratio, induction pressure, exhaust gas recycling, valvetrain, induction geometry, exhaust system, combustion chamber design and so on. Efficiency values can be found for various fuels in table 1.1. The conversion efficiency reaches its peak at high p_{BME}, which is when the ICE produces its maximum torque according to equation 1.6. This results in a lower efficiency at low loads, unless techniques such as cylinder deactivation or hybridization in some form are used.

Expressing the torque curve of an ICE over the gear ratios in a multi-speed gearbox gives a result similar to the torque curve of a field weakened electric traction machine. In figure 1.8, a truck diesel ICE [32] is combined with gear ratios in a 12-speed gearbox and rear axle [33], as wheel torque vs road speed, excluding transmission losses, together with the load at different speeds up a 2.5% grade. This combination results in a top speed of around 90 km/h in the 11th gear, at such high load the brake thermal efficiency of the ICE can be expected to be about 0.4. At lower loads, e.g. on flat ground, during descents, or in vehicles with oversized engines, the p_{BME} at normal operating points is

typically lower, meaning in turn that the efficiency is lower, unless the previously mentioned strategies such as cylinder deactivation or hybridization are utilized to intermittently shift the torque operating point.
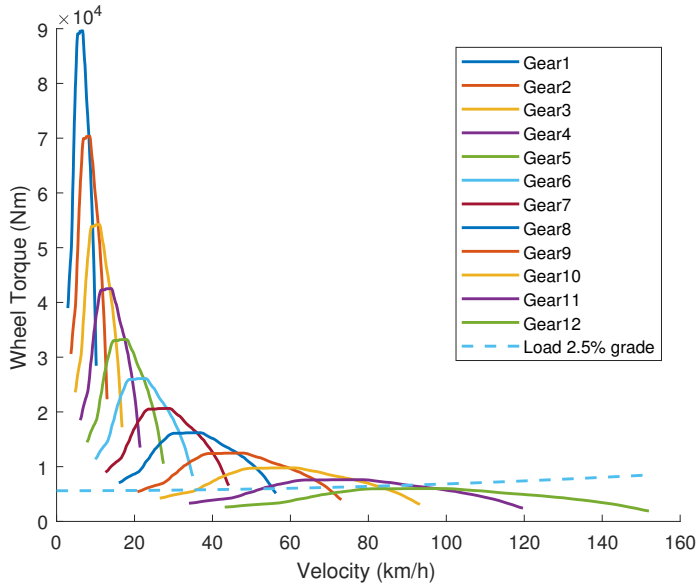
Figure 1.8: Torque curve of a diesel ICE truck, through its gearbox and rear axle [32, 33], giving a resulting wheel torque excluding transmission losses at different road speeds. The torque slopes in each gear form a near continuous constant power line. The resulting wheel torque load from equation 1.2 for a 2.5% grade is also shown.

Chapter 2

Background, Objectives and Scope
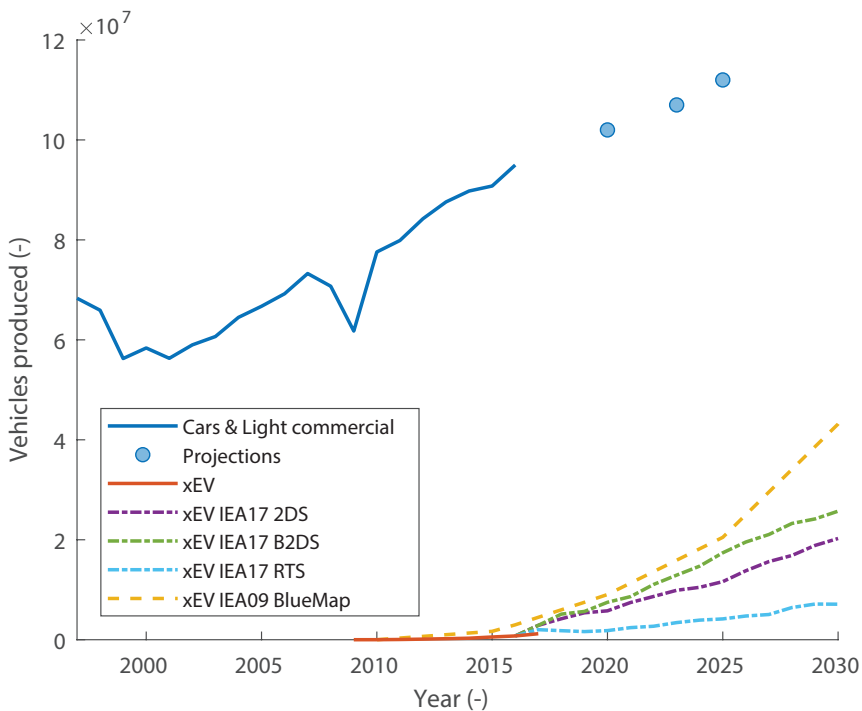
Figure 2.1: Yearly production of cars and light trucks, from Organisation Internationale des Constructeurs d'Automobiles [34]. Plug-in hybrids and battery electric vehicles, called xEV, data from [35], 2017 xEV data [36], projections from BlueMap, RTS, B2DS, and 2DS [37, 35].

2.1 Background

Road transport was estimated to be the source of 18.75% of global CO_2 emissions in 2009 [38], road vehicles also emit NO_x and particulates. Emissions could be reduced significantly by a shift to electrified traction systems, due to the increased efficiency of the system, see figure 1.1, equation 1.1, and table 1.1. The energy source can be shifted from fossil fuels, to electric energy, which can be generated from low emission sources. This work focuses on electric drivetrains, by analysis of the components that generate the tractive effort on the road surface in various levels of detail regarding their mechanical, electrical, thermal and economical performance. This is done in an effort to analyze the trade-offs inherent to electric drivetrain components and the implications of these trade-offs from a systems perspective. Electrified vehicles are sold in fewer numbers than internal combustion counterparts, as shown in figure 2.1. Despite high growth rates and subsidies through tax credits, electrified vehicles (EV and PHEV, summarized as xEV) only represented 1.2% of new vehicle sales in 2017.

Production technology in the road vehicle sector has been continuously developed for more than a century, leading the manufacturing industry as a whole forward with the introduction of the Olds assembly line in 1901, which was improved upon by the use of conveyors in 1913 by Ford motor company [39]. Further cost reduction by widespread adoption of the Toyota Production System [40], has made road vehicles highly cost and manufacturing optimized products. In certain cases, the industry's obsession with lowering costs, as described by Nader [41], Lee [42] and the recent emissions manipulation described by Thompson et al. [43], suggest that spending on technology which does not add perceived consumer value, or technology required by regulators, will be avoided.

Stronger emission regulations are expected to increase costs for conventional powertrains [44], where the shift in Europe from the non-representative New European Drive Cycle (NEDC) cycle to World Harmonised Light Vehicles Test Procedure (WLTP) will produce more accurate results, while still not representing real world emissions [44]. This shift is due for all new vehicles in 2019, followed in 2021 by the fleet average target of 95 g CO_2/km, which includes a credit system for vehicles emitting less than 50 g CO_2/km, that is due to be phased out gradually from 2020 to 2023. The less than 50 g CO_2/km category can be divided into zero-emission vehicles (BEV and FCEV) and low emitting vehicles (PHEV), for simplicity's sake these have been grouped into xEV in figure 2.1.

Hybrids, ranging from 48 V based mild hybrids to higher voltage low energy storage hybrids are expected to be important in achieving the 95 g CO_2/km fleet average, while vehicles that rely mainly on their electric propulsion systems fall in the sub 50 g CO_2/km category. The work in this thesis applies to all these

vehicles, but does not concern itself with integration between the electric traction system and ICE, though it should be noted that these systems can be utilized on a sliding scale and are not mutually exclusive. The technologies for emission reduction add costs to the vehicle powertrain [44]. New technologies such as electrified propulsion, compete with existing systems, thus new methods and data regarding electric traction systems and their costs are required.

2.2 Objectives

The materials used and production systems that shape them define the costs of electric traction systems. It is possible to oversize or otherwise design components so that they use more materials than necessary, or high cost processes in manufacturing. The focus in this work has been on components that are connected between the DC-bus and the drive-shafts. The decision not to include analysis on batteries or fuel cells can be questioned, however, batteries are thoroughly described in works such as Nelson et al. [45], Patry et al. [46], Sakti et al. [47] and Nykvist and Nilsson [48], while machines, transmissions, drives and auxiliary power-electronics components are generally primarily analyzed on performance [49, 50], efficiency and size in literature. Thus there is a knowledge gap regarding manufacturing and material economics in regard to these components [26], from this the following objectives are formulated:

Objective one is to provide insight into what costs can be expected in the deployment of electrified traction systems, related to their performance in driving vehicles along roads. Figures of this nature support reasoning around achievable future fleet average emissions goals and guides decisions on policy regarding incentives.

Objective two is to provide data, methods and tools for industrial actors to develop and produce electrified traction systems. As these systems feature many interconnected aspects, often produced by separate entities, it can be beneficial to adopt the academic mindset presented in this thesis and allow deeper dives into certain subsystems, with minimal bias, in order to present insights from specific fields in the context of the system as a whole.

Objective three is to scale the economic models with relevant parameters, regarding both vehicle performance such as torque and power, as well as production performance, such as yearly output and yield. Within this objective, the models should also provide a division of cost between subcomponents. In order to provide robust results, the models must also accept uncertain data, such as the cost of raw materials from potentially narrow sectors, or estimating the cost of production for processes that are not yet established on the market.

2.3 Scope and Limitations

The cost analyses have been made based on available information in literature e.g. regarding operating costs and processing times, supplemented by data from suppliers and factory visits. The data presented in this work does not reflect true costs in all production environments, for example costs of wages and power vary over different regions. Furthermore, overheads such as the cost of space, ventilation and administrative expenses have been left out. The motivation for such an omission is that these costs are expected to be the same regardless of the technology choice, and would only dilute differences between competing technologies by adding flat cost additions. The primary purpose of the figures in this work then is for comparative studies. The models have also been constructed to allow for rapid runtimes, allowing for the inclusion and re-calculation with less uncertain data once it is available. A reduction of input uncertainty propagates to a reduction of output uncertainty.

The manufacturing processes in this work are primarily those identified at factory visits, marketed by suppliers and presented in literature. The scope limits are such that the processes typically occuring at the site of, or directly defined by a hypothetical drivetrain supplier. This means for example that wire drawing of copper is not analyzed as a manufacturing process, instead drawn and coated copper wire is considered to be a pre-processed material that is purchased, while for example die casting of a housing is likely to be performed at a separate foundry but with product specific tools, thus it is considered a manufactured part.

2.4 Publication Scope

Connections between appended publications are depicted in figure 2.2.

Paper I The demand for rare earth magnet materials in the global vehicle industry's transition to electrified vehicles for a number of scenarios. One scenario projected rapid adoption of EVs, which together with large scale expansion of wind power would consume more than the supply of neodymium and dysprosium. The other scenarios presented lead to different fractions of neodymium and dysprosium consumption by electrified vehicles, but the projected supply is greater than the demand. The adoption rates for electrified vehicles have been lower than what was predicted in the scenarios. I conceived the idea, performed calculations and authored the paper.

Paper II A framework for analysis of multiple process options is presented. The framework assumes that there exists a number of processes that yield an equivalent output, such as cutting electric steel sheets by laser, water or stamp-
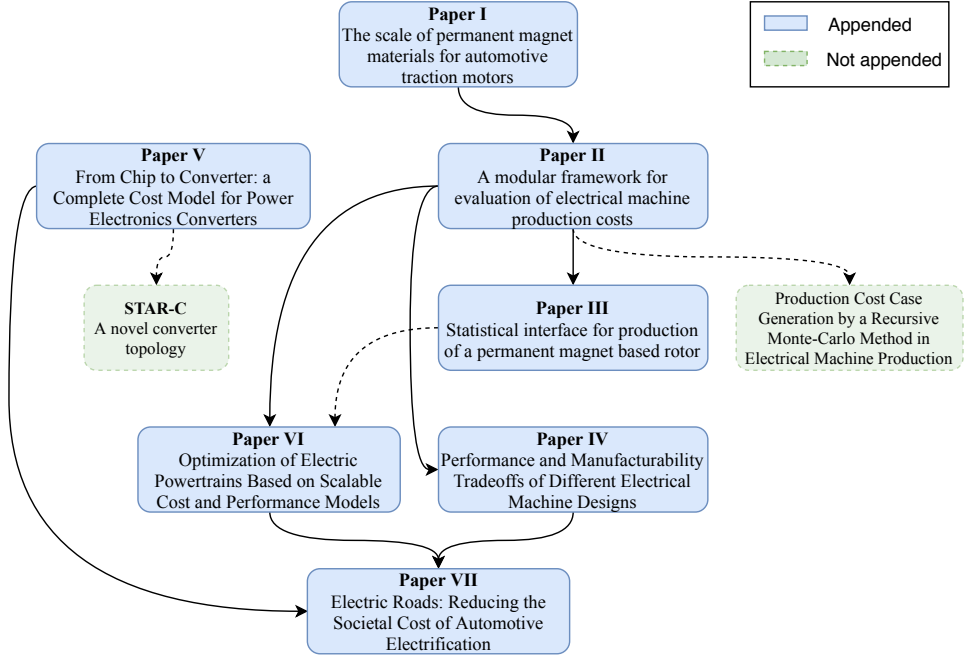
Figure 2.2: Publications, connected by flow of inspiration or data.

ing with different tool materials. The lowest cost process is selected for each production volume studied, which then propagates down the process chain. The method allows for rapid calculation of the economic viability of for example a new winding method, but does not consider the effects the manufacturing processes have on performance. I conceived the idea, performed calculations and authored the paper.

Paper III is an extension of Paper II, introducing non-deterministic terms into the economic analysis of a permanent magnet rotor. This allows for the inclusion of time-series variation of commodity prices, assembly time variations for processes and uncertainty regarding investments in tooling. As numerous sources of uncertainty exist in the input data for the calculation of both material and processing costs. I conceived the idea, performed calculations and authored the paper.

Paper IV connects the performance of three different types of machines, with a number of manufacturing methods, consisting of three different winding configurations using the same stator and rotor size, and a segmented stator for each of the three winding-types. This work shows the importance of connecting economic models to models that evaluate performance, one example of this is segmentation of the stator, which increases reluctance, while reducing costs.

This leads to a trade-off between cost and performance, furthermore the hairpin winding increased peak torque by 30% compared to insertion winding, but increased cost of the machine by 10%. I conceived the idea, collaborated on calculations, primarily regarding materials and processes and co-authored the paper.

Paper V introduces a model for the scaling of costs in Power Electronic Converters. The idea is to map the problem space with solutions in different parameter ranges, such as voltage, current, switching frequency, cooling, redundancy and so on. A case study on an automotive three phase two level voltage source inverter. The case study includes output power from 20-200 kW, over production volumes from 100 to 20000 units/year. The work concludes that the use of a fixed measure such as €/kW is not viable, because of costs that do not increase linearly with output power. I contributed to the main author's idea, performed calculations on parts, components and production system, and co-authored the paper.

Paper VI investigates a large set of powertrains, consisting of an electric machine, transmission and power electronic converter. The powertrain configurations are scaled to meet the required specifications regarding wheel torque of a segment B battery electric vehicle. As the specification can be met by a large number of configurations, either all configurations are evaluated or an optimization routine is used. The work draws from Papers IV and V and concludes that the total system cost can be reduced by utilizing high speed machines with two-speed transmissions. For this configuration a substantial fraction of the total system cost is the power electronic converter. I contributed to the main author's idea, performed calculations on specifications, components, manufacturing processes, and co-authored.

Paper VII is based on results from papers IV-VI, the societal costs of road transport in a Swedish context. A number of dynamic charging systems were analyzed. Based on the premise that the current vehicle fleet is made fully electric, instantly, the work concludes that there exists a large economic potential in electric road systems if they can be used by all road vehicles. If they are deployed only for heavy vehicles the potential cost reduction is limited. I expanded upon the original idea by Profs. Alaküla and Bängtsson, collaborated on calculations and co-authored.

Chapter 3

Methodology
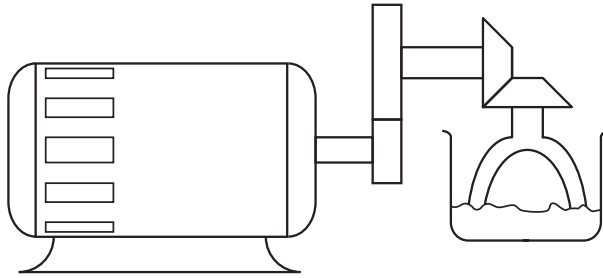
Figure 3.1: The Toscanini's Problem, from Ward and Seering [51] describes an ice-cream mixer. It consists of a grid connected electric machine, a gear-set and, the varying torque requirement from the mixing mechanism as the ice-cream solidifies. Electric vehicle powertrains are not very different.

The methodology in this thesis is inspired by, and builds upon the work by Ward and Seering [51] which is illustrated by figure 3.1. In their work the solution to a problem is inferred from its constraints by a compiler that combines components from a number of sets. This differs from traditional design approaches where either a previous solution is improved upon, or a solution is generated and developed from an ideation process and iterated upon until specifications are met [52].

In my work the sets of solutions are not limited to some predefined catalog list of motors, gearboxes and loads. The design space here consists of what could be produced, and how, based on common design and production practices for components involved in electric traction. In order to achieve this, a certain knowledge of the building blocks of these major components is required. The level of detail for each component is arbitrary, for some it reaches towards the chemical elements.

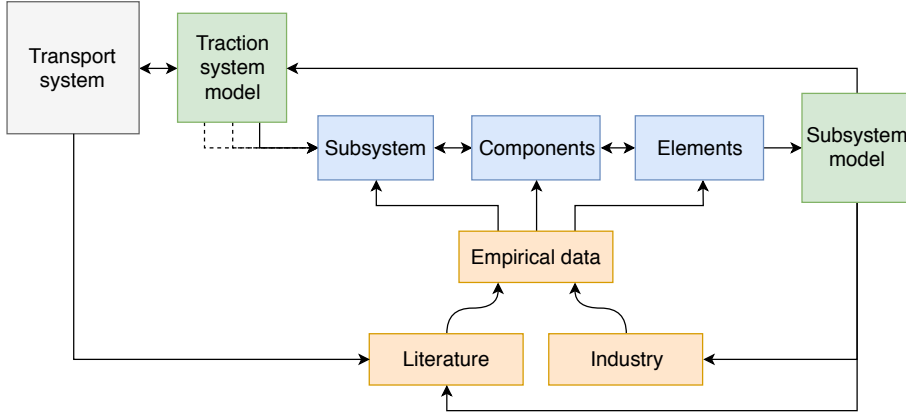**Figure 3.2:** Methodology flowchart, which starts with some understanding of the transport system, from which a model of traction systems can be inferred. This is in turn broken into smaller and smaller models using empirical data from industry and literature. The results are used to reformulate the original larger models, and presented as literature and to industry. The process then repeats ad infinitum.

In order to perform calculations on ranges of input parameters, discrete solutions are defined and scaled over a number of parameters, to allow for automated analysis regarding technical and economical performance. An illustration of how the methodology is structured is shown in figure 3.2, for which the long explanation follows:

The transport system places a number of demands on our road vehicle traction systems, they should move people and things from one place to another. In doing so they should consume the lowest amount of resources, which can be fossil fuels, metals or the time of people and goods. These demands could therefore be quantified in mass, torque, numbers of individual units, money and so on. The traction system model then starts as something of a blank slate, to be broken down onto a number of subsystems: electric machines, power-electric converters and reduction gearsets or gearboxes, all of which affect each other. The subsystems consist of components, stators, rotors, bearings, housings, bus-bars, shafts, more bearings, power modules and PCBs, which in turn affect each other, and the properties of the subsystem they create. The larger components are consist of of smaller components, turns of conductors, permanent magnets, individual gears, resistors, capacitors, semiconductors, insulation, seals, screws and so on. The smallest components comprise a number of elements, each contributing to the desired properties of the component, which can have many dimensions such as, stiffness, conductivity and cost. Each dimension is not of equal importance to the property of each component, so some engineering judgment is applied here. The properties, defined by empirical data from industry and literature,

reflect back to the definition of the constituents. The data can define how many screws of what size should be strained, to hold a power module of a particular type into a surface of some roughness value, or it can define how many strands of a given diameter conductor will result in a reasonable maximum temperature so that the insulation does not turn from polymer to soot. Physical limits govern how much of a specific item is needed to achieve the goal of the subsystem, which might be to provide another subsystem with a current of desired amplitude and frequency for example. Once those limits are defined, the quantities of components and operations required to shape them into desired form, in order to achieve the previously defined tasks. The curves that are defined by those limits can be formulated into a model that is presented back to literature and industry and stored for later use in the system model. The task is then repeated for another subsystem, or one previously described is improved, due to either new knowledge or an expansion of some dimension. Once the traction system model is arbitrarily finished, the information inside it can be used to re-formulate a transport system model.

Herein lies one of the key challenges with the approach, as it attempts to define a continuous space of solutions that by definition contain many discrete subsystems; windings are integer turns of integer conductors, while strand diameter is a continuum. In a similar fashion motor length is a continuum, created by stacks of integer number of sheets, which themselves could be produced to any thickness, but for practical purposes exist only in fixed dimensions. The same can be said for switching devices, that could be produced for a range of currents or voltages, but in practice are made and marketed in sparse discrete voltage steps. Yet intermediate solutions *could* be made if there were a strong enough demand, and likely they would exist in between their respective higher or smaller valued counterparts that *do* exist on the market. Though both performance and cost do not need to scale in a linear fashion between two existing points.

In practical terms, the models described in this work have been implemented in MATLAB and Python code, as this allows for interaction with model parameters as outputs and inputs to software such as FEMM and xFEMM [53] for electromagnetic simulations, Simulink for drive-cycle simulation and so on. Input data regarding materials is based on regression models, which by nature are limited by the available data. In order not to lose the inherent uncertainty data, distributions and confidence intervals are derived using a bootstrapping method as described in Efron [54].

There are a number of drawbacks associated with the chosen research approach, the main issue is analysis of products and processes that are not used in high volume production, or in some cases do not exist at all, which makes it very difficult to validate the results. To some extent this is dealt with by

the introduction of uncertainty into the production cost model in Paper III. Another drawback is that actual total production costs are more relevant than the manufacturing costs that disregard overheads, storage and so on. Total production costs may be of more interest to companies, which all have different accounting standards, overhead levels and write-off times. These parameters affect the results to such a degree that the uncertainty range would grow very large. Furthermore, a comparison of the costs of different components or manufacturing operations in the drivetrain, using the same methodology, should yield valid comparison data.

Chapter 4

Design Considerations
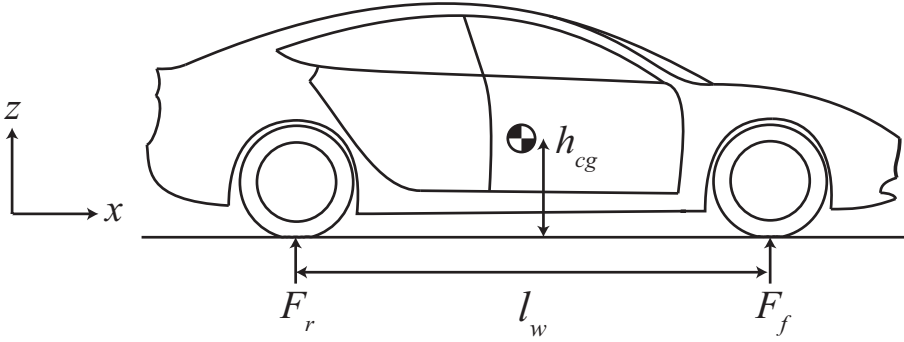
Figure 4.1: A vehicle with relevant parameters for longitudinal performance. Load will shift from F_f to F_r during acceleration, which limits the available acceleration $\ddot{x}$ and with that also the useful wheel torque, which will depend on powertrain layout, wheelbase l_w and centroid height h_{cg}.

4.1 Longitudinal Performance

$$m_v g = F_r + F_f$$
$$F_d \mu_t h_{cg} = (F_r(1 - w_r) - F_f w_r) l_w \qquad (4.1)$$
$$m\ddot{x} = F_d \mu_t$$

Figure 4.1 shows a stationary vehicle, with normal loads F_f and F_r that combined equal the gravitational load of the vehicle. When the vehicle accelerates due to a force F_d applied to the ground by the driving wheels, the torque reaction around the vehicles mass centroid must be balanced by shifting load from the front to the rear, if $F_d \mu_t$ is positive. The magnitude of the loads during

acceleration is determined by the static load condition, given by the static load fraction $\{w_r, 1 - w_r\}$, the wheelbase, l_w and the applied force F_d. The latter force is limited by the tire friction coefficient μ_t, and the load at the driven wheels.

Table 4.1: Vehicle parameters for performance calculation. Data from [29, 55, 56].

Vehicle	m_v (kg)	l_w (m)	h_{cg} (m)	$c_d a_f$ (m^2)	w_r (-)	r_w (m)	t_{0-100} (s)
BMW i3	1370	2.57	0.35	0.69	0.53	0.35	6.6
Nissan Leaf	1591	2.70	0.45	0.658	0.42	0.32	10.5
VW e-Golf	1585	2.63	0.45	0.59	0.45	0.32	9.8
Tesla Model 3	1843	2.88	0.47	0.504	0.52	0.33	5.3
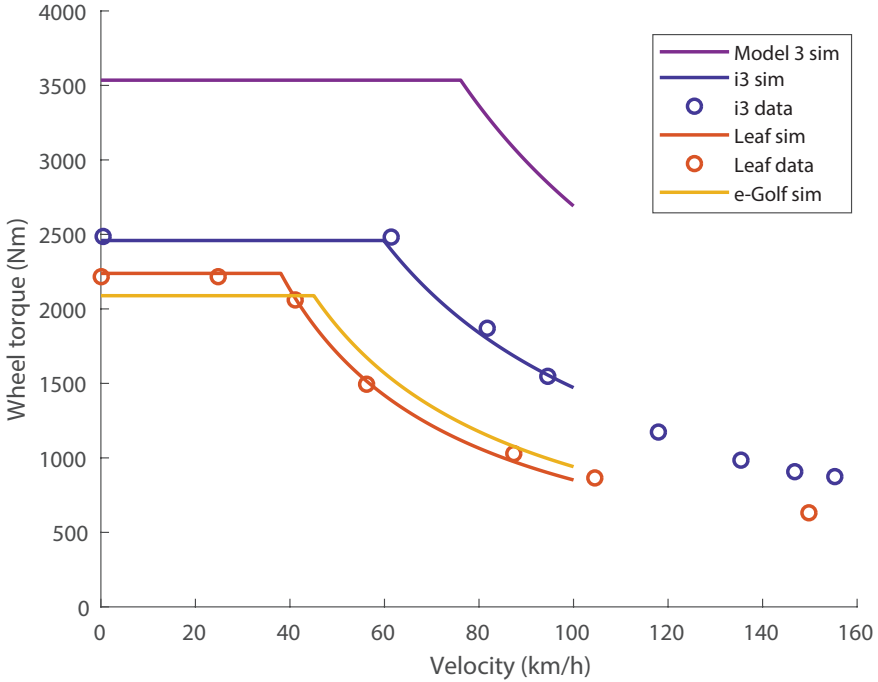
Figure 4.2: Wheel torques, as simulated by minimum power and the load transfer from equation 4.1. Compared with torque curves from [55, 57].

The linear system in equation 4.1 disregards any dynamic load effects from the suspension or tires. The result is expressed as wheel torque, meaning that rotational inertia in the drivetrain is not included. If equation 4.1 is combined with equation 1.2, using common parameters for the desired vehicle performance, such as the time required to accelerate from 0 to 100 km/h, the peak wheel torque and base speed can be found by minimizing the allowed maximum power

that will meet the performance requirement. The parameters required for generation of a wheel torque curve are listed in table 4.1, all the vehicles were assumed to have $\mu_t = 0.9$, except the Model 3 which has $\mu_t = 0.95$ due to its high performance. Estimated torque curves, for the parameter sets in table 4.1, are shown in figure 4.2. The results agree well with torque data from the BMW i3 [55] and Nissan Leaf [57], torque data for the Model 3 and e-Golf have not been obtained. The measured torque drops from constant power as speed increases, due to increased losses. Considering the simplicity of the model, the results are in good agreement with measurements, and it serves as a good starting point for dimensioning drivetrains. Desired top speed gives the peak machine speed for a known gear ratio, together with the power requirement described in section 1.2, from a known gear ratio and transmission loss the machine torque, power and base speed can be inferred.

4.2 Permanent Magnet Synchronous Machines
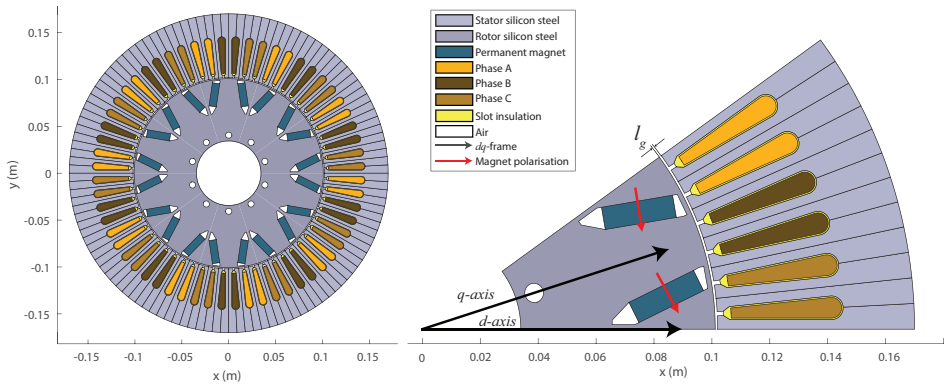
Figure 4.3: A three phase permanent magnet synchronous machine, with embedded magnets in a V-configuration. This machine is configured as Q2, meaning two slots per pole per phase, it has 10 poles and thus 60 stator slots. l_g is the air gap distance, the gray areas are soft magnetic material, gray-green are permanent magnets with red arrows indicating the direction of polarization, and the three phases are represented in orange-brown hues.

There is a multitude of possible electric machine configurations, too many to describe in this work. All of them make use the Lorentz force [58], which describes how a charged particle moving in an electric and magnetic field experiences a force. Rotating electric machines are common. They exist in the forms of in-

duction machines, synchronous and switched reluctance machines, electrically excited and permanent magnet synchronous machines. These can be made as inner rotor, outer rotor, axial flux and claw-pole or vernier configurations.

Internal rotor permanent magnet synchronous machines (PMSM) have been the focus of this work, as this type of machine is ubiquitous in electrified vehicles [29]. One such machine is depicted in figure 4.3. This machine has embedded magnets in a V-shape and a distributed winding stator with round wires. Paper IV and Paper VI discuss the machine configurations in this work in more detail. The $\vec{d}$ and $\vec{q}$ axes represent a rotating frame that follows the rotor, presented by Park [59], the rotating frame enables simplified control of three phase synchronous machines by reducing three parameters to two and as it follows the rotor sinusoidal parameters are transformed to constants.
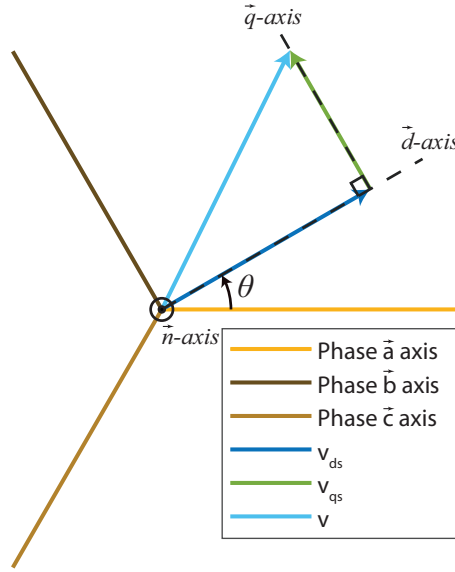
Figure 4.4: Three fixed phases in space, seen on a dq-plane, separated by the angle $2\pi/3$, represented by the same colors as in figure 4.3, transformed to the rotating $\vec{dq}$-frame Park [59]. The $\vec{n}$-axis is normal to the plane, orthogonal to $\vec{dq}$, the angle θ refers to the position of the rotor, to which the $\vec{dq}$-frame is fixed.

An illustration of Parks rotating frame can be seen in figure 4.4. The transform from *abcs* to *dqns* in matrix form, using the notation of Lipo [60] is shown in equation 4.2. The transform is valid for other vectors, such as current, $\vec{i}_{abcs}$ or

flux linkage $\vec{\lambda}$. Reverse transforms can also be found in [60, 61].

$$
\begin{bmatrix} v_{ds} \\ v_{qs} \\ v_{ns} \end{bmatrix} = \frac{2}{3} \begin{bmatrix} \sin(\theta) & \sin(\theta - 2\pi/3) & \sin(\theta + 2\pi/3) \\ \cos(\theta) & \cos(\theta - 2\pi/3) & \cos(\theta + 2\pi/3) \\ 1/\sqrt{2} & 1/\sqrt{2} & 1/\sqrt{2} \end{bmatrix} \begin{bmatrix} v_{as} \\ v_{bs} \\ v_{cs} \end{bmatrix} \tag{4.2}
$$

The flux linkages are, again from Lipo [60], in matrix form

$$
\begin{bmatrix} v_{ds} \\ v_{qs} \\ v_{ns} \end{bmatrix} = \begin{bmatrix} r_s i_{ds} + \dot{\lambda}_{ds} - \omega_e \lambda_{qs} \\ r_s i_{qs} + \dot{\lambda}_{qs} + \omega_e \lambda_{ds} \\ r_s i_{ns} + \dot{\lambda}_{ns} \end{bmatrix} \tag{4.3}
$$

in a PMSM λ_{ms} is the permanent magnet flux linkage, $\vec{\lambda}$ is

$$
\begin{bmatrix} \lambda_{ds} \\ \lambda_{qs} \\ \lambda_{ns} \end{bmatrix} = \begin{bmatrix} L_{ds} & 0 & 0 \\ 0 & L_{qs} & 0 \\ 0 & 0 & L_{ns} \end{bmatrix} \begin{bmatrix} i_{ds} \\ i_{qs} \\ i_{ns} \end{bmatrix} + \begin{bmatrix} \lambda_{ms} \\ 0 \\ 0 \end{bmatrix} \tag{4.4}
$$

The power into the circuit is P_{abcs}, the *dqns* voltage and current are scaled by a factor $\sqrt{3/2}$, due to the geometry of the transform [60].

$$
P_{abcs} = \vec{v}_{abcs} \cdot \vec{i}_{abcs} \tag{4.5}
$$

$$
P_{abcs} = \sqrt{\frac{3}{2}} \vec{v}_{dqns} \cdot \sqrt{\frac{3}{2}} \vec{i}_{dqns} \tag{4.6}
$$

Power P can be deduced from

$$
P = \tau \omega_m \tag{4.7}
$$

Where the mechanical speed, ω_m, relates to electrical speed, ω_e by the number of poles n_p

$$
\omega_m = \frac{2\omega_e}{n_p} \tag{4.8}
$$

combining equations 4.6 and 4.7 gives the power as electric torque τ_e without mechanical losses, times mechanical speed

$$
\tau_e \omega_m = \frac{3}{2} \vec{v}_{dqns} \cdot \vec{i}_{dqns} \tag{4.9}
$$

Voltages from equations 4.3, assuming balanced voltages, meaning $v_{ns} = 0$. Also assuming negligible resistive losses, and steady state operation, the power becomes, in matrix form

$$
\tau_e \omega_m = \frac{3}{2} \begin{bmatrix} -\omega_e \lambda_{qs} \\ \omega_e \lambda_{ds} \\ 0 \end{bmatrix}^T \begin{bmatrix} i_{ds} \\ i_{qs} \\ i_{ns} \end{bmatrix} \tag{4.10}
$$

In scalar form, by using the relationship between mechanical and electrical speed from equation 4.8 and flux linkages from equation 4.4

$$\tau_e = \frac{3n_p}{4}((L_{ds} - L_{qs})i_{ds}i_{qs} + \lambda_{ms}i_{qs}) \qquad (4.11)$$

which is very useful. In machines with magnets mounted on top of the rotor surface, such that the magnetic air gap is constant yields $L_{ds} \approx L_{qs}$. Hence the first term does not contribute to torque. In machines with embedded magnets such as the one in figure 4.3 $L_{qs} > L_{ds}$, which gives a positive torque contribution for negative i_{ds} and positive i_{qs}. Due to saturation, L_{qs} drops whenever i_{qs} is large, more on this can be read in for example Emadi [62] or Hall [63]. The terms $-\omega_e\lambda_{qs}$ and $\omega_e\lambda_{ds}$ define the induced voltage that will limit the ability to control current, unless it is actively suppressed by introducing negative i_{ds} counteracting λ_{ms}, called field weakening. The equation also describes a limit defined by currents as the resistive losses are not negligible and the cooling will limit the maximum sustainable current.

4.3   Rotor Structural Mechanics

The magnets and the rotor steel are subject to a centrifugal force

$$F = mr\omega_m^2 \qquad (4.12)$$

The load is supported by thin bridges in the rotor laminations for inset V magnet machines, as shown in figure 4.5. In practice the magnet is held in place by a resin, which is necessary to hold the shear component of F_{mag}, and the torque τ_{mag} that exists due to higher forces at mass elements at a larger radial distance from the center, giving in this case a negative torque. The resin is assumed to have a negligible effect on F_{mag} and F_w, because its stiffness is significantly lower than that contributed by the bridges for this geometry, on the order of 3-5 GPa. F_r on the inner section of the rotor is not considered, as it does not affect the small bridges that hold the magnet [64].

The rotor must have the capability to withstand a peak stress for a repeated number of cycles. How many cycles this peak stress is repeated depends on the actual use drive cycles and design lifetime, the peak stress for a certain speed can be calculated with FEM, one rotor geometry is depicted in figure 4.6. Stiffness and Poisson's ratio for electric steel stacks are described by van der Giet et al. [65], and Dehmani et al. [66] characterize the fatigue behavior of a 0.35 mm electric steel. Load to the stated yield stress results in $3 \cdot 10^5$ cycles to fracture for punched samples. A stacking factor [67] of 0.95 gives an allowed peak stress
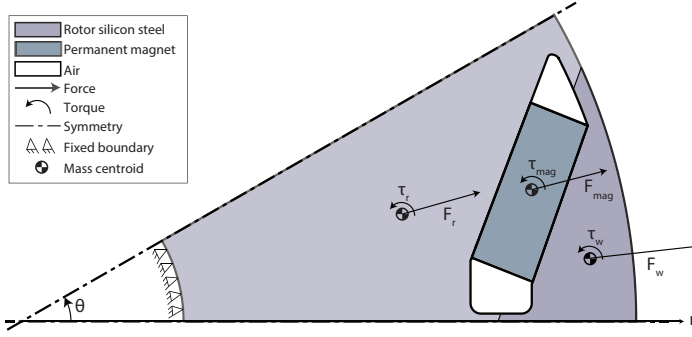
Figure 4.5: A rotor section, loaded by forces according to equation 4.12. The model has a fixed traction boundary at the inner rotor radius, symmetry boundaries along the dashed lines. The radial forces considered are only those acting on the magnet and the darker shaded region of the rotor F_w and F_{mag}. F_w acts as traction on the rotor outer radius. The magnet load F_{mag} acts only on the long boundary towards the rotor, the shear and torque components are transfered to the outer section by the resin.
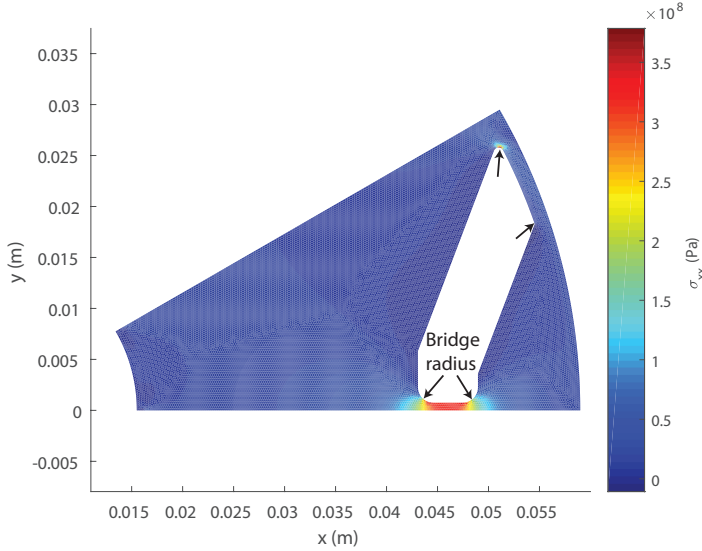
Figure 4.6: A FEM generated stress distribution, showing σ_{xx} resulting from F_{mag} and F_r. The von Mises stress level in the bridge is 2% higher than σ_{xx} the for this geometry. The bridge radius influences the stress concentration, with a $r = 1.5$ mm on the axially loaded bridge, the $3 \cdot 10^5$ cycle fatigue speed is 18000 rpm. The maximum deformation in the radial direction is 25 μm.

of 380 MPa. For the corner radius selected in figure 4.6 a peak speed of 18000 rpm is viable for this rotor.

Tong [68] describes numerous design considerations, primarily focused on induction machines, many of which are transferable to PMSM. Rotor and shaft

resonances should also be considered for high speed machines, as experienced and described by Ede et al. [69].

The experimental data in Dehmani et al. [66] are all measured in the rolling direction, and despite that stiffness, yield and tensile strength are lower in the rolling direction, even in non-oriented steels due to anisotropy generated by the rolling process. The expected fatigue strength in the transverse direction is lower, as described in Hariharan et al. [70]. Because literature and data-sheets are insufficient in the description of mechanical properties for electric steel, especially for elevated temperatures, this makes analysis of high speed machines difficult.

4.4   Magnetic Circuits

As the magnetic circuits of machines in this work are all simulated in 2D, a method for estimating the reluctance increase for different types of segmented stators is needed. Effects such as stacking factors are often added as modified material parameters. Segmented stators were investigated in Paper IV, with some assumptions on the effects of segmentation and the tolerances involved, in order to learn about the effects of different ways to segment a stator, a basic gapped inductor model was created, depicted in figure 4.7.
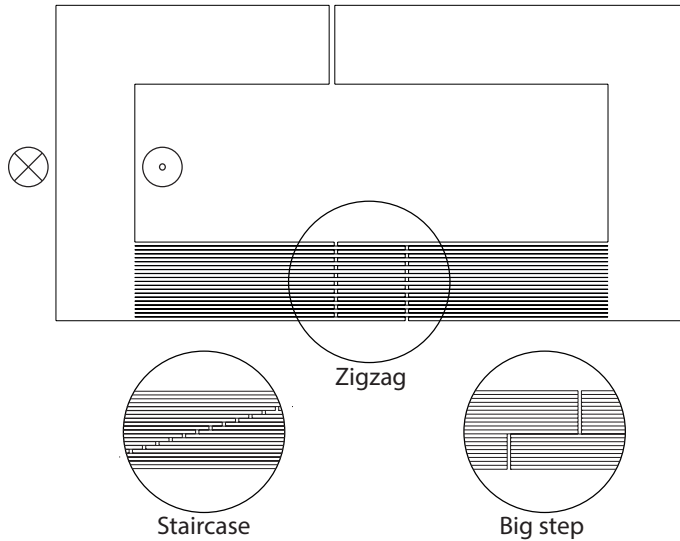

Figure 4.7: A gapped inductor made with segmented sheets, in order to quantify the effects of tolerances in different stacking strategies. The two dimensional inductor is a simplified model of the flux path in a machine that is loaded by a coil applying a varying magnetomotive force.

Uniform magnetic circuits can be described in an analogous way to resistive electric circuits

$$\mathcal{R} = \frac{l}{\mu_0 \mu_r a_c} \tag{4.13}$$

$\mathcal{R}$ is reluctance, l is flux path length μ_0 the permeability of free space, μ_r is relative permeability and a_c is cross sectional area. In a general circuit

$$\mathcal{R}\vec{B}a_c = \vec{\mathcal{F}} \tag{4.14}$$

where $\vec{B}$ is flux density, $\vec{\mathcal{F}}$ is the magnetomotive force (MMF), from number of turns n times current $\vec{i}$. The model of the inductor uses ideal material for the core except where the segmented sheets are located, the sheets have a typical $\mu_r = 1500$ at $1.5\,T$ and saturate at $|\vec{B}| = 1.8\,T$.

As the magnetomotive force $\vec{\mathcal{F}}$ increases, the different layouts begin to exhibit local saturation at the small air gaps. Figure 4.8 shows how the resulting flux density $\vec{B}$, depends on the relative size of the small tolerance gap to the larger intentional air gap. With tighter tolerances for the segmentation gaps, the reluctance is reduced. Tolerances close to the sheet to sheet gap, which is $17.5\,\mu$m are difficult to achieve for blanked parts [71]. It is clear that of the stacked solutions, from an electromagnetic standpoint a staircase type is preferable to the other solutions. Freitag [72] reached similar conclusions regarding transformers.

Flux plots for the different inductors are shown in figure 4.10, in which localized increases in flux density for the zigzag and big step geometries are apparent. In the staircase layout the flux is more evenly distributed which explains why the reluctance is lower over all. If the tolerance gap were to approach the sheet to sheet gap, the different solutions should converge. It is also interesting to note that the length of the overlap does not affect the reluctance to a large extent as long as it is large in comparison to the sheet thickness. Edge effects are pronounced in the big step layout, a higher stack with more steps would reduce these effects.

Paper IV described cost reduction due to reduced material waste, together with the possibility of using a different rotor and stator material. Separate rotor and stator materials are useful where rotor stresses are high, as in high speed machines, or when a thin, high cost, low loss stator material is combined with a thick, low cost rotor material. Segmented stators also enable the use of for example linear winding of fractional slot concentrated winding machines, with high fill factor and design freedom regarding tooth geometry. Some potential layouts of the same stator are depicted in figure 4.9. Paper IV is based on two dimensional reluctance models, which do not capture the axial behavior of
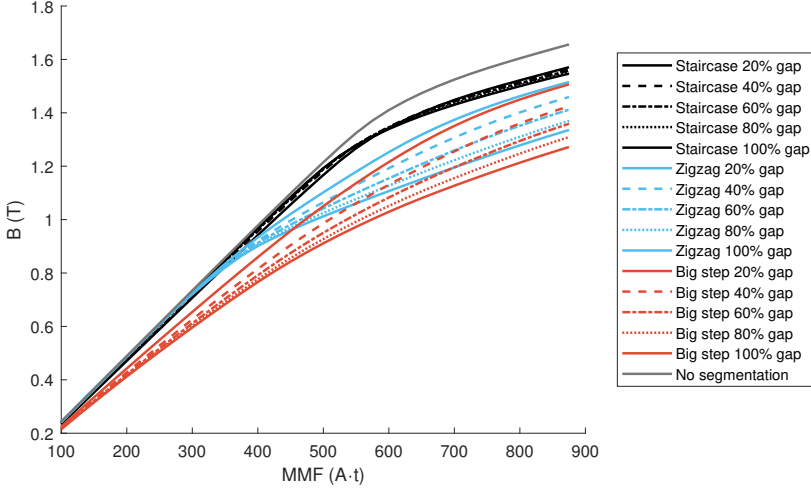
Figure 4.8: Resulting air gap flux for the three different stacking layouts for different sheet to sheet tolerances, as compared to a non-segmented inductor.
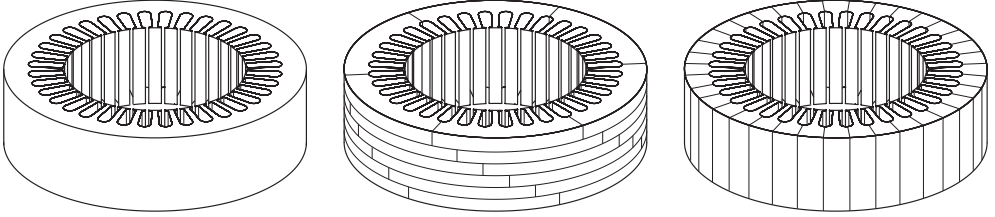
Figure 4.9: The same stator, produced with different blanking layouts, one non-segmented and two segmented stator layouts. Segmentation enables lower tool cost and material scrap, at the expense of increased reluctance.

the flux. The results in figure 4.8 show that the reluctance in machines with segmented stators could be reduced. Very fast pick-and-place robots would be needed to assemble the staircase stator, but it may be interesting to note that due to the rotational symmetry of the stator stack in figure 4.9, such a geometry could be produced with a single tool.

No analysis of eddy-current losses due to segmentation has been performed in this work, and such an analysis should include the effects on the cut edges. But the results in figure 4.8 indicate that by use of an appropriate stacking strategy and small modifications to the stator back, it is possible to produce well performing machines at a lower cost, due to reduced material waste. To investigate the implications of introducing additional cut edges in the stator, mixed order models as described by Sundaria et al. [73] could be used.
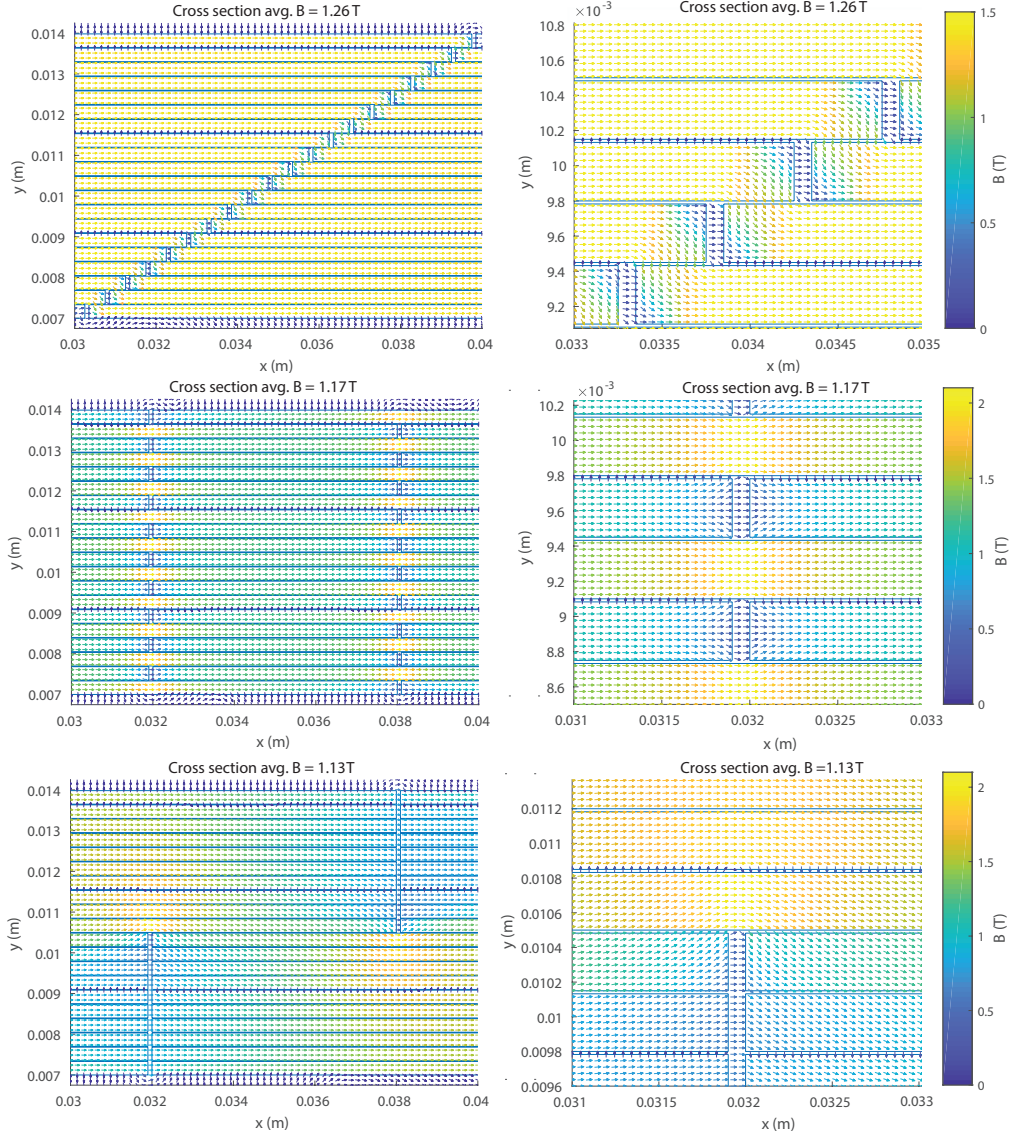
Figure 4.10: Flux density plots of the staircase, zigzag and bigstep layouts, at 500 kA/m, with 0.1 mm tolerance air gaps. Note that the peak flux densities in the zigzag and bigstep geometries are higher than the in staircase, which has a more even flux density distribution over the gaps.

Chapter 5

Materials and Commodities
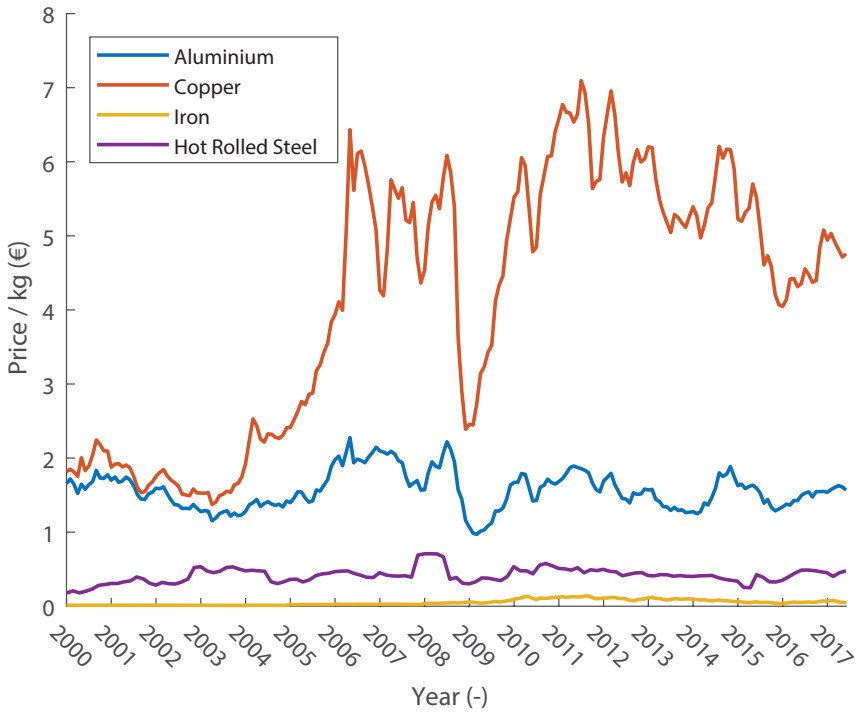
Figure 5.1: Historic metal spot prices of base metals [74], converted from nominal US Dollar to nominal Euro with data from the European Central Bank [75].

All physical products consist of one or more elements, alloyed, shaped and combined through a number of refinement steps. These refinement steps serve to give the product its desired properties and each step incurs an added cost or added value. The latter two terms are here used interchangeably and imply

the extent to which the refined part has increased in value. One example of this can be seen in figure 5.1, which depicts the difference in the price of iron and hot rolled steel. The iron ore has gone through a smelting process into pig iron, which in turn goes through a basic oxygen furnace to produce steel, which is then rolled into steel sheet. These steps have incurred costs for the steel producers, who sell the refined product at a higher price determined by the market.
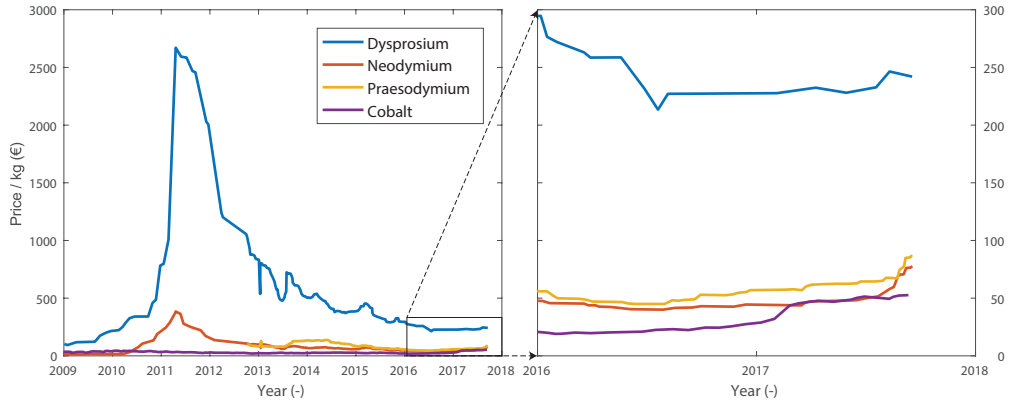
Figure 5.2: Historic price data for some critical elements [76]. The materials used in NdFeB magnets experienced a speculative bubble, but remain higher than historic levels. The price of cobalt, praesodymium and neodymium is increases towards the end of the dataset.

A commodity is defined here as a material or part, available from more than one supplier at significant volume. The commodity is considered purchased for use in the production of the more highly refined parts described in this work. In this case, the price of the part or material equals the cost of the parts purchased to be used for further refinement.

Metallic materials are typically traded on commodities markets as pure ores or oxides, as depicted in figures 5.1-5.2. The prices of ores or oxides does not correlate directly to the price of a useful refined alloy, it does however constitute a lowest cost limit of production for the supplier, in all but exceptional cases. An example of this is the difference in price between iron ore and hot rolled steel in figure 5.1. The refined materials are traded at a premium to the base commodity, which will be described in more detail in the following sections.

5.1 Soft Magnetic Materials

The role of soft magnetic materials in an electromagnetic component is to provide a low reluctance path for the flux. A common soft magnetic material is

ferrite silicon alloy, $Fe_{bal}\,Si_{0.01-0.065\,wt}$, in which the alloyed silicon content can reach $3-4wt\%$ [77]. The upper limit silicon content can not be reached without using unconventional methods, such as chemical vapor deposition [78].
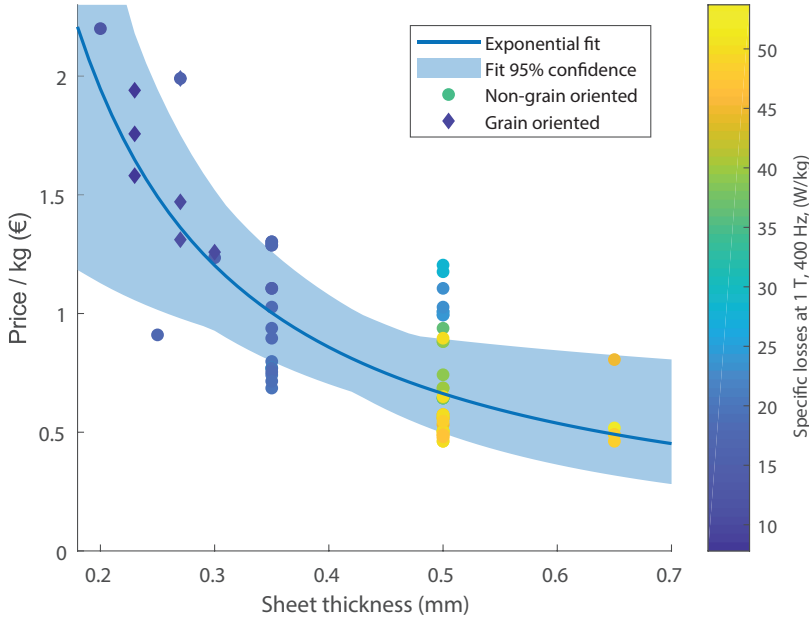
Figure 5.3: Electrical steel sheet price [79] vs sheet thickness. Exponential fit and confidence interval of fit. The colorbar indicates manufacturer specified losses at 1 T, 400 Hz (W/kg). Loss data from [80, 67, 81].

Electrical steels can be produced in both grain oriented (GO) and non-grain oriented (NGO) configurations, the price of thinner, lower loss steel is higher than thicker steel as figure 5.3 shows. The goal of GO and NGO steel is to produce anisotropic magnetic performance or isotropic in the plane respectively, the former is commonly used in transformers or inductors where it is possible to align fluxes with the grains. In rotating machines, the flux moves with the rotation of the rotor and remains aligned only in parts of the machine. Thus non-grain oriented materials are commonly used. The effects of rolling direction anisotropy arise in the cold rolling processes required to reach the final material thickness. The rolling processes are often followed by annealing in order to reduce the anisotropy [82]. Some anisotropy typically remains in the material, resulting in mechanical and electromagnetic property differences on the order of $10-20\%$ in the rolling and transverse direction [83, 84, 81]. This effect can be reduced further by rotation of sheets, or partial stacks around the center axis of the machine. One rotational pattern for achieving planar-isotropic composites is $[-60°\,0°\,60°]$, but practical rotational symmetries are dictated by the slot and

pole combinations in each design.

Other forms of soft magnetic materials, such as powder composites have been used in Paper V for components such as inductors and transformers. Powder materials allow for lower losses at high frequencies due to the three dimensional insulation of each particle with the trade-off being a lower permeability and magnetic saturation [85]. Component size is also limited by the compaction and sintering process, as discussed by Chen et al. [86], meaning that large parts are assembled from smaller individually sintered parts.

5.2   Hard Magnetic Materials
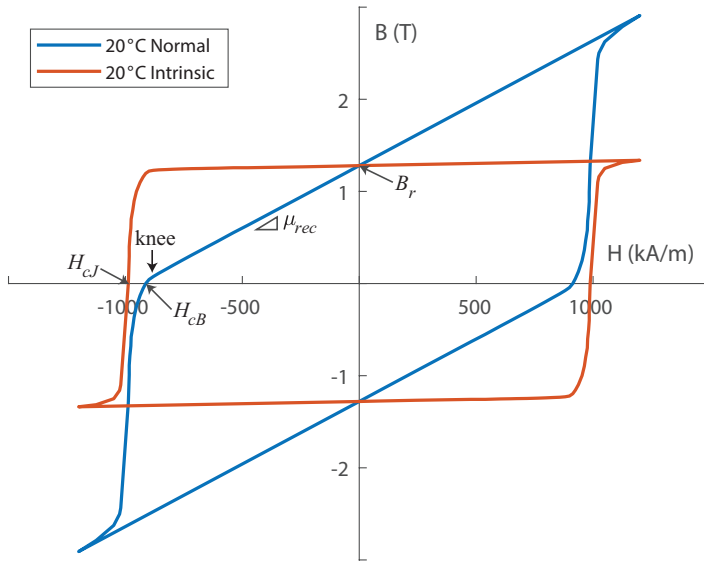
Figure 5.4: Four quadrant intrinsic and normal curves for a NdFeB magnet, based on values from Arnold Magnetics [87]. The locations of remanent induction B_r, intrinsic coercivity H_{cJ}, coercive force H_{cB}, recoil permeability μ_{rec} and the so-called knee are indicated.

Most automotive traction machines on the market are permanent magnet synchronous machines [29], often with embedded magnets made from NdFeB, as they offer the highest achievable energy product of all currently available hard magnetic materials. In order to understand the operation and costs associated with these magnets, some nomenclature is needed, figure 5.4 shows intrinsic and normal curves of a N42 NdFeB magnet [87], as measured in a closed magnetic circuit by a hysteresiograph. Where the normal curve is the sum of an applied external field and that of the permanent magnet. The intrinsic curve is a construct to show only the part of the field contributed by the permanent magnet

in the circuit, where the external applied field is subtracted.

When the external field H is zero, the permanent magnet is at its remanent induction point, B_r, see figure 5.4. In the intrinsic curve, with an external field H, so that $B = 0$ T, the point of intrinsic coercivity, H_{cJ}, is reached. In the normal curve, the corresponding point is denoted coercive force H_{cB}, which equals the magnetic field of the magnet. The recoil permeability μ_{rec} is the slope of the normal curve.
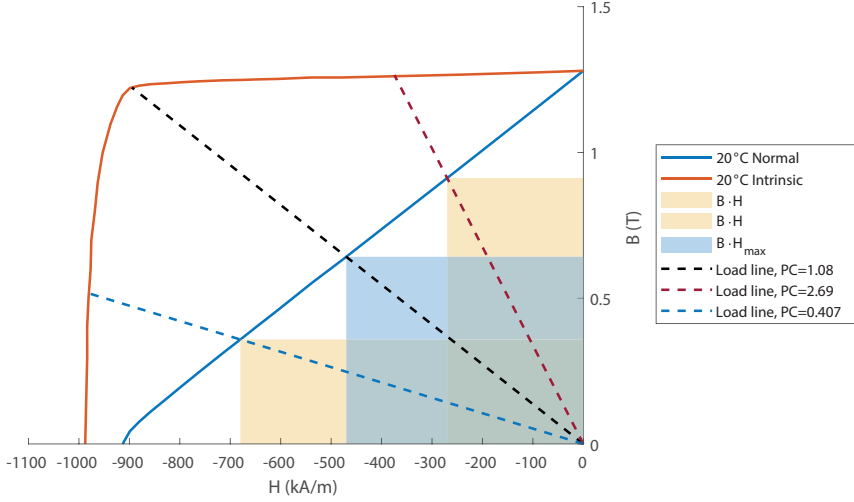
Figure 5.5: The second quadrant of figure 5.4, showing the maximum energy product, BH_{max}. Also shown are two other possible energy products, each with its associated load line.

Demagnetization measurements are typically shown in the second quadrant, as in figure 5.5. The maximum energy product BH_{max} is shown as a blue shaded area, it is the largest possible square under the normal curve. With it are two other roughly equal but smaller energy products, shaded in yellow. The diagonals plotted through the energy products are the load lines, called permeance coefficients (PC), which can be found in datasheets [87] or calculated for a gapped circuit with no external field [62]

$$\frac{B_m}{H_m} = -\mu_0 \frac{a_g l_m}{a_m l_g} \tag{5.1}$$

where B_m and H_m are the magnetic induction and coercive force at the load point, a_g and a_m are the air gap and magnetic pole areas, and l_g, l_m are the air gap and magnet lengths respectively, as depicted in figure 5.6.

In the air gapped magnetic circuit with no external field, the flux is

$$B_m a_m = B_g a_g = \mu_0 H_g a_g \tag{5.2}$$

The line integral of H is

$$H_m l_m + H_g l_g = 0 \qquad (5.3)$$

Isolating H_g from equations 5.2-5.3 yields

$$H_g = - H_m \frac{l_m}{l_g} \qquad (5.4)$$

$$H_g = \frac{B_m a_m}{\mu_0 a_g} \qquad (5.5)$$

Multiplying equations 5.4 and 5.5 gives

$$H_g^2 = - \frac{H_m B_m a_m l_m}{\mu_0 a_g l_g} \qquad (5.6)$$

$$H_g = \sqrt{- \frac{H_m B_m a_m l_m}{\mu_0 a_g l_g}} \qquad (5.7)$$

From equation 5.2, $H_g = B_g / \mu_0$. The volume of the magnet is $V_m = a_m l_m$ and the volume of the gap is $V_g = a_g l_g$

$$B_g = \mu_0 \sqrt{- \frac{H_m B_m V_m}{\mu_0 V_g}} = \sqrt{- \frac{\mu_0 H_m B_m V_m}{V_g}} \qquad (5.8)$$

Equation 5.8 demonstrates that if the air gap flux density is to be increased, either the air gap volume must go down, or the energy product or magnet volume go up, by the square of the desired increase.
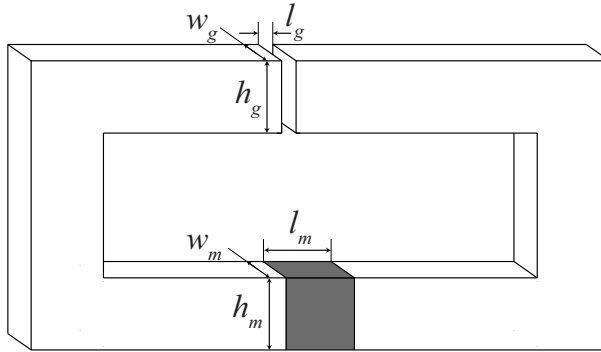

Figure 5.6: An air gapped magnetic circuit, showing the parameters $a_g = w_g h_g$, $a_g = w_m h_m$, l_g and l_m.

In traction applications, the operating temperature is often much higher than room temperature as depicted in figures 5.4 and 5.5. The remanent induction and intrinsic coercivity of NdFeB magnets are reduced with increased temperature, these are denoted reversible temperature coefficients of induction, α and coercivity, β, see equations 5.9-5.10. These can typically be found as linear values under a specified temperature limit in datasheets. For the material in figures 5.4-5.7 they are $\alpha = -0.12$ and $\beta = -0.75$. According to Parker [88] the linear parameters are not accurate enough, and nonlinear regressions based on measurements at many temperatures can give a more accurate models.
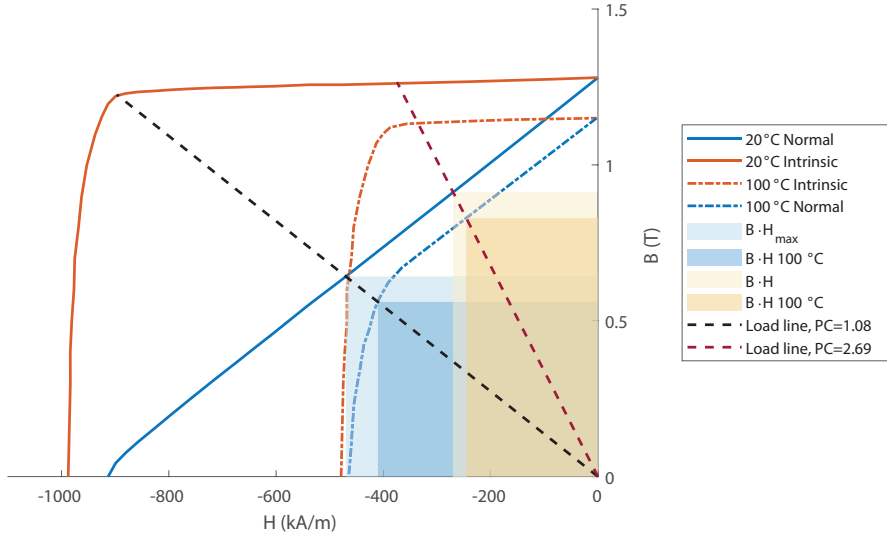
Figure 5.7: The demagnetization curve from figure 5.5, with a calculated curve at $100°\,C$, using the reversible temperature coefficients $\alpha = -0.12$ and $\beta = -0.75$. The shaded areas represent the energy product at the two temperatures, for two of the load lines from figure 5.5.

$$B_r(T) = B_r(1 + \alpha\Delta T) \tag{5.9}$$

$$H_{cJ}(T) = H_{cJ}(1 + \beta\Delta T) \tag{5.10}$$

Datasheets [87] provide demagnetization curves at multiple temperatures, with that for $100°$C shown in figure 5.7. Here the load line that gave BH_{max} at $20°$C would lead to partial demagnetization at $100°$C as the load line enters the nonlinear region of the normal curve, often called the knee. The more conservative load line of $PC = 2.69$, that gave an energy product of 246.3 kJ/m^3 at $20°$C, gives 203.6 kJ/m^3 at $100°$C for this magnet, and there is little room to demagnetize further without risking partial demagnetization.

If the N42 magnet is switched out for a more suitable N38SH, with a lower room temperature B_r, but higher $\beta = -0.535$, as shown in figure 5.8, the load line which would partially demagnetize the N42 material at $100\,^\circ\text{C}$ could now be used. The introduction of field-weakening current, shifts the geometrically determined load-line, as is indicated by the field-weakening 2.69 dashed blue load line. More detailed models have been described by for example Ruoho et al. [89].
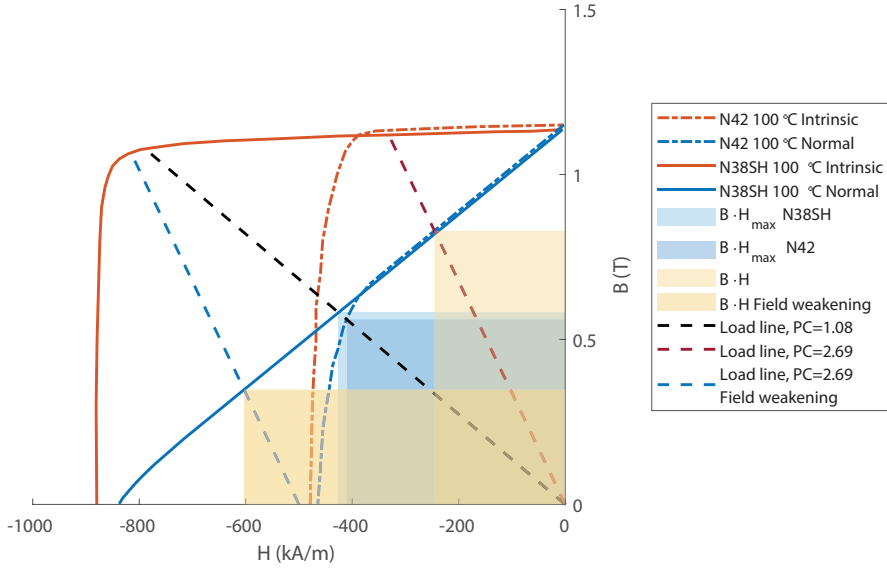
Figure 5.8: Two commercial NdFeB magnet grades at $100\,^\circ\text{C}$, where the load lines from figure 5.7 are kept. The N38SH grade does not risk partial demagnetization with the 1.08 load line, but that load line has little room for field weakening. The 2.69 load line with a field weakening of 500 kA/m is added.

For operation of NdFeB magnets at high temperatures, the literature offers many strategies, Hirosawa et al. [90] substitute iron for molybdenum or vanadium, in addition to cobalt and some neodymium is substituted with dysprosium. Sagawa et al. [91] attempts a wide array of substitution combinations and concludes that only 0.5-1.5% dysprosium can be added without affecting B_r. Honshima and Ohashi [92] describes a two-alloy powder metallurgy process, that allows for increased oxidation resistance, and increased coercivity from grain boundary coating of praesodymium, dysprosium, and cobalt provided by the second alloy. Hono and Sepehri-Amin [93] achieves high coercivity with no dysprosium, by controlling the microstructure.

The nomenclature of commercial grades of NdFeB magnets [87] feature suffixes M, H, SH and so on, that indicate both higher coercivity, and higher β. The higher temperature grades limit the remanent induction B_r that can be
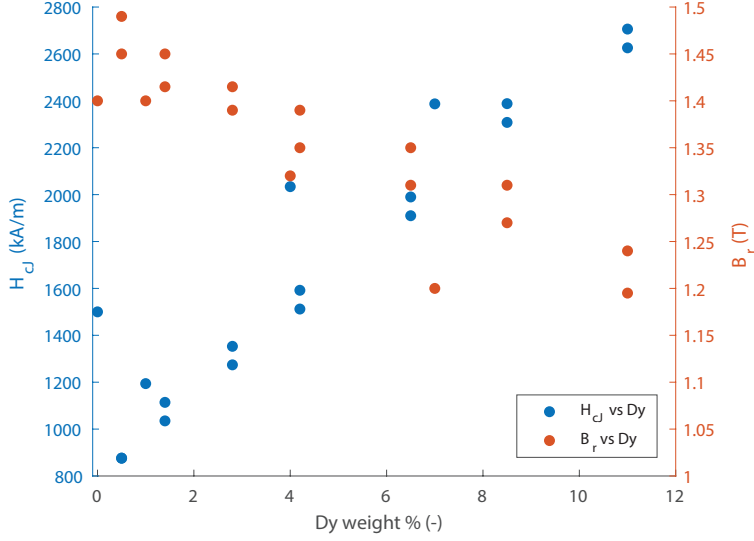
Figure 5.9: The effects of increased dysprosium content on B_r and H_{cJ}. More dysprosium leads to higher H_{cJ}, at the expense of reduced B_r, representing a clear trade-off depending on required operating temperature. Data from [87, 94, 93, 95].

achieved, as stated in Paper I. The dysprosium content in different grades [94] are combined with data from the literature in figure 5.9, which shows that B_r decreases while intrinsic coercivity H_{cJ} increases, with a higher dysprosium content. The highest values of both B_r and H_{cJ} can not be achieved simultaneously.

The addition of elements such as dysprosium, praesodymium, cobalt, copper or even terbium carries an increased cost compared to the elements they substitute, neodymium and iron, as can be seen in figures 5.1-5.2. Publicly available price data for NdFeB magnets is scarce, but some data has been gathered in figure 5.10, which shows that the high temperature rated magnets carry a cost premium, this trade-off is further illustrated by the material cost of the composition from literature. The resulting cost is higher for magnets with a lower room temperature energy product, but high β. The highest median cost composition is N38AH grade, consisting of materials of the order of five times the cost of the composition suggested by Hono and Sepehri-Amin [93] and two to three times those suggested by Bai et al. [95]. The commercial grades do manage to achieve higher β and coercivity due to the use of more dysprosium. No direct correlation between the import price data and the calculated material prices have been found, there may exist differences in quality, performance, tolerances, shape, and order quantities. A model for manufacturing of sintered magnets is not included, a starting point could be the manufacturing processes to produce different grades as described by Honshima and Ohashi [92].
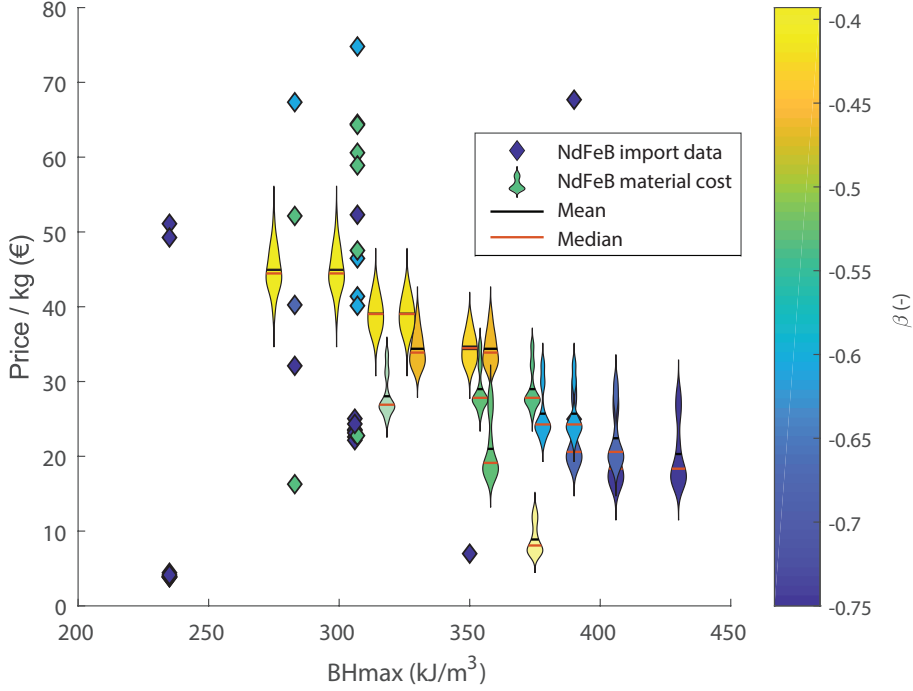
Figure 5.10: NdFeB Magnet price data at import, with temperature rating and energy product based on reported magnet grade, where available [79]. Included is also a material cost estimate of three compositions described by Bai et al. [95], which corresponds to *SH* grade, a composition described by Hono and Sepehri-Amin [93], and high B_r compositions in [94] as distributions based on historic commodity prices between 2014 and the end of the dataset in figure 5.2.

5.3 Insulation and Coatings

Insulation systems for machines and generators are defined in IEC 60085 [96], which refers to the maximum hotspot temperature allowed by the insulation system. Numerous coating materials are used in machines and drives, providing desirable properties at the boundaries of base materials. For example the insulating coatings on electrical steel, and copper wires, slot liner in the form of film or porous sheets in stators, or for protection against corrosion in magnets or electrical contacts.

Coatings on electrical steels serve two purposes: the primary one being electric insulation of one sheet from the next, and the secondary is to reduce wear in the cutting process. The selection of an application specific coating also requires consideration of thermal, mechanical and chemical properties, as well as thickness [97]. Coating materials range from organic to inorganic, where the inorganic coatings provide a higher operating temperature, increased per lamination re-

sistance for a given thickness. Organic coatings provide better lubrication for punching, but limit operating temperature to 180 °C [82].

Conductor coatings limit the peak operating temperature, but as shown in figure 5.11, the price of a drawn and coated copper wire is not affected significantly by the rated temperature of the insulation. The higher grade insulation material can carry a cost premium, but in the context, it is small and can be offset by tolerances or order quantities. Both the pre-applied enamel coating and the secondary coating, which is applied after the winding is attached to the stator, serve to provide insulation and conduct heat to the cooling medium. As they are subject to combined thermal, mechanical and electric stresses, the lifetime of a machine is often limited by these systems [98].
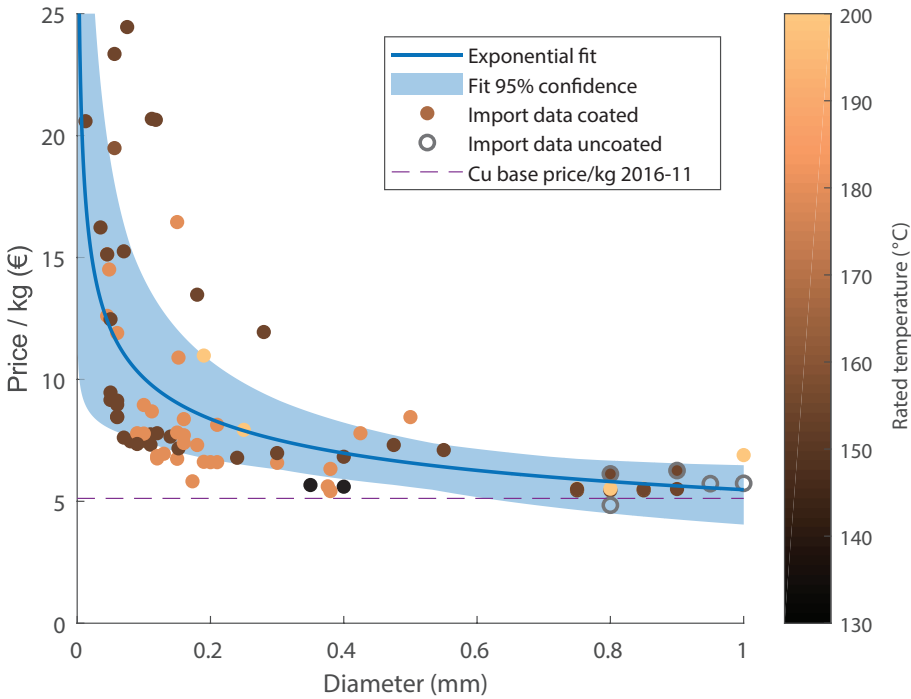
Figure 5.11: Copper wire price per kg as a function of wire diameter at an average 2016-10 copper spot price, import declaration prices [79]. Exponential fit and fit confidence interval. The color bar represents different temperature classes of the coating.

5.4 Electrical Conductors

Metallic materials are electrical conductors, the lowest room temperature resistivity conductors are shown in figure 5.12, with two high resistivity steels.
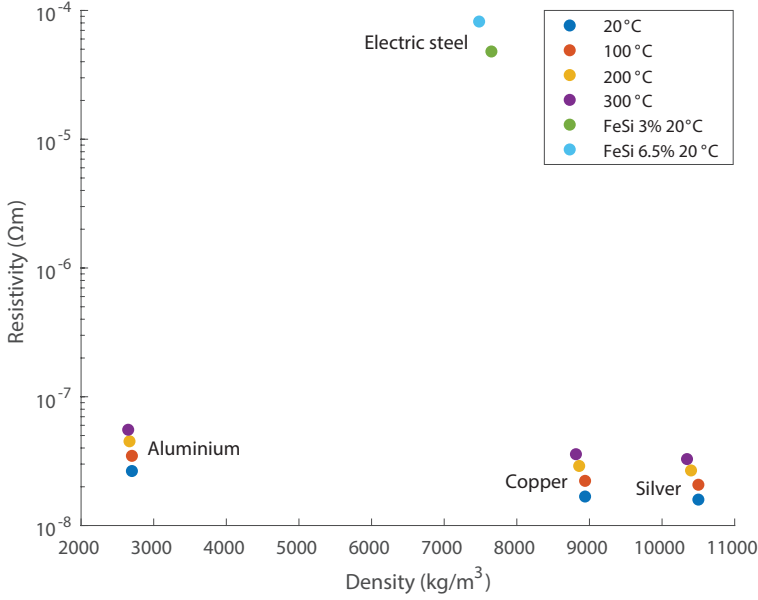
Figure 5.12: Metallic conductors with low resistivity, at different temperatures [99] and the resistivity of electric steel with different silicon content [100].

Their resistivity and density vary with temperature according to equations 5.11-5.12. These linear terms are only valid within a temperature range which is far from 0 K and each materials melting point, see Matula [99].

$$\varrho = \varrho_0(1 + \alpha_c \Delta T) \tag{5.11}$$

$$\rho = \rho_0/(1 + \alpha_v \Delta T) \tag{5.12}$$

Copper is used to a large extent in industry, the price of copper and aluminium is shown in figure 5.1. Silver is rarely used due to the high cost, about one hundred times that of copper. All electrical conductors are assumed to be made of copper in this work. Copper wire or magnet wire, is produced by casting of unalloyed copper with very low oxygen content. The cast metal is rolled into a wire with a diameter on the order of 8-10 mm, these coils are then drawn into the desired wire diameter. The drawing processes is performed gradually in steps of for example $l_1 = 1.2l_0$. Drawing a 0.7 mm wire from 8 mm stock therefore requires $n = 27$ steps, according to equation 5.13. Each drawing step incurs a cost, leading to a higher cost for thinner strands, which can also be seen in the empirical data in figure 5.11.

$$\left(\frac{r_o}{r_1}\right)^2 = \left(\frac{l_1}{l_0}\right)^n \tag{5.13}$$

46

The resistance of conductors for alternating currents is increased by a phenomenon called skin effect [101]. The phenomenon arises due to the induction of eddy currents from the alternating magnetizing field H, around the conductor. These eddy currents counter the current flow in the center of the conductor and follow the flow at the edges. The effective current carrying area becomes reduced, so while the resistivity remains constant the resistance increases due to the reduced area. In practical engineering terms this is defined as skin-depth δ, shown in equation 5.14, where δ is the depth at which the current density is $1/e$ of the current density on the surface.

$$\delta = \sqrt{\frac{2\varrho}{\omega_e \mu}} \tag{5.14}$$

For practical windings in components, the AC resistance of a winding is also affected by the proximity effect, for which an efficient model is described by Sullivan [102].

5.5   Enclosures and Housings

Enclosures can be produced in a multitude of materials, including cast iron, steel, aluminum or magnesium. In the case of power electronics components for stationary applications such as chargers, folded sheet-metal structures have been investigated in Paper V, with results from that work utilized in Paper VII. Certainly more exotic mixed material combinations could be considered, such as fiber-reinforced injection moulded parts for EMI shielding [104]. For drivetrain components cast aluminum parts are assumed, as they offer good mechanical properties, thermal conductivity and EMI shielding, die-casting also allows for production of parts in a range of sizes, see figure 5.13.

Housings for machines and gearboxes must support the reaction torque to some mechanical ground in the vehicle. The thermal constraints of all machines in this work are based on Márquez-Fernández et al. [105], and have been further elaborated on by Huang [106]. The latter describes two major cooling principles, direct and indirect cooling, in which the coolant flows between the stator and the housing in the direct case and only inside the housing in the indirect case. Other solutions have been reviewed by Liu et al. [107]. Shared cooling between components is an interesting topic, as cooling imposes thermal constraints on designs. Research on the multi-functional aspects of housings also extends to mechanical loads and vibrations. The costs of pumps and air to coolant heat exchangers are left for future work.
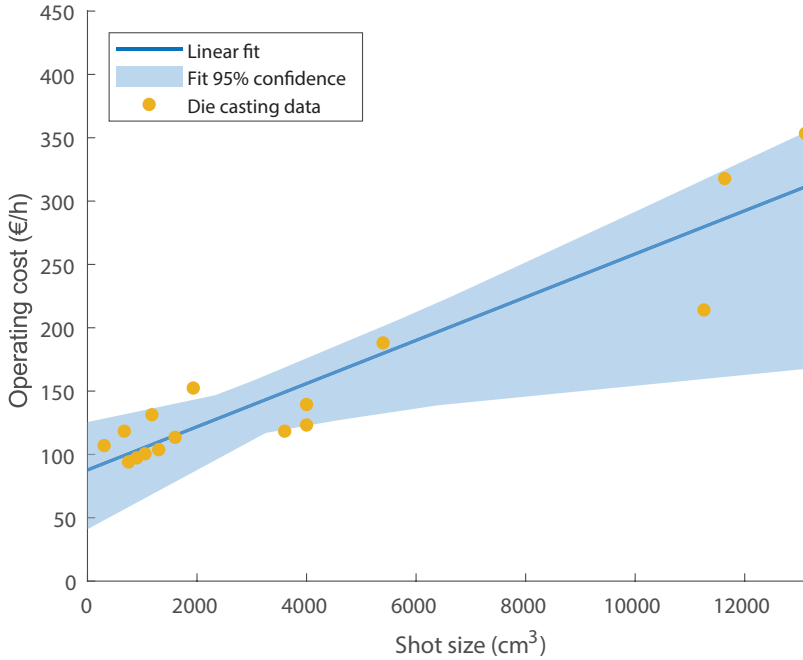
Figure 5.13: Operating expenses for two different types of aluminium die casting processes [103], with a linear fit model including the confidence interval range.

5.6 Semiconductors

The semiconductors used in Paper V are silicon based metal oxide semiconductor field effect transistors (MOSFETs), insulated gate bipolar transistors (IGBTs) and diodes. Wide-bandgap devices, made from silicon carbide (SiC) are gaining traction. A common application is freewheeling diodes for switches used in power components with inductive loads. SiC MOSFETs, gallium arsenide junction-FET and heterojunction-FET [108] are available on the market. Ward et al. [109] suggest that they are irrelevant for automotive power electronics, while they may not be suited for low pole number, low speed motor drives, they do enable for example high frequency converters [110], and alternative cooling strategies [111]. In other converters, such as insulated on-board chargers, SiC enables size reduction of magnetic components, leading to a higher power density [112].

In simplified terms, the semiconductor blocking voltage depends on the thickness and the substrate material, illustrated by the height in figure 5.14. Moreover, the current carrying capability depends on the chip area, seen as width and depth in figure 5.14. There is continuous development in semiconductor technology within different substrate materials, leading to reduced device height

and area for a given voltage and current rating. As an example for 1200 V devices, the height reduction is of the order of 220 to 120 μm and the reduction in required chip area is 50% over a 12 year period [109]. Rahimo et al. [113] reports thicknesses of less than 70, 140 and 210 μm for 600, 1200 and 1700 V respectively, devices for intermediate blocking voltages could certainly be made.
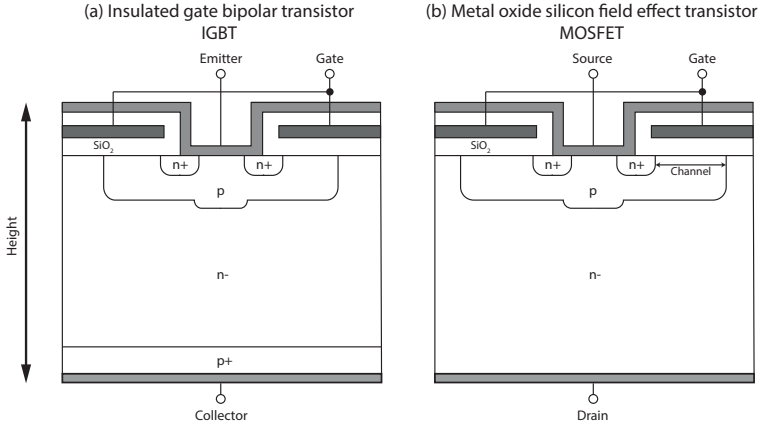
Figure 5.14: Idealized layer models of (a) an insulated gate bipolar transistor, IGBT, and (b) a metal oxide semiconductor field effect transistor MOSFET.
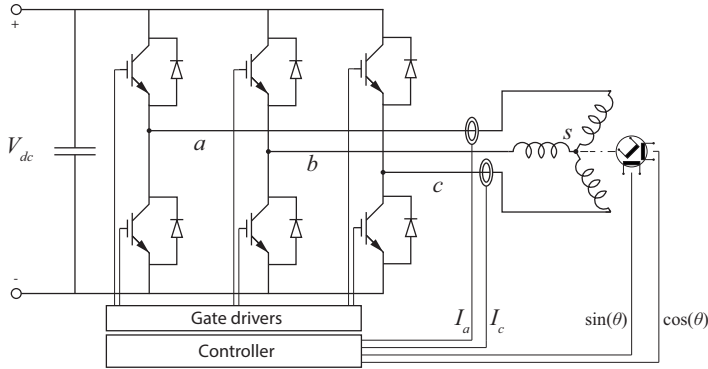
Figure 5.15: A DC to AC three-phase two-level converter connected to a three phase machine, controlled by current and position feedback from a resolver and two current sensors.

The energy loss from one switching event can be found by the analysis of the desired fundamental frequency at any given time and the switching frequency used in the converter. A typical two-level converter connected to an inductive load is depicted in figure 5.15. The converter can be controlled by a sinusoidal PWM switching scheme, shown in figure 5.16. The losses from switching and conduction determine the size of the switching devices in conjunction with the
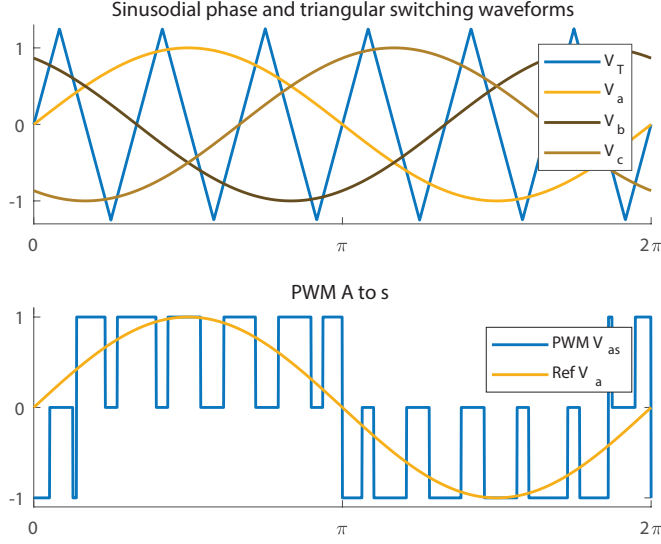
Figure 5.16: Three phase PWM switching of a two level converter, with modulation index m=0.8 and a switching frequency $f_c = 6 \cdot f_f$.

available cooling, as described in Paper V. The switching frequency also limits the maximum frequency of the fundamental waveform the converter outputs, which in turn may limit the rotational speed of some machines.

In Paper VI the rotational speed limit from the switching frequency was used in conjunction with the mechanical limit described in section 4.3. There exists numerous other converter topologies for different tasks, not all of which can be described here. In the case of automotive converters, Paper V describes insulated AC/DC converters [14] and DC/DC converters which were not included in the case study. A qualitative insight from the work in Paper V is that the magnetic components, transformers and inductors, are cost drivers in insulated converters due to their material, manufacturing and space requirements. Wide-bandgap devices enable a reduction in the size and cost of magnetic components, as switching frequencies can be increased with maintained switching losses.

Alternative cooling solutions, such as double sided cooling[114] and pin-fin equipped baseplates that lower the thermal resistance of power modules are developments that can lower the required chip area for such devices. Liang [115] reports approximately 50% higher current for the same area with maintained junction temperatures. A reduction in chip area within a substrate material translates to lower cost power modules, and enable reduced converter size and production effort. Furthermore, increasing the system voltage is shown to reduce total converter costs in Paper V, though only selected device and package types were analyzed in conjunction with conventional packaging and cooling.

5.7 Energy Cost
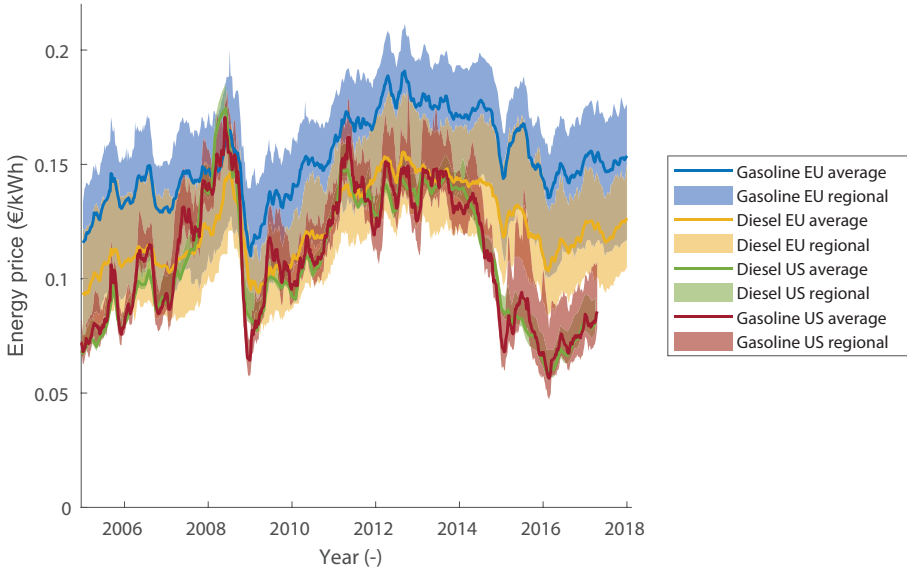
Figure 5.17: Consumer prices of energy in the two most common automotive fuels in different regions. The line graphs represent regional averages, while the shaded areas represent regional prices in different states. US fuel price data from US Energy Information Administration[116] including taxes and levies. EU fuel price data from the European Comission [117]. Conversion to €/kWh with data from [18, 75].

A significant portion of vehicle cost over its lifetime is the cost of energy [24, 118]. The price of a kWh of common automotive fuels is depicted in figure 5.17, which shows first of all that the price has varied significantly in recent history. These variations are mainly due to price variations on the global oil markets, whereas the regional differences within both the US and EU depend on taxation and transport to the region in question. It may be interesting to note that the per energy content fuel price remains very close for the two fuels in the US, whereas in Europe the difference on average is larger. The total inter-regional variation within Europe is also larger than in the US. The prices in Europe are consistently higher for gasoline, while diesel has become more expensive only recently. Other fuels are sold for automotive use such as Ethanol (E85), Liquefied Natural Gas (LNG), Methanol (M100) etc, are left out for clarity.

Consumer prices for electric energy are depicted in the same way, for Europe and the US in figure 5.18. The data is less detailed, but on average the prices on the two continents are similar. The regional differences are greater still, where in Europe, residents of countries such as Denmark and Germany pay the highest electricity prices. In the US the differences between regions is even more
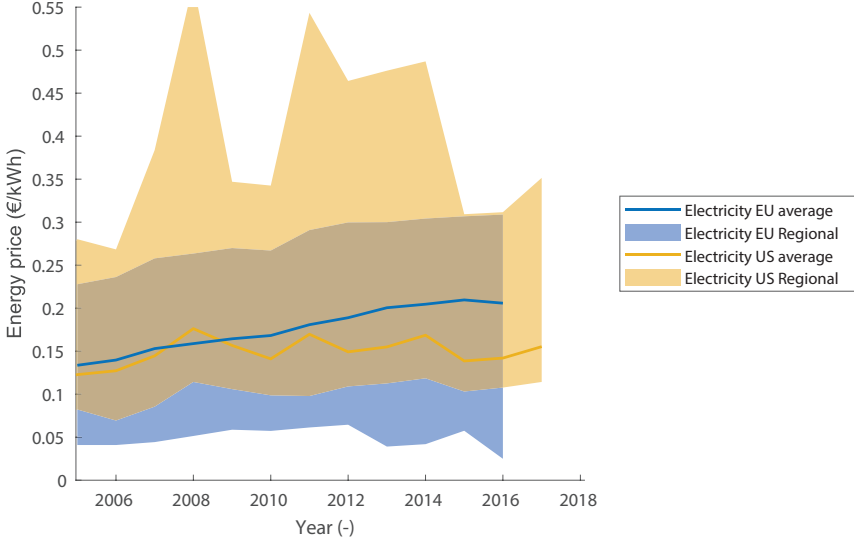
Figure 5.18: Prices of electrical energy in different regions. The line graphs represent regional averages, while the shaded areas represent regional prices in different states. Electricity prices are for household consumers, including taxes, levies and VAT [119, 120, 75].

prominent. Remote regions, such as Hawaii and Alaska see the highest prices. It may be interesting to note that the price per kWh for consumers in the two most commonly purchased forms, electricity and fuel, is lower on average for fuel.

5.8 Statistical Modeling

In order to quantify the confidence interval in datasets, such as the ones presented in figures 5.3 and 5.11, a robust method is needed. Monte Carlo approximations of the bootstrap distribution, as described by Efron [54], are used in this work. The method estimates a confidence interval of a sampled dataset $\mathbf{X}$, with an unknown distribution function f, by sampling a large number of bootstrap samples $\mathbf{X}^* = (X_1^*, X_2^*, ..., X_n^*)$, from a probability distribution $\widehat{f}$. This is done in order to approximate the true distribution $R(\mathbf{X}, f)$, by R^*.

$$R^*(z(\mathbf{X}^*), p(\widehat{f})) \approx R(\mathbf{X}, f) \tag{5.15}$$

where $z(\mathbf{X}^*)$ is a function of the bootstrap samples and the probability function $p(\widehat{f})$. Least squares is used to fit a suitable regression model to each of the bootstrap samples X_i^*

$$X_i^* = g_i(\widehat{\xi}) + \epsilon_i^* \tag{5.16}$$

The bootstrap regression models $\mathbf{X}^*$ are sorted, and the desired confidence interval of R^*, $(2p - p^*_{1-\kappa/2}, 2p - p^*_{\kappa/2})$ can be found by removing $\kappa/2$ samples from each tail of the sorted array of regression models $\mathbf{X}^*$. Examples of these regression models are depicted in for example figures 5.3 and 5.11.

The bootstrap method for determining confidence intervals is very useful. But there exists limits to its capability, as it assumes that the available data is a representation of all data. In cases where the data is so scarce that only two or three points have been found, so few data points are unlikely to represent all data, so no confidence intervals can be established.
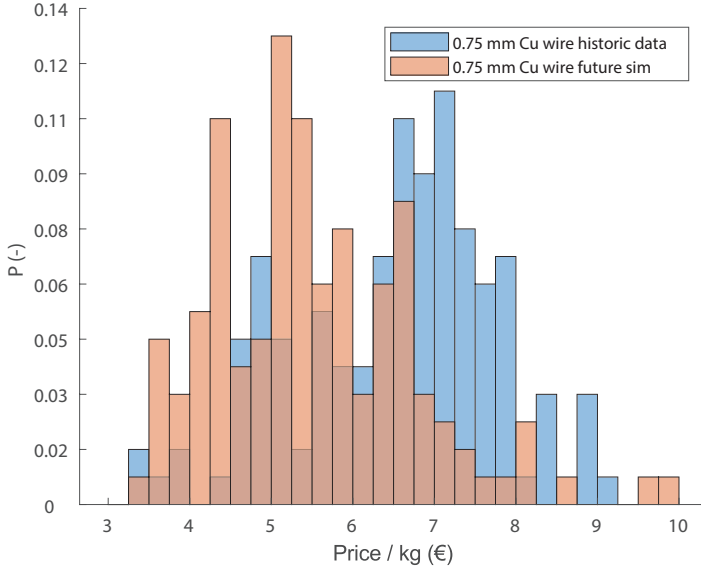
Figure 5.19: Simulated and historic 0.75 mm copper wire price per kg probability densities, based on the data in figure 5.1. The darker shaded region is the historic and future data overlapping.

The prediction of spot prices from futures contracts gathers much attention in economic research, for which a wide range of modeling approaches exist. Fama and French [121] describe and investigate the difference between spot and futures prices of precious metals, as a lost revenue from nominal interest in the spot price at a certain time versus the future contract at a later time. Smith and McCardle [122] suggest models based on Brownian motion and mean-reverting Brownian motion, while Gibson and Schwartz [123] and Schwartz and Smith [124] propose more complex two-factor models using Kalman filtering of futures observations in order to estimate the point to which mean reversion should occur.

There are merits to all approaches, but one clear conclusion is that one needs to deal with the stochastic nature of commodity prices if they are a part of total

product cost, which is discussed in section 6.3. By applying a mean-reverting brownian motion model to rearward time-series data (such as the one in figure 5.1) and extracting the added value for a specific wire diameter and insulation class, a simulated forward wire cost probability density can be generated, as shown in figure 5.19. This probability density can be fed in as cost of materials, K_B, as described in section 6.3 and Paper III. Machines with a large quantity of any specific commodity are affected by fluctuating material cost, especially induction machines with copper rotors such as the ones used in Tesla Model S and X. A potential model application is finding price levels of commodities, where it would be beneficial to switch from one material to another despite the added costs of re-engineering and investments in tooling. Examples of this could be changing permanent magnet or conductor materials respectively.

Chapter 6

Production Processes
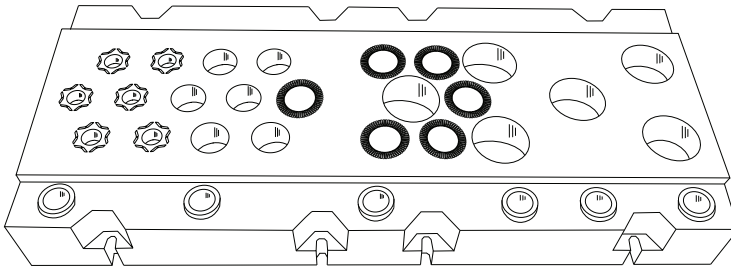
Figure 6.1: A multi-stage blanking tool, producing six stators and rotors per stroke.

A large number of processes exist that can produce the same part, a tool that produces six parts at once is depicted in figure 6.1. The intent in Paper II was to formulate a method to investigate when to move from one process, for smaller series or prototype manufacturing such as laser cutting of stator and rotor, or manually inserting windings, to another such as blanking or automated insertion winding. From the approach offered in Paper II, where all the processes were considered to produce equal results in all aspects but cost, the effect of design factors were not included.

Tools and machinery incur costs, which are divided between the machine and the tool, where the tool is something specific for a particular design, while the machine can also be used for other products. Furthermore, handling systems for steel coils, conveyor belts and other associated auxiliary equipment, is assumed to be included in the operating cost of the associated process or machine. The operating expenses for presses is shown in figure 6.2. Robots are seen here as a handling system, often serving a number of processes as an operating cost, while gripper tools, welding heads or measurement probes are seen as investments.
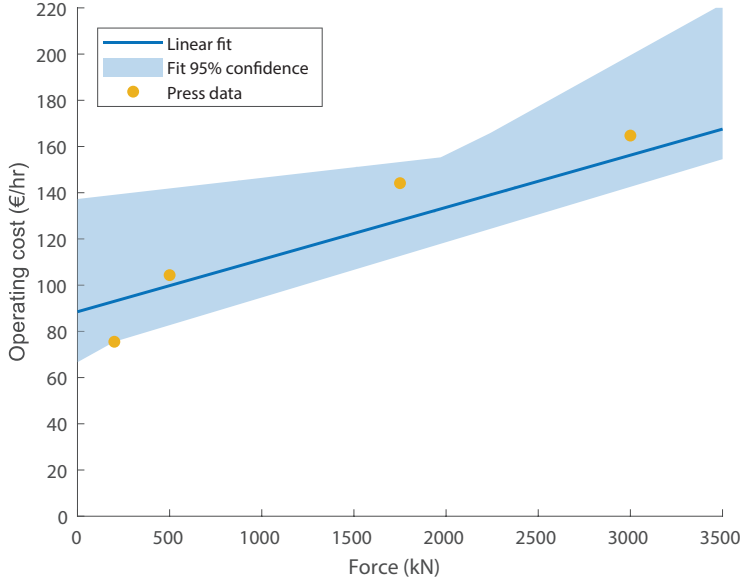
Figure 6.2: Operating cost as a function of force for presses, data from [125] currency conversion from [75] with linear fit and confidence interval.

The major cost driving processes identified in Papers II-VI are described in the following sections. Data and descriptions of general manufacturing processes can be found in for example Todd et al. [71], electric machine specific processes focused on induction machines can be found in Tong [68]. It should be noted that in many cases, the transition from for example winding one coil and the next, can make up a majority of the cycle time, especially when there are few turns and a large amount of parallel strands. Generally quality losses are assumed to be low, representing well tuned processes. Whenever a machine has a large fraction of idle-time (i.e not downtime due to maintenance) it is assumed to be put to use elsewhere and thus does not incur costs.

6.1 Blanking and Piercing

In electric machine production one of the major investments is the blanking tool for stator and rotor, which for large series production is exclusively piercing and blanking due to the amount of thin sheets required to produce a traction machine. A large multi-stage tool is illustrated in figure 6.1. The geometry of the machine is an important input to production analysis of any electric machine stator and rotor design. The euclidian distance in equation 6.1 gives the distance d along all the line segments defined by the points $p_0, p_1, ...p_n$, which is used to

calculate the circumference of any machine part to be cut, an example for a stator slot is shown in figure 6.3.

$$\mathrm{d}(\mathbf{p}_0, \mathbf{p}_1, ...\mathbf{p}_n) = \sqrt{(\mathbf{p}_1 - \mathbf{p}_2)^2 + (\mathbf{p}_2 - \mathbf{p}_3)^2 + ... + (\mathbf{p}_{n-1} - \mathbf{p}_n)^2} \qquad (6.1)$$
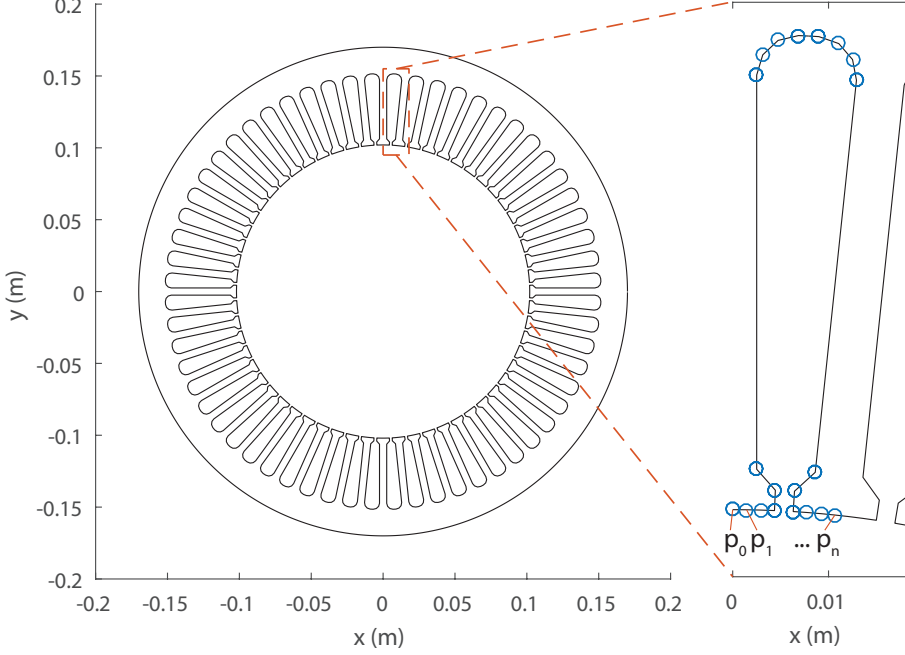
Figure 6.3: An illustration of the cut edge length calculation for a stator.

When the circumference of the cut is know, the total punch line area can be calculated with the sheet thickness. In Paper VI and Paper IV the sheet thicknesses considered were 0.35 mm and 0.5 mm, in high speed machines thinner sheets could be needed to control the losses. Sheet thickness and the circumference, together with the cutting forces in figure 6.4 allows for the sizing of required stripping force, defined by Lyman et al. [77] as equation 6.2. This relation denotes a linear behavior between the force that the press needs to provide, F_{st}, and the material parameter k_p, and the area of the cut, $a_c = dt$, which relates to equation 6.1 and the material thickness t.

Knowledge of the tool size, cut periphery length, number of parts required, and material parameters known, an empirical relation for calculation of die cost[125] based on these parameters, is shown in equation 6.3.

$$F_{st} = k_p a_c \qquad (6.2)$$
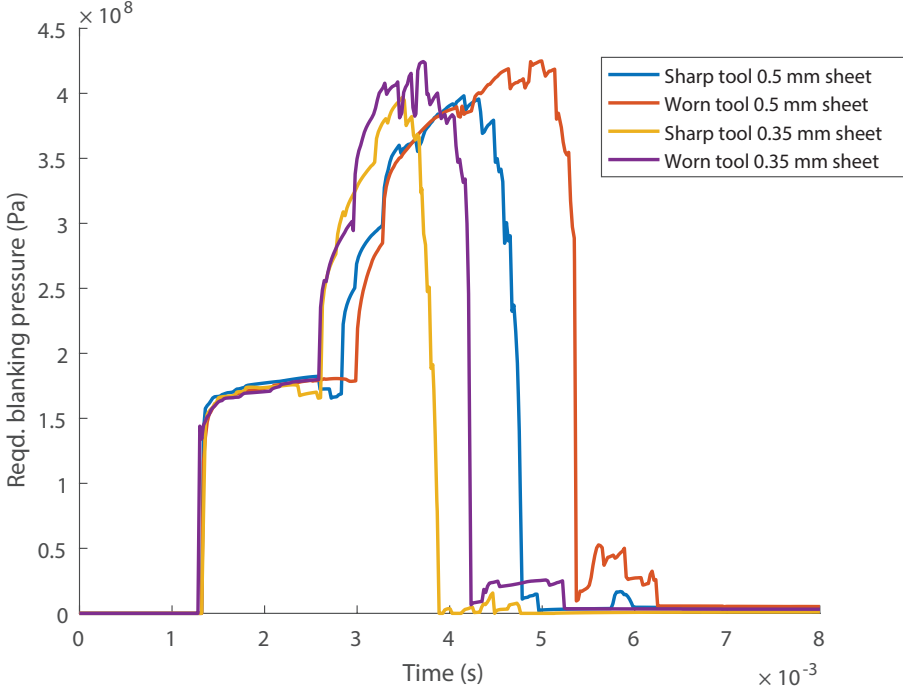
Figure 6.4: Required blanking pressure k_p for M400-50A and M330-35A sheet with a sharp and worn cutting tool [126]. Showing a very linear increase from 0.35 mm to 0.5 mm thickness in both the worn and sharp tool cases. Peak forces increase 6.7% and 6.9% for 0.5 mm and 0.35 mm respectively, with a worn tool compared to a sharp tool. The peak pressure difference is 0.1% in the worn case and 0.3% in the sharp case. Relative force increase of a similar magnitude have been found by adjusting blanking clearance by Fang et al. [127].

$$K_{die}(K_B, K_{prod}, C, C_{ref}, n, t, a_d, d) =$$
$$K_B + K_{prod} \cdot (0.68 + 0.05 \ln \frac{C}{C_{ref}} n t^2) f_{lw}(\propto d^2/a_d) M_{po}(\propto a_d) \qquad (6.3)$$

where K_{die} is the cost of the die, K_B is the cost of the die steel, K_{prod} is the average hourly rate for the electric discharge machining (EDM), hardening, finishing and associated personnel, Moreover, C is the ultimate tensile strength of the material to be cut and C_{ref} represents a reference mild steel (here 245 MPa), n is the number of parts to be made in the die, t is material thickness in mm. Finally a_d denotes the useful die area and d the peripheric length to be cut. The empirical term f_{lw}, proportional to d^2/a_d is a measure of the useful die area and associated geometry complexity, for which electric machine dies typically score very high due to intricate slots. In the formula, the number of produced

parts n has a large influence, but cannot be extended indefinitely, because a new tool must be made eventually. It is evident from equations 6.2 and 6.3 that a lower ultimate tensile strength sheet material is desirable in lowering the die and press cost respectively. The one term lacking in the formula would be material hardness, both of the tool and workpiece, as hardness affects the tool wear, together with punch-die clearances [77].

The topic of sheet thickness comes into play both for the required press force, and wear. Blanking of 0.27 mm sheets, in comparison with 0.35 mm, should generate less wear per sheet. But an assumption on the order of a similar stack height before a die regrind is required serves as a starting point until data is available. Some increase in wear due to the narrower tool clearances required for achieving acceptable burr heights with the thinner sheets is expected. The finer tolerance requirement in the die should also increase its cost, a factor not included in equation 6.3.
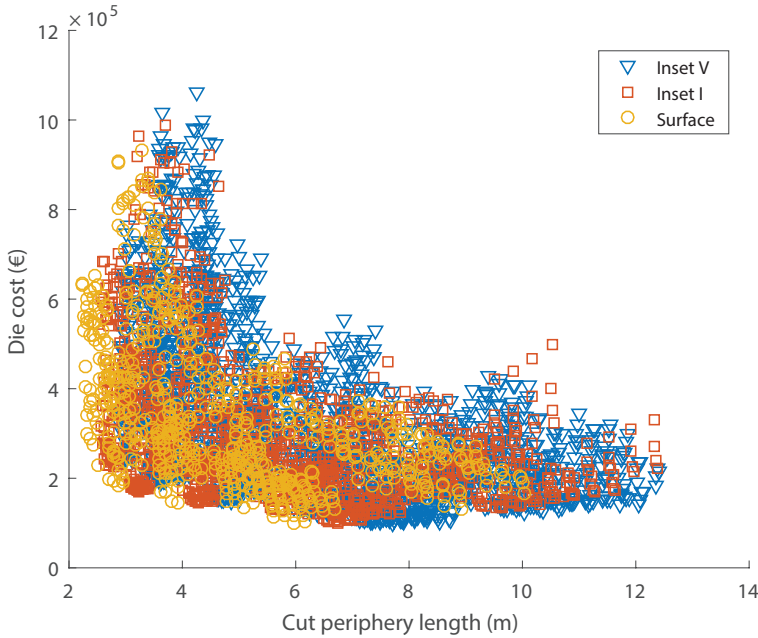
Figure 6.5: Die costs for different machine designs used in Paper VI, calculated from the empirical formula in equation 6.3 for each of the fixed gear ratio machine geometries in Paper VI. D6 steel die costs in the range €$1.5 \cdot 10^5$ to €$2.5 \cdot 10^5$ and carbide die costs in the range €$6 \cdot 10^5$ to €10^6 have been obtained from industrial suppliers.

In Paper VI a large number of machine geometries are scaled in length to meet the performance requirements of the vehicle with the associated reduction gear. This results in different production requirements for different machine diameters. Typically a low diameter machine will be long to meet a torque requirement for

specific gear ratio, thus requiring more sheets to be cut for one machine. In the design dataset used, many designs exist that are large, both in stator outer diameter and in length. The die costs of all fixed gear designs in Paper VI is shown in figure 6.5. The resulting die costs represent a wide range, but it can be inferred that some of the designs simply perform poorly and require a large machine length to meet the torque and power requirements set by the vehicle. Some of the designs need to be scaled to active lengths approaching one meter, thus requiring about 3000 sheets per machine, which in turn equates to high tooling costs due to wear. Conversely some designs of moderate stator diameters (25-30 cm) can achieve the performance target using 272 and 215 sheets respectively, which gives a tool cost of €$1.5 \cdot 10^5$ to €$2 \cdot 10^5$, due to the reduced wear from fewer strokes per machine.
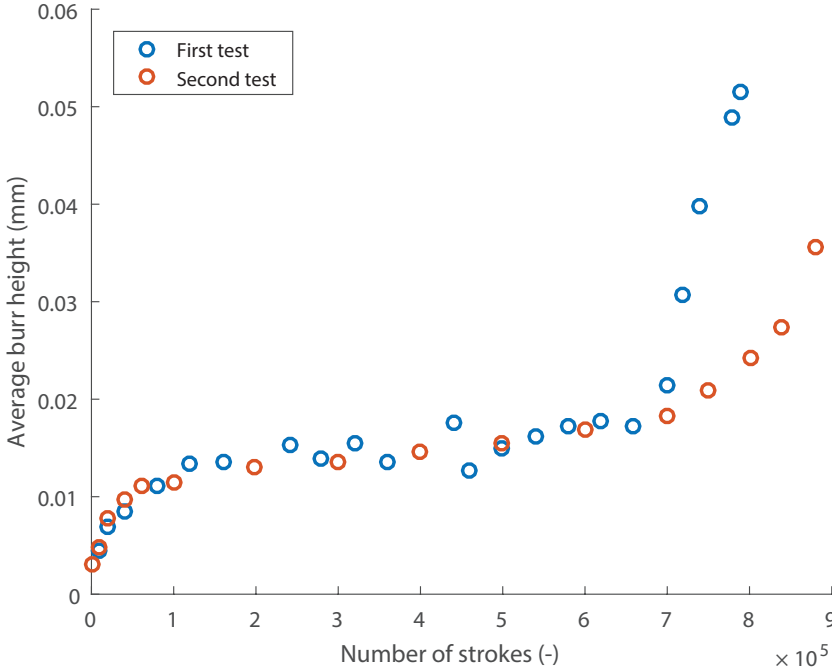
Figure 6.6: Resulting average burr height vs number of strokes between tool re-grinds for D6 tool steel cutting M330-35A electric steel sheet, as reported by Kraemer et al. [128].

Focusing on wear, Kraemer et al. [128] have performed experiments for D6 tool steel wear in cutting M330-35A, as shown in figure 6.6. They reported that the burr height quickly increases after 700000 strokes in the first series and at approximately 800000 strokes in the second series. Both wear behavior and die costs are in reasonable agreement with data provided by die suppliers.

There also exist practical limits to what blanking layouts can be achieved,

if not limited by press width [129], then by the coil width from steel producers. Electric steel coils typically have a coil width of about 1.2 m, which limits the potential material yield for larger round stators. If blanking gaps and other practical limitations are disregarded and circles of the largest radius possible are packed on a continuous strip of a width of one, then the best packing layouts are square or hexagonal depending on how the radius of the circles relates to the width of the strip. Figure 6.7 illustrates the problem, for which the solution to each of the three packing ratios is provided by equation 6.4. The square strategy provides the same solution irrespective of radius, given that strip is adjusted to the sum of the radii or vice versa. The two hexagonal packing solutions are better than the square solution only if 3.5 or 4 circles fit on the strip. They both converge to the same limit of $\pi/4\sin(\pi/3)$ as $r \to 0$.

$$
\begin{aligned}
R_{hexUn} &= \frac{\pi(2-r)}{8\sin(\pi/3)}, & r \in \left\{\frac{1}{4}, \frac{1}{6}, \frac{1}{8}, ...\right\} \\
R_{square} &= \frac{\pi}{4} \\
R_{hexEv} &= \frac{\pi(1-r)}{4\sin(\pi/3)}, & r \in \left\{\frac{1}{3}, \frac{1}{5}, \frac{1}{7}, ...\right\}
\end{aligned}
\tag{6.4}
$$
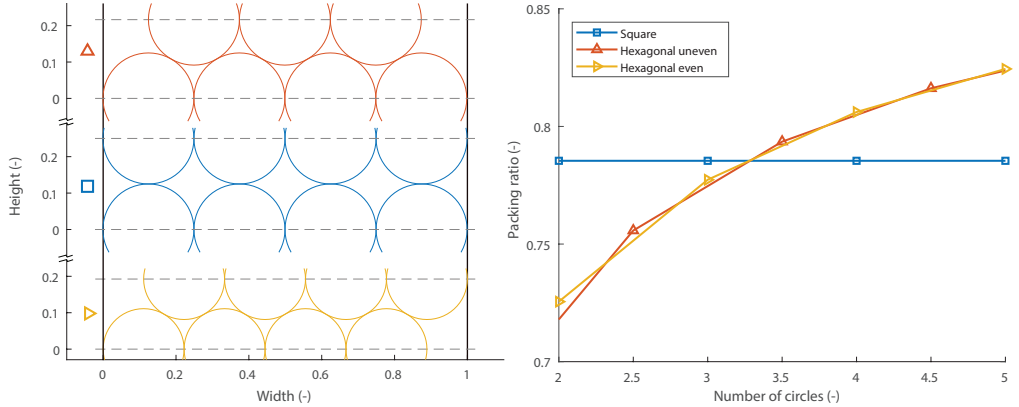
Figure 6.7: Ideal circles in different packing configurations on an infinite strip of finite width. The packing ratio of the different strategies is illustrated on the right, showing that the square strategy is superior if fewer than four circles fit inside the finite width.

In practical terms, the limited strip and press-bed widths limit the potential material yield for large stator diameters unless segmentation or non-round outer geometries are used. A case study with segmentation in a fixed width press was presented in Paper IV. Problems of similar nature are recurring in this type of work, edge effects also strongly influence semiconductor die yields and the number of strands that fit inside a slot.

6.2 Winding

Winding is a central process in both electric machines and in magnetic components such as transformers and inductors. The winding process can be executed in a number of ways, depending on the design of the component. The most common winding processes are, insertion winding, linear winding, needle winding, flyer winding and hairpin winding, which are presented below. Cost and process speed data are summarized in table 6.1.

Table 6.1: Data for different winding processes, lower figures represent flexible pilot plant equipment, higher represent fully automated high throughput machinery [130, 131, 132].

Process	Machine investment (k€)	Winding rate (turns/s)
Linear winding	40-500	5-500
Needle winding	150-450	2-40
Insertion winding	200-3800	4-10
Flyer winding	100-350	200

6.2.1 Needle Winding
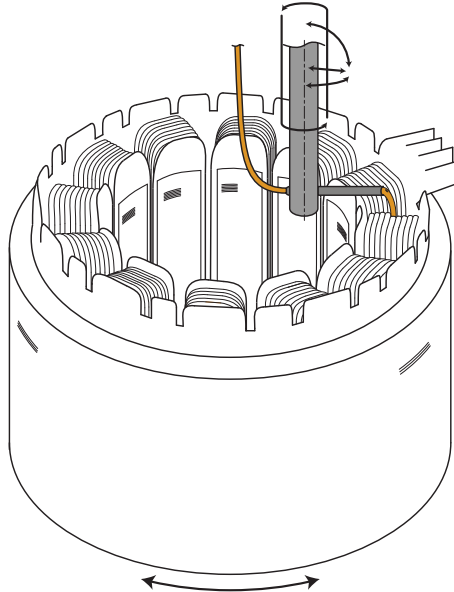
Figure 6.8: A needle winding process, the winding nozzle can have 1-3 degrees of freedom and the workpiece has 0-1 degrees of freedom. Depending on the workpiece size, multiple nozzles can wind the machine simultaneously.

A common process to wind stators is needle winding, depicted in figure 6.8, where the wire is guided by a needle tool. The primary tool-path is a translation in the axial direction, while either the workpiece or tool performs a small rotation around the center axis. These movements are accompanied by a small translation in the radial direction, which allows for very exact placement of the wire, resulting in an ortho-cyclic winding.

One downside of traditional needle-winding is the gap left by the needle, which reduces the fill-factor of the winding. This can be circumvented by using a chain-pole stator [133], which increases reluctance in the magnetic circuit as described in section 4.4. Alternatively one could introduce wire tension control to either drag or push the wires to the desired location[134]. Another negative aspect is that due to the movement of the tool, if two or more wires are fed through simultaneously, then each turn will also twist the wires, which reduces the placement accuracy and fill factor. Multiple parallel strands are often desired in traction machines because of high currents and frequencies. In Paper IV the needle-wound stator used pre-twisted wire bundles, the bundles led to a poor fill factor that combined with the low pole number yielded a low cost machine with low performance.

By introducing another rotational degree of freedom to the tool, the transition to the next tooth of the same phase or termination points can be performed with an uncut wire. This is an advantage over linear winding, as no bus-bar is required for termination of the winding. Winding speed is typically around 10 turns/s while winding one tooth [130], and slower for transitions between teeth or termination points, higher speeds can be reached with multiple winding heads [132].

6.2.2 Linear Winding

The simplest form of winding is linear winding, sometimes called spool winding, an illustration is shown in figure 6.9. One to several wires are attached to the workpiece, the workpiece is rotated until the desired number of turns has been achieved. The wire feed location can be controlled along one axis to achieve either an ortho-cyclic or a helical winding. When winding long workpieces, it is beneficial to control the wire tension along the long side in order to avoid ballooning of the winding. The force dynamics in winding different tooth form factors has been described in Blanc et al. [135]. One key benefit, with respect to fill-factor in linear winding is the possibility to wind multiple parallel strands without twisting, because of the the rotation of the workpiece instead of the wire feed. The linear winding process can be performed on a bobbin separate from the stator, which increases flexibility. In order to assemble a separate bobbin onto the stator, the tooth protrusions must be removed or be attached to the
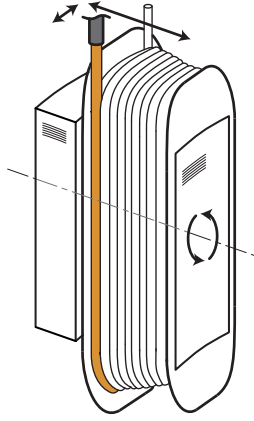
Figure 6.9: A linear wound stator tooth, where a rotation of the workpiece is the primary motion, and the wire-nozzle has 1-2 degrees of freedom to control the placement of the wire.

bobbin itself in a structurally sound manner. A stator segment can also form the bobbin to be wound, as described in Paper IV.

6.2.3 Flyer Winding
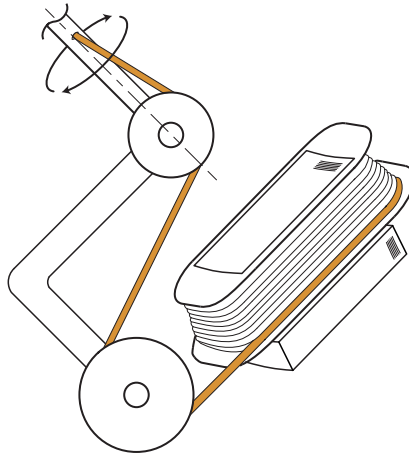
Figure 6.10: A flyer wound stator tooth, where a single axis rotation of the winding arm is the primary motion. It is possible to add a depth axis to control the placement of the wire. This process is very fast, but limited by force dynamics in the wire and the inherent twisting of the wire due to the rotation of the winding arm.

The flyer winding process features grooved wheels to guide the wire as depicted in figure 6.10, or nozzles similar to needle winding. However it does not have the same degree of control, as the nozzle instead follows a circular path when it generates the winding. In some cases this is combined with an axial motion of either the nozzle or the workpiece to more accurately position the individual strands. Actuation of the tool is simpler, and due to the circular motion, high speeds can be reached. In long and slender workpieces, the wire force dynamics will limit winding speeds, similar to linear winding.

6.2.4 Insertion Winding
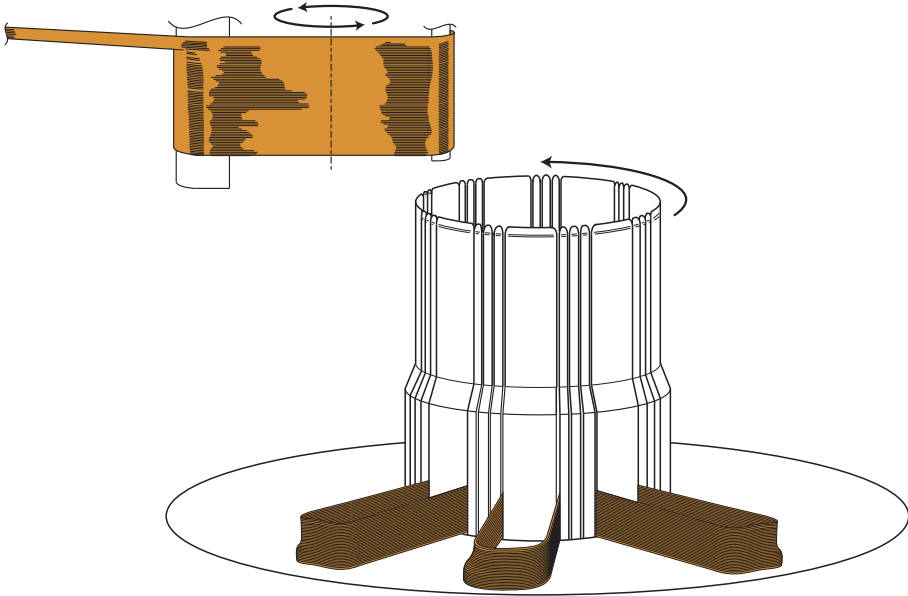
Figure 6.11: Insertion winding with hoop coils wound and placed on a coil carrier. A linear winding process prepares the next hoop coil on the top left.

Insertion winding is a multiple step process, where hoop coils are wound on an adjustable bobbin by a flyer or linear winding process, and subsequently placed on a coil carrier as illustrated in figure 6.11. Each coil is placed in a specific location, corresponding to the desired winding layout as illustrated in figure 6.12. Once the hoop coils are completed, the coil carrier is moved to the insertion station, where the stator is placed onto the coil carrier and a linear actuator pushes or pulls the coils into the stator slots. This process receives surprisingly little attention in literature, despite being one of the most common processes in industry. One simulation effort is presented by Hofmann et al. [136], for a small amount of wires and an insertion tool speed of 50 mm/s, this

work demonstrated potential for determining individual wire tensions during the insertion process, which could be used to improve process speeds.
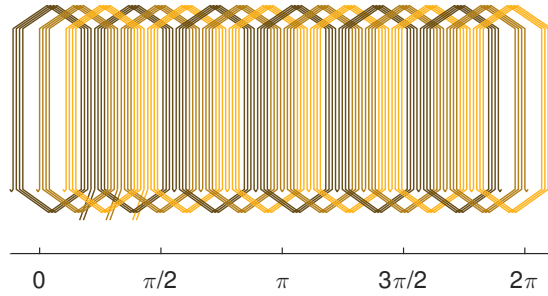
Figure 6.12: A Q2 insertion winding layout, depicting the relative location of the three phases.

The winding layout, exemplified in figure 6.12, impacts the material use and how the winding is placed on the winding carrier. The winding function shapes the electric field and with that, some of the harmonic content in the stator. Windings with less than full pitch can be used in machines such as the one depicted in figure 4.3. For certain slot/pole combinations, short pitched windings can reduce the number of layers in the winding from three to two.

6.2.5 Hairpin Winding
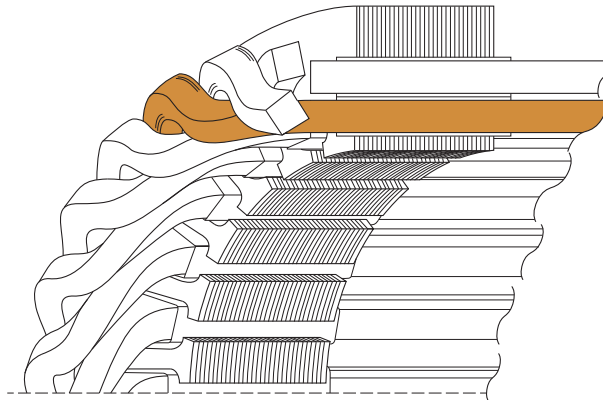
Figure 6.13: A partially completed hairpin stator, with formed square conductors inserted from one side. On the other side straight conductors extend to the right, still to be shaped and connected in order to complete the winding.

A hairpin or bar-wound stator, see figure 6.13, is typically produced by first preforming a number of hairpins that are subsequently inserted from one side of the stator. The ends of the hairpins are then re-formed on the opposite side and

contacted to complete the turns of the winding around the full circumference of the stator. The hairpins must be shaped to avoid interference from neighboring conductors. The hairpins form a repeating structure that originates from a slot near the stator back, spans half the pole distance, arcs inward one slot and descends into a slot closer to the rotor. On the opposite side this pattern is repeated, spanning half a pole distance, being joined across from the slot close to the rotor to another hairpin originating from a slot close to the stator back. The geometry is such that only even numbers of turn combinations can be created using this method.

Recently a new hairpin winding method called continuous hairpin, or s-winding, circumvents the number of turns limitation and the required termination process. The drawback is that the winding must be fed in radially through the slot opening, which means no stator tooth-tips can be present during winding. Paper IV presents a comparison of hairpin windings with insertion winding, needle winding and linear winding.

6.3 Economic Modeling

Figure 6.14: A manufacturing process, illustrated by a box, with some item, such as a coil of steel entering from the left. Some form of work is performed on it, such as a forming operation. A higher value part or product then exits the process.

A manufacturing process is defined here as some work performed on an object to increase its value, shown in figure 6.14. Not to be confused with a development process, which in this work is not accounted for. All manufacturing processes in this work are modeled using equation 6.5, which is a simplified form of that first published in Ståhl et al. [137]. It contains a significant amount of parameters, but it has the straightforward form: $\text{cost}(n) = \text{investment} \, / \, n + \text{constant}$, where n is the nominal number of units produced. The annuity cost of product specific assets K_A, such as tools and fixtures, is determined by the useful life of the asset, its initial cost and the cost of capital, all depreciations are assumed linear.

The cost is given by

$$k(\gamma, n) = \frac{K_A}{n} + K_B \left[\frac{1}{1 - q_Q} \right] + K_{CP} \left[\frac{t_0}{1 - q_Q} \right] +$$
$$K_{CS} \left[\frac{t_0 q_s}{(1 - q_Q)(1 - q_s)} \right] + K_D \left[\frac{t_0}{(1 - q_Q)(1 - q_s)} \right] \quad (6.5)$$

The notation $k(\gamma, n)$, is used in order to describe different processes γ. All terms on the right hand side of equation 6.5 are functions of γ, K_A is shared by each of the n units produced.

To include the cost of the v previous manufacturing operations in a subsequent one, the material cost at the process γ_w is

$$K_B(\gamma_w, n) = \sum_{u=0}^{v} k(\gamma_{w-1,u}, n) \quad (6.6)$$

an illustration of the notation used in equations 6.5 and 6.6 is shown in figure 6.15. The index v distinguishes the processes $\gamma_{w-1,v}$.
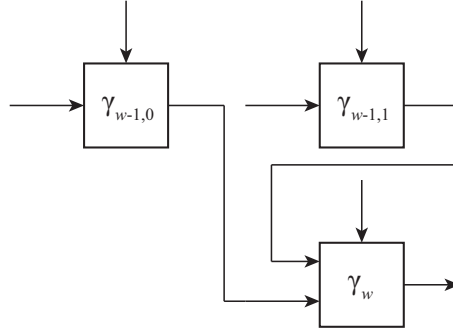
Figure 6.15: Two parallel manufacturing processes, $\gamma_{w-1,0}$ and $\gamma_{w-1,1}$, preceeding the current one γ_w, in a system. γ_w uses materials produced by the two preceeding processes γ, the index $v \in \{0, 1\}$.

Combining equations 6.5 and 6.6 gives the cost for a number of manufacturing operations as

$$k(\gamma_w, n) = \frac{K_A}{n} + \sum_{u=0}^{v} k(\gamma_{w-1,u}, n) \left[\frac{1}{1 - q_Q} \right] + K_{CP} \left[\frac{t_0}{1 - q_Q} \right] +$$
$$K_{CS} \left[\frac{t_0 q_s}{(1 - q_Q)(1 - q_s)} \right] + K_D \left[\frac{t_0}{(1 - q_Q)(1 - q_s)} \right] \quad (6.7)$$

which enables a description of a system and an analysis of its costs. A small system consisting of three processes is depicted in figure 6.15. Even this tiny system gives a long expanded equation, which is cumbersome for systems containing more than a few operations.

Equations 6.5-6.7 are only valid under the condition

$$Y_s \geq \frac{nt_0}{(1 - q_Q)(1 - q_s)} \tag{6.8}$$

where Y_s is the number of seconds in a year. If the condition is not fulfilled, either n units can not be produced, or two or more of the same manufacturing operation must be run simultaneously.

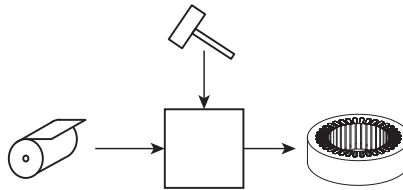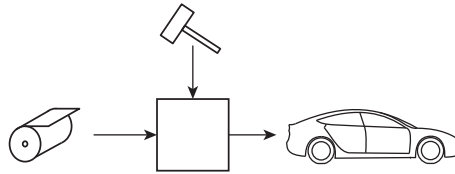**Figure 6.16:** A process, illustrated by a box, with some item, such as a coil of steel entering from the left, having some work performed on it. Exiting on the right is a highly refined product.

It is clear that the boundaries of each system are highly relevant to the model. Some draw the box in figure 6.14 around the entire production system, and simply ask how much the system cost, and what the cost of capital is. Then count the number of crates filled with goods that exit the box per hour, then open one crate to see how many items are inside. The large black-box method can yield very useful results, provided access to that particular factory is granted, it is however not very robust to altered specifications, external conditions or new processes. An illustration of such models is shown in figure 6.16.

In this work, the boundary around the production system is limited by the commodities described in chapter 5 that enter the first processes, and each box in the subsequent flowcharts depicts only one of the many of the individual processes that were described previously in section 6, with an emphasis on the workings of each process, measured as a cost. How cost scales with decisions made regarding the process, such as cycle times from extra turns of winding, or the number of cycles required to generate a longer machine, or a larger casting in a higher power converter, in relation to material cost is relevant to total calculated cost.

Equations 6.5 - 6.7 can be used with probability distributions for parameters that are either uncertain or vary over time. The cost of commodities, as described in chapter 5, tends to vary on the global market, leading to uncertain costs of raw materials on the first row of any production system. In order to

capture how these effects propagate through the system, equation 6.9, accepts probability distributions as input, it was used to study the effects of variance in cycle times in Paper III, and cascading downtime in Fyhr et al. [138].

$$
\begin{aligned}
\mathbf{k}(\gamma_w, n) = & \frac{\mathbf{K_A}}{n} + \sum_{u=0}^{v} \mathbf{k}(\gamma_{w-1,u}, n) \left[\frac{1}{1 - \mathbf{q_Q}} \right] + \mathbf{K_{CP}} \left[\frac{\mathbf{t_0}}{1 - \mathbf{q_Q}} \right] + \\
& \mathbf{K_{CS}} \left[\frac{\mathbf{t_0 q_s}}{(1 - \mathbf{q_Q})(1 - \mathbf{q_s})} \right] + K_D \left[\frac{\mathbf{t_0}}{(1 - \mathbf{q_Q})(1 - \mathbf{q_s})} \right]
\end{aligned}
\tag{6.9}
$$
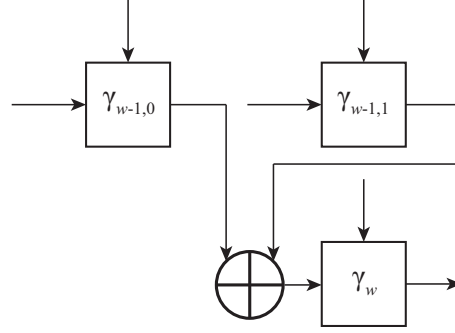
Figure 6.17: Three processes in a system, where there exists a decision between the first two $\gamma_{w-1,0}$ and $\gamma_{w-1,1}$, either of these may be used as materials in γ_w. The symbol $\oplus$ is exclusive or.

Potential decisions regarding manufacturing operations are considered to be made by a rational actor, based on the results of the cost equation 6.7, or in the case of uncertain problems, the probability distribution formulation in equation 6.9. The rational actor simply chooses the lowest cost part in the deterministic case, based on Paper II. In an uncertain case decisions could be made on either expected values, or when arbitrarily high confidence conditions are met.

Table 6.2: Data for the simplified production system.

Parameter name	K_A (€)	K_B (€/n)
$\gamma_{w-1,0}$	15	$1 \pm 2s$
$\gamma_{w-1,1}$	10	$1.5 \pm 2s$

The simple system from figure 6.15 is redesigned, to instead be a decision problem, between processes $\gamma_{w-1,0}$ and $\gamma_{w-1,1}$, where one of them should feed into process γ_w and there exists a difference in investment (K_A) and some variance to the constant parameters K_B, and all other costs are zero. The problem is illustrated in figure 6.17 and table 6.2, in order to make any decision both paths
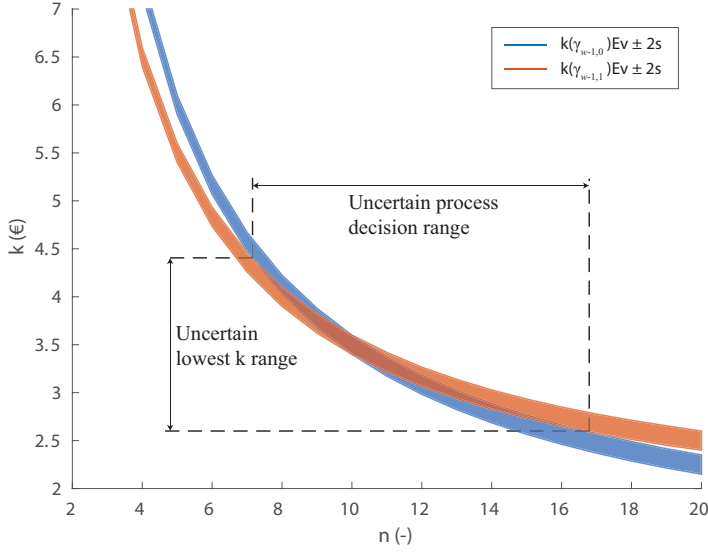
Figure 6.18: Result of a three processes decision system, where either $\gamma_{w-1,0}$ or $\gamma_{w-1,1}$, but not both, are used as materials in γ_w. s is the standard deviation.

must be investigated in full and thus equation 6.9 is used. The result can be seen in figure 6.18, where the lower investment process $\gamma_{w-1,1}$ is with more than 95% confidence the better decision when n is less than 7, and $\gamma_{w-1,0}$ is with more than 95% confidence the better decision for n larger than 17 but in between exists an uncertain process decision range, where the expected value for k can provide some guidance, but with lower confidence.

Chapter 7

Results and Discussion
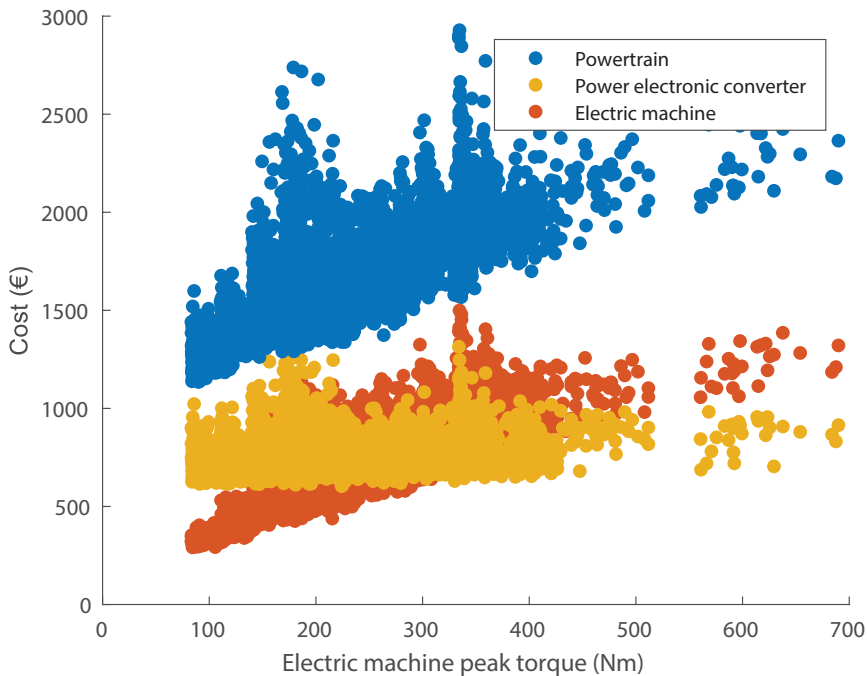
Figure 7.1: The calculated cost of a number of powertrains for a car, plotted against peak electric machine torque, showing how the same specification at the wheel can be fulfilled by different configurations of electric machine, power electronic converter and transmission, the latter is included in the powertrain cost.

Calculated cost data for more than 7000 powertrains generated for a battery electric vehicle, as described in Paper VI, are shown in figure 7.1, production volume is set to 50000 units/year. From the figure a linear relationship between

the lowest cost machines and torque can be observed, while the cost of the corresponding power electronic converters depend on the peak output power and power factor of the machines they drive. The powertrain cost also includes the cost of a gear set for either a two-speed gearbox or a fixed reduction gear and a housing. The latter two costs are based on empirical data from an industrial actor.
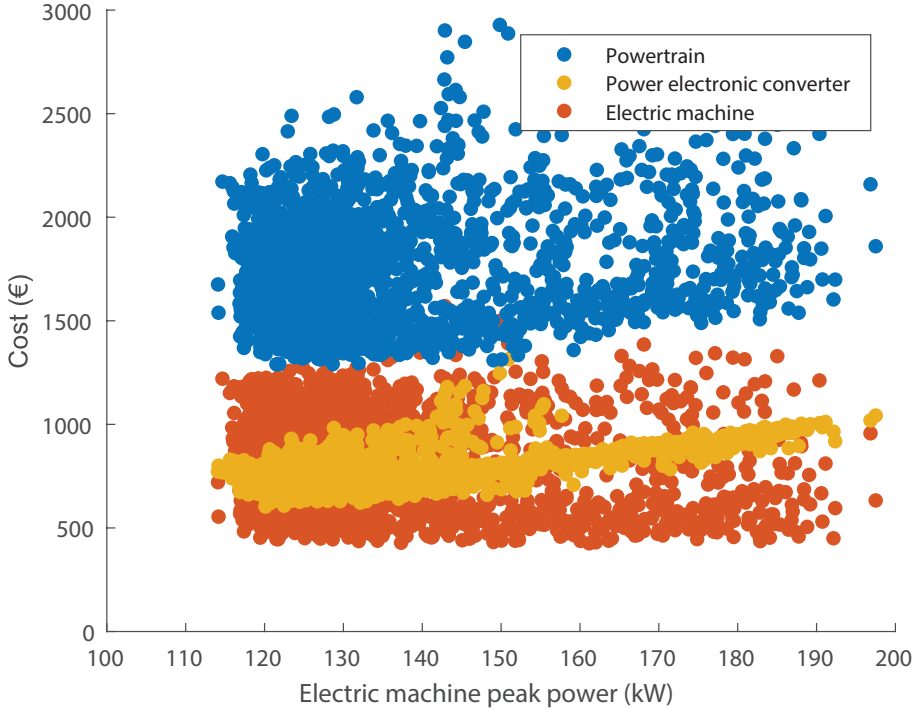
Figure 7.2: The calculated cost of a number of powertrains with fixed reduction gears, electric machine peak power vs cost. The powertrain cost is primarily driven by the increased output of the power electronic converter.

If the same cost data is viewed as a function of peak power, shown for fixed reduction gear-sets in figure 7.2, the machine cost does not increase significantly with peak power and the main cost driver is the power electronic converter. The machine cost is lower still due to to the two transmission ratios, enabling smaller machines with lower torque to reach the starting torque requirements at the wheels. The two-speed powertrains are shown in figure 7.3.

As discussed in previous chapters, the peak speeds are governed by mechanics, bearings and the switching frequency, and with the introduction of a two-speed gearbox the low torque machines can meet the starting torque requirements. High rotational speeds allow the machines to produce the required

power, and the second gear ratio enables them to reach the desired peak wheel speeds. The small machines carry a fractionally larger portion of their cost from production processes. They require a higher transmission ratio, which also adds costs, but the cost gradient for a higher torque machine is higher than the cost gradient for introducing a two speed gearbox for the calculated interval.
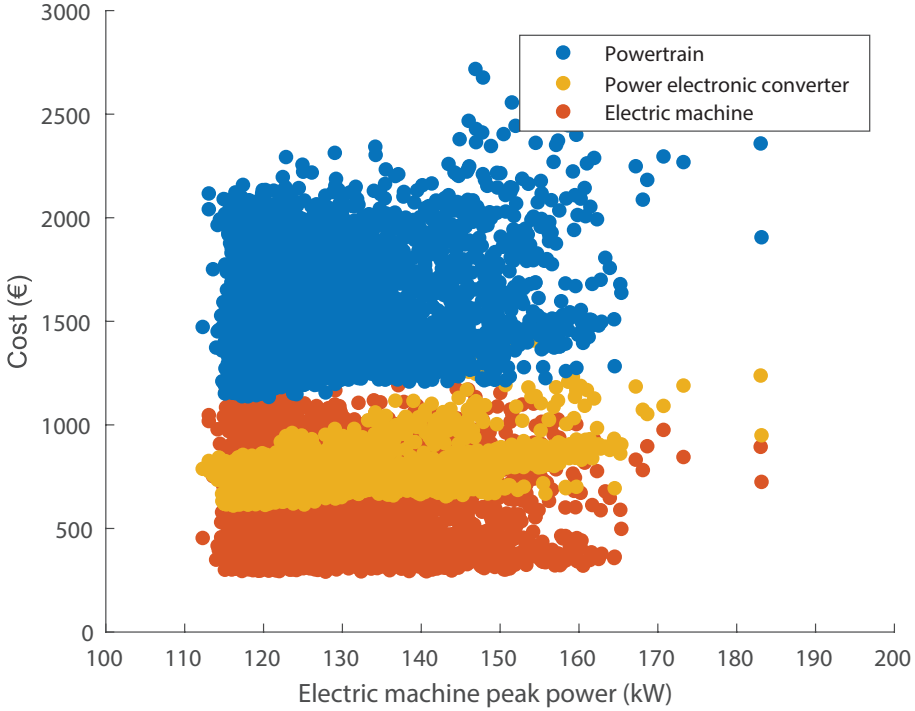
Figure 7.3: The calculated cost of a number of powertrains with two-speed gearboxes. Here the power electronic converter makes up an even larger part of the powertrain cost, due to smaller, lower cost machines using a higher cost two-speed gearbox.

From figures 7.1-7.3 two simple but important conclusions can be drawn. The first is that by accounting for the requirements at the wheels, and considering the system as a whole, enables identification of the lowest cost combination that will fulfill those requirements. The importance of this is emphasized by the increased cost per machine torque if the gear ratio would be fixed, and the increased cost of the power electronic converter if the power requirement is increased, with all other parameters fixed.

The second insight from the results point to the importance from a cost perspective in using the components in the powertrain to their physical limits, as well as reducing manufacturing expenses. The manufacturing expenses in Paper VI range from 17-35% of costs for the fixed gear electric machines and 22-41%

of costs for the two-speed machines, these figures include an axle, resolver, two bearings, and the cost of the housing, part of which is shared with the powertrain. As figures 7.1-7.3 show, the power electronic converter represents a large fraction of the total powertrain cost. The cost breakdown of the power electronic converter can be seen in Paper V, figure 12, where the power components make up about 50% of total costs at high production volumes and the control components near 20%, around 30% for manufacturing, assembly and testing for a 100 kW converter.

A similar conclusion can be drawn from Paper IV, where the peak torque increased by 35% with a hairpin winding compared to the insertion wound machine at a cost increase of 10%. This occurs due to a higher fill-factor, lower nominal current density and improved thermal conductivity, and a different manufacturing process for the winding. The cost increase was also shown to be possible to offset by segmenting the stator and using a lower cost, and thicker rotor sheet material. Using a segmented stator resulted in a torque of 80% compared to the non-segmented stator. This reduction is due to a reduction in flux linkage with segmentation. The calculated decrease in the flux linkage in that work was based on a two dimensional model as in figure 4.3, not from the inductor representation discussed in section 4.4. Further investigation of hairpin winding machines would be very interesting, but scaling such designs is difficult, due to the discrete nature of the number of turns in the winding.

Two variants of single tooth fractional slot concentrated winding machines were included in Paper IV where the base-machine was not well suited for this type of winding. The low cost of manufacturing that machine warrants further investigation, but as stated for the winding methods described in section 6.2, it is difficult to produce fractional slot concentrated windings with multiple parallel strands in full circumference inner rotor stators. This points to higher pole number machines with parallel connected windings, to keep the induced voltage reasonable, which in turn can limit speed due to switching frequency limits. A problem in using parallel connected windings is that each winding may not share currents evenly, due to dynamic effects, differences in induced voltage, and differences in resistance created by the winding process.

Results from Papers IV, V, and VI have been combined into the larger system perspective in Paper VII, in the shape of the Swedish road transportation system, where the current situation is compared to one where all transport is electrified in a number of ways. Márquez-Fernández et al. [139] expanded on Paper VII with a less binary approach, which reiterates the importance of sharing electric road infrastructure between light and heavy vehicles, and highlights important points on charging infrastructure.

Despite the hopeful results from Paper VII, it is important to also realize that electric roads, especially for light vehicles, may not be possible to deploy, due

to standards not being accepted by all OEMs. Political issues across borders is another potential obstacle, as the idea essentially is to invest in an infrastructure that once completed will reduce tax incomes for governments. In case of this eventuality, battery electric vehicles and plug-in hybrid vehicles could make up the majority of very low emissions vehicles. A large part of the future uncertainty stems from battery pack costs, exemplified by the confidence interval in Nykvist and Nilsson [48] and results from Nelson et al. [45]. In the sensitivity study for battery cost in Paper VII, the break even societal cost for the first scenario is around 140 €/kWh compared to ICEs, with the fuel and electricity prices used in that work. And despite all the uncertainties in the production of drivetrain components the uncertainties regarding battery production, which in part depends on prices of critical elements required to produce the various battery chemistries, nickel, manganese, cobalt, lithium and graphite, have a substantial impact on vehicle costs.

Comparison of calculated cost data for electric drivetrains, with conventional ICE drivetrains is difficult, as data on the latter is scarce. Blanco-Rodriguez [140] present drivetrain cost for different vehicle segments, e.g. €3300 for a segment B vehicle, including a manual transmission, fuel injection, exhaust system, and electronics. In this context, the cost of the electric drivetrain is low, partly due to omitted overhead costs and profit margins. If the data is accepted as comparable regardless of these omissions, an on-board charger and insulated DC/DC converter are needed at a cost of around €400-700 depending on power levels. Nelson et al. [45] report a battery pack cost of €3400-8200 for 23.5-88 kWh at 10^6 cells/year, with lower costs per kWh for larger packs. Energy consumption of 0.075-0.15 kWh/km, depending on battery state of charge and drive cycle, were reported by Grunditz and Thiringer [141]. Range assessments require drive-cycle simulation, as the on-road efficiency is a function of many parameters. The resulting cost of a battery electric vehicle traction system is high, even if the drivetrain has a lower cost and higher efficiency than its ICE counterpart, however further cost reduction in electric traction systems is possible.

The number of combinations of machine, transmission and power electronic converter in Paper VI would consume impractical computational time if the Monte-Carlo based calculations were used. The results allow for picking certain promising powertrains, in which the selected components can be recalculated using non-deterministic models. Four electric machines using a fixed reduction gear and four using two-speed gearsets are shown in figure 7.4. The confidence interval for each machine is sizable relative to its total cost, stemming from each regression model. The time uncertainty of the copper wires in figure 5.12 is not included here, which depending on the timescale considered could yield a distribution with a variance larger than the total machine cost variance presented in
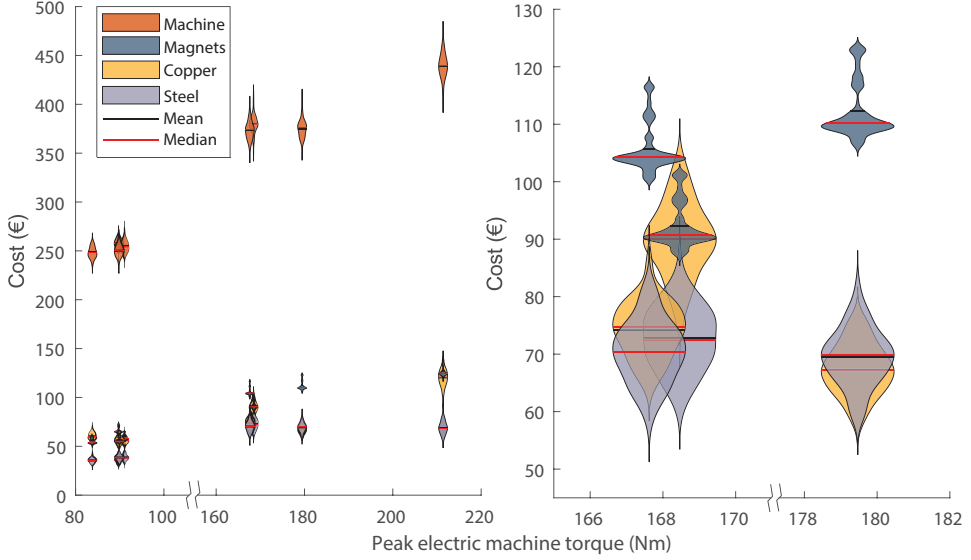
Figure 7.4: The calculated cost of eight selected machines excluding housing, at separate peak machine torques, including the uncertainty from regression model on electric steel sheets, copper wire, and press cost. The uncertainty of the permanent magnet cost is based on the raw materials time series with an offset.

figure 7.4. From this it is important to note that the confidence interval for any input propagates to an equal output variance, if the same amount of that input is used in different designs. In contrast the effect of a wide confidence interval for a particular input can be relatively low in the context of the machine, if the fraction of that input is low.

The high cost of permanent magnets motivated Paper I, but recent data shows a lower cost for the critical materials required to produce NdFeB permanent magnets. The cost of magnets in figure 7.4 are based on material costs observed in figure 5.10, offset to match industry supplied data. The cost of permanent magnets in the machine is in the same range as the mean cost of copper wires, and electric steel. If high speed, high efficiency machines is a future direction, stator sheet thicknesses of 0.2 mm or even 0.1 mm may be necessary. Such a change leads to an increase in active length due to a lower stacking factor or a higher flux density for the same length, resulting in changes in performance, material cost fractions and manufacturing operations required to produce the machine. This highlights the importance of multi-disciplinary collaboration, such as the methodology presented in Paper VI.

Chapter 8

Conclusions and Future Work

8.1 Conclusions

An economic model for calculation of materials and manufacturing costs has been introduced. The first addition to this model is a structure to investigate alternative manufacturing processes in the context of varying production volumes. Furthermore, the model has been adapted to accept uncertain input data by using Monte-Carlo methods sampling from different distributions. The division between in-house processes and what is considered a commodity is to an extent arbitrary. A factory producing electric machines can purchase fully processed stators, ready to be wound, while another cut and stack their own stators and rotors. In either case, regardless of whether a part is produced in house or seen as a commodity, the methodology is valid.

An important development has been to connect the economic models to the design process, linking the generation of performance requirements to the design of and manufacturing steps required to realize components. By developing this link for the three major components in the drivetrain; power electronic converter, electric machine and transmission, a dynamic analysis tool has been created. The tool allows for automated analysis of a very large number of configurations, which facilitates a large design-space that does not need to be reduced prematurely. While the results should not be seen as products ready to produce, it serves to identify combinations of subsystems for further development.

The cost fractions for manufacturing machines appears low in comparison to the cost of the materials, but it is important to note that the chosen manufacturing methods govern the material yield. This impact is especially large for the soft magnetic sheets, but also affects magnets and conductors, depending on shape and winding type. Changing the manufacturing strategy to segmented sheets not only improves material yield, it also enables the introduction of different

rotor materials, e.g high strength magnetic steel, which in turn can withstand higher rotational speeds.

Results from the cost analyses have been used as input data in the study on the societal economics of a transport system. This has shown the cost magnitudes of different parts of the system. The potential cost reduction an electric road system can enable if the technology is shared among all types of road vehicles is clear, compared to if the electric road is only available to heavy vehicles.

8.2   Future Work

Figure 3.2 states that the process of adding data and reformulating subsystem models repeats without end. An interesting place to start is to go all the way to the bottom, and build upwards from there. One example of that would be to include aspects of semiconductor manufacturing, from how the relationship between wafer size and chip area affects yield and costs in wide-bandgap devices, to packaging types such as double side cooled and integrated pin-fin. Magnetic components in insulated converters are closely linked to these devices, as increased switching frequencies enable a reduction in their size and cost.

Economic analysis of aluminium, or copper clad aluminum [142], conductors in machines and converters should be considered due to the current difference in material cost depicted in figure 5.1. Increased cost for manufacturing operations due to strain hardening [143] in wire drawing, and winding processes can be expected. Stator design must also be altered due to higher resistivity, resulting in higher electric steel and blanking cost. Another aspect for high speed machines is that a higher resistivity gives an increase in skin depth as stated by equation 5.14.

The cross-disciplinary field of electric machine and transmission also needs further attention, from torque ripple in the machine affecting transmission components, to gear meshes introducing machine vibrations. Closely related to the machine and transmission are bearings, which limit achievable speeds at the load levels in powertrains.

Tolerances have been discussed briefly, in the context of achieving the same performance at a lower cost. Tolerances play an important role that is difficult to quantify. Machines could be made with smaller air gaps, increasing flux linkage, leading to higher torque ripple and pronouncing the effect of any rotor eccentricity. The complicated relationship between these parameters and the manufacturability of the machine is not yet fully understood.

References

[1] O. Bičáková and P. Straka, "Production of hydrogen from renewable resources and its effectiveness," *International Journal of Hydrogen Energy*, vol. 37, no. 16, pp. 11 563 – 11 578, 2012.

[2] J. Turner, G. Sverdrup, M. K. Mann, P. Maness, B. Kroposki, M. Ghirardi, R. J. Evans, and D. Blake, "Renewable hydrogen production," *International Journal of Energy Research*, vol. 32, no. 5, pp. 379–407, 4 2008.

[3] L. Das, R. Gulati, and P. Gupta, "A comparative evaluation of the performance characteristics of a spark ignition engine using hydrogen and compressed natural gas as alternative fuels," *International Journal of Hydrogen Energy*, vol. 25, no. 8, pp. 783 – 793, 2000.

[4] R. Tirnovan and S. Giurgea, "Efficiency improvement of a pemfc power source by optimization of the air management," *International Journal of Hydrogen Energy*, vol. 37, no. 9, pp. 7745 – 7756, 2012, 7th Petite Workshop on the Defect Chemical Nature of Energy Materials, 14-17 March 2011, Storaas, Kongsberg, Norway.

[5] M. Wang, "Estimation of energy efficiencies of u.s. petroleum refineries," in *Center for Transportation Research Argonne National Laboratory*, 2008.

[6] X. Zhen and Y. Wang, "An overview of methanol as an internal combustion engine fuel," *Renewable and Sustainable Energy Reviews*, vol. 52, pp. 477 – 493, 2015.

[7] A. Boretti, "Comparison of fuel economies of high diesel and hydrogen engines powering a compact car with a flywheel based kinetic energy recovery systems," *International Journal of Hydrogen Energy*, vol. 35, no. 16, pp. 8417 – 8424, 2010.

[8] D. Turner, H. Xu, R. F. Cracknell, V. Natarajan, and X. Chen, "Combustion performance of bio-ethanol at various blend ratios in a gasoline direct injection engine," *Fuel*, vol. 90, no. 5, pp. 1999 – 2006, 2011.

[9] M. Han, K. E. Kang, Y. Kim, and G.-W. Choi, "High efficiency bioethanol production from barley straw using a continuous pretreatment reactor," *Process Biochemistry*, vol. 48, no. 3, pp. 488 – 495, 2013.

[10] Y. Dong and M. Steinberg, "Hynol—an economical process for methanol production from biomass and natural gas with reduced co2 emission," *International Journal of Hydrogen Energy*, vol. 22, no. 10, pp. 971 – 977, 1997.

[11] F. Puerari, B. Bosio, and G. Heyen, "Energy efficiency optimisation in different plant solutions for methanol production from biomass gasification," *Chemical Engineering Transactions*, vol. 37, 2014.

[12] J. V. Barreras, E. Schaltz, S. J. Andreasen, and T. Minko, "Datasheet-based modeling of li-ion batteries," in *2012 IEEE Vehicle Power and Propulsion Conference*, Oct 2012, pp. 830–835.

[13] S. Skoog, "Electro-thermal modeling of high-performance lithium-ion energy storage systems including reversible entropy heat," in *2017 IEEE Applied Power Electronics Conference and Exposition (APEC)*, March 2017, pp. 2369–2373.

[14] J.-S. Kim, G.-Y. Choe, H.-M. Jung, B.-K. Lee, Y.-J. Cho, and K.-B. Han, "Design and implementation of a high-efficiency on- board battery charger for electric vehicles with frequency control strategy," in *2010 IEEE Vehicle Power and Propulsion Conference*, Sept 2010, pp. 1–6.

[15] B. Whitaker, A. Barkley, Z. Cole, B. Passmore, D. Martin, T. R. McNutt, A. B. Lostetter, J. S. Lee, and K. Shiozaki, "A high-density, high-efficiency, isolated on-board vehicle battery charger utilizing silicon carbide power devices," *IEEE Transactions on Power Electronics*, vol. 29, no. 5, pp. 2606–2617, May 2014.

[16] International Energy Agency, "Energy balance Sweden," accessed: 2018-04-10. [Online]. Available: http://www.iea.org/Sankey/index.html#?c=Sweden&s=Balance

[17] S. Satyapal, J. Petrovic, C. Read, G. Thomas, and G. Ordaz, "The u.s. department of energy's national hydrogen storage project: Progress towards meeting hydrogen-powered vehicle requirements," *Catalysis Today*, vol. 120, no. 3, pp. 246 – 256, 2007.

[18] D. gang Li, H. Zhen, L. Xingcai, Z. Wu-gao, and Y. Jian-guang, "Physico-chemical properties of ethanol–diesel blend fuel and its effect on perfor-

mance and emissions of diesel engines," *Renewable Energy*, vol. 30, no. 6, pp. 967 – 976, 2005.

[19] M. Wang and H.-S. Huang, "Full fuel-cycle analysis of energy and emissions impacts of transportation fuels produced from natural gas," p. 134, 19991201 1999.

[20] A. K. Agarwal, "Biofuels (alcohols and biodiesel) applications as fuels for internal combustion engines," *Progress in Energy and Combustion Science*, vol. 33, no. 3, pp. 233 – 271, 2007.

[21] M. M. Thackeray, C. Wolverton, and E. D. Isaacs, "Electrical energy storage for transportation-approaching the limits of, and going beyond, lithium-ion batteries," *Energy Environ. Sci.*, vol. 5, pp. 7854–7863, 2012.

[22] C.-X. Zu and H. Li, "Thermodynamic analysis on energy densities of batteries," *Energy Environ. Sci.*, vol. 4, pp. 2614–2624, 2011.

[23] J. Y. Yong, V. K. Ramachandaramurthy, K. M. Tan, and N. Mithulananthan, "A review on the state-of-the-art technologies of electric vehicle, its impacts and prospects," *Renewable and Sustainable Energy Reviews*, vol. 49, pp. 365 – 385, 2015.

[24] S. Campanari, G. Manzolini, and F. G. de la Iglesia, "Energy analysis of electric vehicles using batteries or fuel cells through well-to-wheel driving cycle simulations," *Journal of Power Sources*, vol. 186, no. 2, pp. 464 – 477, 2009.

[25] C. Thomas, "Fuel cell and battery electric vehicles compared," *International Journal of Hydrogen Energy*, vol. 34, no. 15, pp. 6005 – 6020, 2009.

[26] G. Offer, D. Howey, M. Contestabile, R. Clague, and N. Brandon, "Comparative analysis of battery electric, hydrogen fuel cell and hybrid vehicles in a future sustainable road transport system," *Energy Policy*, vol. 38, no. 1, pp. 24 – 29, 2010.

[27] M. F. Felgenhauer, M. A. Pellow, S. M. Benson, and T. Hamacher, "Evaluating co-benefits of battery and fuel cell vehicles in a community in california," *Energy*, vol. 114, pp. 360 – 368, 2016.

[28] R. Rajamani, *Longitudinal Vehicle Dynamics*. Boston, MA: Springer US, 2006, pp. 95–122.

[29] E. A. Grunditz and T. Thiringer, "Performance analysis of current bevs based on a comprehensive review of specifications," *IEEE Transactions on Transportation Electrification*, vol. 2, no. 3, pp. 270–289, Sept 2016.

[30] W. Soong, "Sizing of electrical machines," in *ICEM, XIX International Conference on Electrical Machines*, 2008.

[31] D. R. Lancaster, R. B. Krieger, and J. H. Lienesch, "Measurement and analysis of engine pressure data," in *SAE Technical Paper*. SAE International, 02 1975.

[32] Volvo Truck Corporation, "Volvo D13 Engine Family," accessed: 2018-01-17. [Online]. Available: https://www.volvotrucks.us/-/media/vtna/files/shared/powertrain/revised4147_101-volvo_d13_engine-brochure_low-res.pdf

[33] ——, "Volvo I Shift AT2612D," accessed: 2018-01-17. [Online]. Available: http://productinfo.vtc.volvo.se/files/pdf/hi/AT2612D_Eng_02_953873.pdf

[34] Organisation Internationale des Constructeurs d'Automobiles, "Vehicle production statistics," [Online], Dec 2017, available: http://oica.net/category/production-statistics/.

[35] K. B. Naceur and et al., *Global EV Outlook 2017*, A. Majoe, Ed. International Energy Agency, 2017.

[36] EV Volumes Jose Pontes, "Global Plug-in Vehicle Sales for 2017," accessed: 2018-04-27. [Online]. Available: http://www.ev-volumes.com/country/total-world-plug-in-vehicle-volumes/

[37] F. Birol and et al., *World Energy Outlook*, N. Tanaka, Ed. International Energy Agency, 2009.

[38] L. Fulton and et al., *Transport, Energy and CO2 - Moving toward sustainability*, N. Tanaka, Ed. IEA/OECD, 2009.

[39] R. Domm, *Michigan Yesterday & Today*, 2009.

[40] Y. Sugimori, K. Kusunoki, F. Cho, and S. Uchikawa, "Toyota production system and kanban system materialization of just-in-time and respect-for-human system," *International Journal of Production Research*, vol. 15, no. 6, pp. 553–564, 1977.

[41] R. Nader, "Unsafe at any speed - the designed-in dangers of the american automobile," 1965.

[42] M. T. Lee, "The ford pinto case and the development of auto safety regulations, 1893—1978," *Business and Economic History*, vol. 27, no. 2, pp. 390–401, 1998.

[43] G. J. Thompson, D. K. Carder, M. C. Besch, A. Thiruvengadam, and H. K. Kappanna, "In-use emissions testing of light-duty diesel vehicles in the united states," 2014.

[44] P. Mock, "2020–2030 CO2 standards for new cars and light-commercial vehicles in the European Union," 2016. [Online]. Available: http://www.theicct.org/publications/2020%E2%80%932030-co2-standards-new-cars-and-light-commercial-vehicles-european-union

[45] P. Nelson, K. G. Gallagher, I. Bloom, and D. W. Dees, "Modeling the performance and cost of lithium-ion batteries for electric-drive vehicles," 2011. [Online]. Available: http://www.cse.anl.gov/batpac/about.html

[46] G. Patry, A. Romagny, S. Martinet, and D. Froelich, "Cost modeling of lithium-ion battery cells for automotive applications," *Energy Science and Engineering*, vol. 3, no. 1, pp. 71–82, 2015.

[47] A. Sakti, J. J. Michalek, E. R. Fuchs, and J. F. Whitacre, "A techno-economic analysis and optimization of li-ion batteries for light-duty passenger vehicle electrification," *Journal of Power Sources*, vol. 273, no. Supplement C, pp. 966 – 980, 2015.

[48] B. Nykvist and M. Nilsson, "Rapidly falling costs of battery packs for electric vehicles," *Nature Climate Change*, vol. 5, pp. 329–333, April 2015.

[49] T. R. Hawkins, O. M. Gausen, and A. H. Strømman, "Environmental impacts of hybrid and electric vehicles—a review," *The International Journal of Life Cycle Assessment*, vol. 17, no. 8, pp. 997–1014, Sep 2012.

[50] K. T. Chau, C. C. Chan, and C. Liu, "Overview of permanent-magnet brushless drives for electric and hybrid electric vehicles," *IEEE Transactions on Industrial Electronics*, vol. 55, no. 6, pp. 2246–2257, June 2008.

[51] A. C. Ward and W. Seering, "Quantitative inference in a mechanical design compiler," *Massachusetts Institute of Technology*, vol. 1062, 1989.

[52] J. Liker, I. Sobek, D.K., A. Ward, and J. Cristiano, "Involving suppliers in product development in the united states and japan: evidence for set-based concurrent engineering," *Engineering Management, IEEE Transactions on*, vol. 43, no. 2, pp. 165–178, 1996.

[53] R. Crozier and M. Mueller, "A new matlab and octave interface to a popular magnetics finite element code," in *2016 XXII International Conference on Electrical Machines (ICEM)*, Sept 2016, pp. 1251–1256.

[54] B. Efron, "Bootstrap methods: Another look at the jackknife," *Ann. Statist.*, vol. 7, no. 1, pp. 1–26, 01 1979.

[55] J. Blum, J. Merwerth, and H. G. Herzog, "Modeling and reduction of stator teeth eddy-current losses in ipm machines," in *2014 International Conference on Electrical Machines (ICEM)*, Sept 2014, pp. 1300–1306.

[56] J. Capparella, "2018 tesla model 3 long range," accessed: 2018-04-03. [Online]. Available: https://www.caranddriver.com/tesla/model-3

[57] T. Burress, "Benchmarking state-of-the-art technologies," accessed: 2018-03-10. [Online]. Available: https://www.energy.gov/sites/prod/files/2014/03/f13/ape006_burress_2013_o.pdf

[58] O. Heaviside, "On the forces, stresses, and fluxes of energy in the electromagnetic field." *Proceedings of the Royal Society of London*, vol. 50, no. 302-307, pp. 126–129, 1891.

[59] R. H. Park, "Two-reaction theory of synchronous machines generalized method of analysis-part i," *Transactions of the American Institute of Electrical Engineers*, vol. 48, no. 3, pp. 716–727, July 1929.

[60] T. Lipo, *Analysis of Synchronous Machines.* CRC Press, 2012.

[61] P. Pillay and R. Krishnan, "Modeling of permanent magnet motor drives," *IEEE Transactions on Industrial Electronics*, vol. 35, no. 4, pp. 537–541, Nov 1988.

[62] A. Emadi, *Advanced electric drive vehicles.*, ser. Energy, power electronics, and machines. Boca Raton : CRC Press, [2015], 2015.

[63] S. Hall, "Dynamic testing of permanent magnet synchronous machines," p. 106, 2016, licentiate thesis.

[64] R. Andersson, "Electric traction machine design for heavy hybrid vehicles," p. 111, 2014, licentiate thesis.

[65] M. van der Giet, K. Kasper, R. W. D. Doncker, and K. Hameyer, "Material parameters for the structural dynamic simulation of electrical machines," in *2012 XXth International Conference on Electrical Machines*, Sept 2012, pp. 2994–3000.

[66] H. Dehmani, C. Brugger, T. Palin-Luc, C. Mareau, and S. Koechlin, "Characterization and simulation of the effect of punching on the high cycle fatigue strength of thin electric steel sheets," *Procedia Engineering,*

vol. 133, pp. 556 – 561, 2015, fatigue Design 2015, International Conference Proceedings, 6th Edition.

[67] JFE, "Super Core Electrical steel sheets for high-frequency application," accessed: 2018-01-20. [Online]. Available: http://www.jfe-steel.co.jp/en/products/electrical/catalog/f1e-002.pdf

[68] W. Tong, *Mechanical Design of Electric Motors*. CRC Press, 2014.

[69] J. D. Ede, Z. Q. Zhu, and D. Howe, "Rotor resonances of high-speed permanent-magnet brushless machines," *IEEE Transactions on Industry Applications*, vol. 38, no. 6, pp. 1542–1548, Nov 2002.

[70] K. Hariharan, F. Barlat, M. G. Lee, and R. V. Prakash, "Extension of strain–life equation for low-cycle fatigue of sheet metals using anisotropic yield criteria and distortional hardening model," *Fatigue & Fracture of Engineering Materials & Structures*, vol. 37, no. 9, pp. 977–991, 2014, fFEMS-5413.R4.

[71] R. H. Todd, D. K. Allen, and L. Alting, *Manufacturing Processes Reference Guide*. Industrial Press Inc., 1994.

[72] C. Freitag, "Magnetic properties of electrical steel, power transformer core losses and core design concepts," Ph.D. dissertation, Karlsruher Institutes für Technologie, 02 2017.

[73] R. Sundaria, A. Lehikoinen, A. Hannukainen, A. Arkkio, and A. Belahcen, "Mixed-order finite-element modeling of magnetic material degradation due to cutting," *IEEE Transactions on Magnetics*, pp. 1–8, 2018.

[74] I. M. Fund, "Imf primary commodity prices," accessed: 2017-06-20. [Online]. Available: http://www.imf.org/external/np/res/commod/index.aspx

[75] European Central Bank, "Ecb euro reference exchange rate: Us dollar (usd)," accessed: 2018-01-03. [Online]. Available: https://www.ecb.europa.eu/stats/policy_and_exchange_rates/euro_reference_exchange_rates/html/eurofxref-graph-usd.en.html

[76] Kitco, "Strategic Metals ," accessed: 2017-09-20. [Online]. Available: http://www.kitco.com/strategic-metals/

[77] T. Lyman, H. E. Boyer, and E. A. Durand, *Metals Handbook. Vol. 4*. Asm International, 1969.

[78] T. Yamaji, M. Abe, Y. Takada, K. Okada, and T. Hiratani, "Magnetic properties and workability of 6.5% silicon steel sheet manufactured in continuous cvd siliconizing line," *Journal of Magnetism and Magnetic Materials*, vol. 133, no. 1, pp. 187 – 189, 1994.

[79] Zauba Technologies & Data Services Private Limited, "HTS Code import/export data," accessed: 2018-01-15. [Online]. Available: https://www.zauba.com/

[80] Voestalpine, "isovac 250-35 A," accessed: 2018-01-20. [Online]. Available: http://www.voestalpine.com/division_stahl/content/download/39690/456876/file/DB_isovac_250-35A_E_281015.pdf

[81] Cogent, "Typical data for SURA M250-50A," accessed: 2018-01-20. [Online]. Available: https://cogent-power.com/cms-data/downloads/m250-50a.pdf

[82] ——, "Non-oriented electrical steel," accessed: 2018-04-29. [Online]. Available: https://cogent-power.com/cms-data/downloads/Cogent%20NO%20brochure%202016.pdf

[83] F. Fiorillo, "Chapter 2 - soft magnetic materials," in *Characterization and Measurement of Magnetic Materials*, ser. Elsevier Series in Electromagnetism, F. Fausto, Ed. San Diego: Academic Press, 2004, pp. 25 – 88.

[84] X. Wan, Y. Li, J. Li, C. Liu, and J. Zhu, "Orthogonal decomposition of core loss along rolling and transverse directions of non-grain oriented silicon steels," *AIP Advances*, vol. 7, no. 5, p. 056651, 2017.

[85] Höganäs, "Somaloy 700HR 5P," accessed: 2018-04-30. [Online]. Available: http://www.hoganas.com//globalassets/media/sharepoint-documents/BrochuresanddatasheetsAllDocuments/SomaloyMaterialData_November_2016_1806HOG.pdf

[86] P. Chen, G.-Y. Kim, and J. Ni, "Investigations in the compaction and sintering of large ceramic parts," *Journal of Materials Processing Technology*, vol. 190, no. 1, pp. 243 – 250, 2007.

[87] Arnold Magnetics, "Neodymium Magnets," accessed: 2018-01-15. [Online]. Available: http://www.arnoldmagnetics.com/en-us/Products/Neodymium-Magnets

[88] R. J. Parker, *Advances in permanent magnetism.*, ser. A Wiley-interscience publication. New York : Wiley, cop. 1990, 1990.

[89] S. Ruoho, E. Dlala, and A. Arkkio, "Comparison of demagnetization models for finite-element analysis of permanent-magnet synchronous machines," *IEEE Transactions on Magnetics*, vol. 43, no. 11, pp. 3964–3968, Nov 2007.

[90] S. Hirosawa, H. Tomizawa, S. Mino, and A. Hamamura, "High-coercivity nd-fe-b-type permanent magnets with less dysprosium," *IEEE Transactions on Magnetics*, vol. 26, no. 5, pp. 1960–1962, Sep 1990.

[91] M. Sagawa, S. Hirosawa, H. Yamamoto, S. Fujimura, and Y. Matsuura, "Nd–fe–b permanent magnet materials," *Japanese Journal of Applied Physics*, vol. 26, no. 6R, p. 785, 1987.

[92] M. Honshima and K. Ohashi, "High-energy ndfeb magnets and their applications," *Journal of Materials Engineering and Performance*, vol. 3, no. 2, pp. 218–222, Apr 1994.

[93] K. Hono and H. Sepehri-Amin, "Strategy for high-coercivity nd–fe–b magnets," *Scripta Materialia*, vol. 67, no. 6, pp. 530 – 535, 2012, viewpoint Set No. 51: Magnetic Materials for Energy.

[94] Arnold Magnetics, "The important role of dysprosium in modern permanent magnets," rev. 150903a Accessed: 2018-01-15. [Online]. Available: http://www.arnoldmagnetics.com/en-us/Tech-Library/Technical-Publications

[95] G. Bai, R. Gao, Y. Sun, G. Han, and B. Wang, "Study of high-coercivity sintered ndfeb magnets," *Journal of Magnetism and Magnetic Materials*, vol. 308, no. 1, pp. 20 – 23, 2007.

[96] "Electrical insulation - Thermal evaluation and designation," International Electrotechnical Commision, Geneva, CH, Standard, 2007.

[97] M. Lindenmo, A. Coombs, and D. Snell, "Advantages, properties and types of coatings on non-oriented electrical steels," *Journal of Magnetism and Magnetic Materials*, vol. 215, pp. 79 – 82, 2000.

[98] Z. Huang, "Modeling and testing of insulation degradation due to dynamic thermal loading of electrical machines," Ph.D. dissertation, Lund University, 01 2017.

[99] R. A. Matula, "Electrical resistivity of copper, gold, palladium, and silver," *Journal of Physical and Chemical Reference Data*, vol. 8, no. 4, pp. 1147–1298, 1979.

[100] M. Komatsubara, K. Sadahiro, O. Kondo, T. Takamiya, and A. Honda, "Newly developed electrical steel for high-frequency use," *Journal of Magnetism and Magnetic Materials*, vol. 242-245, pp. 212 – 215, 2002, proceedings of the Joint European Magnetic Symposia (JEMS'01).

[101] G. S. Smith, "A simple derivation for the skin effect in a round wire," *European Journal of Physics*, vol. 35, no. 2, p. 025002, 2014.

[102] C. R. Sullivan, "Computationally efficient winding loss calculation with multiple windings, arbitrary waveforms, and two-dimensional or three-dimensional field geometry," *IEEE Transactions on Power Electronics*, vol. 16, no. 1, pp. 142–150, Jan 2001.

[103] G. Boothroyd, P. Dewhurst, and W. A. Knight, *Product design for manufacture and assembly.* M. Dekker, 2002.

[104] S. H. Lee, Y. Lee, M. G. Jang, C. Han, and W. N. Kim, "Comparative study of emi shielding effectiveness for carbon fiber pultruded polypropylene/poly(lactic acid)/multiwall cnt composites prepared by injection molding versus screw extrusion," *Journal of Applied Polymer Science*, vol. 134, no. 34, pp. 45 222–n/a, 2017, 45222. [Online]. Available: http://dx.doi.org/10.1002/app.45222

[105] F. Márquez-Fernández, A. Reinap, Z. Huang, and M. Alaküla, "Dynamic evaluation of the overloading potential of a convection cooled permanent magnet synchronous motor," in *2011 IEEE International Electric Machines Drives Conference (IEMDC)*, May 2011, pp. 13–18.

[106] Z. Huang, "Thermal design of electrical machines investigation and evaluation of cooling performances," p. 129, 2013, licentiate thesis.

[107] M. Liu, Y. Li, H. Ding, and B. Sarlioglu, "Thermal management and cooling of windings in electrical machines for electric vehicle and traction application," in *2017 IEEE Transportation Electrification Conference and Expo (ITEC)*, June 2017, pp. 668–673.

[108] E. A. Jones, F. F. Wang, and D. Costinett, "Review of commercial gan power devices and gan-based converter design challenges," *IEEE Journal of Emerging and Selected Topics in Power Electronics*, vol. 4, no. 3, pp. 707–719, Sept 2016.

[109] D. Ward, I. Husain, C. Castro, A. Volke, and M. Hornkamp, *Fundamentals of Semiconductors for Hybrid-Electric Powertrain.* Infineon Technologies AG, 2013.

[110] H. Zhang and L. M. Tolbert, "Efficiency impact of silicon carbide power electronics for modern wind turbine full scale frequency converter," *IEEE Transactions on Industrial Electronics*, vol. 58, no. 1, pp. 21–28, Jan 2011.

[111] B. Wrzecionko, D. Bortis, and J. Kolar, "A 120 c ambient temperature forced air-cooled normally-off sic jfet automotive inverter system," *Power Electronics, IEEE Transactions on*, vol. 29, no. 5, pp. 2345–2358, May 2014.

[112] B. Whitaker, A. Barkley, Z. Cole, B. Passmore, D. Martin, T. R. McNutt, A. B. Lostetter, J. S. Lee, and K. Shiozaki, "A high-density, high-efficiency, isolated on-board vehicle battery charger utilizing silicon carbide power devices," *IEEE Transactions on Power Electronics*, vol. 29, no. 5, pp. 2606–2617, May 2014.

[113] M. Rahimo, C. Corvasce, J. Vobecky, Y. Otani, and K. Huet, "Thin-wafer silicon igbt with advanced laser annealing and sintering process," *IEEE Electron Device Letters*, vol. 33, no. 11, pp. 1601–1603, Nov 2012.

[114] C. Gillot, C. Schaeffer, C. Massit, and L. Meysenc, "Double-sided cooling for high power igbt modules using flip chip technology," *IEEE Transactions on Components and Packaging Technologies*, vol. 24, no. 4, pp. 698–704, Dec 2001.

[115] Z. Liang, "Planar-bond-all: A technology for three-dimensional integration of multiple packaging functions into advanced power modules," in *2015 IEEE International Workshop on Integrated Power Packaging (IWIPP)*, May 2015, pp. 115–118.

[116] U.S Energy Information Administration, "Gasoline and diesel fuel update," accessed: 2017-12-30. [Online]. Available: https://www.eia.gov/petroleum/gasdiesel/

[117] European Commission, "Weekly oil bulletin," accessed: 2018-01-05. [Online]. Available: https://ec.europa.eu/energy/en/data-analysis/weekly-oil-bulletin

[118] S. Eaves and J. Eaves, "A cost comparison of fuel-cell and battery electric vehicles," *Journal of Power Sources*, vol. 130, no. 1–2, pp. 208 – 212, 2004.

[119] Eurostat, "Electricity prices by type of user, nrg pc 204 c," accessed: 2017-01-05. [Online]. Available: http://ec.europa.eu/eurostat/data/database

[120] US energy information agency, "Electric Power Monthly," accessed: 2018-01-11. [Online]. Available: https://www.eia.gov/electricity/monthly/

[121] E. F. Fama and K. R. French, "Commodity futures prices: Some evidence on forecast power, premiums, and the theory of storage," *The Journal of Business*, vol. 60, no. 1, pp. 55–73, 1987.

[122] J. E. Smith and K. F. McCardle, "Options in the real world: Lessons learned in evaluating oil and gas investments," *Operations Research*, vol. 47, no. 1, pp. 1–15, 1999.

[123] R. Gibson and E. S. Schwartz, "Stochastic convenience yield and the pricing of oil contingent claims," *The Journal of Finance*, vol. 45, no. 3, pp. 959–976, 1990.

[124] E. Schwartz and J. E. Smith, "Short-term variations and long-term dynamics in commodity prices," *Management Science*, vol. 46, no. 7, pp. 893–911, 2000.

[125] G. Boothroyd, P. Dewhurst, and W. A. Knight, *Product design for manufacture and assembly*. M. Dekker, 2002.

[126] S. Laakso, A. Väänänen, S. Bossuyt, and A. Arkkio, "Dull punch line is not a joke – worn cutting edge causes higher iron losses in electrical steel piercing," p. 6, 2018.

[127] G. Fang, P. Zeng, and L. Lou, "Finite element simulation of the effect of clearance on the forming quality in the blanking process," *Journal of Materials Processing Technology*, vol. 122, no. 2, pp. 249 – 254, 2002.

[128] A. Kraemer, J. Stoll, D. Blickle, G. Lanza, and B. Boeker, "Analysis of wear behavior of stamping tools in the production of electrical steel sheets," in *2015 5th International Electric Drives Production Conference (EDPC)*, Sept 2015, pp. 1–7.

[129] Schuler Group, "Stamping and forming system special applications," accessed: 2018-03-07. [Online]. Available: https://www.schulergroup.com/major/us/technologien/produkte/stanzautomaten_schnellstanzautomaten/index.html

[130] A. Kampker, C. Deutskens, K. Kreisköther, and C. Reinders, "Selection of transformable production technologies as a reaction on a varying demand of electric traction motors," in *2014 4th International Electric Drives Production Conference (EDPC)*, Sept 2014, pp. 1–6.

[131] J. Bönig, B. Bickel, M. Spahr, C. Fischer, and J. Franke, "Simulation of orthocyclic windings using the linear winding technique," in *2015 5th*

International Electric Drives Production Conference (EDPC), Sept 2015, pp. 1–6.

[132] J. Hagedorn, F. S.-L. Blanc, and J. Fleischer, *Automation.* Berlin, Heidelberg: Springer Berlin Heidelberg, 2018, pp. 245–300.

[133] J. Brettschneider, R. Spitzner, and R. Boehm, "Flexible mass production concept for segmented bldc stators," in *2013 3rd International Electric Drives Production Conference (EDPC)*, Oct 2013, pp. 1–8.

[134] P. Stenzel, P. Dollinger, J. Richnow, and J. Franke, "Innovative needle winding method using curved wire guide in order to significantly increase the copper fill factor," in *2014 17th International Conference on Electrical Machines and Systems (ICEMS)*, Oct 2014, pp. 3047–3053.

[135] F. S. L. Blanc, E. Ruprecht, and J. Fleischer, "Material based process model for linear noncircular coil winding processes with large wire gauge: Investigation of wire material influences on the winding process and compensation approaches," in *2013 3rd International Electric Drives Production Conference (EDPC)*, Oct 2013, pp. 1–5.

[136] J. Hofmann, F. S. L. Blanc, M. Krause, F. Wirth, and J. Fleischer, "Simulation of the assembly process of the insert technique for distributed windings," in *2016 6th International Electric Drives Production Conference (EDPC)*, Nov 2016, pp. 144–148.

[137] J.-E. Ståhl, C. Andersson, and M. Jönsson, "A basic economic model for judging production development," in *Proceedings of the 1st International Swedish Production Symposium*, 2007.

[138] P. Fyhr, J.-E. Ståhl, and M. Andersson, "Production cost case generation by a recursive monte-carlo method in electrical machine production," in *Swedish Production Symposium*, 2014, p. 6.

[139] F. J. Márquez-Fernández, G. Domingues-Olavarria, L. Lindgren, and M. Alaküla, "Electric roads: The importance of sharing the infrastructure among different vehicle types," in *2017 IEEE Transportation Electrification Conference and Expo, Asia-Pacific (ITEC Asia-Pacific)*, Aug 2017, pp. 1–6.

[140] D. Blanco-Rodriguez, "2025 passenger car and light commercial vehicle powertrain technology analysis," 2016. [Online]. Available: https://www.theicct.org/publications/2025-passenger-car-and-light-commercial-vehicle-powertrain-technology-analysis

[141] E. A. Grunditz and T. Thiringer, "Characterizing bev powertrain energy consumption, efficiency, and range during official and drive cycles from gothenburg, sweden," *IEEE Transactions on Vehicular Technology*, vol. 65, no. 6, pp. 3964–3980, June 2016.

[142] N. Guan, C. Kamidaki, T. Shinmoto, and K. Yashiro, "Ac resistance of copper clad aluminum wires," in *2012 International Symposium on Antennas and Propagation (ISAP)*, Oct 2012, pp. 447–450.

[143] A. Korbel, F. Dobrzanski, and M. Richert, "Strain hardening of aluminium at high strains," *Acta Metallurgica*, vol. 31, no. 2, pp. 293 – 298, 1983.

Part II

APPENDED PAPERS

Paper I

Pontus Fyhr, Mats Andersson, Jan-Eric Ståhl
The scale of permanent magnet materials for automotive traction motors

The scale of permanent magnet materials for automotive traction motors

Pontus Fyhr, Jan-Eric Ståhl and Mats Andersson

Abstract—**A mathematical model is developed with the purpose of estimating the scale of permanent magnet materials consumption in hybrid and electric automotive traction systems. These estimations are compared to consumption figures from industries such as wind power, HVAC, consumer electronics and industrial machinery. The estimations generated are useful in strategic decision-making for production planning.**

Index Terms — **Traction motor, Permanent magnet, Rare earth, Dysprosium, Neodymium**

I. INTRODUCTION

The supply of rare earth magnet materials such as Neodymium (Nd) and Dysprosium (Dy) is critical in many aspects of clean energy and transportation [1] [2], the materials are used mainly in compact electric motors and generators (EM).

Neodymium magnets, chemically formulated as $Nd_2Fe_{14}B$, were developed by General Motors and Sumitumo Special Metals in 1982. The material has since found use in permanent magnet synchronous machines offering high torque density and efficiency.

The composition by weight of these permanent magnets is $Nd_{28.8-x}Fe_{bal}B_1Dy_x$ [3], where Dy varies between $1-10\%$. Dysprosium addition improves temperature stability but lowers remanence [4].

The availability and price of these materials has been subject large fluctuations recently, see figure 1. These fluctuations are due to uncertainty in Chinese export quotas, market speculation and low availability [5] [1] [2].

This paper proposes a model for estimation of magnet material mass used in three different industry categories, focus is placed on electrified automotive traction motors and wind power generators. The estimated consumption Nd and Dy that these industries will generate is compared to the consumption generated by fields such as consumer electronics, HVAC systems etc.

The purpose of the work is to assess the scale of the magnet material consumption in the automotive industry's transition

Pontus Fyhr is with Production and Materials Engineering, Lund University, Lund, SE-221 00 Sweden (+4646-222 85 08; e-mail: pontus.fyhr@iprod.lth.se).

Jan-Eric Ståhl is with Production and Materials Engineering, Lund University, Lund, SE-221 00 Sweden (e-mail: jan-eric.stahl@iprod.lth.se).

Mats Andersson is with Production and Materials Engineering, Lund University, Lund, SE-221 00 Sweden (e-mail: mats.andersson@iprod.lth.se).

to electrified traction systems and the simultaneous rise of transmission-less synchronous wind power generators.

The boundary parameters for the calculation are based on production figures from The International Organization of Motor Vehicle Manufacturers (OICA), see figure 3 [6], projections of electrified vehicle adoption in order to meet climate goals from the International Energy Association (IEA), see figure 2 and wind power projections from IEA World energy outlook [7].
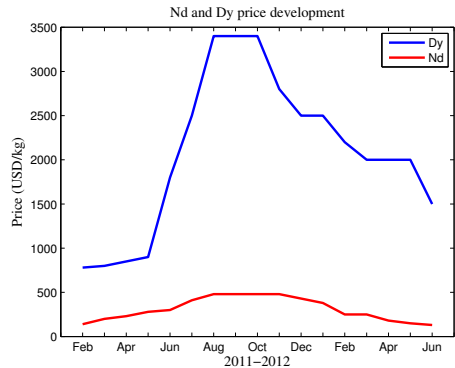
Figure 1. Nd and Dy metal price per kg, Chinese export FOB [8].

A. Traction Motors

Automotive traction motors, especially those in hybrid and plug-in hybrid applications, will be a major consumer of high performance permanent magnets as market shares for the vehicle type continue to rise.

Hybrid (HEV) and plug-in hybrid (PHEV) vehicles can be configured in different ways. These configurations can be divided into three major groups:

Series-hybrids utilize the internal combustion engine (ICE) only for sustaining battery charge, traction power is provided solely by one or several electric machines.

Parallel-hybrids connect the ICE and electric machine to the drive-shaft, rotating at the same speed or linearly coupled via a gear-set.

Complex-hybrids utilize two electrical machines connected to the drive-shaft via a planetary gear-set, allowing de-coupling of the electrical machine and ICE rotational speeds, while still
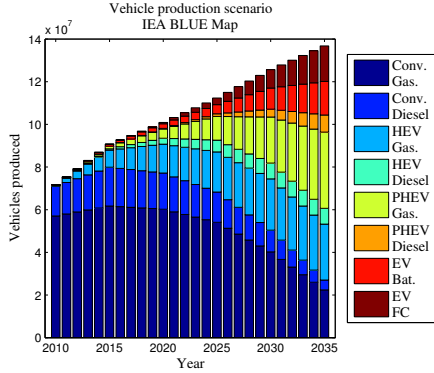
Figure 2. The IEA BLUE Map light duty vehicle production scenario [10].

Figure 3. The OICA vehicle production statistics [6].

Figure 4. The GWEC Wind Energy Outlook projection and a linear fit representing the estimated generator capacity installed per year [11].

Figure 5. Methodology flowchart

with an operating range that equals the turbine driving the generator, thus eliminating the need of gear-sets. These generators consume 100-300 kg of rare earth metals per MW generating capacity [5]. With multiple countries aiming to scale up renewable power generation, wind power rare-earth demand is calculated using scenarios from the IEA World Energy Outlook (IEA WEO) [7] and the Global Wind Energy Councils (GWEC) Global Wind Energy Outlook [11], see figure 4.
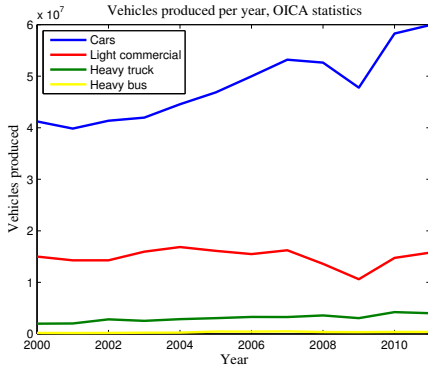
II. METHODOLOGY

The calculations of Nd and Dy consumption are divided into three sub-groups, Automotive traction, wind power and other industries, see figure 5.

Automotive traction motor magnet consumption is based on two separate scenarios, the IEA BLUE Map [10] representing very aggressive electrified traction adoption, see figure 2. The OICA scenario consists of a linear fit on vehicle production statistics from 2000 to 2011, see figure 3 with electrified traction ramping up exponentially to claim 25% to 75% of the market in low and high adoption scenarios respectively.

Wind power generator magnet consumption is based on one scenario, including a low and high adoption of permanent magnet generators. The figures are based on projections by the GWEC. The adoption of permanent magnet generator technology is set to 10% and 75% of global capacity installation in the low and high adoption scenarios respectively.

allowing both to provide traction power. The prime example of this type of system is the Toyota Prius.

The size, configuration and power output of the electrical traction motor varies between topology type, manufacturer and vehicle size.

Parallel hybrids typically have lower electric motor power levels, 5-30 kW in models from Honda and Hyundai.

Examples of PHEV vehicles such as the GM Volt and Volvo V60 PHEV feature more powerful electric motors, the V60 PHEV is a series-hybrid with the ICE powering the front and the EM powering the rear wheels. The GM Volt is denoted an EREV and features two EM coupled to the ICE and front wheels via three clutches and two gearsets [9].

B. Wind power generators

Wind power is also shifting towards the use of permanent magnet synchronous generators, in order to reduce both weight and size. This industry is adopting low base speed generators
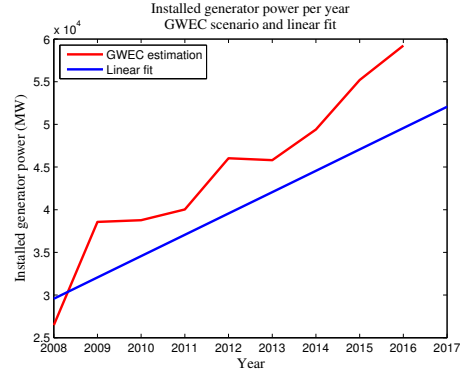
Low demand	High demand
Low supply	Low supply
Low demand	High Demand
High supply	High Supply

Vehicle type	Magnet mass	Magnet use share
HEV	0.8 - 1.2 kg	80-95 %
PHEV	1 - 2 kg	80-95 %
EV	1 - 2 kg	20-75 %
LCV	1.5 - 3 kg	80-95 %
Truck/bus	5 - 8 kg	80-95 %

Assumption	Low	High
Average magnet weight per MW	200 kg	600 kg
Percentage of PM-based generators	10%	75%
Neodymium content (by weight)	24.8%	26.8%
Dysprosium content (by weight)	4%	2 %

The consumption from other industries is based on the current supply and competing demand from the automotive and wind power sectors. The projections for other industries are divided into low and high use scenarios, the low adoption case assumes the consumption to remain at current levels and the high adoption case assumes 3% growth per year.

These resulting consumption is compared to production forecasts and rare earth reserves estimates [12] [5] [13]. The results are divided into a four tiered result matrix, with low demand and supply, high demand and low supply, low demand and high supply and high demand and supply, see table I.

The Nd and Dy consumption figures for automotive traction is calculated from the vehicles produced in each scenario. The total vehicles produced is multiplied with the fraction of electrified vehicles, permanent magnet technology adoption, magnet mass per vehicle and element (Nd and Dy) fraction (1), see table II.

$$Nd|Dy_{auto} = N_{vehicles} \cdot Frac_{hybrid} \cdot Frac_{PM} \cdot \\ m_{magnet} \cdot Frac_{Nd/Dy} \qquad (1)$$

The consumption figures for wind power generators are calculated in a similar manner, from the installed generator capacity per year, denoted P_{wind}, multiplied by the fraction of permanent magnet generator adoption, magnet mass per MW installed capacity and element fraction used (2), see table III.

$$Nd|Dy_{wind} = P_{wind} \cdot Frac_{PM} \cdot \\ m_{magnet} \cdot Frac_{Nd/Dy} \qquad (2)$$

III. SCOPE

The article attempts to estimate the demand for rare earth minerals, especially Nd and Dy used in the production of permanent magnets for automotive electric traction motors and in directly coupled wind power generators. The projected consumption is analysed against projected production from mining and refinement facilities.

The aim is to capture the scale of different industries demand and their impact on the supply of these minerals. As projections become increasingly inaccurate over time, focus is placed on the scale of demand from different industries rather than exact figures. The values used in the calculations aim to capture the high and low limits, to explore possible outcomes of the technology shifts described.

A. Automotive

The automotive traction estimations of the rare earth demand for several motor types, used in a range of vehicle topologies, is divided into four categories. This is done in

order to cover the range of hybrid and plug-in hybrids on the market, as well as hybrid buses and trucks.

The magnet materials required to produce each of these motor types is presented and applied to two electrified vehicle production scenarios, exponential adoption up to 25 and 75% of the global vehicle market as well as BLUE Map scenarios [10].

B. Wind Power

The cumulative installed wind power generation capacity has grown significantly in the last decade, from 17400 MW to 238000 MW, continued growth is expected albeit at a slightly reduced rate due to the uncertain economic climate [11]. The market forecast provided by the Global Wind Energy Council (GWEC) predicts an average annual cumulative capacity growth at 8% until 2016. A linear growth model is adapted to the figures from GWEC [11] and IEA WEO [7], with total installed wind power capacity resulting in 1350 and 1700 GW respectively, see figure 4. This fit is larger than those proposed by IEA WEO, but would be smaller than current growth trends if they were to continue at the present rate.

Resulting data of added capacity per year is then used in calculations for a range of Nd and Dy content as a result of producing the turbine generators. The upper and lower bounds of magnet materials used per MW of installed capacity is defined similarly to those used in [1], with notable differences in the lower bounds, as wind turbine generator production outside of China currently is estimated to produce 5% transmission-less permanent magnet synchronous generators. The Dy content is estimated at 4% wt for the lowest magnet mass per installed MW of capacity (200 kg/MW), as machines with embedded permanent magnets or higher base speeds are required to function at higher temperatures due to lower heat rejection or higher iron-losses. Machines with a higher magnet mass per installed capacity (600 kg/MW) are estimated to use 2% wt Dy as these would typically be exterior magnet types or use a low base speed and thus feature high heat rejection or low iron losses.
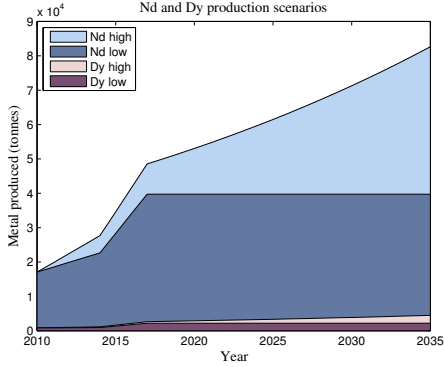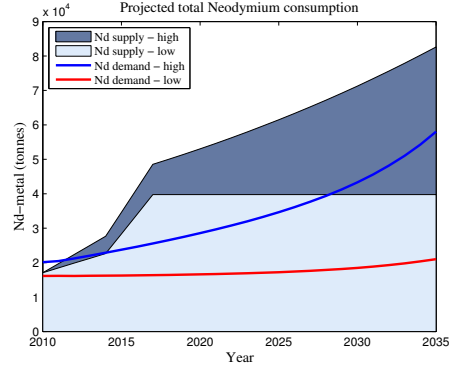
Figure 6.   Production scenarios for Nd and Dy.

Figure 7.   The total estimated Nd consumption

C. Other markets

Industrial- and HVAC-motors are shifting slowly from asynchronous motors running directly on grid, towards more efficient inverter controlled synchronous motors [14]. The scale of magnet materials consumption in small motors used in consumer electronics such as hard-drives, washing machines, refrigerators, cellphones, toys etc. can not be neglected. The magnets used in these appliances are typically not subject to high temperature environments and thus do not require high Dy content.

The other markets' consumption is estimated using a similar approach to sections III-A and III-B, with the low scenario at 0% growth from current consumption and high at 3% yearly consumption growth.

D. Mining and Processing

Over 95% of rare earth mineral supply currently originates from China [15], this supply situation originates from high production at very low cost, forcing previously active mines such as Mountain Pass in California to suspend operation. The Chinese mines operate under a government mandated production quota, which states yearly ore production targets. Figures from Technology Metals Research suggest that the production quotas are typically surpassed by approximately 40% yearly [5].

As the supply of Nd and Dy from Chinese export becomes more uncertain [2], due to increased export restrictions, exploration and production has started in many locations [5]. These mines are due to be operational between 2015 and 2020, the amount of minerals produced and, more critically, their ability to refine the minerals produced, from ores to high concentration metals will be pivotal in meeting demand.

The supply scenarios used here assume that these production facilities meet projected production figures [5], the low and high production scenarios represent the conservative and optimistic production figures respectively. The low scenario

assumes no further growth in production once these facilities reach full capacity, the high scenario assumes further production growth from increased efficiency in mining operations at 3% yearly, see figure 6.

IV. RESULTS

The total Nd consumption figures, see figure 7, show the high Nd demand scenario is close to the current actual demand. This demand is likely to be met soon by mining facilities coming online, in the conservative supply scenario by 2015. The demand will not exceed any of the supply scenarios until 2028, when the high demand case equals the conservative supply.

The Dy total consumption figures show similar traits, see figure 8, the high demand scenario, which resembles current consumption trends with regards to alloy content in high temperature applications, would be met by additional mining capacity around 2015. As hybrid vehicle adoption accelerates, coupled with wind power and other demands, the doubling of current production capacity would be surpassed by demand around 2025 in the conservative supply case and shortly after 2035 in the optimistic supply case.

A. Scale results

The resulting scale of consumption is presented as demand normalized to supply, with values lower than 1 representing an excess of supply and values above 1 representing excess demand. The magnitude of the supply/demand relation can also be derived from figures 12-18. The three industry categories, automotive traction, wind power and other industries are also illustrated for each case. These results are based on the OICA automotive and GWEC wind power scenarios. The supply and demand result matrix, see table I, is used to cover the result spectrum.

The Nd result cases show interesting traits, wind power in the low demand scenarios claim a very small market, at 10% market penetration for permanent magnet technologies
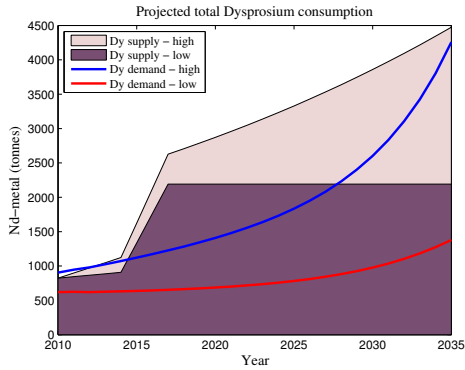
Figure 8. The total estimated Dy consumption

Figure 9. Nd consumption, BLUE Map scenario

Figure 10. Dy consumption, BLUE Map scenario

the impact is unremarkable, see figures 12, 13. In the high demand categories wind power claims a significant portion of the market initially, this is due to the availability of the technology allowing a 75% market penetration, which is a feasible scenario if it proves economically viable compared to traditional gear-set equipped generators.

In all cases the automotive sector gains impact over time as HEV/PHEV/EV adoption ramps up, ultimately claiming a quarter of the market share for Nd in all adoption cases. In the high demand cases the wind power and automotive industries claim approximately equal shares, see figures 13, 14.

As shown in figure 7, the additional supply capacity initially meets demand of Nd. In the conservative supply estimates, the supply is surpassed by the high demand case after 2025, requiring either additional mining capacity or alternative technologies.

The Dy supply and demand fraction results exhibit similar traits to the Nd results, both automotive and wind power have an initially larger impact compared to Nd consumption. This is due to their higher operating temperature requirement compared to many consumers in the other industries category, this may also explain the relatively larger volatility for Dy price shown in figure 1.

In all demand and supply cases, automotive demand has a growing impact, reaching approximately 50% market share towards 2035, see figures 15-18. Wind power claims around 10% of the market share in the low demand cases. In the high demand cases it has a peak market share of 50% around 2020, this share diminishes relative to and gets surpassed by automotive consumption around 2030.

In the low supply high demand case, see figure 17, the additional supply initially meets demand but is exhausted again around 2025. With increasing consumption rates a doubling of supply is required until 2035 if no alternative technologies are used to dampen Dy use.
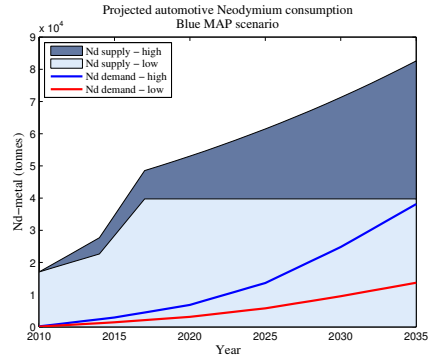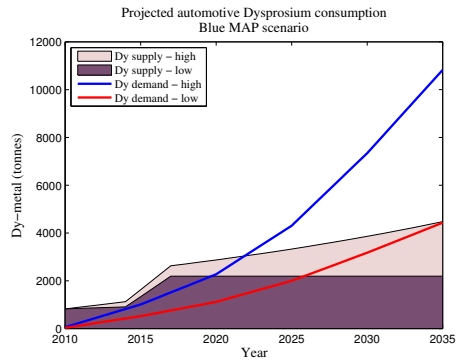
B. BLUE Map results

The BLUE Map scenario is a very high electrified vehicle adoption rate plan developed by the IEA, in order for the transport sector to meet a climate goal of 2° C global temperature increase. Meeting the production figures for electrified vehicles outlined in this scenario, all of the Dy produced in the conservative supply scenario would need to be dedicated to vehicle production with the current state of the art vehicles (high demand scenario), see figure 10. With less Dy intensive technologies (the low demand scenario), the conservative supply estimate would be consumed by 2026, and the optimistic supply estimate by 2035.

The Nd consumption of the automotive industry in the BLUE Map scenario also has a very significant impact, with the high demand case reaching a quarter of the conservative supply by 2020 and claiming it entirely by 2035. In the high supply case the automotive industry would claim 50% of world supply.
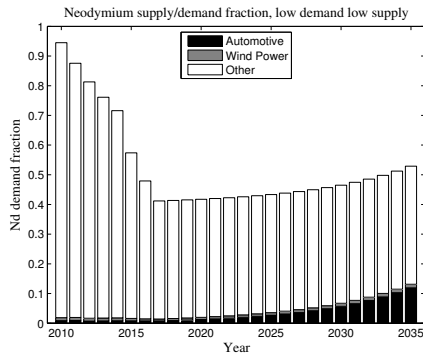
Figure 11. Nd consumption, low demand low supply

Figure 12. Nd consumption, low demand high supply

Figure 13. Nd consumption, high demand low supply

Figure 14. Nd consumption, high demand high supply

Figure 15. Dy consumption, low demand low supply
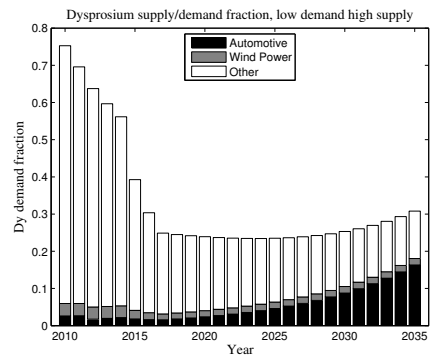
Figure 16. Dy consumption, low demand high supply
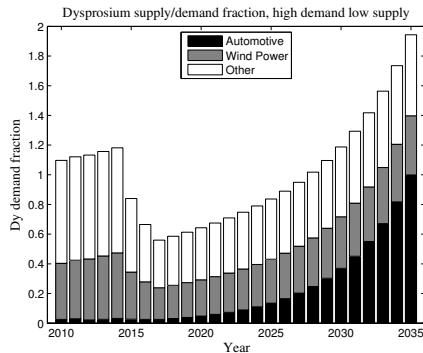
Figure 17. Dy consumption, high demand low supply
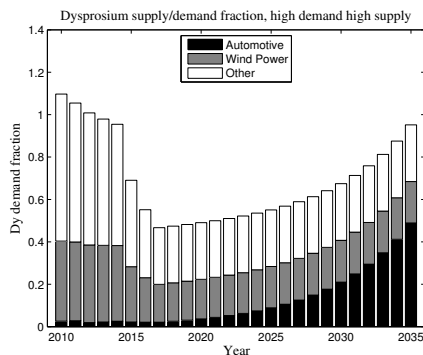
Figure 18. Dy consumption, high demand high supply

V. CONCLUSION

The four case result scenarios illustrate a myriad of possible outcomes. The automotive and wind power industries can have a remarkable impact on Nd and Dy supply, claiming approximately half the Nd market in the high use case scenarios and two thirds of the Dy market. While the additional supply brought by the production from several new rare earth mining operations will initially cover demand, the continuous expansion of wind power and the automotive transition to electrified traction will surpass supply again.

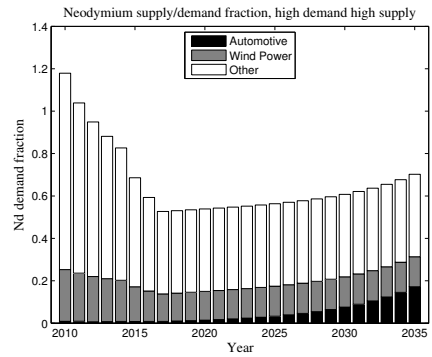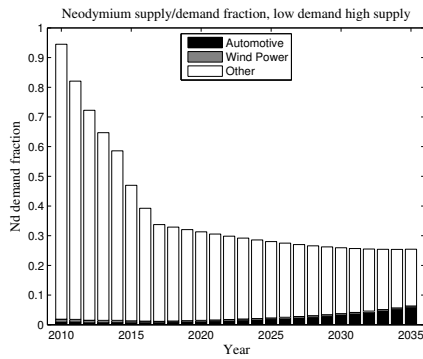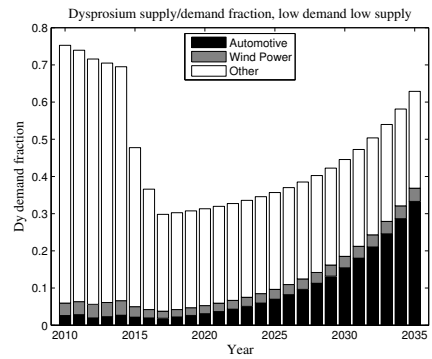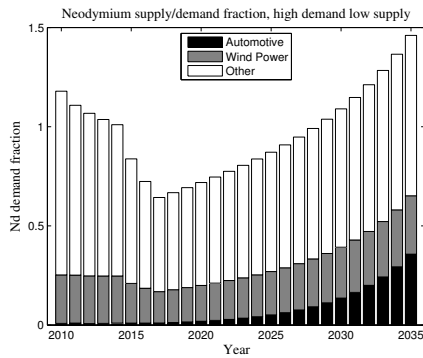Unless technical progress can be made to reduce magnet mass and Dy content required, or compact high torque density non-permanent magnet motors can be developed, the essential transition from fossil fuels, both in power generation and transport, will face significant supply issues of the materials used in their production again.

REFERENCES

[1] J. Li, D. Bauer, D. Diamond, M. McKittrick, D. Sandalow, and P. Telleen, *Critical Materials Strategy*.   US Department of Energy, 2011.
[2] R. Moss, E. Tzimas, H. Kara, P. Willis, and J. Kooroshy, *Critical Metals in Strategic Energy Technologies: Assessing Rare Metals as Supply-Chain Bottlenecks in Low-Carbon Energy Technologies*.   Publications Office of the European Union, 2011.
[3] M. Takahashi, K. Uchida, F. Taniguchi, and T. Mikamoto, "High performance nd-fe-b sintered magnets made by the wet process," *Journal of Applied Physics*, vol. 83, p. 6402, 1998.
[4] D. Brown, B.-M. Ma, and Z. Chen, "Developments in the processing and properties of ndfeb-type permanent magnets," *Journal of Magnetism and Magnetic Materials*, vol. 248, no. 3, pp. 432 – 440, 2002. [Online]. Available: http://www.sciencedirect.com/science/article/pii/S0304885302003347
[5] G. P. Hatch, "Critical rare earths - global supply & demand projections and the leading contenders for new sources of supply," Technology Metals Research, Tech. Rep., 2011.
[6] "Oica vehicle production statistics," [Online], Jun 2012, available: http://oica.net/category/production-statistics/.
[7] F. B. et al., *World Energy Outlook*, N. Tanaka, Ed.   International Energy Agency, 2009.
[8] "Metal-pages," [Online], Jun 2012, available: http://www.metal-pages.com.
[9] M. A. Miller, A. G. Holmes, B. M. Conlon, and P. J. Savagian, "The gm voltec 4et50 multi-mode electric transaxle," *SAE International Journal of Engines*, vol. 4, no. 1, pp. 1102–1114, 2011. [Online]. Available: http://saeeng.saejournals.org/content/4/1/1102.abstract
[10] L. F. et al., *Transport, Energy and CO2 - Moving toward sustainability*, N. Tanaka, Ed.   IEA/OECD, 2009.
[11] K. Rave, S. Teske, and S. Sawyer, *Global Wind Energy Outlook*, A. Pullen and J. Jones, Eds.   Global Wind Energy Council, 2010.
[12] C. Zhanheng, "Global rare earth resources and scenarios of future rare earth industry," *Journal of Rare Earths*, 2011.
[13] K. R. Long, B. S. V. Gosen, N. K. Foley, and D. Cordier, *The Principal Rare Earth Elements Deposits of the United StatesA Summary of Domestic Deposits and a Global Perspective*.   U.S. Geological Survey, 2010.
[14] I. Xenergy, "United states industrial electric motor systems market opportunities assessment," U.S Department of Energy, Tech. Rep., 2002.
[15] D. J. Cordier, "Mineral commodity summary, rare earths," U.S. Geological Survey, Tech. Rep., 2012.

Paper II

Pontus Fyhr, Mats Andersson, Jan-Eric Ståhl
**A modular framework for evaluation of electrical machine
production costs**

A modular framework for evaluation of electrical machine production costs

Pontus Fyhr, Mats Andersson and Jan Eric Ståhl
Production and Materials Engineering
Lund University
Lund, Sweden
pontus.fyhr@iprod.lth.se

Abstract—A framework structure for solving multiple option production economic models is described, showing the possibilities in defining independent process modules according to a defined set of rules. The modules are then scanned and inserted into appropriate locations in the solver framework based on naming scheme and linking information, allowing both re-use of knowledge as well as rapid development and deployment of models for new production.

The methodology is applied to the production of an electric machine, showing the ability to assess options with regard to for example technical infeasibilities such as the combination of incompatible production method selections, splitting and joining process flows and maintaining a continuous solution space.

The structured framework approach also allows extraction of data from any point in the production flow, for any option or nominal batch size.

Index Terms — Electric machine, Production costs, Decision-making, Graph traversal, Concurrent engineering, Set-based

I. Introduction

In production planning, one key element in lowering costs is choosing production processes and automation levels appropriate to the estimated demand. As prototyping and trial and error of production methodologies are cost intensive, other methods of selecting the correct manufacturing technology for each step of a production line is necessary. One tool for investigating costs is production-economic modeling, where a set of processes are detailed in sequential and parallel order, see figure 1. Each process step is abstracted to parameters related to investment, working materials, labour, cycle and set-up times, various loss factors and overheads. This approach will yield applicable results for one specific production apparatus, if these results are to be compared to another analysis of some competing technologies, care must be taken that this analysis is performed in the manner previously used, when further options are added the amount of models may grow very large.

Contrary to investigating point solutions, a set-based concurrent engineering approach strives to perform product and production processes design and development in parallel, defining possible solution ranges and inferring commonality
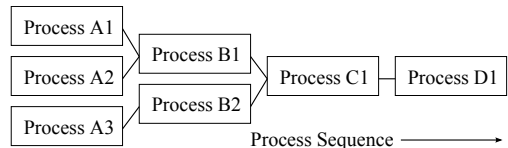
Figure 1: A typical production schematic, containing parallel and sequential operations

[1] [2]. Selection of production solutions has been previously implemented in problems such as tool-path optimisation [3], supplier selection [4] and optimization under uncertainty [5].

This paper proposes a modular multiple-choice production-economic framework, see figure 2, suitable for production economic analysis of complex products such as an automotive traction motor. Where the named modularity implies that one production cost model may be applied in a similar manner for a number of production operations, this calculation is self contained within one module and may be re-used in other scenarios where the same or similar operations are utilized. The framework itself denotes the ordering and solving method for combining and selecting between the operations. The case of electrified traction machines is of particular interest as there is a high uncertainty in volume-demand coupled with an industry sector with narrow margins.

II. Scope

For each individual component in an electric machine, multiple manufacturing technologies are available. For example a laminate sheet stack may be manufactured by progressive blanking [6], rotational cutting [7], laser cutting, or abrasive water-jet [8]. The joining of the stacks in turn may be performed by different welding processes [9], riveting or bonding.

Within coil-winding, either pre-wound complete coil packages may be pulled into the stator slots, manually or automated. Individual spindle wound coils on bobbins may be fitted to the stator teeth and attached to a bus bar. With new production methods such as needle winding being researched and tested [10]. Some decisons may force others, such as spindle wound coils requiring a bus bar, thus adding an additional

production steps to be included in the calculation. Seen from a electromechanical design standpoint there are performance differences between for example distributed and concentrated windings [11], for this work however, the results of the manufacturing process options is considered as equivalent.

The different production technologies require investments of varying magnitude and will output the desired result of each operation with a range of performance and quality characteristics, described by equation 1.

By generating discrete process-cost modules for the manufacturing technologies available to the individual components, as well process technologies and automation levels for component assembly steps. Inserting these modules into a framework of process options, option groups and sequences, allows a structured search algorithm to find a near-optimal process combination for a given parameter, such as cost, over a range of production volumes.

Focus is placed on the development and implementation of the algorithm as well as discussion regarding result output.

III. Methodology

In cost calculation modelling, the degree of accuracy chosen should reflect the level of uncertainty found within the contributing input data. The model should however be detailed enough to provide a sound basis for decisions [12]. The model chosen to be used in each module within this work is described by equation 1 [13], where:

- **I** refers to annuity cost of investments
- **II** refers to material cost per part, including rejections
- **III** refers to equipment costs per part in processing
- **IV** refers to equipment costs in connection to downtime or switchovers
- **V** refers to wage costs
- **VI** refers to auxiliary costs

$$
k_i = \frac{K_A}{N_0}\left[\frac{1}{n_{pA}}\right]_I + \frac{K_B}{N_0}\left[\frac{N_0}{1-q_{Qi}}\right]_{II} +
$$
$$
\frac{K_{CP}}{60N_0}\left[\frac{t_{0i}N_0}{1-q_Q i}\right]_{III} + \frac{K_{CS}}{60N_0}\left[\frac{t_{0i}N_0 q_s i}{(1-q_{Qi})(1-q_{si})}\right]_{IV} +
$$
$$
\frac{K_D}{60N_0}\left[\frac{t_{0i}N_0 q_{si}}{(1-q_{Qi})(1-q_{si})}\right]_V + \left[\frac{K_{Addi}}{N_0}\right]_{VI}
$$
$$\tag{1}$$

Discrete options are contained in a module consisting of process specific data, see table I. The operations are arranged in groups, and connected by paths describing the sequence by which the groups are ordered, see figure 2.

IV. Algorithm

In order to enable efficient framework traversal, the modules are stored in a three-dimension matrix by arranging processes utilizing a strict matrix structure and nomenclature, see figure 3.

- **Axis C** contains process alternative modules
- **Axis R** contains processes sequentiality

Table I: Cost model parameters

Parameter	Unit	Description
k_i	Euro	Unit cost
K_A	Euro	Annuity cost of machine investment
K_B	Euro	Working material cost
K_{CP}	Euro	Running costs during production
K_{CS}	Euro	Running costs during downtime
K_D	Euro	Wage costs
K_{Addi}	Euro	Auxiliary costs
t_0	min	Cycle time
N_0	units	Batch size
q_s	-	Standstill factor
q_Q	-	Rejection rate
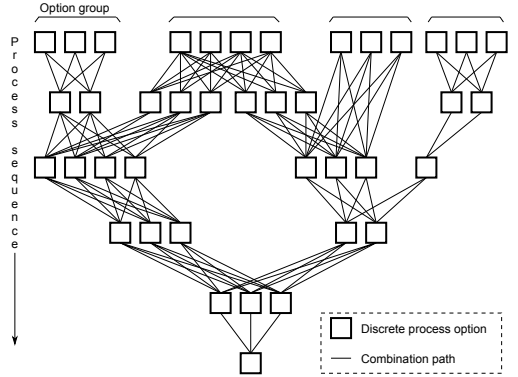
Figure 2: Modular multiple-choice production schematic

- **Axis S** contains process groups

Processes within a group (along C) are considered as interchangeable as seen by subsequent processes (along axis R) unless they are specifically blocked by a flag passed to the framework solver by a subsequent module.

Traversable tree generation is performed automatically, from the available modules, by generating a left-top-forward centred three-dimensional matrix.

A. Modules

Each discrete processes, as represented by boxes in figures 2 and 3, is contained within a module which returns three variables. The first is returning a cost value $k_i(N)$ according to the model described in section III and equation 1, the second is returning information about linking within the graph, for example if the current process flow (current S) is to be combined with another in subsequent rows. Module operation is independent from the search tree itself and is only passed information regarding the working material costs (K_B) of the previous operations at the same output point (N_0), and the amount and direction of process flows joining it. This enables re-use of modules within a different process framework as well as rapid development and insertion of new modules into the current model.

B. Operations

In order to accurately include added value (k_i) from previous process modules a number of specific operations need to be identified and implemented. The default operation of the traversing algorithm is *down* where a the preferable module (C) in a given production batch range (N_0)in a row is selected and its added value is passed along to the subsequent row R.

In order for the process flows to converge a number of process flows may be combined within an assembly process, this is denoted a *join* function, when this function is invoked the resulting added value from module that passed on the instruction will be included in the working materials value of the process options located at the network point the *join* points to.

Process flows may also diverge, when a module contains a *split* operation, which in the same way as *join* contains direction where part of the process flow is directed to, as well as a value-fraction in order to pass on added value correctly.

Handling instances where selecting one process option prohibits the use of one or more subsequent processes requires a *block* operation. The implementation of blocking is similar to *join*, the *block* flag excludes values from the linked modules on the following row when that module is selected.
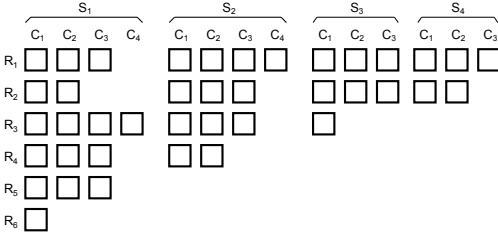
Figure 3: Traversable multi-process matrix structure with addressing along C, R and S axes

$$k_R = \sum_{S=1}^{S_{max}} \frac{K_{(R-1)min}}{N_0} \left[\frac{N_0}{1-q_{Qi}} \right]_{II} \quad (2)$$

The algorithm implementation modifies part **II** of equation 1 in order handle process sequentiality, by recursively searching for the lowest cost alternatives (C) for linked groups (S) on the previous row (R) as working materials in the current module, see equation 2.

V. DISCUSSION

The current implementation of the modular framework for evaluation of electrical machine production costs searches for lowest cost production technology alternatives, from multiple options, over a range of production volumes. The process flows are joined in accordance with common assembly orders in electrical machine production, see figure 2 and 4 respectively. But as the rejection rate of individual processes may be

unequal and the added value in process flows varies, this may not be the optimal strategy, for example permanent magnets with a very high working material cost (K_B) would ideally be included in other operations as late as possible in order to reduce the likelihood of an out of specification rejection. While this could generate practically infeasible operations, e.g. mounting magnets on the rotor inside an enclosed housing. Forcing convergence at given points not be the optimal solution, a non-restricted graph search of the full process space may suggest process flow convergence at different points than those chosen by a model designer, hard linking of convergence points guarantees a feasible endpoint solution but foregoes possibilities in both cost minimizing as well as process flows that could be found by less strict definitions.
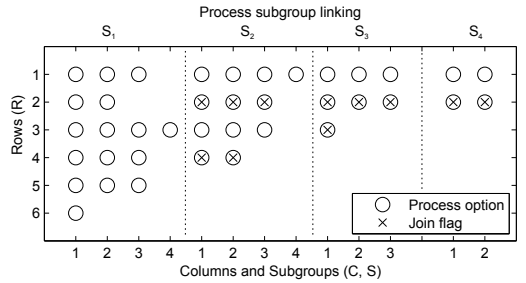
Figure 4: Output of process modules containing the *join* flag

VI. RESULTS

The full output of the multiple-choice framework described above is stored as three 4-dimension structures, as the primary purpose is illustrating the decision-making capabilities of the approach a number of excerpts a various nominal batch sizes (N_0) are shown in figures 5-8.

Studying the first row of figure 5 the algorithm output shows that the lowest cost for $N_0 = 100$ is found by selecting a distributed coil ($R_1C_1S_1$) and a lamination stack produced by rotational blanking ($R_1C_1S_2$), where as in figure 6-8 the corresponding selections made are C_2 in both cases, representing a concentrated winding in S_1 and progressive blanking of the lamination stack in S_2. By searching along the N_0 axis of the selection matrix for ($R_1C_1S_1$) it is also possible to extract that this module outputs a lower cost until the yearly output (N_0) reaches 120 units. Looking at S_3, a turning operation for the rotorshaft, it is apparent that C_2, turning from a near-net cast is preferable to the alternatives at all nominal batch sizes.

The resulting output of the final assembly option operations at R_5 as well as the lowest cost selection are represented in figure 9, where the distinct influences of the recursive search through multiple options can be seen in the final lowest cost selection.
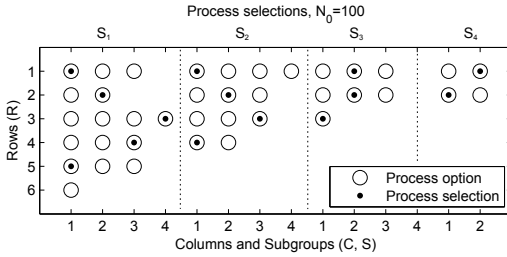
Figure 5: Resulting process selection for $N_0 = 100$
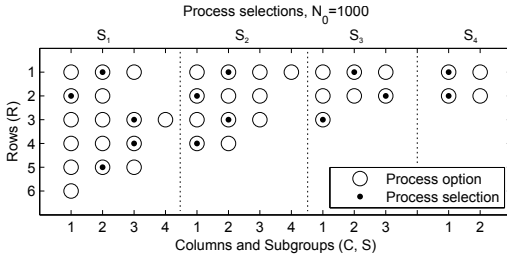
Figure 6: Resulting process selection for $N_0 = 1000$
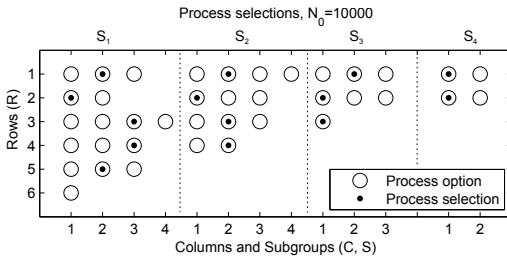
Figure 7: Resulting process selection for $N_0 = 10000$
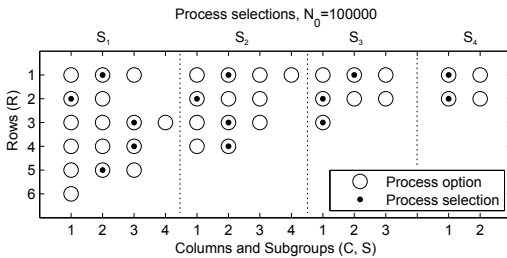
Figure 8: Resulting process selection for $N_0 = 100000$
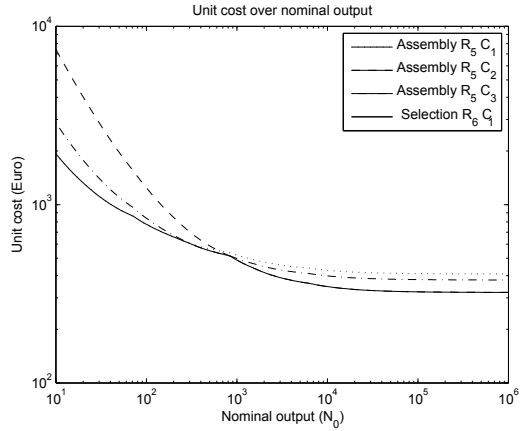
Figure 9: Resulting process costs at all R_5 options as well as the lowest cost selection at R_6

VII. CONCLUSION

In this work a method for structuring and analysing decision-making, with regard to production economic aspects within modular framework, this is a step towards a set-based concurrent engineering approach [1] within production economic analysis.

The search algorithm and cost equation described are closely tied to manufacturing technologies and enable detailed evaluation of economic factors in production systems, in taking a modular approach multiple alternatives and combinations can be evaluated simultaneously.

The structured grouping together with the operations defined in section IV allow insertion of additional modules regardless of what the existing framework contains, this also allows carry-over of defined process modules into a framework describing other production sequences.

REFERENCES

[1] J. Liker, I. Sobek, D.K., A. Ward, and J. Cristiano, "Involving suppliers in product development in the united states and japan: evidence for set-based concurrent engineering," *Engineering Management, IEEE Transactions on*, vol. 43, no. 2, pp. 165–178, 1996.

[2] A. C. Ward and W. Seering, "Quantitative inference in a mechanical design compiler," 1989.

[3] T. Dereli and H. Filiz, "Optimisation of process planning functions by genetic algorithms," *Computers and Industrial Engineering*, no. 36, pp. 281–308, 1999.

[4] G. Wang, S. H. Huang, and J. P. Dismukes, "product-driven supply chain selection using integrated multi-criteria decision-making methodology," *International Journal of Production Economics*, vol. 91, no. 1, pp. 1 – 15, 2004. [Online]. Available: http://www.sciencedirect.com/science/article/pii/S0925527303002214

[5] N. V. Sahinidis, "Optimization under uncertainty: state-of-the-art and opportunities," *Computers and Chemical Engineering*, vol. 28, no. 67, pp. 971 – 983, 2004, ¡ce:title¿FOCAPO 2003 Special issue¡/ce:title¿. [Online]. Available: http://www.sciencedirect.com/science/article/pii/S0098135403002369

[6] Schuler, *Metal Forming Handbook*. Springer, 1998, ch. Sheet metal forming and blanking.

[7] J. Tremel, J. Hackert, V. Thoms, and J. Franke, "Rotational cutting of lamination sheets for electrical machines," *Proceedings, Electric Drives Production Conference*, pp. 54–57, 2012.

[8] A. Schoppa, H. Louis, F. Pude, and C. von Rad, "Influence of abrasive waterjet cutting on the magnetic properties of non-oriented electrical steels," *Journal of Magnetism and Magnetic Materials*, vol. 254-255, no. 0, pp. 370 – 372, 2003, proceedings of the 15th International Conference on Soft Magnetic Materials (SMM15). [Online]. Available: http://www.sciencedirect.com/science/article/pii/S030488530200882X

[9] T. Markovits and J. Takcs, "Edge welding of laminated steel structure by pulsed nd:yag laser," *Physics Procedia*, vol. 5, Part B, no. 0, pp. 47 – 52, 2010, laser Assisted Net Shape Engineering 6, Proceedings of the LANE 2010, Part 2. [Online]. Available: http://www.sciencedirect.com/science/article/pii/S1875389210004542

[10] T. Albrecht, W. Knig, and B. Bickel, "Proceedings for wiring integrated winding of segmented stators of electric machines," *Proceedings, Electric Drives Production Conference*, pp. 132–138, 2011.

[11] H.-W. Lee, C.-B. Park, and B.-S. Lee, "Performance comparison of the railway traction ipm motors between concentrated winding and distributed winding," in *Transportation Electrification Conference and Expo (ITEC), 2012 IEEE*, 2012, pp. 1–4.

[12] J.-E. Ståhl, *Metal Cutting - Theories and Models*. SECO Tools, 2011, ch. Economic aspects of cutting processes.

[13] M. Jönsson, C. Andersson, and J.-E. Ståhl, "Implementation of an economic model to simulate manufacturing costs," *Manufacturing Systems and Technologies for the New Frontier*, pp. 39–44, 2008.

Paper III

Pontus Fyhr, Mats Andersson, Jan-Eric Ståhl

Statistical interfaces for production of a permanent magnet based rotor

Statistical interfaces for production of a permanent magnet based rotor

Pontus Fyhr, Jan-Eric Ståhl and Mats Andersson
Production and Materials Engineering
Lund University
Lund, Sweden
pontus.fyhr@iprod.lth.se

Abstract—A production-system simulation model for manufacturing cost of a permanent-magnet based rotor, analyzing the influence of uncertain parameters by utilizing the monte carlo method. The uncertain parameters studied include investment and bill of materials costs as well as cycle time. The resulting influence of these uncertainties are presented for each case individually, as well as all possible combinations, giving seven total cases studied. Cutting tool costs over a range of batch sizes show that investment uncertainty has rapidly declining impact even within fairly low batch sizes. BOM cost variations, especially for the permanent magnets maintain a sizeable influence over the range of batch sizes. The Weibull distribution based model for permanent magnet insertion shows that profit margins derived from point based nominal data is not reliable for pricing of manual production processes. The presented approach is useful both for decision making regarding new production, as well as pricing in competitive markets with narrow margins.

Index Terms — Electric machine, Production system, Decision-making, Concurrent engineering, Uncertainty, Stochastic Programming

I. Introduction

With increasing energy production and more stringent demands on energy efficiency from both the US Department of Energy and the European Union Energy Efficiency Directive [1], and increasing interest in e-Mobility [2][3]. The need for both new and more efficient production systems especially in a market such as electric machine production, where an increasing demand is clear, but demand levels and timing investments for start of production are uncertain.

In designing or re-designing a production system for complex products such as electrical machines a multitude of inputs must be used in order to ensure a commercially successful product, some of the fundamental uncertainties are:

- What is our target price and profit margin?

- How large is market demand for the product, and what market share is attainable?

- What investments must be made in order to realize production?

- What cycle times are achieveable within the production system?

- Are bill of materials costs stable over time?

This work models the influence of the uncertainties above. By applying three monte-carlo based models, and all possible combinations of these as described in table IV, to the production of a permanent magnet based rotor, see figure 1, analysis of production costs can be performed, despite vague or uncertain input data.

Process modules from the production-economic decision tool described in [4] are used as a baseline. The addition of statistical interfaces in the model can be divided into three parts: Investment uncertainty, bill of materials uncertainty and cycle-time variations.
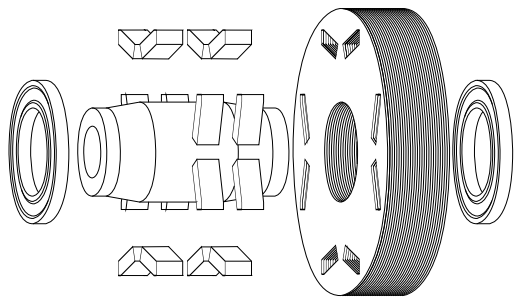
Figure 1. Schematic rotor assembly, consisting of bearings, rotor-shaft, magnets and lamination stack.

A. Materials

The baseline bill of materials used for these calculations are a general estimate of an automotive traction motor rotor, the values used are shown in table I.

Magnetic steel sheet is available in a multitude of variants and thicknesses, with relatively stable markets as compared to the permanent magnet materials. With notably increasing costs for lower sheet thicknesses. Bearings and rotor-shaft material are standard components for any machine and available from a multitude of suppliers.

Table I.   BILL OF MATERIALS BASELINE

Name	Price
Permanent magnet	55 €
Magnetic steel	27 €
Shaft and bearings	10 €
Additional materials	1 €

The permanent magnets are subject to the largest price variance and is therefore selected as the item on the BOM list to be modelled as a stochastic variable. Rare-earth prices have recently increased to extreme levels only to fall again [5], see figure 2. However, despite increased demand from new industries such as automotive and wind-power, the supply of magnet materials is likely to cover demand within the forseeable future [6].
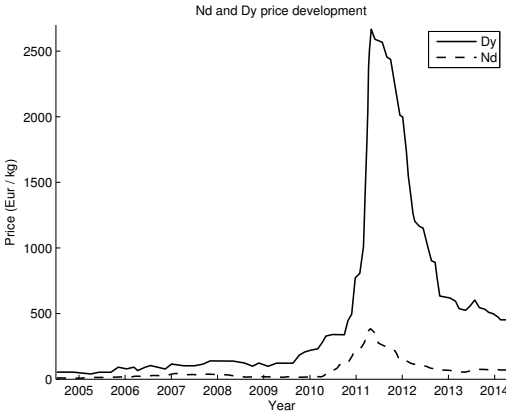
Figure 2. Historical Nd and Dy metal price per kg, Chinese export FOB [7] [8].

B. Production processes

Production of this electric machine rotor starts with cutting magnetic steel sheet, which serves as a flux conductor and a structural part of the rotor, encapsulating the permanent magnets.

The most common method for magnetic steel sheet cutting is blanking, see figure 3, but as high tooling costs may be prohibitive for lower production volumes, alternative technologies such as water-jet, laser-cutting or roll blanking may be used [9].

The annuity cost of the cutting tool is modelled to between 80.000-100.000 € with adjustments for minimizing burr formation [10] and tolerances. After the cutting process, the sheets are stacked and joined, see figure 1. Welding is common for industrial drives, as it provides a high strength connection with rapid cycle times. Adhesives also provide a strong bond, but require a curing time. Interlocking connections are common for stators with sufficient structural support inside a housing. For this rotor bonding is selected as the joining method.
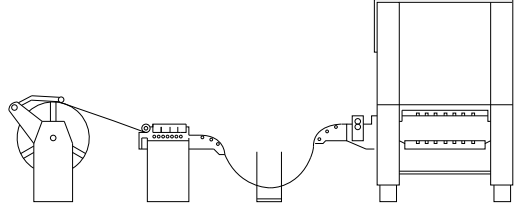
Figure 3. Components of a typical press line, the press is fed from a roll of magnetic steel sheet.

Table II.   PROCESS CYCLE TIME BASELINE

Name	Time t_0 (seconds)
Blanking	3
Bonding	240
Shaft assembly	180
Magnet assembly	360

When the bonded rotors have cured, the rotor-shaft is fitted to the lamination stack. The following operation is insertion of the magnets into the rotor slots, this process is especially sensitive for pre-magnetized magnets [11] [12]. A strong trend towards automation is clear, as reduction of cycle times and increased quality is desireable. In order to analyze the effects of cycle-time variance an semi-manual process model is used here. The nominal cycle times in table II, are used as a baseline for the Weibull distributed cycle time model, with a probability density from equation 1.

$$p(x) = \frac{k}{\lambda} \left(\frac{x}{\lambda} \right)^{k-1} e^{-(x/\lambda)^k} x \geq 0 \qquad (1)$$
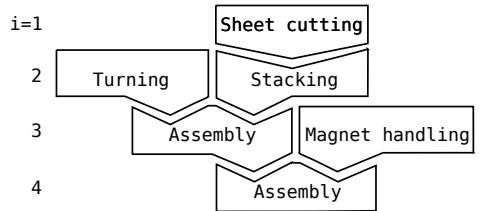
Figure 4. Production processes and flow in rotor production

II. METHODOLOGY

A. Production costs

In order to calculate the costs involved in production of a part, a multitude of models exist [13][14][15]. In this work a model developed specifically for the economic analysis of production processes is applied.

The cost of a value adding process $k_i(N_0)$ is a continous function as described by equation 2, originally detailed in the works by Ståhl and Jönsson [16][17][18]. The production cost equation, equation 2, describes the cost $k_i(N_0)$ of a part on

row i in the production system as a sum of costs from different sources, with parameter definitions in table III.

$$k_i(N_0) = \frac{K_A}{N_0}\left[\frac{1}{n_{pA}}\right] + K_B\left[\frac{1}{1-q_{Qi}}\right] +$$
$$\frac{K_{CP}}{60}\left[\frac{t_{0i}}{1-q_{Qi}}\right] + \frac{K_{CS}}{60}\left[\frac{t_{0i}q_{si}}{(1-q_{Qi})(1-q_{si})}\right] +$$
$$\frac{K_D}{60}\left[\frac{t_{0i}q_{si}}{(1-q_{Qi})(1-q_{si})}\right]$$

$$(2)$$

Table III.   COST MODEL PARAMETERS

Parameter	Unit	Description
k_i	€	Unit cost
K_A	€	Annuity cost of tool investment
K_B	€	Working material cost
K_{CP}	€	Running costs during production
K_{CS}	€	Running costs during downtime
K_D	€	Wage costs
n_{pA}	-	n batches until maintenance
t_0	min	Cycle time
N_0	units	Batch size
q_s	-	Standstill factor
q_Q	-	Rejection rate

In a production system the part cost generated by a number of sequential processes, i, will be the result of solving the recursive function generated by combining equation 2 and 3. In cases where two or more production flows are joined in an assembly (see rows 3 and 4 in figure 4), previous costs are defined by equation 4.

$$K_B(i) := k_{i-1}(x) \qquad (3)$$

$$K_B(i) := \sum_{x=a}^{b} k_{i-1}(x) \qquad (4)$$

B. Stochastic models

The stochastic models described in section I, redefine the parameters K_A, K_B and t_0 as random samples from their respective sets. The tool investment (K_A) and material cost (K_B) models draw samples from a uniform random, where the cycle time (t_0) model is based on the Weibull distribution, see equation 1, with $\lambda = t_0$ and $x = 1$. The resulting individual influence from each model, as well as all of the possible combinations shown in table IV are presented in section IV.

Each set contains 1000 samples for each of the 49 logarithmically spaced points for N_0 samples, the set generation is performed in *Python* with *numPy*, using seeds $S \in [1:1000]$ for each case in the table IV.

Table IV.   COMBINATION CASE TABLE

Name	Investment	Material cost	Cycle time
K_A	x		
K_B		x	
t_0			x
$K_A + K_B$	x	x	
$K_B + t_0$		x	x
$K_A + t_0$	x		x
$K_A + K_B + t_0$	x	x	x

III. SCOPE

A. New Production

As a product and production system is developed, uncertainties regarding both investment levels and production performance are present. There may also exist some items in the BOM which are subject to price fluctuations as described in section I. With continous development more information about the production system is gained, the uncertainty will be reduced and more accurate model results can be calculated. Each of these uncertainties will influence the resulting product cost (k_i) in different ways, see section IV. When the production-system is in use variations will exist, predominantly with regard to cycle times (t_0). Especially with regard to processes manual assembly steps, this also holds true for the handling of standstills in automated processes as automated equipment may or may not be able to cope with critical events outside the defined process window.

B. Model Robustness

Once a production system has been designed, and a high model fidelity has been achieved, the model is often used for pricing products before the start of production [14][15]. Here the model result will be compared to the baseline model costs with an arbitrary profit margin. This provides a measure of how initial point based estimates compare to the monte-carlo based production model.

IV. RESULTS
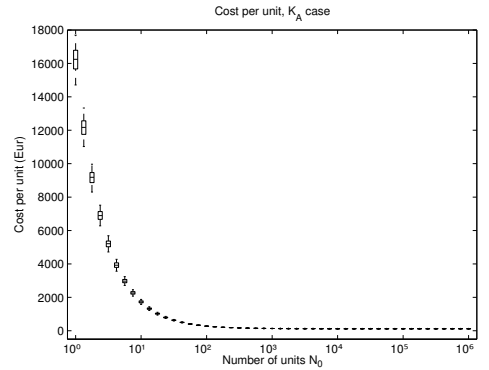
Figure 5.   Isolated investment cost variance case results.
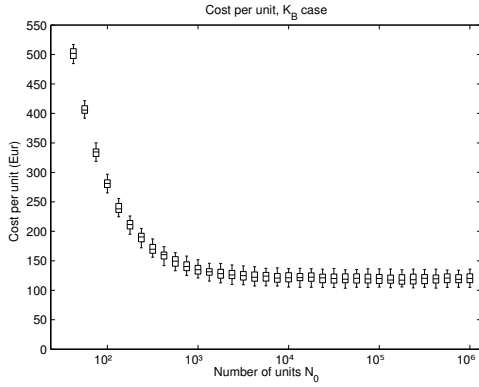
Figure 6. Isolated material cost variance case results.

Figure 7. Isolated cycle-time variance cost case results.

Figure 8. Combined investment and material cost case results.

Figure 9. Combined material and cycle-time cost case results.

Figure 10. Combined investment and cycle-time cost case results.
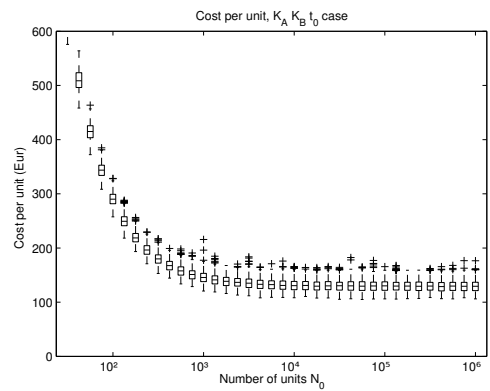
Figure 11. Combined investment, materials and cycle-time cost case results.
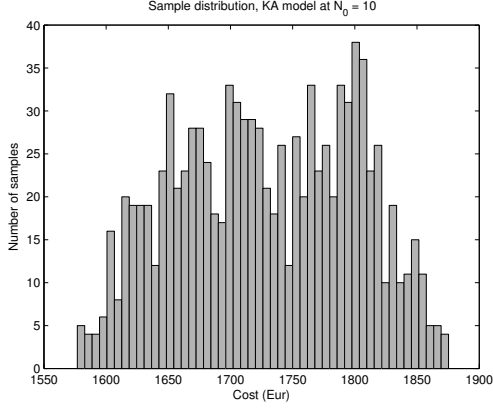
Figure 12. Sample distribution at $N_0 = 10$ for the K_A model
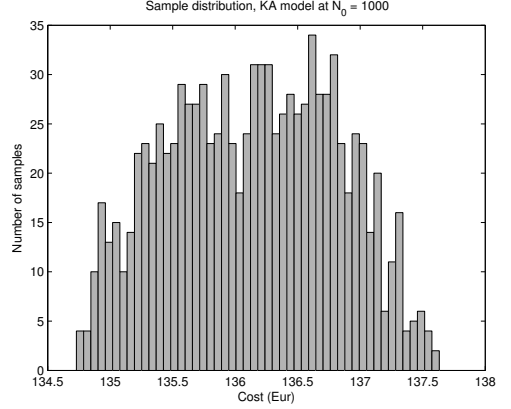
Figure 13. Sample distribution at $N_0 = 1000$ for the K_A model

Figure 14. Sample distribution at $N_0 = 1000$ for the t_0 model

The resulting product cost $k_i(N_0)$, as described by equations 2-4, for the cases detailed in table IV. As shown in figures 5-11, all seven cases converge to a median product cost k_i of 125-140 € after N_0 exceeds 2500 units.

The isolated results of the tool investment (K_A) variation case, see table IV, and figure 5, show that the influence of the uncertain investment level required for the blanking process rapidly diminishes with increasing N_0. This is due to the N_0 denominator in equation 2 in combination with the number of sheets used in each rotor, causing N_0 for the blanking process to grow more rapidly, reducing the influence of K_A for higher N_0.

In the case of material cost (K_B) uncertainty, the influence remains constant across the range of production volumes. As the material cost influences each part equally in equation 2. The presence of the loss factor q_Q, operating on the material cost (K_B) widens the distribution, due to parts deemed as out of specification. The frequent outliers in the cycle-time cases (t_0), may give an impression of high cost values, see figures 7, 9 and 11, this is analyzed in closer detail in section V.

V. DISCUSSION

The results shown in section IV, display that despite the inclusion of a large uncertainty range for tool investments, the influence of this uncertainty on product cost is minimal at $N_0 > 100$. Looking closer at the cost distributions for $N_0 = 10$, in figure 13 and $N_0 = 1000$, in figure 14, the cumulative distribution funcion is clearly the same. Normalizing the upper adjecent and 75th percentile to the median cost, gives 8.6% and 3.7% for $N_0 = 10$. The same values for $N_0 = 1000$ are only 1.2% and 0.4%.

The results of the t_0 variance case at $N_0 = 1000$ in figure 12, shows the distribution of costs resulting from the manual magnet insertion process. The high 75th percentile and frequent outliers, shows the potential benefits of automation, not only for cycle time reduction but also for better process control allowing a narrower distribution with less irregular cycle times.
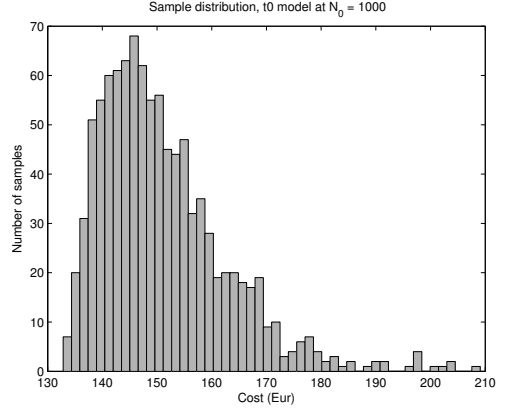
Table V. ACTUAL MARGIN FROM MEDIAN, COMBINED CASE

N_0	10%	25%	50%
100	6.1%	21%	45%
1000	2.9%	17%	40%
10000	1.9%	16%	39%

By introducing profit margins of $10 - 50\%$ over the baseline costs to the combined case result, see figure 15, it is possible to analyze how the inclusion of the stochastic models, especially for cycle times and material cost variation may be used for more accurate pricing, as mentioned in section III-B. In table V, the profit margins from median product cost are shown for the three initial profit margins at three production volume points. The results clearly show that initial estimates from a point-based model are unreliable for setting price points to an expected margin, all of the measured margins from median are lower than from the baseline model. Monte-carlo
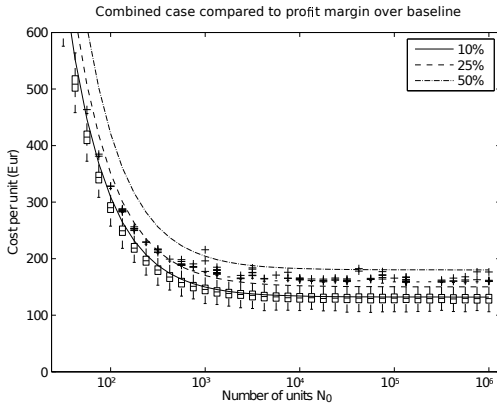
Figure 15. Combined model results, with profit margins over baseline costs.

based pricing may very relevant in markets with narrow profit margins.

VI. CONCLUSIONS

Despite the uncertainties mentioned in section I, it is possible to perform production cost calculation and analysis with meaningful results early on in the production development process. In doing this, insight will not only be gained into product costs, but also in which areas to focus further development efforts.

The results in section IV and closer analysis in section V, show the isolated influences that uncertainty in investment, cycle time and materials cost have on the production system. From the investment ucertainty (K_A) case, the results show that for the investment levels used, the uncertainty in tool investment is reduced to minimal levels for larger batch sizes.

In the combined cases, the drawbacks of using point-based initial calculations for pricing is shown, see figure 15. For a supplier in a competitive market, it may be preferable to develop accurate stochastic models for cycle-times, in order to be able to offer accurate pricing to customers.

REFERENCES

[1] F. Birol and et al., *World Energy Outlook, Redrawing the Energy and Climate Map*, R. Priddle, Ed. International Energy Agency, 2013.

[2] L. Fulton and et al., *Transport, Energy and CO2 - Moving toward sustainability*, N. Tanaka, Ed. IEA/OECD, 2009.

[3] F. B. et al., *World Energy Outlook*, N. Tanaka, Ed. International Energy Agency, 2009.

[4] P. Fyhr, M. Andersson, and J.-E. Ståhl, "A modular framework for evaluation of electrical machine production costs," in *Electric Drives Production Conference, 2013 IEEE*, 2013, pp. 1–5.

[5] V. L. Smith, G. L. Suchanek, and A. W. Williams, "Bubbles, crashes, and endogenous expectations in experimental spot asset markets," *Econometrica*, vol. 56, no. 5, pp. pp. 1119–1151, 1988. [Online]. Available: http://www.jstor.org/stable/1911361

[6] P. Fyhr, J. Stahl, and M. Andersson, "The scale of permanent magnet materials for automotive traction motors," in *Electric Drives Production Conference (EDPC), 2012 2nd International*, Oct 2012, pp. 1–7.

[7] "Metal pages," May 2014, available: http://www.metal-pages.commetalprices/rareearths/.

[8] S. Barber, "Thompson reuters," May 2014, available: http://alphanow.thomsonreuters.com/2012/10/chart-of-the-week-rare-earths-not-quite-as-rare/.

[9] J. Tremel, J. Hackert, V. Thoms, and J. Franke, "Rotational cutting of lamination sheets for electrical machines," *Proceedings, Electric Drives Production Conference*, pp. 54–57, 2012.

[10] E. Lamprecht and R. Graf, "Fundamental investigations of eddy current losses in laminated stator cores created through the impact of manufacturing processes," in *Electric Drives Production Conference (EDPC), 2011 1st International*, Sept 2011, pp. 29–35.

[11] E. Joseph, J. Tremel, B. Hofmann, A. Meyer, J. Franke, and S. Eschrich, "Automated magnet assembly for large pm synchronous machines with integrated permanent magnets," in *Electric Drives Production Conference (EDPC), 2013 3rd International*, Oct 2013, pp. 1–6.

[12] A. Kampker, P. Burggräf, and D. Wowreczko, "Development of technological competence innovations in disruptive changes using the electric motor as an example," in *Electric Drives Production Conference (EDPC), 2013 3rd International*, Oct 2013, pp. 1–4.

[13] R. Sundkvist, R. Hedman, and P. Almström, "A model for linking shop floor improvements to manufacturing cost and profitability," *International Journal of Computer Integrated Manufacturing*, vol. 25, no. 4-5, pp. 315–325, 2012. [Online]. Available: http://dx.doi.org/10.1080/0951192X.2011.608725

[14] E. Shehab and H. Abdalla, "An intelligent knowledge-based system for product cost modelling," *The International Journal of Advanced Manufacturing Technology*, vol. 19, no. 1, pp. 49–65, 2002. [Online]. Available: http://dx.doi.org/10.1007/PL00003967

[15] "Product cost estimation: Technique classification and methodology review," *Journal of Manufacturing Science and Engineering*, vol. 128, 2006.

[16] J.-E. Ståhl, *Industriella Tillverkningsystem*. Lund University, 2011, ch. Deterministisk produktionsutveckling.

[17] M. Jönsson, C. Andersson, and J.-E. Ståhl, "Implementation of an economic model to simulate manufacturing costs," *Manufacturing Systems and Technologies for the New Frontier*, pp. 39–44, 2008.

[18] J.-E. Ståhl, *Metal Cutting - Theories and Models*. SECO Tools, 2011, ch. Economic aspects of cutting processes.

Paper IV

Performance and Manufacturability Tradeoffs of Different Electrical Machine Designs

Pontus Fyhr[1], Gabriel Domingues[2], Avo Reinap[2], Mats Andersson[1], Mats Alaküla[2]

[1]Lund University, Dept. of Mechanical Engineering, Div. of Production and Materials Engineering, Lund, Sweden
Pontus.Fyhr@iprod.lth.se

[2]Lund University, Dept. of Biomedical Engineering, Div. of Industrial Electrical Engineering and Automation, Lund, Sweden
Gabriel.Domingues@iea.lth.se

Abstract—**This work addresses the manufacturability challenges in traction machine production systems and design. The tradeoffs between performance and manufacturability of a heavy duty traction machine for buses and trucks, are investigated for four different winding designs, with multiple stator combinations, all using the same interior permanent magnet rotor. We present an analysis of electromagnetic, thermal, cost and production system performance for 6 primary combinations.**

Keywords-Traction machine, Design, Production, Decisions, Manufacturability.

I. Introduction

As vehicle electrification advances, the requirements on the components broaden past only providing the required performance for the available space. Cost, dependency on scarce materials, expected life, reliability, ease of maintenance and manufacturability are becoming important aspects for the OEM to consider before selecting an electrical machine (EM) design.

In this context, addressing manufacturability challenges during early stages of the design process of an electrical machine is a valuable practice that can reduce the overall development time/cost and limit the number of iterations required to produce a manufacturable design. However, to do so effectively, the designer must have the understanding and the tools to quantify how performance-based decisions affect the required manufacturing processes needed to produce the machine at different volumes.

Studies that quantify how different machine designs influence the manufacturability and final cost of the machine, at different production volumes, while keeping performance implications in mind, are scarce in peer-reviewed literature. Nonetheless, attempts of quantifying either production, or performance implications of different designs are abundant.

For example in [1] a number of methodologies and necessary inputs are discussed, with a focus on winding systems. This work is followed by an in depth requirement specification of electric machine components with an example focused on housings [2], these works hint at useful methodologies and

provides some machine data, but they do not apply them to any designs. A noteworthy approach to design decisions coupled with the material cost is presented in [3], where the authors discuss how material cost ratios (for major constituents) can be coupled to predicted torque from finite element analysis and expressed as a ratio. However, it provides limited insights on the manufacturing challenges that different designs might present.

On the other hand, a performance comparison that is highly relevant for the case study presented in this paper is shown in [4], where the thermal and electromagnetic consequences of selecting a different number of slots and winding arrangements are compared. Another interesting work that presents valuable insights in this regard is presented in [5], where a detailed electromagnetic analysis of interior permanent magnet machines with different winding configurations is presented.

Furthermore, in order to study the impact of increasing the electrical steel material utilization in both the cost and performance of the machines, a full phase (6 segments / layer) segmented stator and a single tooth wound segment are considered, see fig. 3. These segmented stators also allow the use of a different grade and thickness rotor material. The segmentation does introduce both a geometric air-gap due to tolerances, and the cut edges degrade the soft magnetic material as described in [6], this degradation is detrimental to machine performance.

The main objective of this paper is to provide insights on the consequences, with regards to cost, performance and productivity, of selecting different winding, segmentation patterns and assembly methods of electrical traction machines. Not to compare separately optimized machine designs.

II. Methodology

In this paper, a comparison of the effects of different windings arrangements have in both the performance and manufacturing cost is presented. The study consists of four different windings, applied to a modified version of the machine presented in [7] [8]. The selected windings are: (a) pulled winding using magnet wire (b) hairpin winding (c) needle-wound fractional slot concentrated windings (FSCW)
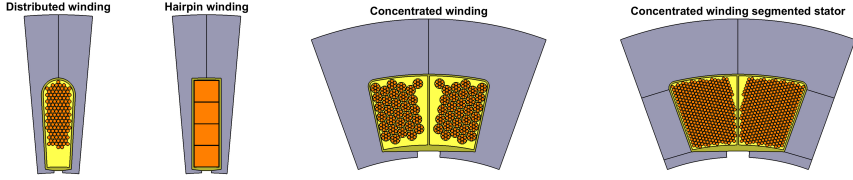
Fig. 1: Slot filling for the four winding layouts, distributed, hairpin, concentrated needle and concentrated segmented winding.

(d) FSCW, using a fully segmented stator [9]. Which are shown in fig. 1.

The machines in this work share one rotor geometry. Moreover, the stator geometry of the different machines is only slightly modified in order to preserve the achievable copper area in the slot and to adapt better to the type of winding.

The production system is modeled as a chain of discrete processes, which are aligned with the material flow as it diverges and converges. In performing some work to a workpiece, cost or value is added to it.

In order to quantify the performance of the different machines under comparison, 2D finite element simulations are used. Firstly, a heat transfer simulation is perform having the same forced cooling conditions [8] for all machines (heat transfer coefficient = 600 W/(m^{2}K) and T$_o$ = 80) in order to determine the maximum allowable current density for each design. Secondly, magnetostatics simulations are carried out at different current combinations and rotor positions in order to estimate the flux and torque maps of the proposed EM. Finally, this data is post-processed in order to extract the torque vs speed characteristics of the machine, its efficiency maps and other relevant performance metrics such as torque ripple, cogging torque and overloading torque at twice the nominal current.

A. Scope limits

In order to maintain the focus of comparing the effects of design and production decisions, small items such as screws, seals etc. are included in a blanket cost for bearings and resolvers, at 112 €. The housing for all machine designs is considered to be the same, as is the lamination stack height, despite differences in end-turn space requirements. Nor are any overhead or warehousing costs included in the cost calculations.

III. PRODUCTION SYSTEMS

The production systems model used to analyze the influences of the decisions regarding winding and stator design described in section I, is depicted as a decision tree in fig. 2. Where one of three exclusive decisions must be made regarding the stator blanking process, the methodology has been described in [10], and an attempt at providing a way of analyzing the uncertain underlying costs was presented in [11]. Each stator decision results in a respective material utilization ratio, shown in fig. 3. All the stator designs are considered
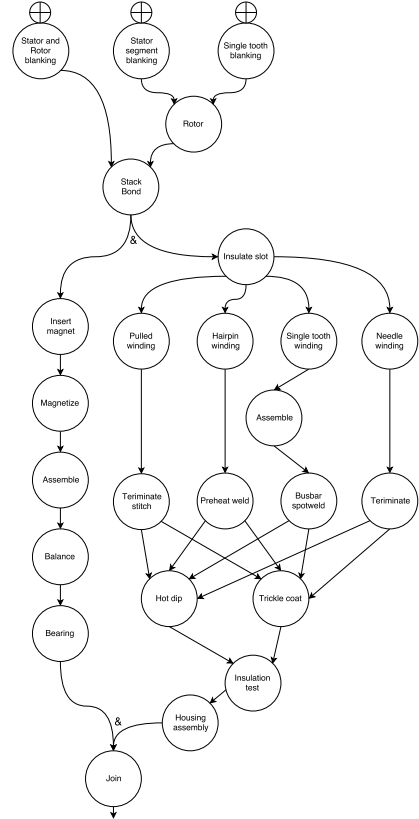
Fig. 2: Decision tree for the processes involved in traction machine manufacturing.

to be stamped on the same type of press, with a 610 mm coil width, working at a peak performance of 1.25 Hz. The coil width is fitted to the highest number of parallel pieces within the 610 mm width restriction, while including margins for blanking [12].

(a) Hexagonally nested rotors   (b) Hairpin phase segments

(c) Stator & Rotor   (d) Single tooth segments
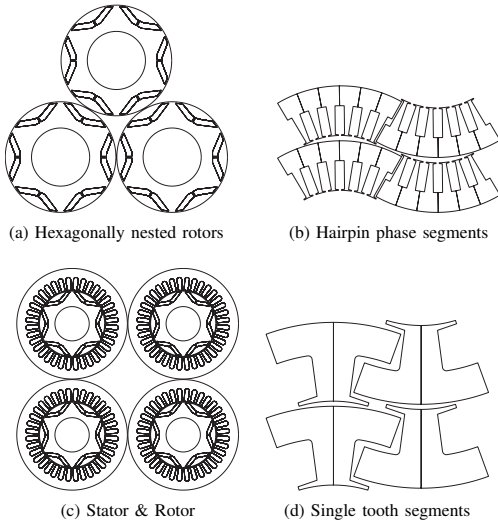
Fig. 3: Nesting of the stamped components, the material yield is: Single tooth stator 77.66 %, Distributed phase segments, incl hairpin 60.03%, Distributed Full stator & rotor incl hairpin 49.15% FSCW Full stator & rotor 49.40%, Rotor 44.59 %

It may be interesting to note that the full stator has a higher yield in a square packing, while the rotor has its highest yield in a hexagonal packing [13], within the strip-width restrictions above, see fig. 3.

1) Blanking: Beside the possible improvements in reduced scrap as depicted in fig. 3, the single tooth segments and to a lesser extent full phase segments offer a productivity benefit. Where the single tooth and phase segments are cut in a two stage progressive die with multiple lanes, the complete stator rotor combination uses a three stage progressive die. All dies are considered to be D6 tool steel (2.1% C, 12 % Cr, 0.7 % W), with similar wear performance as in [14]. Tool wear is modeled here as an investment in the tool itself (K_A) coupled with a production stop (q_S). For higher production volumes it would certainly be interesting to investigate the performance of carbide dies as described in [12], though publicly available wear data for Fe-Si steels using modern coating materials is scarce, and the focus here is coupling design choices to electro-mechanical and production performance, not in depth studies of blanking.

The segmented stators also allow the use of different materials in the rotor and stator. For example in high speed machines with narrow magnet bridges a high strength material may be required, or a lower cost higher thickness material may be used.

The geometries from the 2D FEA are used to estimate the shearing forces, in order to remain within the capability limits of the press. For very accurate calculations, complex models

such as the one presented in [15] are useful.

In a high speed machine that cycles frequently to high bridge stresses, the fatigue behavior of electrical steel needs to be considered [16], this work also shows the effects of punching on the mechanical properties of the material. Higher strength grades with yield strength as high as 600 MPa [17] are available, but the cost premium may be prohibitive for use in the entire lamination stack.

2) Lamination stack assembly: Mechanical joining methods for lamination stacks have been the investigated with regards to loss performance in [18] [19], and a bonding productivity study [20] concludes that 2-component acrylate based bonding methods allow improved productivity compared to traditional baking varnishes.

In the assembly of the rotor, the lamination stack is first bonded, followed by magnet insertion, then magnetization and shaft assembly followed by balancing. This is perhaps a conservative approach compared to balancing partial segment stacks [21], which might be appropriate if introducing rotor skew [22].

3) Winding: Fill factor receives much attention in works on windings, such as [23], where the optimal placement of one strand in a given slot shape is found. This allows very high fill factors for one or few wires, as the placement then can be perfectly controlled. However in traction applications such as the machine considered in this work, a larger number of parallel strands and fewer turns are needed to suit the required power at the given DC-link voltage (300-800 V).

In order to achieve sufficient copper area per turn, the needle wound concentrated winding consists of prefabricated bundles containing 7 strands, which are wound with 3 parallel bundles as shown in fig. 1, as most needle winding machine suppliers are sceptical of more than two or three parallel needles. Though this bundling method leads to a very low fill factor when compared to even the distributed winding.

The segmented single tooth winding allows for a better fill factor, as the stator tooth itself is rotated and the parallel wires do not twist with every turn as in needle winding. This allows for a fill factor that approaches that of perfect ortho-cyclic windings, and the winding performance is assumed comparable to the flyer winding in [24].
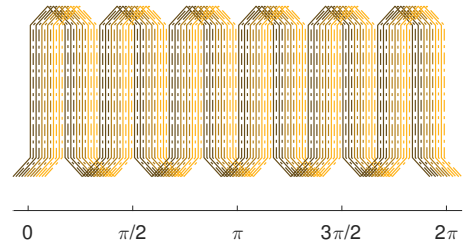
Fig. 4: Hairpin winding pattern for the integer slot windings.

The hairpin winding achieves a very high fill factor, at the expense of a higher cost wire shape, costs are driven also by the welding of the 69 connections on the lower side as depicted in fig. 4. Further limitations are imposed by the winding pattern as the first hairpin in the slot must go down into the second position in the following slot (see fig. 1), to be connected on the welding side and arrive up in the first in the subsequent slot. This means that the number of turns per slot must be evenly divisible by two to remain feasible for hairpin windings.

Drawing accurate winding diagrams, such as the one in fig. 4 help the designer to understand the geometry of the end-turns and how the winding will be placed inside the slot in manufacturing.

A. Production cost

The production costs for the different solutions in this work are calculated with eq. 1, first presented in [25]. Only machine specific tool investments are considered as investments (K_A), such as blanking tools, which are a direct product related cost. Whereas machines such as presses, winding machines or robotics are included as costs during production (K_{CP}) and costs during standstill (K_{CS}), often referred to as machine time costs. Wage costs (K_D) are averaged over shifts, and the processes are automated but not fully, on average requiring one worker for two processes. A full list of the parameters in eq.1 is included in table I, but individual process parameters are left out due to the space required. Material costs are listed in table II, where the wire cost is defined to float with the copper price, at the time of writing it was 5.47 €/ kg.

$$
k(x, N) = \frac{K_A(x)}{N} + K_B(x)\left[\frac{1}{1 - q_Q(x)}\right] +
$$
$$
K_{CP}(x)\left[\frac{t_0(x)}{1 - q_Q(x)}\right] + K_{CS}(x)\left[\frac{t_0(x)q_s(x)}{(1 - q_Q(x))(1 - q_s(x))}\right]
$$
$$
+ K_D(x)\left[\frac{t_0(x)}{(1 - q_Q(x))(1 - q_s(x))}\right]
$$
(1)

Then the cost of a further refined part is denoted x_n which uses x_{n-1} as its constituents. This gives the term K_B the form in eq. 2. In many processes this sum also includes small parts, such as screws, insulation, bonding material etc, which is not included in fig. 2 for clarity, these can be viewed as separate x_{n-1}, in the context of eq. 2. Combining equations 1 and 2 give a final product cost $k(x_n, N)$, that takes the recursive form in eq. 3.

$$
K_B(x_n, N) = \sum k(x_{n-1}, N)
$$
(2)

$$
k(x_n, N) = \frac{K_A(x_n)}{N} + \sum k(x_{n-1}, N)\left[\frac{1}{1 - q_Q(x_n)}\right] +
$$
$$
K_{CP}(x_n)\left[\frac{t_0(x_n)}{1 - q_Q(x_n)}\right] +
$$
$$
K_{CS}(x_n)\left[\frac{t_0(x_n)q_s(x_n)}{(1 - q_Q(x_n))(1 - q_s(x_n))}\right] +
$$
$$
K_D(x_n)\left[\frac{t_0(x_n)}{(1 - q_{Q(x_n)})(1 - q_s(x_n))}\right]
$$
(3)

TABLE I: Cost model parameters

Parameter	Unit	Description
k_i	€	Unit cost
K_A	€	Annuity cost of tool investment
K_B	€	Working material cost
K_{CP}	€	Machine time costs during production
K_{CS}	€	Machine time costs during downtime
K_D	€	Wage costs
t_0	s	Cycle time
N_0	units	Production volume
q_s	-	Standstill factor
q_Q	-	Rejection rate

TABLE II: Material costs

Part	Dimensions (mm)	Base cost (€/ kg)
M250-35A Sheet	0.35	1.3
M330-50A	0.5	1.15
Sintered NdFeB magnet	16x16x6	65
Round magnet wire, coated	0.85	4.9 + Cu
Hairpin bar, coated	6.2x5.4	5.8 + Cu

IV. RESULTS AND DISCUSSION

The production cost curves in fig. 5 show that the hairpin winding with a full stator is the highest cost solution in this study. This is driven mainly by its high copper content (13.1% of total at N_{max}), and the low material yield and productivity of the full diameter blanking tool. It also produces the highest peak and continuous torque, with a large $> 95\%$ efficiency area, as shown in fig. 7.

The truncation point of all three full stator designs in fig. 5, is due to the capacity limits of the chosen press (described in section III). Increasing the productivity is possible by moving to a higher performance press, either with a higher stroke rate, or a larger bed width which in turn would incur additional tool costs.

The discontinuities in the curves are due to the blanking tool wear, as described in section III-1. The difference in frequency of these discontinuities also illustrates the productivity increase
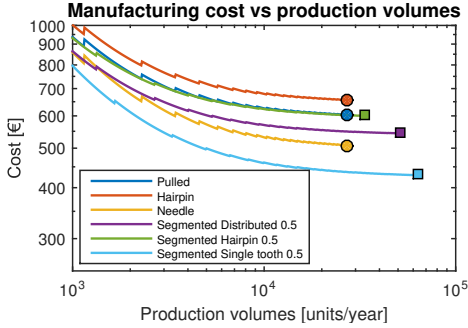
Fig. 5: Resulting costs of the six machine designs, all machines use M250-35A in the stator. The segmented machines use M330-50A as the rotor material, while the non-segmented use M250-35A.

for the segmented designs, where the single tooth design can reach the highest output.

Sensitivity analyses of individual production processes are straightforward to perform. In fig. 6 the relative cost impact of our base case, where the cycle time (t_0) is 30 seconds lead-in, 4 seconds/weld, 15 seconds lead out (total $t_0 = 369\,s$), is compared to a case where the welding speed is halved per-weld time of 2 seconds.

A low throughput case with 6 seconds per individual weld is also included, the slower per weld time could reduce the thermal stress on the insulation material. The absolute cost impact at the highest output volume, is at most 1.5% of the total machine cost compared to the segmented hairpin machine in fig. 5, assuming such changes without capital investment. The productivity boundary would also be moved in cases where this process is the bottleneck.

Figure 7 presents the estimated efficiency maps for the
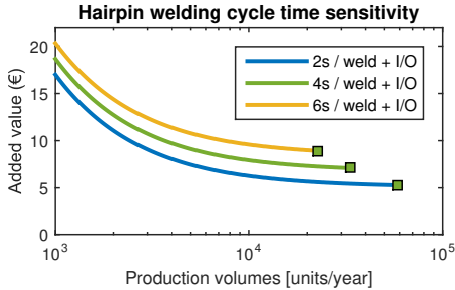
Fig. 6: Sensitivity of per connection weld time for the hairpin stator. Added value is the cost of the part after the particular process minus the cost before.

different electrical machines under consideration, accounting only for iron and copper losses (ac effects in the windings, windage, friction and magnet losses are neglected in this figure). It can be seen that for non-segmented stators, replacing the traditional pulled windings for hairpins significantly increases the fill factor, which in consequence increases the maximum produced torque and power (first and second column in fig. 7) at the expense of a more complex and costly manufacturing as previously explained. On the other hand, a six pole machine is not the best selection for a performance comparison between distributed and concentrated windings as the combination of slot/poles for the concentrated winding version is limited one (0.5 slots per pole and phase) yielding a low winding factor [26] and extremely large slots and lengthy end-turns. This further reduces the allowable electric loading as the thermal resistance between the hotspot and the cooling medium increases with the slot size. The combination of these two effects causes a significant drop in torque and power of this machine type when compared to the other two.

Moreover, segmenting the stator introduces geometrical air-gaps (assumed in this study to be 0.1 mm in accordance with standard manufacturing tolerances [27]) that reduce the flux linkage and therefore the torque/power for the same rotor and stator geometry. This can clearly be seen when comparing the first and second row of fig. 7.

Another interesting aspect is the effect of the selected winding type on the frequency dependent copper losses of the machine. Figure 8 shows how the ac resistance increases with frequency for the four different winding types considered in this study assuming no axial transposition of the strands. It can be observed, that hairpin windings are subject to a more significant increase in the ac resistance, mainly due to the fact that they are made of a single thicker copper conductor per turn. The pulled windings and concentrated windings without segmentation will have a lower increase in the ac-resistance compared to the values presented in fig. 8 as random or intentional transposition of the strands is likely to occur and feasible to implement.

TABLE III: Machine data

Parameter	P_{Nom}	T_{Nom}	$\frac{T_{2xI_{nom}}}{T_{I_{Nom}}}$	T_{cogg}	J_{rms}
Units	[kW]	[Nm]	[-]	[Nm]	[A/mm^2]
Pulled	90	139	1.92	5.2	8.5
Hairpin	125	190.5	1.88	7.1	7
Needle	49.3	67.2	2.16	3.8	5
Segmented Pulled	74.7	115.5	1.86	3.99	8.5
Segmented Hairpin	101	158.9	1.79	6.34	7
Segmented FSCW	36.7	55.5	1.92	9.2	4.3

Fig. 7: Efficiency maps for the six machine designs, including nominal and overloading torque curves.

V. CONCLUSION

This work demonstrates a viable connection between 2D electromagnetic designs and a production systems analysis, based on a decision tree. We illustrate how machine design, materials and production system decisions affect cost and performance. The methodology is capable of handling different stator and winding designs, which is beneficial both in analysis of shifting underlying costs associated with materials, as well as in finding process bottlenecks that may incur large additional investment costs.

Moreover, if an existing production line is to be retooled, to produce a new electrical machine design, the limitations of the existing production equipment can be included in the design process of the EM, in order to maximize the utilization of the equipment and minimize the resulting manufacturing cost. This is exemplified in the present study with the limits imposed by the press and blanking tool productivity.

Additionally, the feasibility and manufacturing implications of different winding technologies have been discussed, showing the importance of maintaining flexibility in decision making, and how keeping a large set of solutions throughout a design process is highly relevant.

The machine selected as the base for this study, does not favor a concentrated winding solution, as it has a relatively low number of poles and low winding factor. However, an independently optimized machine using concentrated windings can offer a comparable (and some times even superior) performance as an optimized design with distributed windings as shown in the literature. In this context, the results from this study, point out that if a similar performance can be achieved at the same volumes, the manufacturing cost of the concentrated

winding machine can be expected to be significantly lower, compared to the distributed winding counterpart.
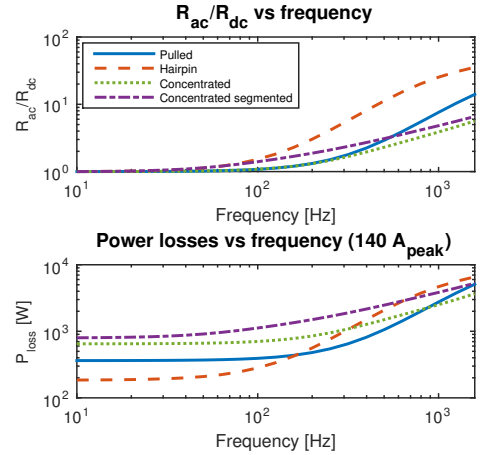
Fig. 8: Relative AC/DC losses for the four winding types (top) and power losses at 140 A_{peak} (bottom) over frequency.

REFERENCES

[1] A. Kampker, C. Deutskens, K. Kreiskther, and C. Reinders, "Selection of transformable production technologies as a reaction on a varying

demand of electric traction motors," in *2014 4th International Electric Drives Production Conference (EDPC)*, Sept 2014, pp. 1–6.

[2] A. Kampker, C. Deutskens, K. Kreiskther, M. K. Bning, and M. Kuhn, "Return on engineering: Design to cost for electric engine production," in *2015 5th International Electric Drives Production Conference (EDPC)*, Sept 2015, pp. 1–6.

[3] C. Du-Bar, T. Thiringer, S. Lundmark, and M. Alatalo, "An electric machine design procedure that includes multiple cost scenarios," in *2016 18th European Conference on Power Electronics and Applications (EPE'16 ECCE Europe)*, Sept 2016, pp. 1–9.

[4] J. Goss, D. Staton, R. Wrobel, and P. Mellor, "Brushless ac interior-permanent magnet motor design: Comparison of slot/pole combinations and distributed vs. concentrated windings," in *2013 IEEE Energy Conversion Congress and Exposition*, Sept 2013, pp. 1213–1219.

[5] J. K. Tangudu and T. M. Jahns, "Comparison of interior pm machines with concentrated and distributed stator windings for traction applications," in *2011 IEEE Vehicle Power and Propulsion Conference*, Sept 2011, pp. 1–8.

[6] A. Schoppa, J. Schneider, and J.-O. Roth, "Influence of the cutting process on the magnetic properties of non-oriented electrical steels," *Journal of Magnetism and Magnetic Materials*, vol. 215216, pp. 100 – 102, 2000. [Online]. Available: http://www.sciencedirect.com/science/article/pii/S0304885300000779

[7] R. Andersson and S. Hall, "Evaluation of a temperature model for an interior permanent magnet synchronous machine for parallel hybrid electric heavy vehicles," in *2016 International Symposium on Power Electronics, Electrical Drives, Automation and Motion (SPEEDAM)*, June 2016, pp. 419–424.

[8] R. Andersson, "Electric traction machine design for heavy hybrid vehicles," Lic. Thesis, Lund University, Lund, Sweden, 2015.

[9] A. M. EL-Refaie, "Fractional-slot concentrated-windings synchronous permanent magnet machines: Opportunities and challenges," *IEEE Transactions on Industrial Electronics*, vol. 57, no. 1, pp. 107–121, Jan 2010.

[10] P. Fyhr, M. Andersson, and J. E. Ståhl, "A modular framework for evaluation of electrical machine production costs," in *2013 3rd International Electric Drives Production Conference (EDPC)*, Oct 2013, pp. 1–5.

[11] P. Fyhr, J. E. Ståhl, and M. Andersson, "Statistical interfaces for production of a permanent magnet based rotor," in *2014 4th International Electric Drives Production Conference (EDPC)*, Sept 2014, pp. 1–6.

[12] T. Lyman, H. E. Boyer, and E. A. Durand, *Metals Handbook, vol. 4 Forming*, 8th ed. American Society for metals, 1969.

[13] B. D. Lubachevsky, R. L. Graham, and F. H. Stillinger, "Patterns and structures in disk packings," *Periodica Mathematica Hungarica*, vol. 34, no. 1-2, pp. 123–142, 1997.

[14] A. Kraemer, J. Stoll, D. Blickle, G. Lanza, and B. Boeker, "Analysis of wear behavior of stamping tools in the production of electrical steel sheets," in *2015 5th International Electric Drives Production Conference (EDPC)*, Sept 2015, pp. 1–7.

[15] S. V. Laakso, A. Vnnen, S. Bossuyt, and A. Arkkio, "Dull punch line is not a joke worn cutting edge causes higher iron losses in electrical steel piercing," *Robotics and Computer-Integrated Manufacturing*, 2017.

[16] H. Dehmani, C. Brugger, T. Palin-Luc, C. Mareau, and S. Koechlin, "Experimental study of the impact of punching operations on the high cycle fatigue strength of fesi thin sheets," *International Journal of Fatigue*, vol. 82, Part 3, pp. 721 – 729, 2016. [Online]. Available: http://www.sciencedirect.com/science/article/pii/S0142112315003230

[17] M. Tietz, F. Herget, G. von Pfingsten, S. Steentjes, K. Telger, and K. Hameyer, "Effects and advantages of high-strength non grain oriented (ngo) electrical steel for traction drives," in *2013 3rd International Electric Drives Production Conference (EDPC)*, Oct 2013, pp. 1–6.

[18] E. Lamprecht, M. Hmme, and T. Albrecht, "Investigations of eddy current losses in laminated cores due to the impact of various stacking processes," in *2012 2nd International Electric Drives Production Conference (EDPC)*, Oct 2012, pp. 1–8.

[19] A. Krings, S. Nategh, O. Wallmark, and J. Soulard, "Influence of the welding process on the performance of slotless pm motors with sife and nife stator laminations," *IEEE Transactions on Industry Applications*, vol. 50, no. 1, pp. 296–306, Jan 2014.

[20] J. Stoll, B. Kemper, and G. Lanza, "Throughput analysis and simulation-based improvement of baked varnish stacking for automotive electric drives," in *2014 4th International Electric Drives Production Conference (EDPC)*, Sept 2014, pp. 1–6.

[21] B. Hofmann, M. Masuch, P. Kmmeth, J. Franke, P. Frey, and M. Merklein, "In-line strategies and methods to reduce balancing efforts within rotor production for electric drives," in *2016 6th International Electric Drives Production Conference (EDPC)*, Nov 2016, pp. 27–31.

[22] J. W. Jiang, B. Bilgin, Y. Yang, A. Sathyan, H. Dadkhah, and A. Emadi, "Rotor skew pattern design and optimisation for cogging torque reduction," *IET Electrical Systems in Transportation*, vol. 6, no. 2, pp. 126–135, 2016.

[23] P. Herrmann, P. Stenzel, U. Vgele, and C. Endisch, "Optimization algorithms for maximizing the slot filling factor of technically feasible slot geometries and winding layouts," in *2016 6th International Electric Drives Production Conference (EDPC)*, Nov 2016, pp. 149–155.

[24] H. Akita, Y. Nakahara, N. Miyake, and T. Oikawa, "New core structure and manufacturing method for high efficiency of permanent magnet motors," in *38th IAS Annual Meeting on Conference Record of the Industry Applications Conference, 2003.*, vol. 1, Oct 2003, pp. 367–372 vol.1.

[25] J.-E. Ståhl, C. Andersson, and M. Jönsson, "A basic economic model for judging production development," in *Proceedings of the 1st International Swedish Production Symposium*, 2007.

[26] F. Magnussen and C. Sadarangani, "Winding factors and joule losses of permanent magnet machines with concentrated windings," in *Electric Machines and Drives Conference, 2003. IEMDC'03. IEEE International*, vol. 1, June 2003, pp. 333–339 vol.1.

[27] T. Y. Lee, M. K. Seo, Y. J. Kim, and S. Y. Jung, "Cogging torque of surface-mounted permanent magnet synchronous motor according to segmented-stator core effect," in *2016 XXII International Conference on Electrical Machines (ICEM)*, Sept 2016, pp. 200–206.

Paper V

Gabriel Domingues-Olavarría, Pontus Fyhr, Avo Reinap, Mats Andersson,
Mats Alaküla
**From Chip to Converter: a Complete Cost Model for Power
Electronics Converters**

From Chip to Converter: A Complete Cost Model for Power Electronics Converters

Gabriel Domingues-Olavarría, Pontus Fyhr, Avo Reinap, Mats Andersson, and Mats Alaküla

Abstract—**The unified knowledge on power converter design and manufacturing technology establishes a powerful tool, where the cost and topology realization can be analyzed simultaneously. This paper collects the design practice and cost estimation of various components in a power electronics converter and unites that to a choice of the assembling and manufacturing processes and resulting cost of the complete converter. The outcome of this work specifies the power converter at predefined power level and cooling condition and demonstrates the cost drivers of the complete unit depending on production volumes. As a case study, the cost of an inverter for a full electric or hybrid vehicle application is estimated and the results are compared with figures available in the literature, yielding the conclusion that the validity of such figures is highly dependent on production volumes and power levels. The essence of this paper is a set of general, reliable, and fast design models and production charts, in accordance with realistic cost estimates for the sake of system optimization and development of cost effective electric drives from small series to large volumes.**

Index Terms—**Converters, costs, design methodology, manufacturing economics, power electronics.**

I. INTRODUCTION

DUE to an increase in environmental awareness [1] and concerns regarding dependence on fossil fuels [2], the interest in power electronics converters (PEC) has increased in recent years. For example, PEC are cornerstone components in most renewable energy installations, and they play a vital role in automotive electrification. Both applications have significantly grown over the past years [3]–[5]. Additionally, they are used in industrial electric drives in order to improve efficiency. This is an especially important application, since these types of drives consume most of the electric energy produced world wide.

To date, research in power electronics has focused on the improvement of performance and reliability, the inclusion of new technologies, and the development of novel converter topologies and control strategies. However, not much attention has been given to converter cost [6], apart from studies dealing exclusively with the minimization of the material cost of the active components of the converters (i.e., transistors, diodes, inductors, etc.).

At least two approaches have been taken to accomplish this cost minimization. The first one uses a component database [7]–[10]. In these works, the cost of a specific component is expressed as a function of a limited number of representative parameters, but information about the used databases and the purchasing volumes at which the costs of the components are taken is scarce.

The second approach is to minimize a quantity that is known to be tightly related to the converter's cost. In [11], the total required semiconductor chip area for different converter topologies is compared and used to determine the cost effectiveness of a solution. It is worth noting that the semiconductor devices are one of the main cost-drivers in most converter topologies and that their chip area correlates directly with their cost. This work is further expanded in [6] where comprehensive cost models for power electronics components are presented. Figures for cooling systems and basic components such as bare dies and core materials are included, providing valuable input data to estimate the material cost of the active components in the converter. All the costs are provided for large volumes.

Although the semiconductor components constitute one of the main cost drivers when the converter is produced in large quantities, the investment required for production machines, tooling, fixtures, and test equipment drives the costs significantly at lower production volumes. Regardless of production volumes, the selection of the correct production process to suit the desired output is important in minimizing total converter cost. Moreover, the impact of low power components such as gate drivers, control, sensing, and communication devices is more pronounced in converters with low power rating.

These factors are not considered in the works cited so far. Thus, a complete cost estimation of PEC that includes the effect of production volume, converter layout, and component selection has not been presented yet. The need for this type of cost model is well established in the literature [12].

The work presented in this paper aims to include all the aforementioned aspects into a comprehensive methodology to estimate the cost of a PEC. The presented model is intended to be used within optimization loops to pinpoint sweet spots in a given solution space, as well as in combination with similar calculations for other components in the design of larger systems.

For these reasons, expedite execution is a priority and accuracy in the selection or design of components is secondary.

The goal of the model is to quickly and yet accurately estimate the cost of a possible solution in early design stages or in the study of technology transitions rather than to provide an optimized and detailed final design.

II. METHODOLOGY

In order to develop a complete understanding on the factors driving the cost of a PEC, an activity-base costing approach is adopted [13].

The first step in the cost estimation procedure is to define the basic characteristics of the converter under study. Knowing the topology of the converter is essential since it provides information on the layout and required set of components. Although several topologies can achieve the same type of energy conversion, their advantages and drawbacks have to be pondered beforehand in order to select the most beneficial topology for the application. Alternatively, an external loop can be added to the cost estimation process to optimize the selection of the topology. However, this work focuses only on estimating the cost of a predefined converter topology. In a similar manner, the operating point(s) and modulation scheme have to be specified in advance, due to the fact that they have great influence on determining the stresses over the different components. Additionally, information about the operating conditions and available cooling needs to be provided in order to ensure that the converter can operate effectively in the targeted environment and that the housing fulfills the demands of the application. Finally, the expected sales volumes are included to account for their impact on the selection of manufacturing processes and their impact on final cost of the converter.

After all the input parameters are defined, the next step consists on determining which components need to be designed and which can be selected directly from a component database. The general approach is that all the signal and control components (i.e., microcontroller, voltage and current sensors, CAN transceiver, etc.) are selected from a component database while power electronics components (i.e., power modules, inductors, transformers, dc-link capacitors, snubbers, filters, etc.) are designed and optimized to work under the operating point and predefined conditions.

Once all the components are either selected or designed, the layout is established based on the size of the components and the topology of the converter. The size of the control PCB is determined as a function of the components that must be mounted and the required connections to other components. At this point, the sizes of all the components are available and their layout is known, so the process continues with the sizing of the housing and cold plate or heat sink dimensions. Finally, the selection of manufacturing and assembly processes required for the producing of magnetic components, PCB, housing, and cooling is optimized for the targeted production volumes.

The final step involves adding the cost of manufacturing, assembly, and quality assurance to the material cost (of components) to obtain the complete manufacturing cost. An overview of the presented methodology is shown in Fig. 1. A detailed explanation of all the processes involved in the presented cost estimation procedure is provided in the upcoming sections.

III. COMPONENT MODELING AND SIZING

This section describes the sizing methodology for the design of the power electronics components.

A. Semiconductor Devices

This paper focuses on power levels ranging from some tens of kilowatt to a few hundred. In this range, the dominant enclosure for semiconductor devices is the power module. This type of packing provides a good thermal conductivity between the semiconductor device and the heatsink or cold plate, which enables higher power densities. Alternatively, to reduce costs, discrete devices packed in through-hole enclosures can be used in conjunction with PCBs in low power applications. However, the advantages of this implementation are significantly reduced when several devices need to be connected in parallel [14]. For the exposed reasons, and to allow the cost model to be valid in a wide power range, this work assumes power modules to be the package of choice for semiconductor devices.

With the package defined beforehand, the challenge is to determine the minimum size of the semiconductor device that would fulfill the necessary requirements under the specified operating conditions. In order to achieve this, a similar approach as the one presented in [11] is adopted, as illustrated in the left part of Fig. 1.

The size of the semiconductor influences the losses and thermal characteristics of the device. In order to model these effects, a database of components is created and their attributes are correlated with their die area. Interpolation is used to estimate the attributes of devices that are not among the initial set of samples but are within the size range of the semiconductors in the database. Since most datasheets do not specify the area of the semiconductor, a relationship between the nominal current and semiconductor area is extracted from bare die datasheets (see Fig. 2).

The next step consists on modeling the losses as function of the operating conditions and chip area. In line with standard procedure in the literature, only the switching and conduction losses are considered when computing the total power losses in the semiconductor device.

Equation (1) shows how the conduction losses are computed for a semiconductor device. The rms and average current (I_{rms} and I_{ave}) are given by the operating point and modulation scheme while the resistance and voltage are properties that depend on the device size and characteristics. For both IGBTs and diodes, the collector–emitter or forward resistance, respectively, depends on the voltage rating of the device and the chip area, as it can be observed in Fig. 3. On the other hand, the device voltage (forward voltage for diodes and collector–emitter voltage for IGBTs) depends primarily on its voltage rating. Additionally, other factors such as temperature have an effect in these two parameters

$$P_{condT/D} = R_{ce/f}I_{rms}^2 + V_{ce/f}I_{ave}. \qquad (1)$$
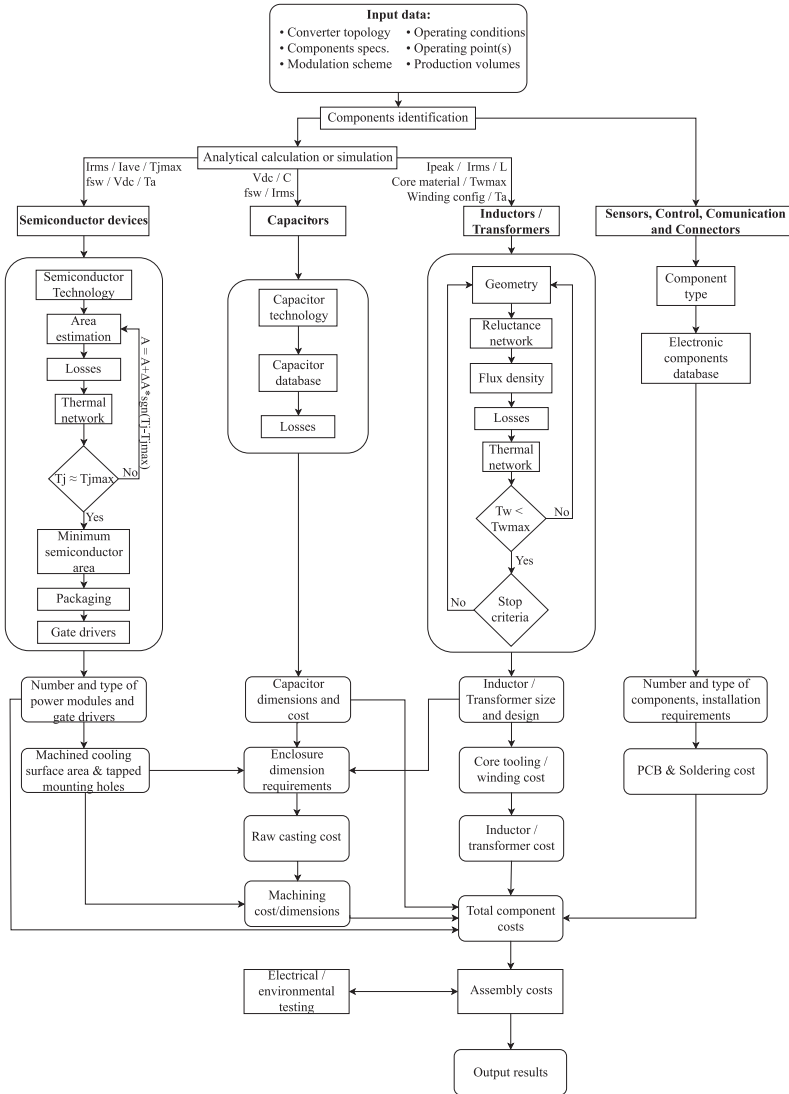
Fig. 1. Flowchart describing the design and manufacturing of the main electrical components of the converter as well as the assembly and testing of the complete converter.

The switching losses are described in (2). The switching frequency f_{sw} is a parameter defined beforehand. T and V represent the operating temperature and blocking voltage while T_{ref} and V_{ref} are the reference values at which the energy losses are defined in the datasheet. k_t and k_v are the temperature and voltage compensation constant [16]. Finally, the energy losses are represented by E_{sw}. This last parameter is described as a function of the current and chip area of the device as it can be seen in

Fig. 4 where the losses for diodes and IGBTs rated for 600 and 1200 V are depicted. Note that the data are fitted to the surfaces with a coefficient of determination greater than 0.94 in all cases

$$P_{sw} = f_{sw} E_{sw} \left(\frac{V}{V_{ref}} \right)^{k_v} \left(1 + k_t (T - T_{ref}) \right). \qquad (2)$$

It is worth mentioning that the presented energy losses are taken directly from datasheets. Hence, they are measured under

Fig. 2. Area as function of nominal current for 600/1200-V IGBTs and diodes. Data from [15].

Fig. 3. On-state resistance as function of die area for 600/1200-V IGBTs and diodes. Data from [15].

required for a given application. The iterative procedure uses as input data the technology of semiconductor, currents, blocking voltage, switching frequency, and heatsink temperature. As the first step of this process, a preliminary estimation of the area is carried out and the losses produced by a chip of that size are estimated. By use of those losses and the heatsink temperature, the junction temperature is calculated (3). If T_j is greater or lower than the predefined maximum value, the size of the chip is adjusted again and the process is repeated until the junction temperature is around the desired level. At this point, the size of the semiconductor device has been optimized for the application. This process can be observed in the semiconductor section of Fig. 1. It is important to keep in mind that this sizing procedure is based on average temperature and losses, meaning that peak temperatures can exceed the maximum allowable junction temperature. This procedure is then repeated for each semiconductor in the converter. It worth noting that the described loss estimation and sizing methodology for IGBTs and diodes is also extendable to other transistor and diode technologies or voltage ratings, as long as it is described how their chip area affects their thermal and electrical characteristics

$$T_j = T_a + R_{\text{th,js}} P_{\text{loss}}. \tag{3}$$

After the total area of all the semiconductor devices is estimated, it is possible to calculate the number and size of power modules required to accommodate all the devices. The ratio between the power module and semiconductor area is usually in the range of 4–10. Reducing this ratio increases the thermal coupling between chips but reduces the size and/or number of power modules which effectively reduces the cost. Finding an optimal value for this ratio requires an in-depth thermal analysis which would be very time consuming. Therefore, a fixed value based on experience is selected in this work. With the size and number of power modules and semiconductor devices calculated, it is possible to estimate the cost of the power module using the cost model presented in [6].

B. Power Capacitor

Among the bulkiest and most expensive components of the PEC are the power capacitors. Together with the magnetic components (i.e., transformers and inductors) they determine, to a great extent, the required dimensions of the housing.

In order to select the most appropriate capacitor for the application, several aspects need to be considered. First, the capacitor technology needs to be defined. The most common type of capacitors used in power electronics are metalized film and electrolytic. The most suited technology varies depending on the application. However, in general it can be said that electrolytic capacitors have a greater capacitance density, shorter life expectancy, and lower current handling capabilities than film capacitors.

The second aspect to consider is the voltage rating of the capacitor. It has to be selected to provide a margin with respect to the nominal operating voltage. This allows the capacitor to cope with voltage transients and extends its life expectancy. Third, the capacitor must withstand the current stresses it is subject

specific testing conditions and by use of a recommended value for the gate resistor. Terms to compensate for different operating temperatures and voltages are included in (2). However, if it is desired to use a different gate resistor it is necessary to experimentally measure the losses in the devices and add them to the database creating a new surface on top or below the ones presented in Fig. 4. In this paper, the converters are calculated assuming that the recommended gate resistor is selected.

The thermal resistance between the junction of the semiconductor device and the heatsink is mostly determined by the structure of the power module. The silicon itself only accounts for about 4% of the total thermal resistance [16]. Considering this, the thermal resistance between the junction and the heatsink of any semiconductor device is modeled solely as a function of its area, as shown in Fig. 5.

Once the loss and thermal modeling of semiconductor devices is complete, an iterative procedure is carried out in order to determine the minimum size of the semiconductor device

Fig. 4. Switching energy losses for 600-V and 1200-V IGBT's and diodes as function of chip area and current. The blue dots are the losses extracted from the datasheets and the surfaces are the fitted losses. Data from [15].
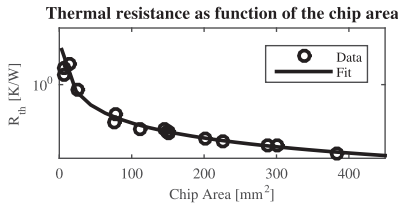
Fig. 5. Thermal resistance between the junction of the semiconductor and the heatsink as function of the chip area. Data from [15].

to without overheating or accelerating its degrading process. As a first approximation, the rated rms current at the operating frequency and temperature can be used as a guide [17], although in a final design a thorough analysis of the losses and the thermal cycling is required. Finally, it needs to be ensured that the peak and inrush currents are within the limits of the selected capacitor.

In order to demonstrate how the capacitor technology influences its characteristics, Fig. 6 presents the volume and current handling capabilities of capacitors for dc-link application as function of technology, voltage, and capacitance. It can be noticed that for a given voltage rating, both the volume and current are quite linear with the capacitance. Deviations from this approximation can be explained by the fact that capacitor manufacturers do not optimize the packaging of each capacitor independently but instead they try to reduce the number of packaging alternatives that they offered in their product range. It is worth mentioning that similar figures can be obtained for capacitors meant to be used in other applications such as snubbers and filters. However, they are not presented in this paper for the sake of brevity.

A database including capacitor technology, volume, cost, voltage rating, and current handling capabilities is created in order to determine the capacitor characteristics for a given application. Interpolation is used to estimate the values if the required capacitor is not among the set of samples used to construct the

database. This approach is feasible in reality since most capacitor manufacturers offer the alternative to produce tailored capacitors as long as they utilize existing technologies and the production volumes are large enough. Once all the characteristics of the capacitor are defined, its cost can be estimated by means of the cost model presented in [6].

C. Inductors and Transformers

The procedure to design inductors and transformers is well known and vastly explained in the literature [22]–[24]. As for the previous components, this paper focuses on producing an estimation of the true size with material specifications and winding arrangement for the inductor/transformer rather than on providing a final, complete, and detailed design.

In this context, the employed sizing procedure starts with collecting the required input data. Operating conditions and frequency, available cooling, current waveforms and transformation ratio or inductance are among the essential parameters required to determine the size and eventually the cost of the specific inductor/transformer.

The winding configuration is defined beforehand by the designer, who has to ponder the benefits and drawbacks of one configuration respect to the others in the application under consideration. For example, the main benefit of round wires is their lower cost compared to alternative solutions. On the other hand, Edge and foil winding provide a high fill factor, while at the same time relieving some of the current penetration issues at high frequencies that may increase the losses in round conductors. Finally, litz wires are an interesting alternative to further reduce the ac losses in the winding at the expense of a higher cost and lower fill factor. If the designer wishes to optimize the winding selection, an external loop can be added to the design of the magnetic component in order to test different winding configurations.

By intention, the core size is not discretized by standard sizes according to the manufacturers' databases. Therefore, it is
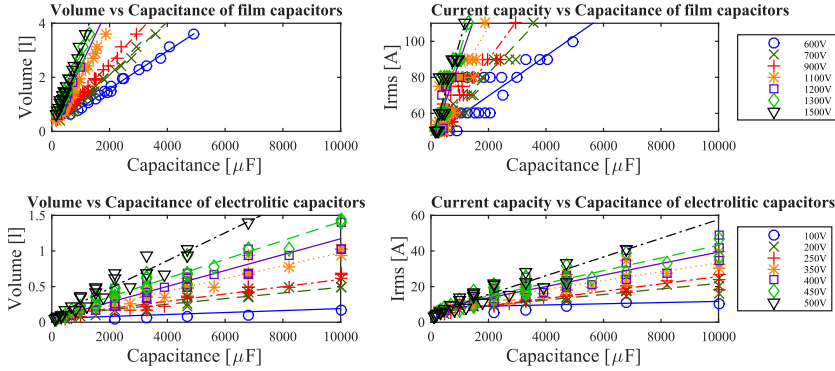
Fig. 6. DC-link capacitors characteristics [18]–[21].

assumed that the core dimensions can be freely varied. The core consists of either pressed and sintered iron powder of different kinds, or stacked electrical steel sheets of various thicknesses and grades. Reluctance networks are used to calculate the air gap(s) length (if applicable), the operating flux densities, and to define possible winding arrangements that allow us to achieve the desired inductance/transformation ratio.

Thermal networks are used to ensure that the temperature in the hot spot of the proposed inductor/transformer is below the maximum allowable limits. To accurately calculate the copper losses, the 2-D analytic approach presented in [25]–[27] is taken, which allows us to include the effect of fringing flux from the air gap, proximity, and skin effect. On the other hand, the core losses are calculated using the modified Steinmetz equation (MSE) [28].

The use of thermal and reluctance networks is preferred over finite element analysis due to fast execution and sufficiently high accuracy. However, it is worth noting that additional steps need to be performed prior to the production of a final design. For example, the stray inductance and capacitance need to be calculated, the estimated losses can be compared with results from finite element simulations (see Fig. 7 where the analytic outcome of loss estimation is compared to FEA), the manufacturability of the proposed winding solution needs to be verified, etc.

The size of these components is determined as follows: first, a large set of core geometries is proposed. Each one of the proposed cores in then evaluated to see if it fulfils the requirements of the application; the number of turns, airgap length (if applicable), and operating flux densities are calculated. Once this is done, the copper and core losses are calculated and it is verified that the hot spot temperature is below the maximum allowable temperature for the selected winding class. From the initial set of proposed core geometries, a subset of feasible cores is found. The final step is to select one geometry from this subset of feasible cores according to a criterion predefined by the designer. This criterion can be highest efficiency, lowest weight, or minimum cost.
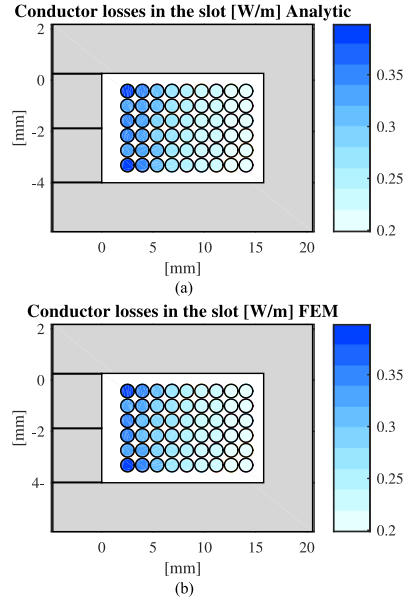
Fig. 7. Comparison between the copper losses calculated analytically and by use of FEM. Each conductor carries a triangular wave current with a duty cycle of 25%, an average value of 3.3 A, a peak of 4 A, and a frequency of 10 kHz. The maximum discrepancy in the calculations occurs close to the airgap where the analytic method overestimates the losses up to 10% with respect to the losses obtained by FEM. The average error in the winding is below 4.5%. (a) Analytic calculation of the copper losses in each conductor. (b) FEM calculation of the copper losses in each conductor.

D. Housing

Depending on the level of protection required by the application [29], two different types of housings are included in this work: cast and folded sheet metal. The first type is preferred in applications where the converter needs to be completely isolated
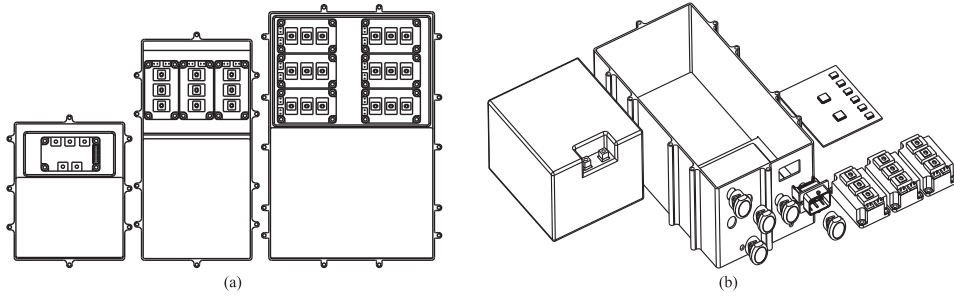
Fig. 8.   Generic housings and enclosures arrangements. (a) Enclosure layouts for a two-level inverter at various power levels. (b) A generic cast housing together with power modules, dc-link capacitor and control PCB.

from the environment it is operating in (e.g., electric vehicle, outdoor PV, etc.). The second type of housing offers a lower cost but can only be used in applications with lower isolation requirements (e.g., indoors industrial installation, home appliances, etc.).

For air cooled converters, an extruded aluminum heatsink is used. The area of the heatsink is determined by the area of the bottom plate of the housing. The height is set so that the thermal resistance of the heatsink combined with the calculated losses yield to the desired heatsink temperature [30]. The airflow is assumed to be constant at all sizes and the cost of the fan is not included in the estimation. On the other hand, for liquid cooled converters the cooling channels are cast under the main housing and a lid with a rubber seal is used to avoid coolant leakage. The cost of the pump and heat exchanger are not included in the estimation.

The size of either type of housing is mainly governed by the size of the capacitors, amount of power modules, and magnetic components (inductors, transformers). The design is scalable in length, width, and height in order to accommodate components, as well as increasing the surface area for cooling, see Section IV-C and Fig. 8(a), (b). For example, a converter layout, similar to those shown in Fig. 8(a), is chosen from a list of predefined layouts, depending on the number and size of power modules and magnetic components required by the converter. This layout, including thermal expansion padding and internal clearance for connectors, determines the part of the enclosure length as well as the width available for the capacitor bank. The height of the capacitor bank is set to a fixed value in order to provide space above the power modules for the bus-bars and control PCB. The capacitor bank length is then scaled to the requirements described in Section III-B. A fixed wall thickness as well as mounting points and lids are added to give the final converter dimensions.

E. Control Unit

The control unit consists of a PCB, populated with gate drivers, one or several microcontrollers (if redundancy is needed), a communication controller (Ethernet for industrial

TABLE I
COST MODEL PARAMETERS

Parameter	Unit	Description
k_i	€	Unit cost
K_A	€	Annuity cost of tool investment
K_B	€	Working material cost
K_{CP}	€	Running costs during production
K_{CS}	€	Running costs during downtime
K_D	€	Wage costs
n_{pA}	–	n batches until maintenance
t_0	min	Cycle time
N_0	units	Production volume
q_s	–	Standstill factor
q_Q	–	Rejection rate

applications, CAN for automotive), connectors as well as a number of discrete components (e.g., capacitors, diodes, resistances, etc.) needed by the drivers and controllers. The placement of the components in the PCB is dictated by a set of predefined rules. For the case presented in Section VI, the number of gate drivers and connectors required by the amount of power modules, as determined in Section III-A, gives the control board width, the level of redundancy, connectors, controllers, and padding for routing and power dissipation give the length.

IV. MANUFACTURING

As the cost-model described in this work handles converters of different topologies as well as voltage and current levels, a scalable generic layout is chosen in order to include the variations in the materials used, processing time, and assembly. The sizing of the power components governs these processes in a multitude of ways, as illustrated in Fig. 1. A representation of how the power module layout and dc-link capacitor size affects the converter enclosure, for a two-level inverter is shown in Fig. 8(a).

Each of the processes involved in the production of the converter is modeled using (4) [31], [32], the parameters of which are listed in Table I. Each of these inputs are specific to the

TABLE II
PROCESS INPUT DATA FOR INCLUDED PROCESSES

	Investment cost (€)	Cycle time (s)	Personnel (n)	Yield (%)
Sand cast	1500–2000	60–300	2-3	92–96
Die cast	10 000–50 000	20–120	1–2	98–99
Machining	30 000-50 000	120–1800	1	99
PCB mfg.	2000–4000	90–180	1–2	99
PCB solder	8000–15000	30–120	1–2	98–99
Bus bar	6000–12000	90–240	1	98
Electrical asm.	20 000–35 000	180–420	1	95–98
Final QA	30 000-100 000	45–225	1	98
Spool winding	150 000-300 000	60–250	1	98
Edge winding	100 000-200 000	180–420	1	98
Foil winding	100 000-200 000	100–300	1	98

current production-process denoted by i. When a sequence of processes are performed, the value added is included as cost of material K_B in the subsequent process, see (5). Input data for various processes are listed in Table II. All investments are considered to be annuitized over 5 years

$$k_i(N_0) = \frac{K_A}{N_0}\left[\frac{1}{n_{pA}}\right] + K_B\left[\frac{1}{1-q_{Qi}}\right]$$

$$+ K_{CP}\left[\frac{t_{0i}}{1-q_{Qi}}\right] + K_{CS}\left[\frac{t_{0i}q_{si}}{(1-q_{Qi})(1-q_{si})}\right]$$

$$+ K_D\left[\frac{t_{0i}q_{si}}{(1-q_{Qi})(1-q_{si})}\right] \tag{4}$$

$$K_{Bi}(N_0) = k_{i-1}(N_0). \tag{5}$$

A. PCB

The bare PCBs are printed with solder paste, SMD component population is performed with pick and place, finally reflow soldering completes the boards. The gate and sensor connections to the power-modules are manually assembled ribbon cables to connectors on the control board.

B. Power Connection

The power components are connected via shaped (edge bending, sheet forming, and stamping) copper bus bars. Its dimensions are sized to match the requirements placed by the physical layout of the power-modules, connectors, and capacitor, power module termination size and current requirements for the given power-output.

C. Casting

The casting must encapsulate the converter components, providing both environmental sealing, electromagnetic-interference (EMI) shielding and cooling of primarily the power-modules and the dc-link capacitor, as well as inductors/transformers where applicable. In this work, an aluminum casing with a water-jacket cooled fin structure is used, this can be produced using a combination of casting and machining.

The casting methods included in this work are sand casting and die casting. Die casting requires less machining in order to achieve the desired surface tolerances for sealing and power module cooling. Both processes assume access to a foundry, and the investment made is only considering the tooling specific to the parts produced for the converter.

The lid is assumed to use the same part for both the top and bottom part of the casing, thus doubling the output of the lid tool.

Many previous works have implemented the selection of appropriate casting processes for geometries of varying size, complexity, and production volumes [33].

It is worth noting that the cycle-times of both casting processes vary with the size and surface area of the casting to be produced, see Table II. This in turn is governed by the layout of the power components, as shown in Fig. 8(b). The generated generic layouts could be further optimized to increase power density. However, such optimization should be performed in final the design of a specific converter.

D. Machining

The machining requirements on the cast parts that are used in the casing consist of face milling surfaces that require tighter tolerances than the as-cast state. In the production cost calculations in this work, these are defined as the surfaces where the power modules are mounted for both sand and die-cast parts, as well as the sealing surfaces for the lids in the sand cast parts. In addition to face milling, drilling and tapping operations are needed for parts that are mounted with screws, such as the power modules, lids, inductors, and capacitors. End milling of ports for power and signal connectors and water jacket fittings is also required.

Machining cycle times t_0 are based on a cutting speed of 2000 m/min for milling with a feed of 2000 mm/min [34]. Drilling is performed with a cutting speed of 150 m/min and a feed of 0.16 mm/rev [35].

Die cast parts are assumed to be machined in one setup, using face milling in two passes to achieve sufficient tolerances for heat transfer from the power modules with normal thermal interface materials. Sand cast parts are machined in two setups, as the sealing surfaces against the lids also need to be machined.

E. Metal Folding

An unfolded metal sheet is cut by a flexible process, such as laser cutting, which can reach speeds of up to 10 m/min. At very high production volumes, this may be replaced with a fixed tooling process, such as blanking. After cutting, the sheet is folded in an edge-press, deburred at critical locations and coated.

F. Magnetic Components

Winding of the magnetic components can be performed by spool winding, edge winding, or foil winding. When spool

winding is employed, the desired amount of parallel strands, of the desired thickness, are wound onto an injection moulded bobbin. The connectors are crimped after winding. The cycle times depend on the selected winding. Round conductors present lower cycle times which further reduces the cost of this winding configuration (approx. 0.5s/turn). Edge, foil, and litz winding usually present higher cycle times (approx. 5 s/turn for edge winding and litz wire, 2 s/turn for foil winding), see Table II.

The flux conducting core material of the magnetic components consists of either stamped and bonded electric steel sheet, or powder-based sintered cores. For steel sheets, the relatively simple geometry allows inexpensive cutting tools, though the tool costs increases with the surface area of the cut geometry. Sintered materials are limited in size by the volume of the sintered material and the press available in preparation of the green body. After assembly of the cores and windings, all magnetic components are potted.

G. Quality Assurance

After assembly, each converter is subjected to one to three quality assurance inspections, the first one for the electrical circuits and control, which is applicable to all converters. The second one is only applicable where water cooling is employed, and consists on a cooling circuit leak test. The third inspection applies to converters which are classified as sealed to some degree (i.e., IP 6X), where the ingress protection from splashed water and/or submersion protection is tested.

V. MODEL LIMITATIONS AND ASSUMPTIONS

A. Assumptions

In order to simplify the process of estimating the cost of a PEC, several assumptions are necessary:
1) the gate resistance used for driving the transistors is the same as the one used for providing the losses in the datasheets;
2) the semiconductors devices are sized so their average operating temperature is below a maximum limit;
3) custom power modules can be purchased and set up costs are included;
4) capacitors can be selected from a continuous range of capacitance/voltage values;
5) the geometry of a powder core can be selected arbitrarily;
6) the manufacturing is carried out in Europe;
7) the cost of workshop space is not accounted for;
8) the cost of bulk materials is fixed;
9) shipping and handling costs are not included.

B. Purchased Parts

A number of components included in the model are considered to be purchased from external suppliers, as their design is not specific for the application and they are produced at large scale. These include:
1) capacitors, resistors and diodes;

2) fully assembled PCB(s);
3) extruded aluminum heatsinks;
4) gate drivers and sensors;
5) microcontrollers and transcievers;
6) connectors;
7) custom made power modules.

C. Processes Carried Out In-House

A list of the processes assumed to be done in-house is:
1) machine or fold the components of the housing;
2) stamp the laminations and wind the coils for the magnetic components;
3) potting the capacitor bank, inductors, and transformers;
4) bus-bar shaping;
5) assembly;
6) electrical and environmental sealing testing.

D. Overheads and Profits

Overhead costs and profit margins depend to a great extent on the specific characteristics of the company that manufactures the equipment and the type of deal they reach with the customer. For these reasons, the presented cost estimation focuses only on determining the manufacturing cost.

VI. EXAMPLE OF APPLICATION AND DISCUSSION

In this section, the presented cost model is used to estimate the cost of a PEC for a hybrid or full electric vehicle. This application represents an interesting case of study since it is highly sensitive to cost variations and some cost projections are available. For example, in [36] is reported that by 2015 a reasonable figure for an automotive PEC is 8 $/kW.

The selected converter topology is a three-phase two-level voltage source converter and the modulation scheme is SV-PWM. The converter is assumed to be liquid cooled with a cold plate temperature of 80 °C. Due to the harsh environment that the converter is expected to operate in, an IP67 ingress protection level is selected.

For the sake of brevity, the sensitivity analysis is only carried out based on production volumes, rated power, and dc-link voltage level. The switching frequency remains the same for all converters at 10 kHz and the semiconductor devices are Si Diode and field stop IGBT4. Film self-healing capacitors are used in the dc-link.

Fig. 9 shows the estimated manufacturing cost of PEC rated for different powers and voltages under varying yearly production volumes. The first thing that can be noticed is that, for high voltage converters, the rated voltage has an impact in the cost. This can be explained by looking into the way that the two main components of the converter interact to the changes in the voltage/current combinations. Semiconductor devices normally lose current handling capabilities and increase their cost for the same die area at higher voltages, but simultaneously, as the voltage increases the current demands in the converter are reduced due to the fact that the power is maintained constant.
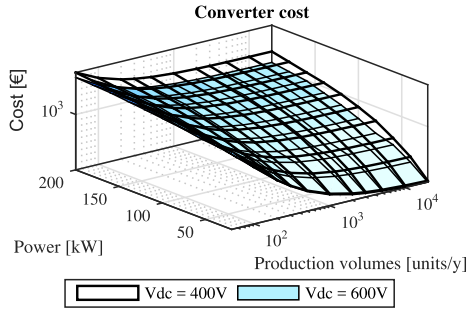
Fig. 9.   Manufacturing cost of three-phase automotive converter for EV/HEV application.

Fig. 11.   Resulting cost breakdown over production volume. For a two-level 100-kW 600-V automotive inverter.

Fig. 10.   Manufacturing cost per kW of three-phase automotive inverter for EV/HEV application.
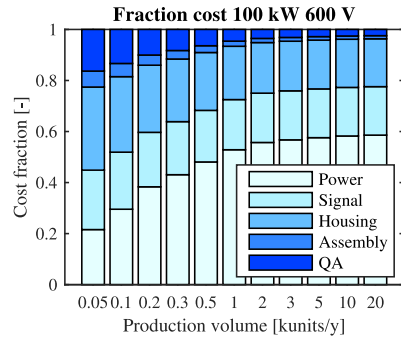
Fig. 12.   Cost fractions of total over production volumes. For a two-level 100-kW 600-V automotive inverter.

This yields to a slight increase in the cost of semiconductors for converters of lower voltages. On the other hand, the capacitor volume and current handling capabilities increase together with the voltage ratings but the capacitance requirement drops due to a drop in the current through the dc-link capacitor, reducing the final cost of the dc-link capacitor for converters of higher voltages.

The second aspect that is important to observe in Fig. 9 is that, at low production volumes, the impact of the rated power in the cost is low. The reason for this phenomenon is that at low production volumes, most of the cost of the converter is related to covering the investments in production machines, tooling, fixtures, and test equipment and the cost of the converters components only represents a small fraction of the total cost. However, with an increase in the production volumes, the investment costs are distributed among a larger number of units and the cost of an individual converter drops significantly. This drop on the production cost also increases the cost difference between converters of different power levels.

A commonly used figure of merit for automotive PEC is their cost per kilowatt. Fig. 10 presents the cost per kilowatt for the same converters presented in Fig. 9 under the same

voltage, power, and production volumes scenarios. It can be noticed that the cost per kilowatt drops together with increased rated power of the converter. the main reason for this behavior is that some of the converter's costs do not scale with power (i.e., control unit, transceivers, sensors) meaning that they have a greater impact in the total cost of lower power converters. Therefore, the use of constant figures of cost per kW, as it is usually done in the literature, can yield to misleading results. For this reason, the use of more accurate cost models, like the one presented in this work, is encouraged. Alternatively, if high level of detail in the cost estimation is not required, a linear cost function with a term that does not depend on the power can provide a better approximation than figures of cost per kilowatt.

A breakdown of costs incurred in each production step for the 100-kW converter is shown in Euro in Fig. 11 and in relative cost in Fig. 12. Both figures show that the power components (switching, capacitor and bus-bars) make up less than one-third of the costs at low production volumes, but

over two-thirds at a higher production output. This is due to the high investment levels required for tooling, production, and qualification equipment, which is distributed over each unit produced, with some refurbishment and service of the equipment over its lifetime. On the other hand, the purchased parts, such as power-modules, capacitors, connectors, etc., do not have the same scaling relationship with production volume. The signal & components cost lumps the finished control PCB, including transceivers, gate drivers, internal and external connectors.

Housing includes the finished milled casting and lid, with correct mating surfaces for power modules and tapped holes for screw mounts. Assembly contains the additional costs for assembling the parts into the housing, completing the circuits, and mounting connectors.

Quality control contains one to three steps depending on the type of housing, circuit testing, and case sealing, both for the water jacket and ingress protection, where applicable.

VII. Conclusion

A methodology for a complete cost estimation of PEC is presented and the sizing, selection, and manufacture of the different components are explained. This model provides a complete view of all the aspects affecting the cost of the converter from design decisions to selection of manufacturing process and expected production volumes. The aforementioned aspects make the presented work a useful tool that allows the designer to evaluate the cost effectiveness of different converter designs in various production systems, given an estimate of sales volume.

Due to the modular nature of the proposed framework, it is possible to modify the sizing procedures in order to include a higher level of detail if computational times are not critical or if the number of converters that are being studied is reduced. This flexibility allows the designer to perform both a preliminary screening over a wide range of possible solutions and a detailed optimization of a selected design.

The modular nature also allows the selection of manufacturing processes and automation levels to suit the desired production volumes of both individual components and finished converters, as well as the possibility to compare designs suited for different environments.

The presented model is used to estimate the cost of inverters for automotive applications. It is shown how some important factors such as power, production volumes, rated voltage, etc. affect the final cost of the converter. Additionally, it is worth noting that the predicted cost per kW is similar to figures available in the literature at high power and large production volumes and that it differs significantly in the opposite case. Therefore, when performing optimization of a full electric or hybrid vehicle, reported figures of €/kW must be handled with care and adjustments to account for power and expected production volumes must be made. For this reason, the use of more accurate cost models, like the one presented in this work, is encouraged.

Appendix

The data presented in Figs. 9 and 10 are summarized in Tables III and IV.

TABLE III
Cost of a 600-V Three-Phase Two-Level Voltage Source Converter for EV/HEV Application

Power-Units	100	1000	5000	10 000	20 000
20 kW	1023	296	232	224	220
40 kW	1120	393	328	320	316
60 kW	1228	501	436	428	424
80 kW	1290	563	498	490	486
100 kW	1409	682	617	609	605
120 kW	1537	810	745	737	733
140 kW	1655	928	863	855	851
160 kW	1790	1063	998	990	986
180 kW	1862	1135	1071	1063	1059
200 kW	1939	1212	1148	1140	1136

TABLE IV
Cost of a 400-V Three-Phase Two-Level Voltage Source Converter for EV/HEV Application

Power-Units	100	1000	5000	10 000	20 000
20 kW	1032	305	240	232	228
40 kW	1169	442	378	369	365
60 kW	1313	586	521	513	509
80 kW	1483	756	691	683	679
100 kW	1633	906	841	833	829
120 kW	1787	1060	996	988	984
140 kW	1926	1199	1135	1127	1123
160 kW	2046	1319	1255	1247	1243
180 kW	2186	1459	1394	1386	1382
200 kW	2337	1610	1545	1537	1533

References

[1] United Nation Framework for Climate Change (UNFCC), "Adoption of the paris agreement." Paris, France, 2015. [Online]. Available: http://unfccc.int/resource/docs/2015/cop21/eng/l09r01.pdf

[2] C. Miller, "3.02–energy resources and policy: Vulnerability of energy resources and resource availability—Fossil fuels (oil, coal, natural gas, oil shale)," *Climate Vulnerability*, 2013, pp. 37–51. [Online]. Available: http://www.sciencedirect.com/science/article/pii/B978012384703400304X

[3] Global Wind Energy Council (GWEC), "Global wind statistics 2014," Brussels, Belgium, 2015. [Online]. Available: http://www.gwec.net/wp-content/uploads/2015/02/GWEC_GlobalWindStats2014_FINAL_10.2.2015.pdf, Accessed on: Jan. 2016.

[4] Solar Power Europe, "Global market outlook for solar power/2015-2019," Brussels, Belgium, 2015. [Online]. Available: http://helapco.gr/pdf/Global_Market_Outlook_2015_-2019_lr_v23.pdf, Accessed on: Jun. 2016.

[5] A. T. de Almeida, F. J. T. E. Ferreira, and A. Q. Duarte, "Technical and economical considerations on super high-efficiency three-phase motors," *IEEE Trans. Ind. Appl.*, vol. 50, no. 2, pp. 1274–1285, Mar. 2014.

[6] R. Burkart and J. Kolar, "Component cost models for multi-objective optimizations of switched-mode power converters," in *Proc. Energy Convers. Congr. Expo.*, Sep. 2013, pp. 2139–2146.

[7] S. Busquets-monge *et al.*, "Power converter design optimization," *IEEE Ind. Appl. Mag.*, vol. 10, no. 1, pp. 32–38, Jan. 2004.

[8] S. Busquets-Monge *et al.*, "Design optimization of a boost power factor correction converter using genetic algorithms," in *Proc. 17th Annu. IEEE Appl. Power Electron. Conf. Expo.*, 2002, vol. 2, pp. 1177–1182.

[9] S. Busquets-Monge *et al.*, "Design of a boost power factor correction converter using optimization techniques," *IEEE Trans. Power Electron.*, vol. 19, no. 6, pp. 1388–1396, Nov. 2004.

[10] A. Kulkarni and A. Bazzi, "A building-block approach to efficiency and cost models of power electronic systems," in *Proc. 29th Annu. IEEE Appl. Power Electron. Conf. Expo.*, Mar. 2014, pp. 2727–2734.

[11] T. Friedli and J. Kolar, "A semiconductor area based assessment of ac motor drive converter topologies," in *Proc. 24th Annu. IEEE Appl. Power Electron. Conf. Expo.*, Feb. 2009, pp. 336–342.

[12] J. W. Kolar, J. Biela, S. Waffler, T. Friedli, and U. Badstuebner, "Performance trends and limitations of power electronic systems," in *Proc. 6th Int. Conf. Integrated Power Electron. Syst.*, Mar. 2010, pp. 1–20.

[13] A. Niazi, J. S. Dai, S. Balabani, and L. Seneviratne, "Product cost estimation: Technique classification and methodology review," *J. Manuf. Sci. Eng.*, vol. 128, no. 2, pp. 563–575, 2006.

[14] D. O. Neacsu, *Switching Power Converters: Medium and High Power*. Boca Raton, FL, USA: CRC Press, 2013.

[15] "Infineon IGBT datasheets," [Online]. Available: http://www.infineon.com, Accessed on: Jan. 2016.

[16] A. Wintrich, U. Nicolai, W. Tursky, and T. Reimann, "Application manual power semiconductors," ISLE, 2011.

[17] Electronicon, "Capacitors for power electronics application notes selection guide," Gera, Germany, 2013, [Online]. Available: http://www.electronicon.com/fileadmin/inhalte/pdfs/downloadbereich/Katalog/neue_Kataloge_2011/application_notes.pdf, Accessed on: Dec. 2015.

[18] "Metallized polypropylene (pp)—capacitors in cylindrical case," [Online]. Available: http://www.wima.com/EN/WIMA_DC_Link_MKP_6.pdf, Accessed on: Jan. 2016.

[19] "Screw terminal aluminum electrolytic capacitors," [Online]. Available: http://www.kemet.com/Lists/ProductCatalog/Attachments/389/KEM_A4031_ALS 30_31.pdf, Accessed on: Jan. 2016.

[20] "Screw terminal aluminum electrolytic capacitors," [Online]. Available: https://en.tdk.eu/inf/20/30/db/aec_2013/B44020_B44030.pdf, Accessed on: Jan. 2016.

[21] "Film capacitors," [Online]. Available: https://en.tdk.eu/inf/20/50/ds/B2562_.pdf, Accessed on: Jan. 2016.

[22] N. Mohan and T. M. Undeland, *Power Electronics: Converters, Applications, and Design*. New York, NY, USA: Wiley, 2007.

[23] C. W. T. McLyman, *Transformer and Inductor Design Handbook*. Boca Raton, FL, USA: CRC Press, 2011.

[24] E. L. Barrios, A. Urtasun, A. Ursua, L. Marroyo, and P. Sanchis, "Optimal dc gapped inductor design including high-frequency effects," in *Proc. 41st Annu. Conf. IEEE Ind. Electron. Soc.*, Nov. 2015, pp. 003 928–003 933.

[25] J. Mhlethaler, J. W. Kolar, and A. Ecklebe, "Loss modeling of inductive components employed in power electronic systems," in *Proc. 2011 IEEE 8th Int. Conf. Power Electron. Conf.*, May 2011, pp. 945–952.

[26] J. Hu and C. R. Sullivan, "Optimization of shapes for round-wire high-frequency gapped-inductor windings," in *Proc. 33rd IAS Annu. Meeting Ind. Appl. Conf.*, Oct. 1998, vol. 2, pp. 907–912.

[27] W. Chen, X. Huang, and J. Zheng, "Improved winding loss theoretical calculation of magnetic component with air-gap," in *Proc. 7th Int. Power Electron. Motion Control Conf.*, Jun. 2012, vol. 1, pp. 471–475.

[28] J. Reinert, A. Brockmeyer, and R. De Doncker, "Calculation of losses in ferro- and ferrimagnetic materials based on the modified steinmetz equation," *IEEE Trans. Ind. Appl.*, vol. 37, no. 4, pp. 1055–1061, Jul. 2001.

[29] *Degrees of Protection Provided by Enclosures*, Indian Standard 60529,1989.

[30] U. Drofenik, G. Laimer, and J. W. Kolar, "Theoretical converter power density limits for forced convection cooling," in *Proc. Int. Conf. Power Electron., Intell. Motion, Power Quality*, 2005, pp. 608–619.

[31] J.-E. Ståhl *et al.*, *Metal Cutting Theories and Models*. Fagersta, Sweden: Division of Production and Materials Engineering and Seco Tools, 2012.

[32] M. Jönsson, "Cost-conscious manufacturing models and methods for analyzing present and future performance from a cost perspective," Ph.D. dissertation, Lund University, Lund, Sweden, 2012. [Online]. Available: https://lup.lub.lu.se/search/publication/030ee6a6-0edb-490c-afbd-2fe7f6 81e330

[33] S. Darwish and A. El-Tamimi, "The selection of the casting process using an expert system," *Comput. Ind.*, vol. 30, no. 2, pp. 77–86, 1996.

[34] H. Kishawy, M. Dumitrescu, E.-G. Ng, and M. Elbestawi, "Effect of coolant strategy on tool performance, chip morphology and surface quality during high-speed machining of {A356} aluminum alloy," *Int. J. Mach. Tools Manuf.*, vol. 45, no. 2, pp. 219–227, 2005.

[35] M. Nouari, G. List, F. Girot, and D. Coupard, "Experimental analysis and optimisation of tool wear in dry machining of aluminium alloys," *Wear*, vol. 255, no. 712, pp. 1359–1368, 2003.

[36] C. L. Whaling, "Technology roadmap analysis 2013: Assessing automotive technology R&D relevant to doe power electronics cost targets," Status Report Presentation, 2013.

Gabriel Domingues-Olavarría was born in Venezuela in 1989. He received the M.Sc. (*summa cum laude*) degree in electronic engineering from Simón Bolívar's University, Miranda, Venezuela, in 2013. He is currently working toward the Ph.D. degree in the Division of Industrial Electrical Engineering and Automation, Faculty of Engineering, Lund University, Lund, Sweden.

Pontus Fyhr was born in 1984 in Sweden. He received the M.Sc. degree in mechanical engineering from Lund University, Lund, Sweden, in 2009. He is currently working toward the Ph.D. degree at the Division of Production and Materials Engineering, Faculty of Engineering, Lund University.

Avo Reinap was born in Estonia in 1973. He received the Diploma degree in engineering and the M.Sc. degree in power engineering from Tallinn University of Technology, Tallinn, Estonia, in 1998 and 2000, respectively. He received the Ph.D. degree in technology from Lund University, Lund, Sweden, in 2005.

From 2005 to 2010, he was an Associate Professor in the Department of Electrical drives and Power Electronics, Tallinn University of Technology and from 2007 to 2011 a Postdoctoral Fellow in the Division of Industrial Electrical Engineering and Automation, Faculty of Engineering, Lund University.

Mats Andersson was born in 1961 in Sweden. He received the Graduate degree in mechanical engineering from Lund University, Lund, Sweden, in 1988 and the Ph.D. degree in metal cutting in 1993.

He is currently an Associate Professor in the Division of Production and Materials Engineering. He has specialized in process dynamics in machining operations and measuring of high-frequency cutting forces. His current research focuses on development manufacturing technologies for electric drives and on development of soft magnetic composites.

Mats Alaküla was born in 1961 in Sweden. He received the Graduate degree in electrical engineering from Chalmers University of Technology in Gothenburg, Gothenburg, Sweden, in 1986. He received the Licentiate degree from Chalmers University of Technology in 1989 and the Ph.D. degree from Lund University, Lund, Sweden, in 1993.

Since 1994, he has been a Full Professor in the Division of Industrial Electrical Engineering, Faculty of Engineering, Lund University. He is the Coordinator for the Electrical Machines and Drives area in the Swedish Hybrid Vehicles Center. At present time, he combines his academic duties with a position as a Senior Specialist in Hybrid Technology at Volvo Powertrains.

PAPER VI

Gabriel Domingues, Francisco J. Márquez-Fernández, Pontus Fyhr, Mats
Andersson, Mats Alaküla

**Optimization of Electric Powertrains Based on Scalable Cost and
Performance Models**

Optimization of Electric Powertrains Based on Scalable Cost and Performance Models

Gabriel Domingues-Olavarría* *Student Member, IEEE*, Francisco J. Márquez-Fernández *† *Member, IEEE*,
Pontus Fyhr‡, Avo Reinap*, Mats Andersson‡, Mats Alaküla*†

*Lund University	†Swedish Electromobility Centre	‡Lund University
Dept. of Biomedical Engineering	Electrical Machines and Drives	Dept. of Mechanical Engineering
Div. of Industrial Electrical Engineering	Chalmers Univ. of Technology	Div. Production and Material Engineering
and Automation, Lund, Sweden	Göteborg, Sweden	Lund, Sweden
Gabriel.Domingues@iea.lth.se	Fran.Marquez@iea.lth.se	Pontus.Fyhr@iprod.lth.se

Abstract—This work presents a methodology for modeling, designing and scaling the electromagnetic, mechanical and thermal characteristics of the main components in an electric powertrain i.e. power electronics converter, electrical machine and mechanical transmission. Additionally, a framework for estimating the cost of these components is described. This framework takes into consideration not only the material cost but also all major manufacturing steps required for the production of a component and their dependency in expected production volumes. Moreover, a procedure to optimize the design of an electric powertrain, taking advantage of the aforementioned models, is proposed. Finally, the powertrain for a passenger electric vehicle is optimized using the proposed methodology and the results are compared in terms of electrical machine topology, powertrain concepts, cost, weight, gear ratio(s) in the transmission and overloading capabilities.

Keywords - Modeling, Design methodology, Optimization methods, Electric machines, Power electronics, Vehicles, Transportation, Manufacturing economics, Costs.

I. INTRODUCTION

The optimization of an electric powertrain aims to provide a system design that is able to meet all performance and packaging requirements while minimizing e.g., the overall cost and/or energy consumption of the vehicle. Moreover, the optimization process itself must have the following characteristics: it must use components and system models with sufficient level of detail in order capture all relevant interactions between the different components; it has to provide results that can serve as a starting point for a final design; it should require a short setup time and be computationally efficient to execute in order to reduce development times and associated costs; it has to be flexible, allowing the introduction of new technologies, components, topologies or system layouts as they emerge; and finally, if cost minimization is a major objective of the optimization, then accurate cost models for the different components are needed in order to ensure that the cost trade-offs between the components are being correctly captured.

Several efforts have been devoted to addressing these challenges, mainly improving the modeling and scalability of the different components in the powertrain and proposing new optimization techniques. For example, a methodology to generate new electrical machine (EM) designs by performing dimensional and number of turns scaling of a "base machine" is presented in [1]. Similarly, a set of scaling rules for permanent magnet machines is described in [2] and used in [3] together with a loss model for a Power Electronics Converter (PEC) to perform a multi-objective optimization, aiming to reduce both the EM volume and the average losses over a driving cycle. Another approach is to consider the impact of the dimensional scaling on the parameters of the equivalent circuit of an EM as presented in [4]. These methodologies allow to quickly adjust the performance and efficiency characteristics of the EM and are therefore valuable tools in powertrain simulations and optimizations, but they tend to neglect the impact of scaling in the thermal performance of the EM.

On the other hand, efficiency maps for PECs are often used in powertrain simulations [5] as they present a good balance between accuracy and required computational time. This approach is easy to apply when specific properties of the components in the converter are known. However, if the design of the PEC is to be included within the optimization of the powertrain, a rule-based approach [6] or an approach that relates the characteristics of the components to their physical size [7] can be applied.

Moreover, investigations of the impact of the Mechanical Transmission (MT) topology on the overall efficiency of the powertrain are carried out in [8]. Usually, if the transmission is included in the powertrain optimization, the scope is limited to the selection of the correct gear ratio(s), and its cost, weight and/or size are considered by means of simple linear models [9] [10].

Finally, some attempts at integrating performance and cost models for EM, PEC and MT in the optimization of an electric powertrain are presented in [10] [11]. However, details on how the different models are constructed are scarce.

This work aims to find a balance between modeling the components with a sufficient level of detail in order to capture all the relevant interactions between the different components, and keeping the required computational time at reasonable levels thus allowing the methodology to be a valuable tool
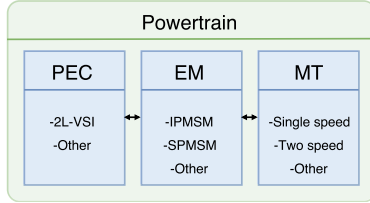
Fig. 1. Main powertrain components and variants.

in the pre-design of electric powertrains. Compared to the previously cited publications, this work:

- includes detailed cost models for all components (EM, PEC and TM), considering the same assumptions for every alternative in order to enable for as fair a comparison as possible
- uses a thermal model to adjust the current rating of the EM during the scaling process, taking into account the effect of the end-winding losses
- assesses the EM temperature evolution during drive cycle simulations by means of a dynamic thermal model, limiting the performance accordingly and taking that into account in the energy consumption calculations.

In the following sections, the modeling of the different components shown in Fig. 1 is described to prepare for a system optimization of a pure electric drivetrain for a passenger vehicle, with either a one or two speed transmission.

This article is a substantial extension of the work originally presented in [12]. Among the new contributions are: i) the possibility to optimize the number of turns of the EM's windings together with its axial length, ii) the inclusion of an optimization algorithm in order to determine the number of turns, axial length and overloading factor for the EM in conjunction with the design of the PEC and the selection of the gear ratio(s) of the MT for each EM geometry considered, iii) a new section explaining the powertrain optimization methodology as well as a iv) significant expansion on the results and discussions derived from the case study. Additionally, the section describing the cost modeling of the EM is significantly enhanced and the overall layout has been revised.

II. COMPONENTS MODELING

In this section the performance and cost models for the different powertrain components are presented.

A. Electrical machine

The EM converts electrical to mechanical energy and vice versa. It is the interface between the PEC and the MT, and for this reason, its characteristics and properties have a direct impact on all other components in the powertrain.

The selection of an optimal EM is highly dependent on the powertrain concept. For this reason, having a single electrical machine design to serve as a "base machine" can lead to biased results. Moreover, most scaling methods ensure that the
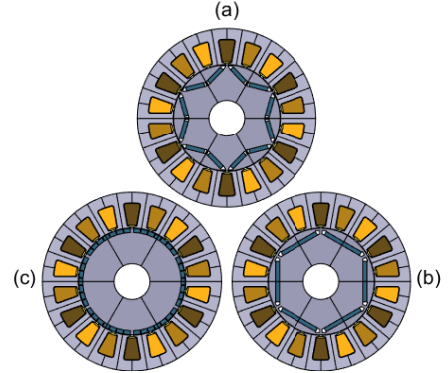
Fig. 2. Electrical machine geometries included in this work. (a) VIPMSM, (b)IPMSM and (c) SPMSM.

electromagnetic characteristics of the scaled machine remain similar to those of the "base machine" but they do not guarantee the same for the thermal loading. This might cause some scaled machines to require additional cooling or to not take full advantage of their thermal potential. As cooling and thermal management of the EMs is a great concern when designing an electric powertrain, in this work a more empirical approach is suggested for the selection and scaling of the EM. This approach is based on the generation of a database of relevant EM designs and the use of thermal lumped parameter models to adjust the nominal current loading when adjusting the number of turns and/or axially scaling the machine.

1) Database generation: The number of electrical machine topologies to be included in the machine database is decided by the designer. In this work, three different EM topologies are selected to be included in the database. The first two topologies are interior permanent magnet synchronous machines (IPMSM), one with the magnets placed in "V" and one with the magnets placed tangentially. The last geometry is a surface mounted permanent magnet synchronous machine (SPMSM) as shown in Fig. 2. However, it should be noted that other EM topologies can be included in the database using the same procedure as presented in this section.

For each EM topology, the main geometrical parameters are varied in order to map the performance implications of such changes [13]. Some of these parameters are: the outer diameter, slot width and height, number of poles and slots, ratio between rotor and stator outer diameters and rotor magnets size and position. During this process each geometry is analyzed in order to determine their thermal and electromagnetic characteristics using minimum size 2D FE models (refer to Fig. 2 for geometry/CAD models) [14]. This analysis starts with a thermal simulation in order to calculate the nominal current loading, then a series of magnetostatic simulations, including all non-linear properties of the materials, are performed at different current combinations,

TABLE I
EM DATABASE PARAMETERS

Symbol	Meaning
N_p	Number of poles
$I^*_{so,dq}(w,t)$	Single turn current
$\Psi^*_{so,dq}(w,t)$	Single turn linked flux
$R^*_{so,act}$	Single turn resistance inside the slot
$R^*_{so,end}$	Single turn resistance in the end windings
$pf^*(w,t)$	Power factor
$P^*_{cu,act}(w,t)$	Copper losses inside the slots
$P^*_{cu,end}(w,t)$	Copper losses in the end windings
$P^*_{hys,yk}(w,t)$	Hysteresis Losses in the stator yoke
$P^*_{eddy,yk}(w,t)$	Eddy current Losses in the stator yoke
$P^*_{exc,yk}(w,t)$	Excess Losses in the stator yoke
$P^*_{hys,th}(w,t)$	Hysteresis Losses in the stator tooth
$P^*_{eddy,th}(w,t)$	Eddy current Losses in the stator tooth
$P^*_{exc,th}(w,t)$	Excess Losses in the stator tooth

Fig. 3. Thermal lumped parameter model for EM.

both above and below the nominal current loading, and rotor positions in order to estimate the corresponding torque, flux linkage and loss values.

This information is then used together with a pre-defined voltage limitation to calculate the single turn current, fluxes and losses at each torque / speed combination within the operating range of the machine according to the selected control strategy (MTPA in this case). The use of a pre-defined voltage limitation does not impose a constraint in the optimization, as this can be later modified by adjusting the number of turns as explained in section II-A3. By doing this, the computational time required to scale the performance of a given machine can be reduced. For each electrical machine design, its geometry and material specifications are stored in the database, together with all the information summarized in Table I.

Each machine in this database can be axially scaled and its number of turns can be adjusted in order to meet the torque/power requirements and their efficiency and thermal characteristics can be derived using the information available in the database.

2) Thermal modeling: A dynamic lumped parameter thermal model is used both to assess the thermal performance of the machine during the scaling process and to evaluate the temperature evolution and overloading potential of the EM in drive cycle simulations. The model used in this paper, shown in Fig. 3, is based on the work presented in [15].

The proposed 8-node thermal network estimates the temperature of the end windings, the windings inside the slots, the stator iron yoke and teeth, the rotor magnets and shaft, the bearings and the outer case of the machine. Loss maps are used to supply the model with the losses corresponding to each of the nodes which are derived from the EM database as explained in II-A3.

All the heat generated in the machine is dissipated through the outer case, assuming forced convection ($600\,W/(m^2K)$)
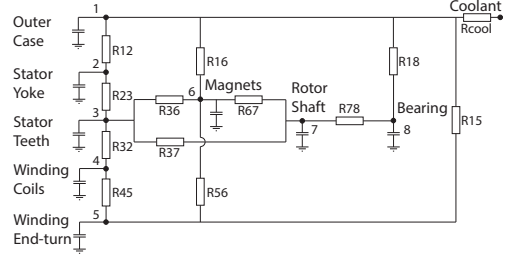
towards 80^oC coolant fluid. Other cooling concepts may be considered by changing these values. However the thermal constrain is the maximum allowed temperature in the winding and in the magnets, which are $150^\circ C$ for the windings (class F insulation assumed) and $120^\circ C$ for the magnets (H rated).

3) Scaling: The electrical machine performance and characteristics are scaled based on three factors: the change in the EM length (k_L); the desired number of turns (N_t) and the ratio between nominal and peak current (k_{ov}). Additionally, thermal and mechanical constraints are observed throughout the scaling process.

When performing axial scaling of an EM thermal aspects need to be considered. In general, when the EM is being cooled by conventional methods, a significant portion of the heat generated in the end-windings travels first into the slots and then to the stator core, from which it is dissipated by convection (natural and/or forced) in the housing or water jacket. If the cooling conditions are kept constant, when the active length of the machine is reduced its nominal current density (and therefore its performance) needs to be reduced accordingly since the heat from the end windings represents a higher fraction of the total heat transferring from the slot to the core. On the other hand, when the machine length is increased the nominal current density can be potentially increased.

Scaling the number of turns (N_t) is essential to adjust the EM voltage to the desired dc-link voltage and to change the base speed value. The main premise of the N_t scaling is that the current density inside the slot is kept constant, thus for a given dc-link voltage increasing N_t decreases the base speed and vice-versa. Additionally, since the current density is kept constant the EM torque does not change when the number of turns is adjusted, however the phase currents and therefore the PEC rating and cost increase as N_t is reduced.

The overloading factor only defines which operating points (w_n, t_n) are attainable above the nominal current loading. Its main influence is on the PEC rating and cost.

Changing all these factors directly affects the machine properties, as well as the quantities stored in the database. In order to calculate the different values for the new scaled machine for a given speed/torque operation point (w_n, t_n) the

following equations apply:

$$R_s = (k_L \, R^*_{so,act} + R^*_{so,end}) \, N_t^2 \tag{1}$$

$$I_{s,dq}(w_n, t_n) = I^*_{so,dq}(^{w_n/k_{nt}}, \, ^{t_n/k_L})/N_t \tag{2}$$

$$\Psi_{s,dq}(w_n, t_n) = \Psi^*_{so,dq}(^{w_n/k_{nt}}, \, ^{t_n/k_L}) \, N_t \tag{3}$$

$$V_d(w_n, t_n) = R_s \, I_d(^{w_n/k_{nt}}, \, ^{t_n/k_L}) \\ - w_n \, \Psi_q(^{w_n/k_{nt}}, \, ^{t_n/k_L}) \tag{4}$$

$$V_q(w_n, t_n) = R_s \, I_q(^{w_n/k_{nt}}, \, ^{t_n/k_L}) \\ + w_n \, \Psi_d(^{w_n/k_{nt}}, \, ^{t_n/k_L}) \tag{5}$$

$$V_{s,max} = max\left(\sqrt{V_d^2(w_n, t_n) + V_q^2(w_n, t_n)}\right) \tag{6}$$

$$pf(w_n, t_n) = pf^*(^{w_n/k_{nt}}, \, ^{t_n/k_L}) \tag{7}$$

$$N_{t,ideal} = m_{max} \, V_{dc} \, / \, (\sqrt{2} \, V_{dq,max}) \tag{8}$$

$$P_{cu,act}(w_n, t_n) = k_L \, P^*_{cu,act}(^{w_n/k_{nt}}, \, ^{t_n/k_L}) \tag{9}$$

$$P_{cu,end}(w_n, t_n) = k_L \, P^*_{cu,end}(^{w_n/k_{nt}}, \, ^{t_n/k_L}) \tag{10}$$

$$P_{fe,eddy}(w_n, t_n) = k_L \, k_{nt}^2 \, P^*_{fe,eddy}(^{w_n/k_{nt}}, \, ^{t_n/k_L}) \tag{11}$$

$$P_{fe,hys}(w_n, t_n) = k_L \, k_{nt} \, P^*_{fe,hys}(^{w_n/k_{nt}}, \, ^{t_n/k_L}) \tag{12}$$

$$P_{fe,exc}(w_n, t_n) = k_L \, k_{nt}^{1.5} \, P^*_{fe,exc}(^{w_n/k_{nt}}, \, ^{t_n/k_L}) \tag{13}$$

Where k_L is the ratio between desired EM length and the one used in the FE simulations (1 m). k_{nt} represents the ratio between the scaled EM's base speed and the one obtained when calculating the MTPA with the pre-defined voltage limitation. This approximates to the ratio between the ideal number of turns and the selected one ($^{N_{t,ideal}/N_t}$), and can be found with a simple line search around this point. m_{max} is the maximum desirable modulation index (0.9 in this case).

Once all these quantities have been scaled, a lumped parameter thermal model is used to determine the new nominal current density, and both the nominal and peak torque vs speed envelopes are adjusted accordingly. After that, new efficiency and loss maps are generated to be used in powertrain simulations.

It worth pointing out that the presented scaling equations are linear combinations and thus extremely fast to execute. However, for N_t different than $N_{t,ideal}$ these equations are not an exact solution to the MTPA for the scaled EM. This is due to the fact that the impact of the change in the winding resistance (R_s) in the selection of the current vector (I_{dq}) in a given operating point (w_n, t_n) is being neglected. Nonetheless, the difference between the re-calculation of the MTPA and the results obtained by the proposed set of equations is rather small within the voltage/power levels studied in this work.

4) Cost modeling: The cost of the EM is calculated by adding together the cost incurred in all the manufacturing processes required to produce the EM. The major cost drivers are the processed materials such as electromagnetic steel, coated copper wire, sintered and coated permanent magnets, electric insulation system etc. Subcomponents such as bearings and resolver, and manufacturing steps such as blanking, including tool wear, winding and assembly are also included.

The model used is a simplified version of a general production cost model, presented first in [16] and further developed in [17], [18]. The model is adapted for electric powertrain components in [19]. The cost of a part, from one process, is $k(x, N)$. This cost depends on the process itself x and the number of units N it produces. The input parameters are different for each process x. These are, investment in tooling K_A, cost of material K_B, quality loss q_Q, cost during standstill K_{CS}, cycle time t_0, standstill fraction q_s, cost during production K_{CP} and wage cost K_D. Overhead, storage and handling costs are disregarded in this implementation.

$$k(x, N) = \frac{K_A(x)}{N} + K_B(x)\left[\frac{1}{1 - q_Q}\right] + K_{CP}(x)\left[\frac{t_0(x)}{1 - q_Q}\right] + \\ K_{CS}(x)\left[\frac{t_0(x)q_s}{(1 - q_Q)(1 - q_s)}\right] + K_D(x)\left[\frac{t_0(x)}{(1 - q_Q)(1 - q_s)}\right] \tag{14}$$

As electric powertrain components are complex, and produced by many consecutive operations, the cost of parts produced in a process are counted as input materials when used in subsequent processes. The cost of material for these processes is defined as the calculated cost for that previous operation. The input materials for these operations can be sourced from one or more processes. The same applies when purchased parts, such as bearings, are assembled with produced parts. The first index $x_{1,n}$ denotes the process order, the second index n denotes the number of inputs.

$$K_B(x_{1,0}, N) = \sum_{m=0}^{n} k(x_{0,m}, N) \tag{15}$$

Combining equations 14,15 gives a recursive formulation of the final cost at process $x_{n,0}$.

$$k(x_{n,0}, N) = \frac{K_A(x_{n,0})}{N} + \sum_{m=0}^{n} k(x_{n-1,m}, N)\left[\frac{1}{1 - q_Q}\right] + \\ K_{CP}(x_{n,0})\left[\frac{t_0(x_{n,0})}{1 - q_Q}\right] + K_{CS}(x_{n,0})\left[\frac{t_0(x_{n,0})q_s}{(1 - q_Q)(1 - q_s)}\right] + \\ K_D(x_{n,0})\left[\frac{t_0(x_{n,0})}{(1 - q_Q)(1 - q_s)}\right] \tag{16}$$

In this study, the number of different EM designs considered requires the production system model to be parameterized to scale with the designs. This applies particularly to the blanking and stacking of stator and rotor laminated cores, which have very different geometries in the different machine designs. As axial scaling is performed, machines are also built from vastly different stack heights.

In order to calculate the required force F_S for blanking a particular design, the circumference l of the design, the sheet thickness t and the shear strength S_8 (400-430 MPa [20]) must be known. Equation 17 gives the required force.
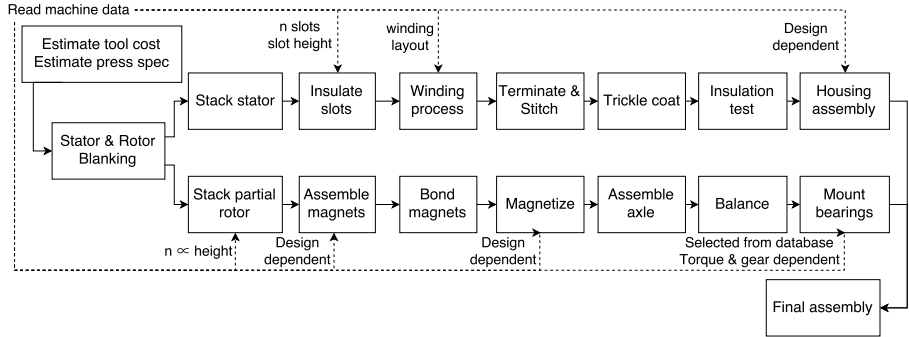
$$F_S = lt S_8 \tag{17}$$

Fig. 4. Flowchart depicting the material and information flow through the processes considered in manufacturing the electrical machines.

The press force must exceed F_S or the blanking would need to be performed in steps. A higher press force means a higher machine cost. An axially longer machine, means more cycles to produce the stator and rotor.

The cost of the die itself is estimated according to an empirical formula described in [21]. The blanking tool accumulates wear, which eventually leads to larger burr formations on the sheets, meaning that the tool must be re-ground [22], this creates a process stop and incurs a cost in refurbishing the tool.

The stator and rotor blanks are separated and bonded to stacks, the cost division here is based on mass. These parts are subject to independent operations until they can be joined inside the housing. As packaging space in the automotive industry is scarce, the EM housing can be shared with the transmission and/or PEC. The cost of shared parts is split based on the mass of the respective part.

EMs can be wound in a number of ways, some of which are analyzed in [19]. Depending on the chosen process, cycle times scale with the number of turns, poles and phases. Hairpin windings, for example, are sensitive to the number of turns and poles, but not very sensitive to stack length. Insertion winding is sensitive to the number of turns, pole pitch and stack length [23] and concentrated windings, when produced by needle winding, are affected by all previous parameters as well as multiple parallel strands. All the aforementioned winding types require distinct manufacturing processes, leading to different investment levels and resulting cycle times.

Automated assembly of surface mounted and interior permanent magnets is discussed in [24] and [25] respectively. In situ magnetization is discussed in [26] and for embedded magnets in [27]. The varying height and layout of different designs is dealt with by scaling the number of operations required to complete a stack.

The bearings used in EMs are selected to withstand the loads generated from the nominal torque figures over the first gear mesh in the transmission including axial loads due to both the helix and pressure angles. The design lifetime of the bearings is set to $L_{1h} = 5000$ [28]. This design decision could be improved by rainflow-counting over the torque values used in some drive-cycles, but for simplicity, the nominal torque is used.

Process data for the processes in Fig. 4 is indicated as ranges in Table II, in order to capture the different machine designs and the associated uncertainty. The yield figure includes material waste and quality, for well tuned processes. Operating cost includes European wage costs [29].

The use of the proposed cost model, not only provides an accurate estimation of the EM cost at different production volumes but also helps to identify the major cost drivers for a given EM design. To exemplify this point, the cost of a large set of EMs produced in high volumes (50000 u/y) is presented in Fig. 5. The resulting cost of active materials and production is depicted in the upper plot of Fig. 5 while the lower plot shows the relative distribution of these partial costs with respect to the total production cost. The most interesting aspect to take from this figure is that EMs with similar material cost can present differences in the production cost depending on the required investment in tools, ease of manufacturing, etc. This shows that comparing the EMs cost based solely on material costs, as it is common practice in the literature, can yield to inaccurate conclusions; especially when comparing different EM topologies.

B. Power Electronics Converter

When the power factor, phase current and voltage of the electrical machine are known for each torque and speed operating point the process to first determine the size, cost and finally efficiency maps of the PEC is initiated. This process includes sizing the semiconductor devices, DC-link capacitor, control unit, housing and cooling. It must be ensured that all components can operate safely in every valid operating point, for this reason the most demanding operating points for each components are used as sizing criteria. A detailed outline of the sizing process is presented in [30]. Besides the cost and physical dimensions of the converter, an interesting outcome

|	Tool investment (k€)	Cycle time (s)	Personnel (#)	Operating Cost (€/hr)	Yield (%)
Blanking	100-1000	60-300	1-2	45-120	73-75
Stacking	5-10	30-60	0-0.5	15-20	98-99.5
Slot insulation	5-10	33-87	0-0.5	20-30	99.5-100
Insertion Winding	30-40	415-775	1-2	30-40	99-99.5
Terminate & Stitch	8-13	120-180	0.5-1	20-30	99.5-100
Trickle Coat	10-15	300-450	0-0.5	15-20	-
Insulation test	5-8	30-60	1	30-45	99-99.9
Housing assembly	17.5-25	70-100	1-2	35-50	99-99.9
Magnet Insertion	10-20	240-960	0-0.5	15-25	99-99.9
Magnetization	200-500	60-110	0.5-1	15-25	99-99.9
Assemble Axle	5-15	90-150	0.5-1	15-30	99-99.9
Balance	7.5-12.5	120-240	1	25-30	99-99.9
Bearing assembly	5-12	45-75	1	25-30	99-99.9
Assembly	8-20	80-150	1-2	30-45	99-99.9
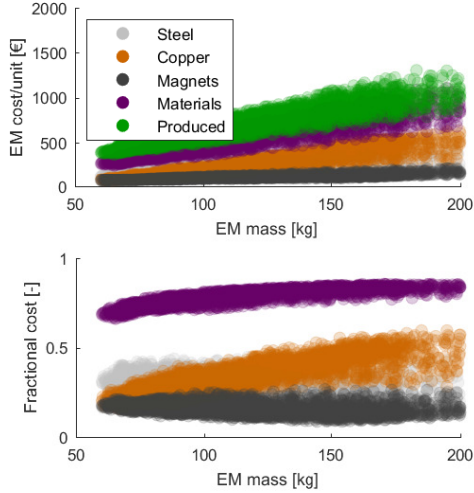
Fig. 5. The resulting cost of active materials and production vs the active material mass of the electrical machines. The upper plot is presented in absolute values while the lower one shows the relative distribution of costs respect to the production cost.

of this sizing procedure is the required chip area for each semiconductor inside the converter.

Once the chip area of each semiconductor device is known, it can be used in conjunction with the calculated power factor, phase voltage and current for each torque vs speed combination in order to compute the converter losses at each operating point. As it is common in the literature, only switching (P_{sw}) and conduction losses (P_{cond}) are considered. Equations (18)

and (19) show how the losses are computed. It can be noticed that the switching energy (E_{sw}) and the device's resistance (R_{on}) are both dependent on the chip area [31], while the currents through the device depend on the phase current and voltage, modulation strategy and power factor. In this work, sinusoidal pulse width modulation (SPWM) is the selected modulation strategy.

$$P_{sw} = f_{sw}E_{sw}(A_{chip}, I_{ph}, pf)$$
$$\left(\frac{V_{dc}}{V_{ref}}\right)^{k_v} (1 + k_t(T - T_{ref})) \tag{18}$$

$$P_{cond} = R_{on}(A_{chip})I_{rms}(V_{ph}, I_{ph}, pf)^2$$
$$+ V_{on}I_{ave}(V_{ph}, I_{ph}, pf) \tag{19}$$

C. Mechanical transmission

To determine the cost and size of the MT it is necessary to know the EM torque vs speed characteristics, the required gear ratio(s) and transmission topology. Additionally, the material used and the gear's helix and pressure angles are defined in advance in order to reduce the computational time.

The number of gear stages and the respective size of each gear are optimized in order to minimize the overall mass of the transmission while ensuring that for each gear, the bending (S_t) and contact (S_c) stresses are lower than the permissible stresses of the material (S_{at} and S_{ac} respectively), including a series of influencing factors to account for the operating conditions and nature of the load as calculated in (20)-(24) [32]–[34].

$$S_t = \frac{W_t}{F\ m\ Y_j}K_oK_vK_sK_mK_b \leq \frac{S_{at}}{S_f}\frac{Y_n}{K_tK_r} \tag{20}$$

$$S_c = C_p\sqrt{\frac{W_t}{Fd}\frac{K_oK_vK_sK_mC_f}{I}} \leq S_{ac}\frac{Z_nC_h}{S_hK_tK_r} \tag{21}$$

$$C_p = \sqrt{\frac{1}{\pi^2 (K_1 + K_2)}} \qquad (22)$$

$$K_i = \frac{1 - \nu_i^2}{\pi E_i}; \; i = 1, 2 \qquad (23)$$

$$I = \frac{cos\phi \; sin\phi}{2} \frac{m_g}{m_g + 1} \frac{F_{min}}{F} \qquad (24)$$

Where W_t is the tangential force applied on the gear tooth at the pitch diameter, F is the face width, m is the gear's module, ϕ is the pressure angle, m_g is the gear ratio in that particular mesh, ν is the Poisson's ratio, E is the Young's modulus, d is the pitch diameter and F_{min} the section of the tooth width that is in actual contact with the load. Y_j, K_o, K_v, K_s, K_m, K_b, S_f, Y_n, K_t, K_r, C_f, C_h, Z_n and S_h are the form, overloading, dynamic, size, load distribution, rim thickness, safety against bending, bending stress cycle, temperature, reliability, surface condition, hardness ratio, contact stress cycle and safety against pitting factors respectively. Values and guidelines for the selection of the aforementioned factors are available in the literature [33], [34].

Once each gear mesh is sized, the cost of the whole MT is then estimated based on data gathered from gear manufacturers as presented in [13]. In general, it can be said that the gear cost is affected by its material, size/weight, helix angle, finishing requirements and the presence or not of splines and/or dog teeth. The cost of bearings, shafts, housing, shifting mechanism (if applicable), manufacturing and assembly are included.

III. VEHICLE SIMULATION MODEL

A forward-looking vehicle simulation model (VSM) based on the work presented in [35] is used in order to estimate the energy consumption and powertrain efficiency over a given drive cycle. In this model the different components are described by look-up tables and a PI-controller is used to emulate the driver's behavior. The VSM has been adapted to include both electric and hybrid vehicles. Additionally, the thermal lumped parameter model described in section II-A2 is included in order to study the evolution of the EM temperatures over the drive cycle and to limit the overloading capabilities at any point in time accordingly.

IV. POWERTRAIN OPTIMIZATION PROCEDURE

This section outlines the integration of the previously presented cost and performance models in the optimization of an electric powertrain. An overview of the proposed optimization methodology is presented in Fig. 6.

The optimization procedure starts by clearly defining the powertrain concepts under consideration, including the transmission type, powertrain placement and number of EMs, and specifying the main performance requirements and constrains that the powertrain must fulfill. The requirements are expressed in a wheel torque - speed diagram. Among the most relevant of these are curb climbing, maximum speed at

different road gradients, acceleration times, etc. Additionally, the battery voltage, switching frequency, semiconductor technology in the PEC, available cooling and packaging constraints need to be specified in order to ensure the compatibility of the powertrain with the energy storage system, the correct sizing of the PEC and the overall feasibility of installation.

Each powertrain concept is separately optimized and then the results are compared (see the yellow loop in Fig. 6). For each of the selected powertrain concepts, an optimization loop is executed (shown in red in Fig. 6). This loop starts with the selection of an EM geometry from the database. Subsequently, the number of turns, axial length and overloading factor that result in an optimal powertrain design for the selected EM geometry are obtained inside the design optimization loop (shown in purple in Fig. 6).

The existence of both continuous (EM length and overloading factor) and discrete (number of turns) variables requires the use of an optimization algorithm able to handle mixed integer problems. In this work particle swarm optimization (PSO) is used. In order to rule out solutions that do not satisfy the requirements of the application, constraints on the total size, weight and/or required overloading time may be included. The objective function for the design optimization loop consists of a weighted combination of certain features such as cost, weight or size, normalized to the desired ranges. An estimation of the powertrain efficiency over a drive cycle may be included in the objective function, but a complete drive cycle simulation should be avoided at this stage as it would significantly increase the required computational time.

Once the optimal powertrain design for the selected EM geometry is obtained, the previously calculated efficiency maps for the EM, PEC and MT are used in a full vehicle simulation over a drive cycle to determine the actual powertrain efficiency and temperature evolution in the different sections of the EM and PEC. At this point the design optimization loop is completed for the selected EM geometry and the process is repeated for different EM geometries until the stop criterion for the concept optimization loop is met. This criterion can be, for example, when the cost of the powertrain is below certain threshold or when all EM geometries in the database have been evaluated.

After the concept optimization loop is completed for the selected powertrain concept, the process is repeated until all concepts have been optimized. This optimization approach allows to evaluate a large number of EM designs in a relatively short period of time, which provides a holistic view of the problem and can help to identify areas of interest to explore further, e.g. by generating new EMs geometries to be added in database.

V. CASE STUDY

In this section, the proposed models and methodology are used in the design and optimisation of a powertrain for a compact passenger vehicle. The 2018 Nissan Leaf specifications are used in this case study. The goal is twofold: (i) to provide an optimized powertrain concept that serves as the initial step
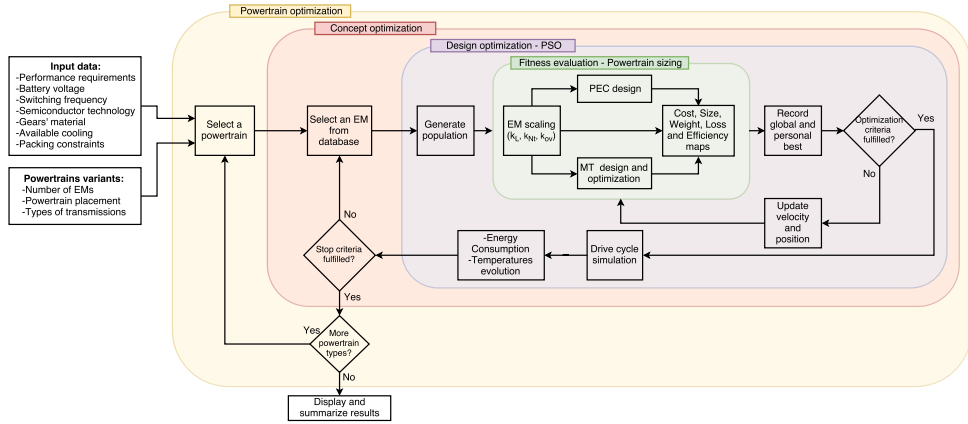
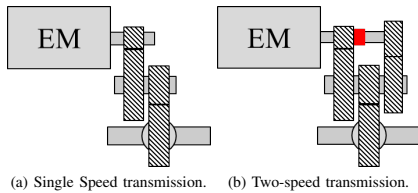Fig. 6. Proposed powertrain optimization procedure.

(a) Single Speed transmission. (b) Two-speed transmission.

Fig. 7. Considered powertrain concepts.

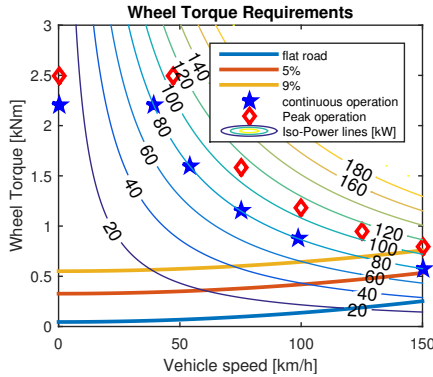| Electric vehicle specifications	
Vehicle weight	1600 kg
Top speed	150 km/h
Battery Capacity	40 kWh
Time 0-100 km/h	$\sim 9\ s$
DC-link Voltage	$400V$
Drag coefficient·Area (CdA)	$0.26 \cdot 2.5\ m^2$

Fig. 8. Performance Requirements.

for a product development, and (ii) to highlight the tradeoffs and trends between different components in alternative powertrain configurations. To do so, two powertrain configurations are considered, one with a single speed gearbox and one with a two speed gearbox (see Fig. 7). The characteristics of the

vehicle are summarized in Table III and Fig 8. Moreover, it is worth mentioning that the red diamonds and blue stars in Fig 8 represent the performance requirement vectors used as inputs in the optimization process.

For the PSO algorithm used in the design optimization loop, the initial population set consists of 75 individuals uniformly distributed through the space of search. The optimization stops when the distance between the best individual and the farthest one is below a threshold level (set to 2% of the space of search size) or when the maximum number of iterations (50 based on preliminary runs) is reached.

The tradeoffs obtained from the optimization between powertrain weight, cost, gear ratio and the nominal power needed to meet all the requirement are presented in Fig. 9. Each row in the figure corresponds to an electrical machine topology (corresponding to those shown in Fig. 2) while the columns represents alternative powertrain concepts (depicted in Fig. 7). Note that for the powertrain concept with a two-speed gearbox the lowest gear ratio (highest gear) is the one plotted in the x axis. Each colored point represents a complete powertrain design where the EM is scaled together with the gear ratio(s) of the transmission until all the demands of the application are fulfilled.
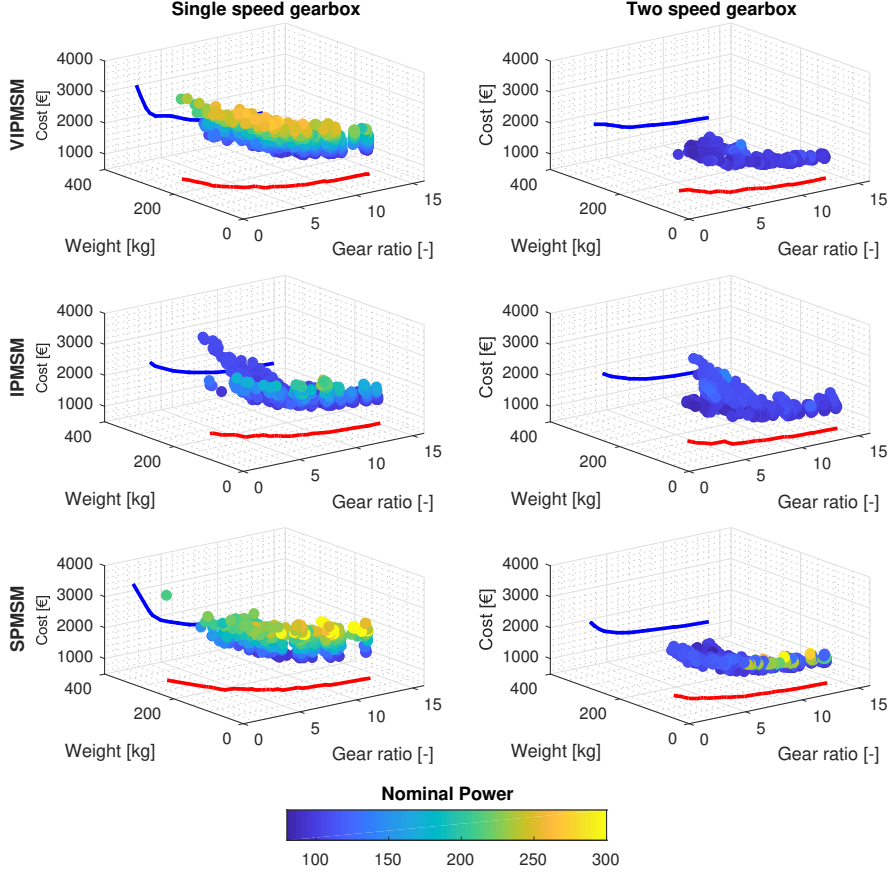
Fig. 9. Comparison between cost, weight, gear ratio and EM rated power for different powertrain concepts using three EM topologies. The blue curve is the projection of the pareto front on the Cost/Gear ratio plane. The red curve is the projection of the pareto front on the Weight/Gear ration plane.

For this study, the EM database consists of around 4000 EM designs with outer diameters varying from $170 - 340mm$. It is worth noticing that all machines in the database are evaluated in order to accurately capture as many relevant interactions between the design parameters as possible. Additionally, a pre-selection of representative designs presents a challenging task, as different EM designs have different torque vs speed characteristics, and these vary slightly when the EM is scaled. Moreover, once the database of machines is generated, evaluating all of them is a relatively quick process, and the additional gained insights outweigh the increased computational time.

Since a large number of EM designs are evaluated for each powertrain concept, it is clear that some are not well suited

for the specific application. For example, for the powertrains under consideration, machines with low CPSR need to be oversized in order to meet both the starting torque and power at maximum speed. This can be clearly seen in Fig. 9 at low gear ratios for both powertrain concepts and all EM topologies considered.

It is interesting to notice that in all cases, a slightly lower system cost can be obtained by the addition of a second speed to the transmission. This is due to the fact that the second speed helps to avoid oversizing the EM, which in turn lowers the current demands from the PEC and thus its cost.

Moreover, it can be observed that for all cases the cost and weight tend to decrease together with the gear ratio.

Nevertheless, the benefits of increasing the gear ratio become less significant above a certain level. For the designs with a single-speed gearbox, this occurs between 12-13 (see blue line projections in the left column of Fig. 9). There are several reasons for this behavior. First, both the cost and weight of the mechanical transmission increase with the gear ratio. Additionally the power density of the EMs does not increase significantly at higher speed, as no special high speed machines are included in the database. On the other hand, for those powertrains with two speeds the cost and weight flatten for ratios in the range of 9-10, where the combination of machines with slightly lower maximum speed and smaller transmissions yields to a reduction in the overall system cost.

Another interesting tradeoff that is worth mentioning is the selection of electrical machine topology. Although in this study the VIPMSM presents the highest power density of the three considered topologies, this does not translate directly into a lower system cost, as the price per kW of EM does not relate only to the power density. Material content and manufacturability determine to a great extent the cost effectiveness of a solution, as illustrated in section II-A4.

An additional factor to ponder when designing a powertrain is the optimal constant power speed range (CPSR) of the EM, as usually an increase in CPSR comes at the expense of a decrease in power density. Fig. 10 shows how the total cost of the powertrain varies as a function of the CPSR of the EM for both powertrain types. It can clearly be observed that for a single speed gearbox transmission, the optimal powertrain cost is achieved for an EM with a CPSR between 3 and 3.5; this is the interval where the EM has sufficient CPSR to achieve all performance requirements with minimum oversizing and without sacrificing too much power density. On the other hand, it can be observed that for a two speed gearbox transmission, the optimal CPSR is significantly lower (around 1.5-1.7). This is due to the fact that now the EM does not need a wide CPSR to meet all the performance requirements, as it can take advantage of the second speed in the transmission. Therefore, machines with higher power density and lower CPSR are a better fit for this powertrain concept as it is shown in Fig. 11.

VI. CONCLUSIONS AND FUTURE WORK

The simulation and optimization of an electric powertrain requires the use of models that can accurately describe the thermal, mechanical and electromagnetic behavior of the different components. The accuracy of the results is highly dependent on the level of detail put into modeling the components. On the other hand, comprehensive models tend to be computationally slow to execute, so the challenge lays on finding a balance between accuracy and computation time.

This paper describes models and methodology to determine the required size, performance, efficiency and thermal characteristics of the main components in an electric powertrain. The importance of including thermal models in the scaling of EM is discussed and a methodology to scale an EM is described. Moreover, cost models for the different components are presented. These models include the most relevant manufacturing
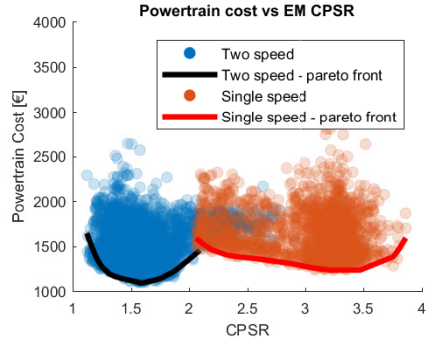
Fig. 10. Powertrain cost vs EM CPSR for the three different EM topologies.
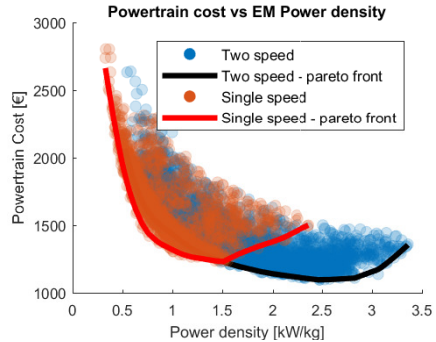
Fig. 11. Powertrain cost vs EM power density for the three different EM topologies.

steps required to produce the components as well as the cost dependency on production volumes.

Finally, an example of the application of the proposed models and methodology to the design and optimization of an electric powertrain for a passenger vehicle is presented and the main tradeoffs and trends are highlighted and discussed. Nevertheless, due to space constraints, interesting trends regarding changes in the EM geometry along the pareto front, powertrain efficiency and thermal cycling of the EM have been left outside this paper and are considered for future publications.

REFERENCES

[1] K. Zhou, A. Ivanco, Z. Filipi, and H. Hofmann, "Finite-Element-Based Computationally Efficient Scalable Electric Machine Model Suitable for Electrified Powertrain Simulation and Optimization," *IEEE Transactions on Industry Applications*, vol. 51, no. 6, pp. 4435–4445, 2015.

[2] S. Stipetic, D. Zarko, and M. Popescu, "Scaling laws for synchronous permanent magnet machines," in *2015 Tenth International Conference on Ecological Vehicles and Renewable Energies (EVER)*, March 2015, pp. 1–7.

[3] D. Zarko, M. Kovai, S. Stipeti, and D. Vuljaj, "Optimization of electric drives for traction applications," in *2017 19th International Conference on Electrical Drives and Power Electronics (EDPE)*, Oct 2017, pp. 15–32.

[4] D. Buecherl, C. Bertram, A. Thanheiser, and H. G. Herzog, "Scalability as a degree of freedom in electric drive train simulation," in *2010 IEEE Vehicle Power and Propulsion Conference*, Sept 2010, pp. 1–5.

[5] J. K. Reed, J. McFarland, J. Tangudu, E. Vinot, R. Trigui, G. Venkataramanan, S. Gupta, and T. Jahns, "Modeling power semiconductor losses in hev powertrains using si and sic devices," in *2010 IEEE Vehicle Power and Propulsion Conference*, Sept 2010, pp. 1–6.

[6] E. Grunditz, "Design and assessment of battery electric vehicle powertrain, with respect to performance, energy consumption and electric motor thermal capability," Ph.D. dissertation, Chalmers University of Technology, 2016.

[7] T. Friedli and J. W. Kolar, "A Semiconductor Area Based Assessment of AC Motor Drive Converter Topologies," *2009 Twenty-Fourth Annual IEEE Applied Power Electronics Conference and Exposition*, no. c, pp. 336–342, feb 2009. [Online]. Available: http://ieeexplore.ieee.org/lpdocs/epic03/wrapper.htm?arnumber=4802678

[8] M. G. Tehrani, J. Kelkka, J. Sopanen, A. Mikkola, and K. Kerkknen, "Transmission configuration effect on total efficiency of electric vehicle powertrain," in *2014 16th European Conference on Power Electronics and Applications*, Aug 2014, pp. 1–9.

[9] X. Wu, B. Cao, X. Li, J. Xu, and X. Ren, "Component sizing optimization of plug-in hybrid electric vehicles," *Applied Energy*, vol. 88, no. 3, pp. 799–804, 2011.

[10] P. Caillard, F. Gillon, M. Hecquet, S. A. Randi, and N. Janiaud, "An optimization methodology to pre design an electric vehicle powertrain," *2014 IEEE Vehicle Power and Propulsion Conference, VPPC 2014*, 2015.

[11] A. Schönknecht, A. Babik, and V. Rill, "Electric powertrain system design of bev and hev applying a multi objective optimization methodology," *Transportation Research Procedia*, vol. 14, pp. 3611–3620, 2016.

[12] G. Domingues, F. J. Márquez-Fernández, P. Fyhr, A. Reinap, M. Andersson, and M. Alaküla, "Scalable performance, efficiency and thermal models for electric drive components used in powertrain simulation and optimization," in *2017 IEEE Transportation Electrification Conference and Expo (ITEC)*, June 2017, pp. 644–649.

[13] G. Domingues, A. Reinap, and M. Alaküla, "Design and cost optimization of electrified automotive powertrain," in *2016 International Conference on Electrical Systems for Aircraft, Railway, Ship Propulsion and Road Vehicles International Transportation Electrification Conference (ESARS-ITEC)*, Nov 2016, pp. 1–6.

[14] G. Bramerdorfer, A. C. Zvoianu, S. Silber, E. Lughofer, and W. Amrhein, "Possibilities for speeding up the fe-based optimization of electrical machines: A case study," *IEEE Transactions on Industry Applications*, vol. 52, no. 6, pp. 4668–4677, Nov 2016.

[15] F. J. Márquez-Fernández, A. Reinap, Z. Huang, and M. Alaküla, "Dynamic evaluation of the overloading potential of a convection cooled permanent magnet synchronous motor," in *2011 IEEE International Electric Machines Drives Conference (IEMDC)*, May 2011, pp. 13–18.

[16] J.-E. Ståhl, C. Andersson, and M. Jönsson, "A basic economic model for judging production development," in *Proceedings of the 1st International Swedish Production Symposium*, 2007.

[17] J.-E. Ståhl, P. Gabrielson, C. Andersson, and M. Jönsson, "Dynamic manufacturing costs describing the dynamic behavior of downtimes

from a cost perspective," *CIRP Journal of Manufacturing Science and Technology*, vol. 5, no. 4, pp. 284–295, 2012.

[18] M. Jönsson, "Cost-conscious manufacturing models and methods for analyzing present and future performance from a cost perspective," Ph.D. dissertation, Lund University, 2012.

[19] P. Fyhr, G. Domingues, A. Reinap, M. Andersson, and M. Alaküla, "Performance and manufacturability tradeoffs of different electrical machine designs," in *2017 IEEE International Electric Machines and Drives Conference (IEMDC)*, May 2017, pp. 1–7.

[20] S. V. Laakso, A. Väänänen, S. Bossuyt, and A. Arkkio, "Dull punch line is not a joke worn cutting edge causes higher iron losses in electrical steel piercing," *Robotics and Computer-Integrated Manufacturing*, 2017.

[21] G. Boothroyd, P. Dewhurst, and W. A. Knight, *Product design for manufacture and assembly*. M. Dekker, 2002.

[22] A. Kraemer, J. Stoll, D. Blickle, G. Lanza, and B. Boeker, "Analysis of wear behavior of stamping tools in the production of electrical steel sheets," in *2015 5th International Electric Drives Production Conference (EDPC)*, Sept 2015, pp. 1–7.

[23] J. Hofmann, F. S. L. Blanc, M. Krause, F. Wirth, and J. Fleischer, "Simulation of the assembly process of the insert technique for distributed windings," in *2016 6th International Electric Drives Production Conference (EDPC)*, Nov 2016, pp. 144–148.

[24] E. Hultman, D. Salar, and M. Leijon, "Robotized surface mounting of permanent magnets," *Machines*, vol. 2, no. 4, pp. 219–232, 2014. [Online]. Available: http://www.mdpi.com/2075-1702/2/4/219

[25] E. Joseph, J. Tremel, B. Hofmann, A. Meyer, J. Franke, and S. Eschrich, "Automated magnet assembly for large pm synchronous machines with integrated permanent magnets," in *2013 3rd International Electric Drives Production Conference (EDPC)*, Oct 2013, pp. 1–6.

[26] L. Chang, T. R. Eastham, and G. E. Dawson, "In-situ magnetization of ndfeb magnets for permanent magnet machines," *IEEE Transactions on Magnetics*, vol. 27, no. 5, pp. 4355–4359, Sept 1991.

[27] H. Schilp, P. Schlag, and M. Kohnhuser, "Optimized handling of permanent magnets within the mass production of electric traction drives," in *2013 3rd International Electric Drives Production Conference (EDPC)*, Oct 2013, pp. 1–6.

[28] "Rolling bearings – Dynamic load ratings and rating life ," International Organization for Standardization, Geneva, CH, Standard, Feb. 2007.

[29] Eurostat, "Hourly labour costs," accessed: 2018-01-03. [Online]. Available: http://ec.europa.eu/eurostat/statistics-explained/index.php/Hourly_labour_costs

[30] G. Domingues-Olavarria, P. Fyhr, A. Reinap, M. Andersson, and M. Alaküla, "From chip to converter: a complete cost model for power electronics converters," *IEEE Transactions on Power Electronics*, vol. PP, no. 99, pp. 1–1, 2017.

[31] M. Schweizer, I. Lizama, T. Friedli, and J. W. Kolar, "Comparison of the chip area usage of 2-level and 3-level voltage source converter topologies," *IECON 2010 - 36th Annual Conference on IEEE Industrial Electronics Society*, pp. 391–396, nov 2010. [Online]. Available: http://ieeexplore.ieee.org/lpdocs/epic03/wrapper.htm?arnumber=5674994

[32] S. Radzevich and D. Dudley, *Handbook of Practical Gear Design*, ser. Mechanical Engineering Series. Taylor & Francis, 1994. [Online]. Available: https://books.google.se/books?id=NOqBnpN7ElIC

[33] *American Gear Manufacturers Association: Geometry Factors for Determining the Pitting Resistance and Bending Strength of Spur, Helical and Herringbone Gear Teeth*. AGMA, Apr. 1989.

[34] *American National Standard: Fundamental Rating Factors and Calculation Methods for Involute Spur and Helical Gear Teeth*. AGMA, Dec. 2004.

[35] K. Jonasson, "Control of hybrid electric vehicles with diesel engines," Ph.D. dissertation, Lund University, 2005.

Pontus Fyhr, Gabriel Domingues, Mats Andersson, Francisco J.
Márquez-Fernández, Hans Bängtsson, Mats Alaküla
**Electric Roads: Reducing the Societal Cost of Automotive
Electrification**
International Transport Electrification Conference (ITEC), Chicago Year:
2017 Pages: 773 - 778

Electric Roads: Reducing the Societal Cost of Automotive Electrification

Pontus Fyhr[†], Gabriel Domingues[*], Mats Andersson[†], Francisco J. Márquez-Fernández[*‡],
Hans Bängtsson[*], Mats Alaküla[*‡]

[†]Lund University	[*]Lund University	[‡]Swedish Electromobility Centre
Dept. of Mechanical Engineering	Dept. of Biomedical Engineering	Electrical Machines and Drives
Div. Production and Material Engineering	Div. of Industrial Electrical Engineering	Chalmers Univ. of Technology
Lund, Sweden	and Automation, Lund, Sweden	Göteborg, Sweden
pontus.fyhr@iprod.lth.se	gabriel.domingues@iea.lth.se	fran.marquez@iea.lth.se

Abstract—In this article five scenarios for fully electric road transport in Sweden are compared, looking at the total system cost for different combinations of battery systems, vehicle equipment and charging solutions, including the use of Electric Road Systems (ERS). The main objective of this work is not to provide accurate price estimations, but to help understanding the main cost drivers of transport electrification and to illustrate how the final system cost is influenced by the different parameters considered. The main conclusion obtained is that, despite the substantial initial investments required for the deployment of electric roads, a system featuring only static charging and vehicles with large size batteries results in a higher total system cost. Moreover, due to the much larger number of light duty vehicles in the fleet, the deployment of an ERS system that can be used by both long-haul and light duty vehicles is substantially more advantageous than a solution restricted only to long-haul vehicles.

I. Introduction

THE transport sector generates 48.3 % of the total CO_2 equivalent emissions in Sweden and road transport in particular, is responsible for 93% of the sector's emissions [1]. This represents a large fraction, especially when compared to Europe as a whole, where transportation emits 24.4% of total CO_2, and road transport makes up to 72.6% of the sector emissions [2]. Similarly, the U.S. transport sector contributes to 26% of the total CO_2 emissions [3].

These figures show that road transport is the single largest pollutant in Sweden, even when compared to electrical power generation and industry. The electricity mix in Sweden is exceptionally clean, with the majority of the electricity produced from hydropower, nuclear and windpower - 47%, 37% and 10.5% in 2015 respectively. For this reason, shifting road transport from conventional fossil fuels to electricity has potentially the largest impact on CO_2 emissions. However, if this shift is to be done without significantly modifying the

modes of transportation and driving patterns of the population, a balance must be reached between the type and capacity of the energy storage on board the vehicles and the availability, type and power of the infrastructure to refill such energy storage.

In this work, the societal cost of electrifying all road transport in Sweden is studied under several scenarios. For each of these, the vehicle fleet is configured depending on the infrastructure provided, while maintaining the overall system functionality. In one extreme, all the Swedish automotive fleet consists of vehicles with high battery capacity; in the other extreme a substantial investment is made in order to provide all major roads with infrastructure that allows to charge the vehicles dynamically while they are driving, thus significantly reducing the battery capacity needs.

It is worth highlighting that all proposed scenarios consider the extreme case of electrifying all road transport in Sweden. The transition from the current situation to the one proposed in the different scenarios is not the focus of this work, but rather it is assumed that in a near future all the required technologies are mature enough to be implemented. Therefore, the societal cost of electrification after that transition is completed is compared and analyzed in order to provide insights on the benefits and drawbacks of the different technologies.

This article builds up on the work initiated by Prof. Mats Alaküla and Assoc. Prof. Hans Bängtsson in 2015 [4] in a first attempt to assess the overall system cost of a fully electrified road transport in Sweden, by reviewing and updating some of the cost assumptions, and refining the cost modeling of power electronic components and electrical machines. Section II outlines the current situation of road transport in Sweden, and it describes the cost models and assumptions used in the analysis. Section III presents a short summary of different ERS technologies, highlighting their particularities. The five different scenarios considered for full-electric road transport are described in Section IV, and finally, their societal cost is analyzed in Section V, discussing the influence of the cost figures used and the assumptions made in the cost modeling process. The article finishes with a summary of the main

conclusions that can be drawn from this work.

II. METHODOLOGY

A. Vehicle fleet

Currently, Sweden has an automotive fleet of about 5.2 million registered vehicles. In this study, rather than classifying them according to the European Commission standard, the vehicles are divided according to driving patterns and weight in four different categories: 1) Light Duty, 2) City Buses, 3) Distribution Trucks, 4) Long-Haul Trucks.

The first category (Light Duty) includes all four-wheel vehicles with a gross combination weight rating (GCWR) below 3.5 tons. The majority of vehicles in the fleet (5.01 million) belong to this category. The second category is formed by buses operating in city routes (14 thousand units). The third category includes all vehicles with a GCWR between 3.5 and 16 tons (20 thousand vehicles). Finally, the fourth category is conformed by vehicles with a GCWR above 16 tons plus coaches operating in inter-city routes as their driving patterns and range requirements are closer to long-haul trucks than they are to city buses (65 thousand). Although this classification is far from perfect, and some vehicles in one class might actually be better represented in another, the bulk of vehicles is expected to have similar performance, requirements and usage patterns as the average vehicle of the class they are placed in.

The aforementioned vehicle groups consume 96% of the energy used in road transportation in Sweden. The remaining 4% is consumed by two-wheelers and construction equipment, which are left outside the scope of this study as their full electrification is more challenging hence it is expected to take longer time.

B. Cost modeling

For each of the proposed scenarios, the investments required for electrification both in terms of on-board components and infrastructure are accounted for using cost estimates from real system implementations or prototypes, projections and academic publications.

Battery price is one of the most sensitive parameters in the analysis. In this study, only Li-ion batteries are considered. According to [5], a figure between 150 and $300 \, €/kWh$ at pack-level could be expected by 2030. However, and due to the latest news from the main electric vehicle and battery manufacturers, a conservative estimation of $100 \, €/kWh$ is used in this study [6].

Besides the battery, there are a number of electric powertrain components on-board the vehicles that need to be taken into account as well. The different power electronic converters needed -namely the inverter(s) driving the traction machine(s), a DC/DC converter to supply the low voltage auxiliary loads, and potentially one additional converter to transfer power between the external energy supply and the vehicle - are sized specifically for each type of vehicle, and their cost is estimated taking into account not only the material cost, but also the manufacturing process, time, and volumes [7]. As a reference, the manufacturing cost of a $100 \, kW$ inverter

for a LDV is estimated in $605 \, €$ for a production volume of $20000 \, units/year$ (giving a specific cost of $\approx 6 \, €/kW$). Since the objective of this study is to estimate the societal cost of each potential scenario, it is worth noticing that profit and overhead costs are not taken into account.

Analogously, the electric traction machines are also dimensioned specifically for each case, starting from an initial database with over 4000 scalable machine geometries. Their estimated cost also takes into account material cost plus all direct manufacturing expenses mentioned before [8].

The cost estimation of the connection device towards the external power supply, whether it is a conventional plug, an automated conductive pick-up (in overhead applications also called pantograph) or a wireless power receiver, as well as the cost of the off-board infrastructure are based on the figures already reported from existing pilot test sites, electrical components catalogs and price assessments performed by the main Swedish utility companies for grid connection points [9], [10].

In order to calculate the annualized societal cost, different amortization times are considered for the on-board components: 10 years; and the infrastructure: 15 years.

In addition to the previous costs, the savings due to the removal of the conventional powertrain and fuel tank, and the difference between the cost of the electricity consumed by the electric vehicles in the alternative scenarios and the cost of the fossil fuel currently being consumed by the automotive fleet need to be included in the calculations [11]. In this study, the price of fuel is based on current prices in Sweden, corresponding to $1.4 \, €/litre$; the price of electricity is also based on current Swedish figures, resulting in $0.09 \, €/kWh$. Since the study considers societal cost, 20% VAT is deduced from both fuel and electricity prices. It is worth noticing that, in contrast to the battery price assumption, no predictions are made regarding the future price of fossil fuel and electricity. Nevertheless, current trends suggest that the electricity price is likely to decrease with increased penetration of solar and wind power in the market, while oil price evolution and therefore fossil fuel price remains uncertain. In light of this, the assumed electricity cost can be seen as slightly pessimistic.

III. ELECTRIC ROAD TECHNOLOGIES

In this section, a brief description of the different ERS technologies that are currently being developed is presented. In a first classification, ERS technologies are divided into three categories: overhead conductive, road-bound conductive and road-bound inductive. Each of these categories, in turn, can be implemented in different ways when it comes to system details such as voltage and current levels, the physical location of the primary energy supply or the type and shape of the connection device.

1) Overhead conductive: The overhead conductive electric road is based on a similar technology to the one used for trams and trolley buses with supply lines mounted at a significant height (more than 5 meter) over the ground, requiring the vehicles that are powered by it to be equipped with an
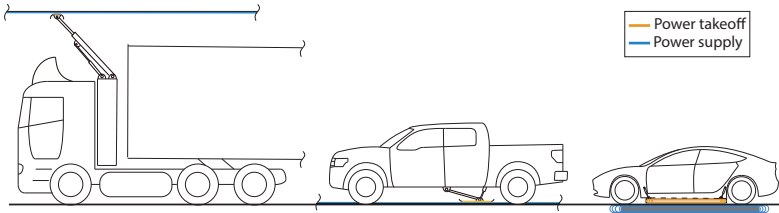
Fig. 1. A long-haul truck, powered by overhead electric road. Followed by a pick-up truck, powered by conductive road bound. Followed by a car, powered by inductive road bound

extensible power take off system of a pantograph type. Only vehicles with a significant height, such as long-haul trucks and buses are able to connect to it, as illustrated in Fig. 1. Since the wires are unlikely to be reached, long stretches ($> 1\,km$) can remain energized while vehicles are traveling under them.

In the overhead ERS currently undergoing trial in a public road in Sandviken, Sweden [9], a 650 - 750 DC voltage supply on two contact lines feeds the vehicle via slip contact between the $Cu + Mg$ alloyed supply line and a graphite power take-off mounted on a pantograph. The pantograph has two degrees of freedom (length and angle), in order to remain connected to the supply over deviations within the lane ($\approx \pm 1m$). Although this technology has been extensively proven in trolley buses and partially also in trams and railway applications, new challenges emerge from the higher speeds and presumably higher utilization expected in the ERS.

2) Road-bound conductive: Several solutions for conductive road-bound ERS are being currently developed [12]; some of them evolve from existing tram technology [13] while some others are specifically designed to be used on normal roads [10], [14].

The concept described in [10] resembles a slot-car, with two parallel slots cut into the existing asphalt where the necessary conductive rails are located. This system could work with either AC or DC, energizing sections of $50\,m$ at a time.

In [13], accumulated experience from tram and railway systems leads to a similar approach, although in this case the two power carrying conductors are placed flush with the road surface. This system uses $750\,V$ DC to energize $22\,m$ long sections at a time under a moving vehicle.

Yet another approach is to mount the supply on top of the road, enclosed in a single track ($400\,mm$ wide, $50\,mm$ height at the top) of alternating positive and negative strips [14]. This solution also uses $750\,V$ DC, and it features much shorter segments ($1\,m$ with $150\,mm$ insulation in between segments) since any moving vehicle needs to cover at least two of them at any time.

Figure 2 illustrates the three solutions described for road-bound conductive ERS, all of which are being tested in Sweden currently.

All of the suggested ground level conductive solutions are energized only when the vehicle is positioned above them. This means that there is a need for switches to activate only short

segments of the supply (in the range $1 - 50\,m$) as compared to the overhead supply with live distances in the km range as described in section III-1. The road-bound conductive system is illustrated as mounted to the pick-up truck in Fig. 1.

Fig. 2. Illustration of different road-bound conductive ERS solutions.

3) Road-bound inductive: Inductive power transfer can be seen in practice as an air-gapped transformer, where the power is transferred through the magnetic coupling of the primary coil, in this case included in the road bound supply side, and the secondary coil in the vehicle side pick-up. There are several solutions already in the market based on inductive power transfer for static charging, however, the fact that the vehicle is moving during the process (dynamic charging mode), introduces new challenges especially related to keeping a near constant air-gap and designing an even flux distribution in order to avoid a sharp efficiency drop when lane-keeping is not perfect. An early demonstration of this technology in Public Transport was made with the OLEV system by KAIST, South Korea [15]. Further modeling and lab scale tests are described in [16]. The inductive road bound ERS, much like the conductive one, is only energized when a vehicle is approaching or on top of it. The system is illustrated on the car in Fig. 1.

IV. SCENARIOS

1) Large batteries: In this scenario all vehicles are equipped with batteries large enough to rely mainly on night charging and occasional fast charging for LDVs. LDVs feature $240\,km$ range, resulting in a $72\,kWh$ battery, which can be charged at fast-charging stations ($120\,kW$). A $6\,kW$ on-board AC-charger is also included for night home charging. City buses and distribution trucks use night charging (at $70\,kW$ and $30\,kW$ respectively) and their batteries provide sufficient range to get through their daily routes ($500\,kWh$ and $340\,kWh$

respectively). On the other hand, it is unrealistic to equip long-haul trucks with sufficient battery capacity to provide the required driving range without sacrificing payload. In order to circumvent this limitation, the driving time (and range) of long-haul trucks is reduced to two hours ($200\,km$ corresponding to $480\,kWh$), and the tractor is swapped for a fully charged one at stop locations, allowing the driver and his cargo to carry on. This change introduces a need for an increase in the number of tractors compared to today, apart from much more complex logistics.

2) Overhead electric road: This scenario introduces overhead ERS for long-haul trucks and coaches on interstate and national roads (amounting up to $15600\,km$), much like the ones currently undergoing testing on public roads in Sweden [9]. This significantly reduces the battery capacity required for long-haul trucks and inter-city coaches (now down to $120\,kWh$ charged at $200\,kW$ from the ERS). A smaller fast charger of $110\,kW$ is also installed on-board for those cases in which the $50\,km$ battery range is not enough. However this technology can not be used by the other vehicle types, therefore LDVs, city buses and distribution trucks remain on large installed battery capacities as in scenario 1.

3) Overhead & opportunity fast-charging: Compared to the previous scenario, in this case city buses receive end-stop DC fast-charging (at $180\,kW$ from an off-board charger) in order to reduce their installed battery capacity by a factor of five, down to $90\,kWh$. Distribution trucks also have the opportunity to charge at major loading/unloading docks, with a $43\,kW$ on-board AC charger, reducing their battery size to almost one third ($120\,kWh$) compared to scenario 2. Overhead lines for long-haul trucks and inter-city coaches and DC fast-charging for LDVs are kept.

4) Road bound inductive: In this scenario, road bound inductive dynamic charging [17][15] is introduced, allowing all vehicles traveling on interstate and national roads (amounting up to $15600\,km$ in Sweden) to charge while moving. This can be done at the expense of a significantly higher infrastructure cost when compared to overhead solutions. On the other hand, it reduces the required battery range to $50\,km$ for both LDVs and long-haul vehicles (trucks and inter-city coaches), resulting in $15\,kWh$ and $120\,kWh$ installed battery capacity respectively. City buses and distribution trucks remain on opportunity charging at the end-stops and loading/unloading docks as in the previous scenario.

5) Road bound conductive: In the last scenario, the inductive electric road technology from scenario 4 is replaced by a conductive solution. This yields to potential cost reductions in the dynamic charging infrastructure, as the component and deployment costs are expected to be lower for the conductive solution. The rest of the fleet and infrastructure remains unaltered with respect to scenario 4.

A summary of the vehicle and infrastructure configurations for the different scenarios is presented in Table I. The charging modes considered for each scenario are illustrated in Fig. 3
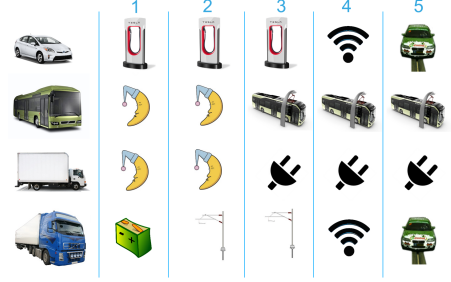

Fig. 3. Summary of the charging modes for the different scenarios.

V. RESULTS AND DISCUSSION

With all the previous assumptions, the societal cost of electrifying all road transport in Sweden is calculated for the five different scenarios described in Section IV. The results are presented as bar charts in Fig. 4, in which the positive segments represent the additional components and infrastructure annualized costs for each solution, and the negative ones reflect the annualized savings corresponding to the removal of the conventional powertrain and the difference in energy cost between fossil-fuels and electricity, which remain the same for all scenarios.
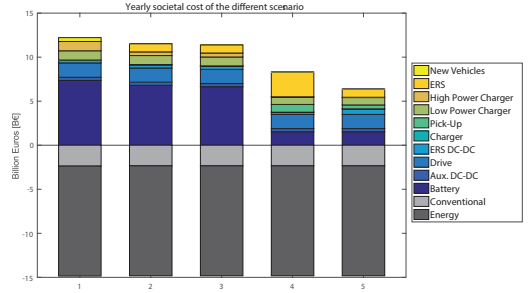

Fig. 4. Societal cost of electrifying all road transport in Sweden for 5 different scenarios.

Several deductions can be made when looking at the results presented in Fig. 4. First and foremost, with the remarkably low cost per kWh assumed for the Li-ion batteries, all presented scenarios result in a net saving for society, with the positive part of each chart (costs) being smaller than the negative one (savings). A sensitivity analysis showing the net societal cost/saving when varying the assumed battery cost (see Fig. 5, left) shows that scenarios 1 to 3, in which the battery represents a significant fraction of the total cost, are quite sensitive to the assumed €/kWh figure, and the cost of transport electrification becomes higher than the expected savings for battery costs over $135\,€/kWh$ for scenario 1 and $150\,€/kWh$ for scenarios 2 and 3. Conversely, scenarios

TABLE I
VEHICLE CONFIGURATIONS

Vehicle	Scenario	Battery energy	Energy consumption	Traction power	Slow charge	Fast charge	E-road
Units	-	kWh	kWh/km	kW	kW	kW	kW
Light duty	1	72	0.2	100	6.0	120	0
	2	72	0.2	100	6.0	120	0
	3	72	0.2	100	6.0	120	0
	4	15	0.2	100	3.3	0	25
	5	15	0.2	100	3.3	0	25
City bus	1	500	1.2	150	70	0	0
	2	500	1.2	150	70	0	0
	3	90	1.2	150	6	180	0
	4	90	1.2	150	6	180	0
	5	90	1.2	150	6	180	0
Distribution truck	1	340	1.5	150	30	0	0
	2	340	1.5	150	30	0	0
	3	110	1.5	150	10	43	0
	4	110	1.5	150	10	43	0
	5	110	1.5	150	10	43	0
Long-haul	1	480	1.6	300	40	400	0
	2	120	1.6	300	10	110	200
	3	120	1.6	300	10	110	200
	3	120	1.6	300	10	110	200
	5	120	1.6	300	10	110	200

4 and 5, in which LDVs can use the ERS hence the total installed battery capacity in the system is significantly lower, are much less sensitive to the battery cost, remaining beneficial for society under the whole range considered.

In order to stress the importance of the battery cost over other assumptions also related to a system largely relying on large batteries, a sensitivity analysis is also conducted on the cost of the fast-charging station network (see Fig. 5, right). The initial assumption in scenario 1 is that, since charging time is on average approximately 5 times longer than re-fueling, in order to cope with the peak demand for example during holidays or long weekends, the number of fast-charging points is estimated to be 5 times the number of fuel pumps available in Sweden: currently 2600 major service stations, only those with a shop/restaurant considered, with an average of 8 fuel pumps in each station. This is of course a very coarse assumption that can be extensively disputed. However, when looking at the sensitivity study results in the right plot of Fig. 5 it is obvious that the impact of the fast-charging infrastructure cost is much less than that of the estimated

battery cost. It is worth noticing that the scale in the x-axis is in p.u., representing either an increase/decrease of the number of fast-charging points available, their power rating or their cost, as well as the wider range considered in this case.

When looking at the overall picture, it is clear that scenarios 4 and 5 are the most advantageous, and that this advantage relies basically in the lower total battery capacity installed, which overcomes the additional infrastructure investment for the ERS. Moreover, in the battery cost sensitivity analysis presented before it can be seen that the battery cost should become much lower than $75 €/kWh$ for the any of the first three scenarios to be comparable to scenario 5 - the one with conductive ERS. This is also partly due to the specific fleet composition in Sweden: over 5 million Light Duty Vehicles (mostly passenger cars) compared to only 65 thousand long-haul vehicles. Nonetheless, in order to understand the influence of the assumed ERS technology cost in the results, additional sensitivity analyses are run on the estimated cost of both conductive ERS technologies: overhead and road-bound. The results are presented in Fig. 6.
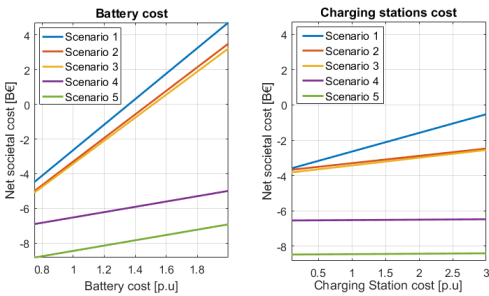

Fig. 5. Sensitivity analysis on the price of Li-ion battery packs (left) and the cost / number of fast-charging stations (right).
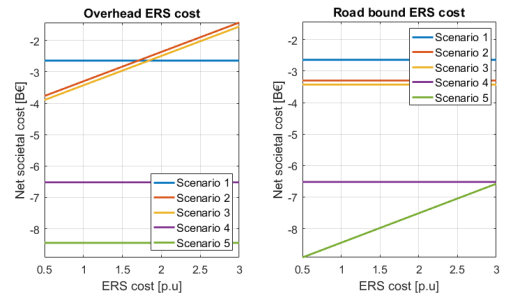

Fig. 6. Sensitivity analysis on the cost of overhead conductive (left) and road-bound conductive (right) ERS.

Looking at the left plot, the electrification of long-haul vehicles with overhead conductive ERS (scenarios 2 and 3) proves to be beneficial compared to the large-batteries approach (scenario 1) even if the cost of the ERS infrastructure increases by 70% from the initial assumption of $1\,M€/km$. On the other hand, reducing the cost of the overhead conductive ERS still leaves a large gap between the overhead and the road-bound solutions.

The impact of the cost of the road-bound conductive ERS, initially estimated to $1\,M€/km$ (equal to the overhead conductive ERS) is analyzed in the right plot of Fig. 6. From this sensitivity analysis follows that even increasing the cost of road-bound conductive ERS 3 times, it still remains advantageous when compared to scenario 1 (large-batteries) and scenarios 2 and 3 (overhead conductive ERS).

Only conductive ERS solutions are currently under test in Sweden, therefore the cost estimate of road-bound inductive ERS is not as strongly supported in this study. However, there is a general consensus in the reviewed literature that inductive ERS systems are more expensive than conductive ERS. The assumed cost for road-bound inductive ERS is $3\,M€/km$, 3 times higher than that of its conductive counterpart.

VI. CONCLUSIONS

In this article five scenarios for full electrification of the road transport in Sweden are compared from a societal perspective, looking at the total system cost for different ERS technologies and a fully battery electric alternative. Due to the novelty and complexity of the technologies presented it is difficult to provide an accurate cost estimation, but the presented results provide insightful views into what the main cost drivers of transport electrification are, and how the final system cost is influenced by the different parameters considered.

The results obtained are largely dependent on the assumed battery cost. However, a sensitivity analysis shows that with a road-bound ERS solution, such that it can be used by most types of vehicles in the fleet (including passenger cars) the total battery capacity installed in the system is significantly reduced, and a fully-electrified system in this way becomes economically advantageous even for today's battery cost levels. An overhead ERS system restricted to large vehicles such as long-haul trucks and coaches, on the other hand, always results in a more expensive alternative, even if the cost of the overhead ERS is estimated to be half of the road-bound conductive ERS' cost. The reason for this is that the number of long-haul trucks and coaches in the Swedish fleet is two orders of magnitude lower than the number of light duty vehicles (65 thousand vs. 5 million).

REFERENCES

[1] Swedish Environmental Protection Agency, "National inventory report sweden 2016 - greenhouse gas emission inventories 1990-2014," 2016. [Online]. Available: https://www.naturvardsverket.se/

[2] European Environment Agency, *Towards clean and smart mobility Transport and environment in Europe*. [Online]. Available: http://www.eea.europa.eu/publications/signals-2016

[3] L. Hockstad and M. Weitz, "Inventory of u.s. greenhouse gas emissions and sinks: 19902014," U.S Environmental Protection Agency, Tech. Rep., 2016.

[4] M. Alaküla and H. Bängtson, "Cost analysis of electric land transport," Swedish Electromobility Centre, Tech. Rep., 2015. [Online]. Available: http://hybridfordonscentrum.se/wp-content/uploads/2016/01/T2_11-Cost-Analysis-of-Electric-Drive-System_IV_Final-report.pdf

[5] B. Nykvist and M. Nilsson, "Rapidly falling costs of battery packs for electric vehicles," *Nature Climate Change*, vol. 5, pp. 329–33, April 2015.

[6] McKinsey and Company, "Electrifying insights: How automakers can drive electrified vehicles and profitability," 2017. [Online]. Available: http://www.mckinsey.com

[7] G. Domingues-Olavarria, P. Fyhr, A. Reinap, M. Andersson, and M. Alakula, "From chip to converter: a complete cost model for power electronics converters," *IEEE Transactions on Power Electronics*, vol. PP, no. 99, pp. 1–1, 2017.

[8] G. Domingues-Olavarria, F. Márquez-Fernández, P. Fyhr, A. Reinap, M. Andersson, and M. Alakula, "Scalable performance, efficiency and thermal models for electric drive components used in powertrain simulation and optimization," in *2017 IEEE Transportation Electrification Conference and Expo (ITEC)*, June 2017.

[9] H.-A. Danielsson and N. G. Vagstedt. Worlds first electric road opens in sweden. [Online]. Available: https://www.scania.com/group/en/worlds-first-electric-road-opens-in-sweden/

[10] G. Asplund and B. Rehman, "Conductive feeding of electric vehicles from the road while driving," in *Electric Drives Production Conference (EDPC), 2014 4th International*, Sept 2014, pp. 1–9.

[11] T. Gustafsson and A. Johansson, "Comparison between battery electric vehicles and internal combustion engine vehicles fueled by electrofuels."

[12] V. S. ICT, "Slide-in electric road system: conductive project," Viktoria Swedish ICT on behalf of Scania and Volvo GTT, Tech. Rep., 2013. [Online]. Available: https://www.viktoria.se/sites/default/files/pub/www.viktoria.se/upload/publications/slide-in_conductive_project_report_draft_phase_1_2013-10-18.pdf

[13] Alstom. (2017) Aps - ground level power supply. [Online]. Available: http://www.alstom.com/products-services/product-catalogue/rail-systems/Infrastructures/products/aps-ground-level-power-supply/

[14] Elonroad. (2017) Elonroad electric road technology. [Online]. Available: http://elonroad.com

[15] I. S. Suh and J. Kim, "Electric vehicle on-road dynamic charging system with wireless power transfer technology," in *Electric Machines Drives Conference (IEMDC), 2013 IEEE International*, May 2013, pp. 234–240.

[16] W. Zhang, S. C. Wong, C. K. Tse, and Q. Chen, "An optimized track length in roadway inductive power transfer systems," *IEEE Journal of Emerging and Selected Topics in Power Electronics*, vol. 2, no. 3, pp. 598–608, Sept 2014.

[17] S. Lukic and Z. Pantic, "Cutting the cord: Static and dynamic inductive wireless charging of electric vehicles," *IEEE Electrification Magazine*, vol. 1, no. 1, pp. 57–64, Sept 2013.